UNIVERSITAT DE BARCELONA

Multiscale modelling of CO_2 hydrogenation reactions on Ni-based catalysts

Pablo Lozano Reis

Multiscale modelling of CO_2 hydrogenation reactions on Ni-based catalysts

Pablo Lozano Reis

UNIVERSITAT DE BARCELONA

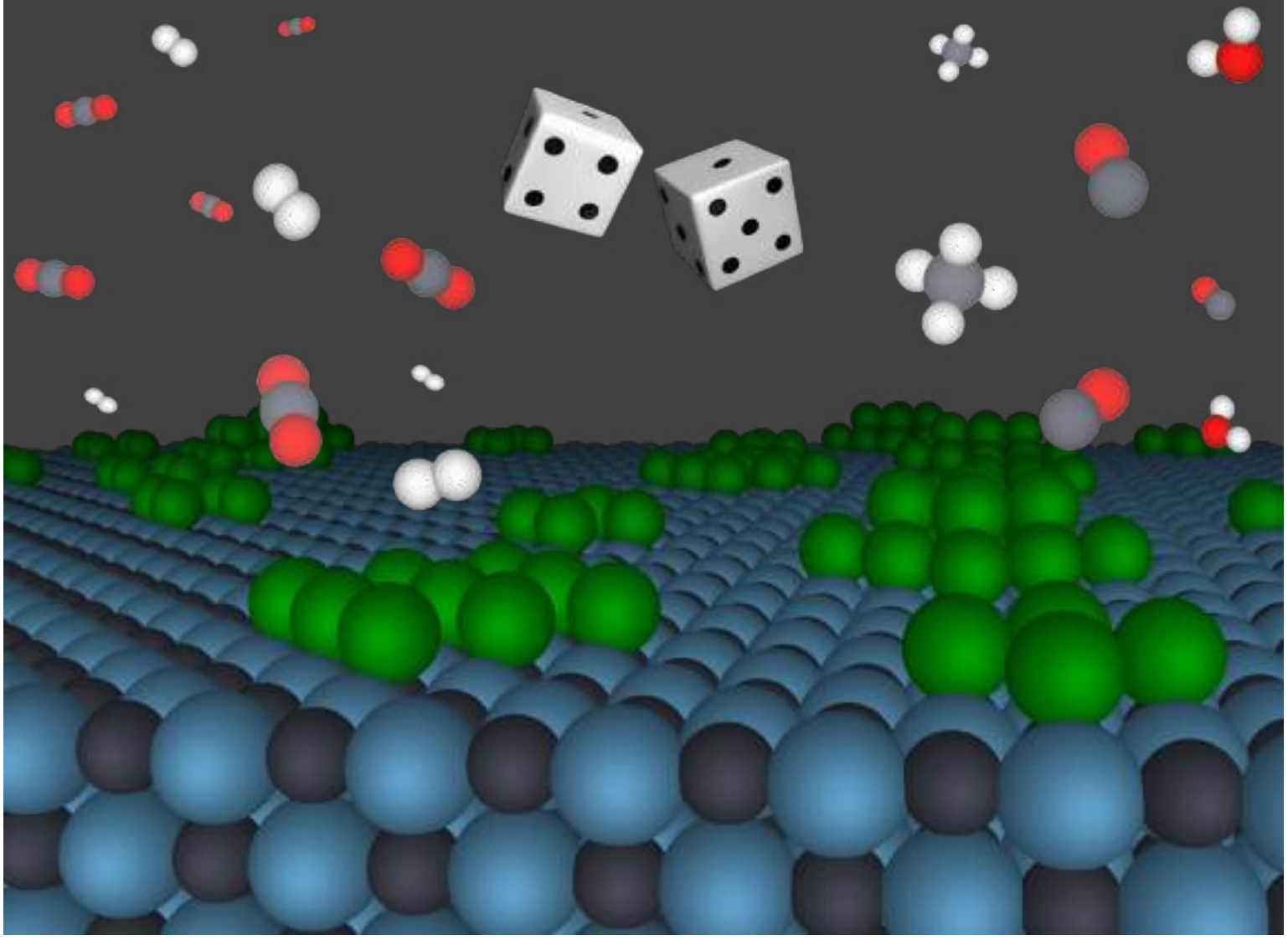

Memòria presentada per

Pablo Lozano Reis

Per optar al grau de Doctor per la

Universitat de Barcelona

Programa de doctorat en Química Teòrica i Modelització Computacional

Multiscale modelling of CO_2 hydrogenation reactions on Ni-based catalysts

Dirigida per:

Prof. Ramón Sayós Ortega
Universitat de Barcelona

Prof. Francesc Illas Riera
Universitat de Barcelona

Tutor:

Prof. Ramón Sayós Ortega
Universitat de Barcelona

UNIVERSITAT DE BARCELONA

Barcelona, 2023

A mi familia

Abstract

Global warming and climate change, mostly due to the increasing concentration of greenhouse gases in the atmosphere, are producing devastating effects. Among the different greenhouse gases, CO_2 is one of the major contributors. It is expected that, as a consequence of the ever increasing industry based on fossil fuels burning, the atmospheric amounts of CO_2 will still rise in the following decades. In that sense, several research groups have focused on different strategies to mitigate the CO_2 atmospheric concentration. Among the different possibilities, an interesting strategy is CO_2 valorization, which reduce the environmental impact related with carbon dioxide and, at the same time, generate new value-added chemicals, thus offering an economic incentive to CO_2 mitigation. In this regard, Ni-based catalysts have emerged as promising catalysts due to their relatively high activity at low cost. The aim of the present doctoral thesis is to study the CO_2 hydrogenation reaction for different well-defined models of Ni-based catalysts through a theoretical multiscale approach.

First, we have studied the complete CO_2 hydrogenation reaction over the extended Ni(111) surface and we have found that this surface produces CO rather than methane. We suggest that the experimental observations of methane are not because of the Ni(111) itself but rather because of other active Ni facets, the cooperation between different facets, the support effect or the interfacial sites lying in between the metal and the support. We have also studied the reverse water-gas shift reaction on a Ni/TiC model system. After a careful inspection of the structural, electronic, magnetic and catalytic properties of different Ni_n supported clusters we have chosen a Ni_4 cluster supported on TiC(001) as a model system for a deeper study. Based on kinetic Monte Carlo simulations, we have unveiled the boost of catalytic activity experimentally observed for the Ni/TiC system with respect to the clean TiC(001) surface, which we attributed to a synergic effect between the supported Ni cluster ant the TiC substrate in such a way that H is produced at the supported Ni cluster that further spillover to the TiC surface, where the hydrogenation reactions occur. Interestingly, coverage effects reveal a mismatch on the activity predictions from the density functional theory calculations and the kinetic Monte Carlo results. Finally, we have studied in detail the CO_2 hydrogenation reaction on a Ni_4 cluster supported on CeO_2(111). We have found that there is a synergic effect between the two three-fold hollow sites of the Ni cluster, which defines the catalytic activity and

selectivity. Moreover, we have shown the important role of the inclusion of some Eley-Rideal reactions on the final mechanism, activity and selectivity.

Agradecimientos

En primer lloc, vull agrair als meus directors de tesi, el Prof. Ramón Sayós i el Prof. Francesc Illas, tots els consells, l'ajuda i els ànims que m'han donant durant aquests anys. Ha sigut molt fàcil treballar amb vosaltres, sempre m'heu donant molta llibertat i molts bons consells, si ara soc millor científic en part és gràcies a vosaltres. També m'agradaria agrair al Dr. Pablo Gamallo que sempre m'ha ofert la seva ajuda i m'ha recolzat en aquelles decisions que a vegades han sigut difícils. I would also like to acknowledge Prof. Henrik Grönbeck for his patience and very good ideas and advices during my stay in Gothenburg. I hope we stay in touch for many years. Tack!

También me gustaría agradecer a aquellas personas que me he encontrado durante estos años de tesis en la Universidad. Una especial mención a mis excompañeros de despacho, los ahora ya doctores Hector Prats y Gerard Alonso. Ha sido un verdadero placer compartir con vosotros estos años juntos. Me habéis ayudado muchísimo siempre desinteresadamente y al final hemos creado una muy bonita amistad. También querría agradecer al Pol, al Dani y al Raúl, una de las cosas buenas de estos años de carrera, master y tesis a sido conoceros. En especial gracias Raúl por aguantar mis malos momentos y siempre aconsejarme de la mejor manera tanto en lo científico como en lo personal. Sé que el futuro te va a traer algo grande.

Por otro lado, me gustaría agradecer a toda mi gente de toda la vida que para mi forman parte de mi familia. Gracias Luis, Miki, Cesar, Alex, Sergio, Albert, Diana, Anna y Vasco por aguantarme durante tantos años. Gracias por apoyarme y comprenderme los días que estaba bajo de animo y por entender que a veces haya estado ausente. Sobretodo gracias por ser como sois y por esta amistad que tenemos. Sabéis que os quiero un montón! Parte de esto también es vuestro.

Quiero agradecer también a mi madre y a mi hermano por todo lo que han luchado y por todo lo que me han ayudado en la vida. No conozco personas más fuertes que ellos. Gracias de todo corazón por contribuir tanto en quien soy. Esto no seria realidad sin vuestro apoyo y paciencia. Seguramente si, tu padre estaría orgulloso. Os quiero!

Por último, quería agradecerle a Laura todo lo que hace por mi. Eres una persona genial, te portas súper bien conmigo y me haces mejor persona. Gracias por hacer que estos últimos meses hayan sido mucho más llevaderos, desde luego que sin ti al lado no hubiera sido igual. Te quiero mucho y me alegro muchísimo de haberte conocido y que formes parte de mi vida!

Muchas gracias a los que están y a los que se fueron.

List of Abbreviations

AIMD	Ab inito Molecular Dynamics
AS-kMC	Accelerated Superbasin kinetic Monte Carlo
BEEF-vdW	Bayesian Error Estimation Functional-van der Waals
DFT	Density Functional Theory
DOS	Density of States
ER	Eley-Rideal
fcc	face centered cubic
FRM	First Reaction Method
GGA	Generalized Gradient Approximation
GTO	Gaussian-Type Orbitals
kMC	kinetic Monte Carlo
LCAO	Linear Combination of Atomic Orbitals
LDA	Local Density Approximation
LDOS	Local Density of States
MFA	Mean-Field Approximation
MM	Microkinetic Modelling
PBE	Perdew-Burke-Ernzerhof
PDOS	Partial Density of States
PED	Potential Energy Diagram
PES	Potential Energy Surface
PtG	Power-to-Gas

PW	Plane Wave
RSM	Random Selection Method
RWGS	Reverse Water-Gas Shift
SMSI	Strong Metal Support Interactions
STO	Slater-Type Orbitals
TMC	Transition Metal Carbide
TS	Transition State
TST	Transition State Theory
vdW	van der Waals
VSSM	Variable Step Size Method
XPS	X-ray Photoelectron Spectroscopy

Table of Contents

List of Abbreviations **i**

1. Introduction **1**

1.1. Motivation and outline of the doctoral thesis 1

1.2. Climate change and CO_2 conversion 3

1.3. A brief introduction on catalysis 4

1.4. References 7

2. Theoretical background **13**

2.1. The Schrödinger equation 13

2.2. Density Functional Theory 15

2.2.1. The Hohenberg and Kohn theorems 16

2.2.2. The Kohn-Sham equations 16

2.2.3. Exchange-correlation functionals 18

2.2.4. Including dispersion 18

2.2.5. Periodic DFT calculations 20

2.3. Transition State Theory 21

2.4. Kinetic Monte Carlo simulations 23

2.4.1. The Markovian master equation 24

2.4.2. kMC algorithms 25

2.4.3. Lattice-gas reaction model 27

2.4.4. Transition probabilities calculation 29

2.4.5. Including lateral interactions 33

2.4.6. Time scale disparity problem 38

2.5. References 40

3. CO_2 conversion over Ni(111) **45**

3.1. Introduction 45

3.2. Complexity of the reaction network 46

3.3. Results 47

3.3.1. DFT results 47

3.3.2. kMC results 52

3.4. Summary and conclusions 54

3.5. Publications 56

3.6. References 69
4. RWGS on Ni_4/TiC and TiC(001) surfaces 75
4.1. Introduction 75
4.2. Models 78
4.3. Results 79
4.3.1. Structural, magnetic and electronic properties of Ni_n/TiC systems 79
4.3.2. CO_2 and H_2 activation on Ni_n/TiC 86
4.3.2.1. CO_2 and H_2 adsorption 87
4.3.2.2. CO_2 and H_2 dissociation 89
4.3.3. Study of the RWGS reaction on the Ni_4/TiC and TiC systems 93
4.3.3.1. DFT results 94
4.3.3.2. kMC simulations 97
4.3.3.3. Comparing Ni_4/TiC and TiC activity for the RWGS reaction 101
4.4. Summary and conclusions 105
4.5. Publications 107
4.6. References 135
5. CO_2 hydrogenation over Ni_4/CeO2 143
5.1. Introduction 143
5.2. Lattice model and reaction network 144
5.3. Results 146
5.3.1. DFT results 147
5.3.2. kMC results 152
5.4. Summary and conclusions 160
5.5. Publications 163
5.6. References 195
Conclusions 201
List of Publications 205
Appendices 207
A. Supporting information: "A Comprehensive Density Functional and Kinetic Monte Carlo Study of CO_2 Hydrogenation on Well-Defined Ni/CeO_2: Role of Eley-Rideal Reactions" **207**

Chapter 1

Introduction

1.1. Motivation and outline of the doctoral thesis

The global warming and climate change, mostly due to the increasing concentration of greenhouse gases in the atmosphere, are producing devastating consequences for the environment and life of many ecosystems which directly turns into a harmful impact on human societies. Among the different greenhouse gases, CO_2 is one of the major contributors to the global warming and in the following years it is likely that the atmospheric CO_2 amounts will still rise as a consequence of the ever-growing industry system based on fossil fuels burning. Even though this issue is on the agenda of several governments which have claimed for the zero-carbon neutrality for the year 2050, one cannot completely trust their statement. Therefore, as a way to reverse this situation, CO_2 valorization turns to be a low-cost strategy to, at the same time, reduce the environmental impact related to carbon dioxide and generate value-added chemical commodities. Thus, this defines the main goal of the present doctoral thesis: to contribute to understand how catalysts, and in particular Ni-based catalysts, act at the atomistic level and how they behave under real working conditions for several CO_2 conversion reactions. The gained insights can guide experimentalists and are thought to be essential for rational catalyst design.

The doctoral thesis is structured in 8 chapters. In Chapter 1 the problematic of climate change and the importance of CO_2 conversion in order to reverse the actual situation is introduced, along with a brief introduction of catalysis. In Chapter 2 an overview of the theoretical framework and computational methods that are used on the present thesis is briefly described. Thus, Chapter 2 starts by introducing quantum mechanics and the Schrödinger equation in Section 2.1. Next, Section 2.2 summarizes the basis of Density Functional Theory (DFT) and its practical implementation. In Section 2.3 the Transition State Theory (TST) is introduced, which allows to compute thermal rate constants of surface processes from the DFT data. Finally, in Section 2.4 the kinetic

Monte Carlo (kMC) method is explained, which using the TST derived rate constants, allows to simulate the time evolution of the system under real working conditions. The description of the original results starts in Section 3 with the study of the CO_2 hydrogenation reaction over the Ni(111) surface by means of kMC simulations that are carried out using the DFT data obtained also in this thesis. The study focuses on the Ni(111) facet as this is the most stable one thus, likely to be abundant on large nanoparticles, which requires a deep understanding on the mechanism that governs the reaction on such surface. Chapter 4 deals with the study of the Reverse Water-Gas Shift (RWGS) reaction catalyzed by TiC(001) and Ni/TiC(001) system, and it is divided in three specific parts. The first part focuses on the structural, electronic and magnetic properties of Ni clusters of different sizes and morphologies supported on the TiC(001) surface, which is required for a proper conceptualization of the different possible models. The next part focuses on the study of the CO_2 and H_2 activation for some of the previous models and gives some insights about the potential of the models to capture the boost of activity that is observed for Ni/TiC with respect to the bare TiC(001) surface. The last part, consist on a thorough study of the RWGS reaction catalyzed precisely by the Ni/TiC(001) and TiC(001) systems by means of kMC simulations based on DFT data. Taking benefit of the two previous studies a Ni_4 cluster supported over TiC(001) is used as the prototypical model to study the effect of the TiC support on the reactivity of Ni small clusters. This last part reveals the reasons of the boost of activity observed for the Ni/TiC system with respect to the bare TiC surface. In Chapter 5, we turn again our interest on the CO_2 hydrogenation reaction to methane and study this reaction for the Ni/CeO_2 system by means of kMC simulations using DFT data. In particular, the Ni_4/CeO_2 model is selected to explain the reactivity under real working conditions. This allows us to unravel the main mechanism that governs the reaction and give some insights about the activity and selectivity patterns observed. Moreover, we also analyze the effect of including some Eley-Rideal (ER) reactions, on the activity, selectivity and main mechanism that drives the reaction. Finally, the main conclusions of this doctoral thesis are reported and a list of the publications that have come out from the following results is provided.

1.2. Climate change and CO_2 conversion

The Industrial Revolution process originated on the 18th century on USA and Western Europe meant the transition from manual to machine manufacture on industries triggering numerous advances for the society while, at the same time, producing a dramatic, at that time unexpected, environmental cost. This change in the goods production caused a drastic increase of anthropogenic CO_2 as the result of the incessant burnt of fossil fuels to provide the energetic requirements that industrial processes require. The amount of atmospheric CO_2 determined from air extracted from ices of Greenland and Antarctica was ~278 ppm in 1750, some years before the Industrial Revolution began.[1] Since 1958, systematic measurements of atmospheric CO_2 began in the Manua Loa laboratory with a first measurement of ~315 ppm that has drastically increased to a value of ~405 ppm in 2017,[1] due to the ever-growing world energy demand. The severe increase of anthropogenic CO_2 is extremely dangerous for the ecosystems as CO_2 is among the different greenhouse gases the major contributor to global warming and ocean acidification.[2,3] Moreover, it is expected that atmospheric CO_2 will be still rising in the following years as unfortunately, satisfying the complete current world energy requirements with only green energies is still remote.[4,5] Therefore, many efforts are being addressed towards the catalytic CO_2 conversion into new value-added chemicals of industrial interest such as CO, CH_4, methanol or formaldehyde to name a few.[6-10] This strategy involves at the same time reduce the amounts of atmospheric CO_2 to generate valuable energy carriers, thus creating a cyclic energy economy.

In the past few decades, the Power-to-Gas (PtG) technology[11,12] has attracted interest as a promising option to absorb and exploit surplus renewable energy to recycle CO_2. The PtG concept is based on using the excess of renewable energies (i.e., excess of wind or solar power) for the water splitting to further utilize the produced H_2 for CO_2 hydrogenation toward different chemicals. The selectivity towards the desired chemical can be tuned by the choice of the metal and support used for the catalytic CO_2 hydrogenation. Among the different products that can be obtained, methanol,[13-18] methane[19-32] and CO,[24,33-38] have gained increasing interest due to the various possible applications either as fuels or in syngas processes. Both, methane and CO can be obtained using Ni-based catalysts. These catalysts are of particular interest due to its relatively high activity and its economic viability in comparison to precious metals.[39,40] Methane is obtained after complete reduction of CO_2 via the well-known Sabatier reaction (Eq. 1.1),

while CO is formed after partial CO_2 reduction via the Reverse Water-Gas Shift reaction (Eq. 1.2).

$$CO_2 + 4\,H_2 \rightarrow CH_4 + 2H_2O \qquad \Delta H^o_{298K} = -165\ kJ/mol \qquad (1.1)$$

$$CO_2 + \ H_2 \rightarrow CO + H_2O \qquad \Delta H^o_{298K} = 41\ kJ/mol \qquad (1.2)$$

Both reactions include the same reactants, CO_2 and H_2, the RWGS reaction being an intermediate step of the complete CO_2 hydrogenation to methane, meaning that both reactions can coexist; for this reason, it is difficult to obtain the desired selectivity towards one of the products. As one can see in Eq. 1.1, the Sabatier reaction is exothermic; thus, favored at lower temperatures while higher temperatures would favor the RWGS reaction. Nevertheless, one always prefers to work at mild conditions to reduce costs but at the same time reach high activity and selectivity. Depending on the nature of the support, shape and size of the Ni subnano clusters or nanoparticles, the metal-support interactions and the working conditions used, it is possible to tune the selectivity towards one of the desired products. For instance, Rodriguez et al.,[38] studied the CO_2 hydrogenation reaction over a series of M/TiC catalysts (M=Ni, Au, Cu) and observe a high selectivity towards CO even working at moderate temperatures (i.e., 500 to 600K) and pressures of 0.5 atm and 4.5 atm for CO_2 and H_2, respectively, which in principle should benefit the CH_4 formation. On the other hand, Zheng et al.[23], studied the CO_2 hydrogenation over three Ni/CeO_2 systems with different nanoparticles sizes and found that smaller nanoparticles were more selective to CO and that larger nanoparticles present superior CH_4 selectivity. These two examples exemplify how choosing different conditions can modify the selectivity and catalytic activities. The understanding of the atomistic properties that are responsible for the activity and selectivity of a specific catalyst are essential for proper rational catalyst design and become the core of the present doctoral thesis.

1.3. A brief introduction on catalysis

Catalysis aims at accelerating the rate of a chemical reaction by a substance, the catalyst, that is neither consumed nor generated in the process. The term catalysis was coined by the Swedish chemist Jöns Jacob Berzelius in 1835 who wrote that by the term catalysis he meant "*the property of exerting on other bodies an action which is very different from*

chemical affinity. By means of this action, they produce decomposition in bodies, and form new compounds into the composition of which they do not enter".[41] Some decades later, Wilhelm Ostwald, who received the Novel Prize in Chemistry in 1909 for his work on catalysis, chemical equilibria and reaction velocities, suggested that a catalyst was a body that modifies the rate of a chemical reaction without changing the thermodynamic equilibrium, introducing thermodynamics on the catalysis definition. Another great contributor to catalysis was Paul Sabatier, who received the Nobel Prize in Chemistry in 1912 for his developments on the methods of catalytic hydrogenation. He formulated a chemical theory of catalysis involving the formation of unstable chemical compounds as intermediate species, which determined the direction and rate of the reaction.[42] Nowadays, the IUPAC definition of catalyst is "*A substance that increases the rate of a reaction without modifying the overall standard Gibbs energy change in the reaction*".[43] In practice, a catalyst is a substance that modifies the reaction mechanism and produce alternative paths with lower activation energies as shown in Figure 1.1.

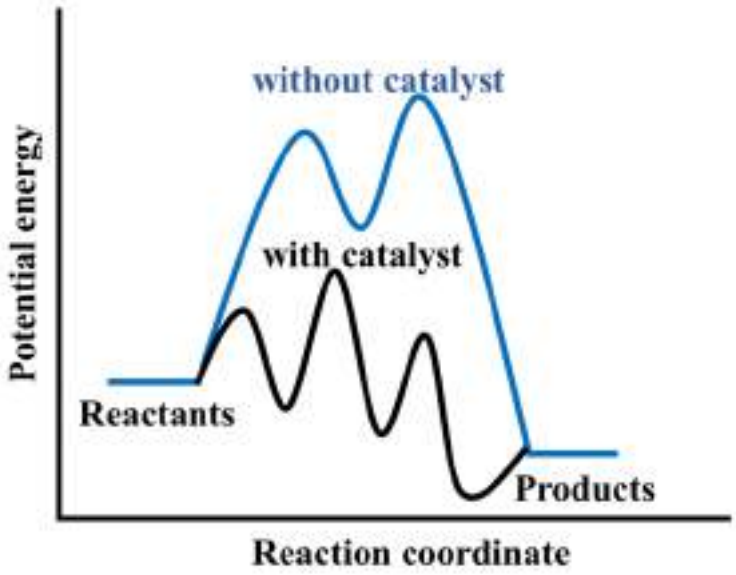

Figure 1.1. Schematic representation of a generic energy profile for a complex reaction. The blue line represents the energy barrieries needed without the catalyst and the black line represents the different energy barriers to surmount the possible elementary steps when the reaction is catalyzed.

The catalyst interacts with the reactants in a specific way to produce some intermediate species that ultimately lead to some products with the catalyst being regenerated to its original form. Since reactants and products are the same for the catalyzed and non-catalyzed reactions, the thermodynamics of the reaction is not

modified while it modifies the kinetics of the chemical reaction. Catalysis can be classified as homogeneous catalysis, in which only one phase is involved, and heterogeneous catalysis, in which the reaction occurs at or near the interface between two phases. The presence of enzymes in some biological reactions is also a type of catalysis.

Catalysis is fundamental in our daily life as it is involved at some point in the processing of over 80% of all manufactured products.[44] However, the ever-growing demand of products and the concomitant effect of chemical industry on the climate change make paramount the exploration of new catalysts that represent a low environmental and economic cost but at the same time with high conversions, activities and selectivity. Therefore, a deep understanding of the principles of catalysis, hereafter heterogeneous catalysis, are required for rational design of novel catalysts. This is the challenge that several experimental and theoretical research groups are taking and carrying out catalysis research. Unfortunately, from the experimental point of view, it is extremely challenging to clearly understand why a given material is very active or selective towards the desired product and how it is affected by working conditions of pressure and temperature. In the end, this is crucial for a rational design of novel catalysts. Despite interesting advances in the use of experimental *operando* techniques[45,48] that allow monitoring in situ and under relevant working conditions the catalyst evolution, a detailed experimental description of the active sites and dominant reaction paths is still out of reach. Therefore, a deep understanding of the catalytic performance is generally unfeasible without a clear guidance from theoretical modelling, ideally going from the atomic and molecular level to the macroscopic regime. Quantum mechanical calculations provide useful insights into the molecular reaction mechanism, such as the energetics of the different adsorbates and transition states involved in the whole reaction. However, this atomistic and static picture is sometimes not enough to really understand the time evolution of the system under real working conditions. Therefore, in order to unravel the dominant mechanisms and deeply understand the role of each specific site, elementary step and intermediate one must couple the quantum mechanical calculations with kinetic modelling techniques[49-53]. Note that theoretical investigations are based on model catalysts, normally idealized catalysts which, even being different from real catalysts, allows one to reach a quite detailed understanding. The study of model catalysts by a multiscale approach is precisely the goal of the present doctoral thesis.

1.4. References

1. E.J. Dlugokencky, B.D. Hall, S. A. Montzka, G. Dutton, J. Mühle, J. W. Elkins, State of the Climate in 2017. Bulletin of the American Meteorological Society, 99, 2018, S46-S49.

2. Seneviratne, S. I.; Donat, M. G.; Pitman, A. J.; Knutti, R.; Wilby, R. L. Allowable CO_2 emissions Based on Regional and Impact- Related Climate Targets. *Nature,* **2016**, 529, 477−483

3. Licker, R.; Ekwurzel, B.; Doney, S. C.; Cooley, S. R.; Lima, I. D.; Heede, R.; Frumhoff, P. C. Attributing Ocean Acidification to Major Carbon Producers. *Environ. Res. Lett.*, **2019**, 14, 124060-124074.

4. Barbir, F. Transition to Renewable Energy Systems with Hydrogen as an Energy Carrier. *Energy*, **2009**, 34, 308−312.

5. Dincer, I. Renewable Energy and Sustainable Development: A Crucial Review. *Renew. Sust. Energ. Rev.*, **2000**, 4, 157−175.

6. Jalama, K. Carbon Dioxide Hydrogenation over Nickel-, Ruthenium-, and Copper-based Catalysts: Review of Kinetics and Mechanism. *Catal. Rev.: Sci. Eng.*, **2017**, 59, 95−164.

7. Kattel, S.; Liu, P.; Chen, J. G. Tuning Selectivity of CO_2 Hydrogenation Reactions at the Metal/Oxide Interface. *J. Am. Chem. Soc.*, **2017**, 139, 9739−9754.

8. Li, W.; Wang, H.; Jiang, X.; Zhu, J.; Liu, Z.; Guo, X.; Song, C. A Short Review of Recent Advances in CO_2 Hydrogenation to Hydrocarbons over Heterogeneous Catalysts. *RSC Adv.*, **2018**, 8, 7651−7669.

9. Wang, W.; Wang, S.; Ma, X.; Gong, J. Recent Advances in Catalytic Hydrogenation of Carbon Dioxide. *Chem. Soc. Rev.*, **2011**, 40, 3703−3727.

10. Nie, X.; Li, W.; Jiang, X.; Guo, X.; Song, C. Recent Advances in Catalytic CO_2 Hydrogenation to Alcohols and Hydrocarbons. *Adv. Catal.,* **2019**, 65, 121−133.

11. Centi, G.; Quadrelli, E. A.; Perathoner, S. Catalysis for CO_2 conversion: A Key Technology for Rapid Introduction of Renewable Energy in the Value Chain of Chemical Industries. *Energy Environ. Sci.,* **2013**, 6, 1711−1731.

12. Götz, M.; Lefebvre, J.; Mörs, F.; Koch, A. M.; Graf, F.; Bajohr, S.; Reimert, R.; Kolb, R. Renewable Power-to-Gas: A Technological and Economic Review. *Renew. Energ.*, **2016**, 85, 1371−1390.

13. Hartadi, Y.; Widmann, D.; Behm, R. J. CO_2 Hydrogenation to Methanol on Supported Au Catalysts under Moderate Reaction Conditions: Support and Particle Size Effects. *ChemSusChem*, **2015**, 8, 456−465.

14. Yang, X.; Kattel, S.; Senanayake, S. D.; Boscoboinik, J. A.; Nie, X.; Graciani, J.; Rodriguez, J. A.; Liu, P.; Stacchiola, D. J.; Chen, J. G. Low Pressure CO_2 Hydrogenation to Methanol over Gold Nanoparticles Activated on a CeO_X /TiO_2 Interface. *J. Am. Chem. Soc.*, **2015**, 137, 10104−10107.

15. Sakurai, H.; Haruta, M. Synergism in Methanol Synthesis from Carbon Dioxide over Gold Catalysts Supported on Metal Oxides. *Catal. Today*, **1996**, 29, 361−365.

16. Qu, J.; Zhou, X.; Xu, F.; Gong, X. Q.; Tsang, S. C. E. Shape Effect of Pd-promoted Ga_2O_3 Nanocatalysts for Methanol Synthesis by CO_2 Hydrogenation. J. *Phys. Chem. C*, **2014**, 118, 24452−24466.

17. Bahruji, H.; Bowker, M.; Hutchings, G.; Dimitratos, N.; Wells, P.; Gibson, E.; Jones, W.; Brookes, C.; Morgan, D.; Lalev, G. Pd/ZnO Catalysts for Direct CO_2 Hydrogenation to Methanol. *J. Catal.,* **2016**, 343, 133−146.

18. Kuld, S.; Thorhauge, M.; Falsig, H.; Elkjær, C. F.; Helveg, S.; Chorkendorff, I.; Sehested, J. Quantifying the Promotion of Cu Catalysts by ZnO for Methanol Synthesis. *Science*, **2016**, 352, 969−974.

19. Yu, K. P.; Yu, W. Y.; Kuo, M. C.; Liou, Y. C.; Chien, S. H. Pt/ titania-nanotube: A Potential Catalyst for CO_2 Adsorption and Hydrogenation. *Appl. Catal. B,* **2008**, 84, 112−118.

20. Falbo, L.; Martinelli, M.; Visconti, C. G.; Lietti, L.; Bassano, C.; Deiana, P. Kinetics of CO_2 Methanation on a Ru-based Catalyst at Process Conditions Relevant for Power-to-Gas Applications. *Appl. Catal. B*, **2018**, 225, 354-363

21. Jimeńez, V.; Sańchez, P.; Panagiotopoulou, P.; Valverde, J. L.; Romero, A. Methanation of CO, CO_2 and Selective Methanation of CO, in Mixtures of CO and CO_2, over Ruthenium Carbon Nanofibers Catalysts. *Appl. Catal. A,* **2010**, 390, 35−44.

22. Eckle, S.; Anfang, H. G.; Behm, R. J. Reaction Intermediates and Side Products in the Methanation of CO and CO_2 over Supported Ru catalysts in H_2 -rich Reformate Gases. *J. Phys. Chem. C,* **2011**, 115, 1361−1367.

23. Zheng, H.; Liao, W.; Ding, J.; Xu, F.; Jia, A.; Huang, W.; Zhang, Z. Unveiling the Key Factors in Determining the Activity and Selectivity of CO_2 Hydrogenation over Ni/CeO_2 Catalysts. *ACS. Catal.,* **2022**, 12, 15451-15462.

24. Park, J. N.; McFarland, E. W. A Highly Dispersed Pd−Mg/SiO_2 Catalyst Active for Methanation of CO_2. *J. Catal.,* **2009**, 266, 92−97.

25. Chang, F. W.; Kuo, M. S.; Tsay, M. T.; Hsieh, M. C. Hydrogenation of CO_2 over Nickel Catalysts on Rice Husk Ash- alumina Prepared by Incipient Wetness Impregnation. *Appl. Catal. A,* **2003**, 247, 309−320.

26. Aziz, M. A. A.; Jalil, A. A.; Triwahyono, S.; Mukti, R. R.; Taufiq- Yap, Y. H.; Sazegar, M. R. Highly Active Ni-promoted Mesostructured Silica Nanoparticles for CO_2 Methanation. *Appl. Catal. B,* **2014**, 147, 359−368.

27. Tada, S.; Shimizu, T.; Kameyama, H.; Haneda, T.; Kikuchi, R. Ni/CeO_2 Catalysts with High CO_2 Methanation Activity and High CH_4 Selectivity at Low Temperatures. *Int. J. Hydro. Energ.,* **2012**, 37, 5527−5531.

28. Ocampo, F.; Louis, B.; Kiwi-Minsker, L.; Roger, A. C. Effect of Ce/Zr Composition and Noble Metal Promotion on Nickel Based CexZr1−xO2 Catalysts for Carbon Dioxide Methanation. *Appl. Catal. A,* **2011**, 392, 36−44.

29. Zhou, G.; Liu, H.; Cui, K.; Xie, H.; Jiao, Z.; Zhang, G.; Xiong, K.; Zheng, X. Methanation of Carbon Dioxide over Ni/CeO2 catalysts: Effects of Support CeO2 Structure. *Int. J. Hydro. Energ.,* **2017**, 42, 16108−16117.

30. Hwang, S.; Hong, U. G.; Lee, J.; Baik, J. H.; Koh, D. J.; Lim, H.; Song, I. K. Methanation of Carbon Dioxide over Mesoporous Nickel− M−alumina (M = Fe, Zr, Ni, Y, and Mg) Xerogel Catalysts: Effect of Second Metal. *Catal. Lett.,* **2012**, 142, 860−868.

31. Heine, C.; Lechner, B. A. J.; Bluhm, H.; Salmeron, M. Recycling of CO2: Probing the Chemical State of The Ni(111) Surface During the Methanation Reaction with Ambient-pressure X-ray Photoelectron Spectroscopy. *J. Am. Chem. Soc.*, **2016**, 138, 13246−13252.

32. Muroyama, H.; Tsuda, Y.; Asakoshi, T.; Masitah, H.; Okanishi, T.; Matsui, T.; Eguchi, K. Carbon Dioxide Methanation over Ni Catalysts Supported on Various Metal Oxides. *J. Catal.*, **2016**, 343, 178−126.

33. Kattel, S.; Yan, B.; Chen, J. G.; Liu, P. CO2 Hydrogenation on Pt, Pt/SiO2 and Pt/TiO2: Importance of Synergy between Pt and Oxide Support. *J. Catal.,* **2016**, 343, 115−126.

34. Kusama, H.; Bando, K. K.; Okabe, K.; Arakawa, H. CO2 Hydrogenation Reactivity and Structure of Rh/SiO2 Catalysts Prepared from Acetate, Chloride and Nitrate Precursors. *Appl. Catal. A*, **2001**, 205, 285−294.

35. Kharaji, A. G.; Shariati, A.; Takassi, M. A. A Novel γ-alumina Supported Fe-Mo Bimetallic Catalyst for Reverse Water Gas Shift Reaction. *Chin. J. Chem. Eng.*, **2013**, 21, 1007−1014.

36. Yang, L.; Pastor-Perez, L.; Gu, S.; Sepulveda-Escribano, A.; Reina, T. R. Highly Efficient Ni/CeO_2-Al_2O_3 Catalysts for CO_2 Upgrading Via Reverse Water-gas Shift: Effect of Selected Transition Metal Promoters. *Appl. Catal. B,* **2018**, 232, 464−471.

37. Sun, F.; Yan, C.; Wang, Z.; Guo, C.; Huang, S. Ni/Ce−Zr−O Catalyst for High CO_2 Conversion During Reverse Water Gas Shift Reaction (RWGS). *Int. J. Hydro. Energy*, **2015**, 40, 15985−15993

38. Rodriguez, J. A.; Evans, J.; Feria, L.; Vidal. A. B.; Liu, P.; Nakamura, K.; Illas, F. CO_2 Hydrogenation on Au/TiC, Cu/TiC, and Ni/TiC Catalysts: Production of CO, Methanol, and Methane. *J. Catal.*, **2013**, 307, 162-169.

39. Aziz, M. A. A.; Jalil, A. A.; Triwahyono, S.; Ahmad, A. CO_2 Methanation over Heterogeneous Catalysts: Recent Progress and Future Prospects. *Green Chem.*, **2015**, 17, 2647−2663.

40. Wei, W.; Jinlong, G. Methanation of Carbon Dioxide: an Overview. *Front. Chem. Sci. Eng.*, **2011**, 5, 2−10.

41. J. Wisniak. The History of Catalysis. From the Beginning to Nobel Prizes, *Educ. Quim.*, **2010**, 21, 60–69.

42. Fechete, I. Paul Sabatier – The Father of the Chemical Theory of Catalysis. *CR. Chim.*, **2016,** 19, 1374-1381.

43. IUPAC. Compendium of Chemical Terminology, 2nd ed. (the "Gold Book"). Compiled by A. D. McNaught and A. Wilkinson. Blackwell Scientific Publications, Oxford, **1997**.

44. Catlow, C. R.; Davidson, M.; Hardacre, C.; Hutchings, G. J. Catalysis Making the World a Better Place. *Phil. Trans. R. Soc. A,* **2016**, 374, 20150089-20150090.

45. Weckhuysen, B. M. Determining the Active Site in Catalytic Process: Operando Spectroscopy is More than a Buzzword. *Phys. Chem. Chem. Phys.*, **2003**, 5, 4351-4360.

46. Topsøe, H. Developments in Operando Studies and in Situ Characterization of Heterogeneous Catalysts. *J. Catal.*, **2003** ,216, 155-164.

47. Handoko, A. D.; Wei, F.; Jenndy.; Yeo, B. S.; Seh, Z. W. Understanding Heterogeneous Electrocatalytic Carbon Dioxide Reduction through Operando Techniques. *Nat. Catal.,* **2018**, 1, 922–934.

48. Feng, K.; Wang, Y.; Guo, M.; Zhang, J.; Li, Z.; Deng, T.; Zhang, Z.; Yan, B. In-situ/Operando Techniques to Identify Active Sites for Thermochemical Conversion of CO_2 over Heterogeneous Catalysis. *J. Energy Chem.*, **2021**, 62, 153-171.

49. Bruix, A.; Margraf, J. T.; Andersen, M.; Reuter, K. First-Principles-Based Multiscale Modeling of Heterogeneous Catalysis. *Nat. Catal.,* **2019**, 2, 659-670.

50. Pineda, M.; Stamatakis, M. Kinetic Monte Carlo Simulations for Heterogeneous Catalysis: Fundamentals, Current Status, and Challenges. *J. Chem. Phys.*, **2022**, 156, 120902-120931.

51. Grajciar, L.; Heard, J. C.; Bondarenko, A. A.; Polynski, M. V.; Meeprasert, J.; Pidko, E. A.; Nachtigall, P. Towards Operando Computational Modeling in Heterogeneous Catalysis. *Chem. Soc. Rev.*, **2018**, 47, 8307-8348.

52. Motagamwala, A. H.; Dumesic, J. A. Microkinetic Modeling: a Tool for Rational Catalyst Design. *Chem. Rev.*, **2021**, 121, 1049-1076.

53. Lozano-Reis, P.; Prats., H.; Sayos, R.; Illas, F. Limitations of Free Energy Diagrams to Predict the Catalytic Activity: The Reverse Water Gas Shift Reaction Catalyzed by Ni/TiC. *J. Catal.*, **2023**, 425, 203-211.

Chapter 2

Theoretical background

This chapter aims to provide a general overview of the theoretical framework behind the present work and to outline the different computational methods used in this doctoral thesis. The computational approaches employed in this work range from quantum mechanics-based methods to kinetic modeling techniques such as Density Functional Theory based calculations and kinetic Monte Carlo simulations, respectively. The former allows to study small to medium size systems containing up to hundreds of atoms with a great level of detail, describing, for instance, the interactions between the different species and the support. The latter, taking benefit of the obtained DFT data and the appropriate derivation of thermal rate constants from Transition State Theory provides the time evolution of the system along with macroscopic observables under real catalytic conditions.

2.1. The Schrödinger equation

The time-dependent Schrödinger equation[1] describes the electronic structure of matter at a given instant (t) through its wave function denoted as $\Psi_t(\vec{R},\vec{r})$ which depends on the positions of nuclei and electrons described by vectors $\vec{R}$ and $\vec{r}$, respectively, and parametrically on *t.* Even though a complete description of the system requires the resolution of the time-dependent Schrödinger equation, for a large number of problems it usually suffices to consider the non-relativistic time-independent Schrödinger equation

$$\hat{H}\Psi\left(\vec{R},\vec{r}\right) = E\Psi(\vec{R},\vec{r}) \tag{2.1}$$

where $\hat{H}$ is the Hamiltonian operator that after applying it to the system wave function give the total system energy, *E*. The Hamiltonian is defined as the sum of the kinetic and potential energy operators

$$\hat{H} = \hat{T}_e + \hat{T}_N + \hat{V}_{ee} + \hat{V}_{eN} + \hat{V}_{NN} \tag{2.2}$$

where $\hat{T}_e$ and $\hat{T}_N$ are the kinetic energy of the electrons and the nuclei, respectively, $\hat{V}_{ee}$ refers to the electron-electron repulsion, $\hat{V}_{NN}$ stands for the nuclei-nuclei repulsion and $\hat{V}_{eN}$ is the electron-nuclei interaction potential. To solve the Schrödinger equation, the Born-Oppenheimer approximation is usually invoked.[2] This approximation assumes that the nuclei velocity is much slower than that of the electrons as a consequence of the considerable superior mass of nuclei compared to electrons. This implies electrons to be moving and almost instantly adapting to the field generated by the fixed nuclei at certain positions. Within this approximation, fixing the nuclei positions it is possible to factorize the total wave function onto its electronic and nuclear counterparts

$$\Psi(\vec{R},\vec{r}) = \Psi_{el,R}(\vec{r})\Psi_{nuc}(\vec{R}) \tag{2.3}$$

where $\Psi_{el,R}(\vec{r})$ is the electronic wave function which explicitly depends on the electrons coordinates but parametrically on the nuclear coordinates and $\Psi_{nuc}(\vec{R})$ is the nuclear wave function that depends only on the nuclear coordinates.

From the electronic wave function it is in principle possible to calculate the electronic energy of the system ($E_{el,R}$) after the resolution of the electronic Schrödinger equation

$$\hat{H}_{el,R}\Psi_{el,R}(\vec{r}) = E_{el,R}\Psi_{el,R}(\vec{r}) \tag{2.4}$$

where $\hat{H}_{el,R}$ is the electronic Hamiltonian that can be defined grouping all the terms that depend on the electrons (i.e., $\hat{T}_e$, $\hat{V}_{ee}$ and $\hat{V}_{eN}$). Then, from the nuclear Hamiltonian ($\hat{H}_{nuc}$) it is possible to calculate the total energy of the system (E_{tot}) after solving the nuclear Schrödinger equation

$$\hat{H}_{nuc}\Psi_{nuc}(\vec{R}) = (\hat{T}_N + \hat{V}_{NN} + E_{el,R})\Psi_{nuc}(\vec{R}) = E_{tot}\Psi_{nuc}(\vec{R}) \tag{2.5}$$

Solving Eq. 2.4 and Eq. 2.5 provide a complete set of solutions either of electronic states or of quantum states for the system of interest. In absence of electromagnetic radiation, all chemical processes take place in the ground state and, consequently, most approaches aim to provide accurate estimates of the ground state energy and properties.

In general, static electronic structure calculations within the Born-Oppenheimer approximation neglect the nuclear kinetic energy ($\hat{T}_N$) and combine the nuclear-nuclear repulsion ($\hat{V}_{NN}$), which is constant for a given nuclear position, with the electronic energy

($E_{el,R}$). This magnitude corresponds to the potential felt by the nuclei and, unless otherwise stated, constitutes the ground state potential energy surface (PES) in which nuclei can move. Overall, the PES defines the system total energy as a function of the nuclei positions which is key as it defines the microscopic mechanisms governing chemistry most often in the ground state but PES for excited states can also be obtained. Unfortunately, solving Eq. 2.4. is not trivial and several approximated methods have been proposed in the past years. These methods can be classified as two main groups: wavefunction methods and Density Functional Theory methods.

2.2. Density Functional Theory

In density functional theory, the goal is to obtain the ground state electronic energy of a system using the electron density ($\rho(\vec{r})$) instead of the wavefunction as done in wavefunction methods. For an N electron system, the electronic wave function of a system ($\Psi_{el,R}(\vec{r})$) is a function that depends on 4N variables (i.e., three spatial and one spin coordinates per electron) while the electron density, $\rho(\vec{r})$, is a function that depends on three spatial coordinates only. The electron density corresponds to the probability of finding any of the N electrons within the volume element $d\vec{r}$ and it is defined as the integral over the spin coordinates of all electrons and over all but one of the spatial variables

$$\rho(\vec{r}) = N \int \cdots \int |\Psi(s_2\overrightarrow{r_2}, \cdots, s_N\overrightarrow{r_N})|^2 \, ds_2 d\vec{r}_2 \cdots ds_N d\overrightarrow{r_N} = \sum_{i=1}^{N} |\phi_i(\vec{r})|^2 \quad (2.6)$$

where s_i, $\vec{r}_i$ and $\phi_i(\vec{r})$ represent the projection on the *z* axis of the spin, the spatial coordinates and the orbital of electron *i*, respectively. In chemistry, biology or material science the systems under study contain many atoms and a huge number of electrons; thus, a proper description of such large systems becomes prohibitive without DFT. This is mainly the reason why the use of DFT is very popular in condensed-matter physics, computational physics and computational chemistry.

2.2.1. The Hohenberg and Kohn theorems

The DFT formalism that we know nowadays started in 1964 when Pierre Hohenberg and Walter Kohn introduced two theorems that stablished the basis of the theory.[3] These two theorems represent the pillars on which all modern DFT is erected:

> 1st theorem: "*The external potential $V_{ext}(r)$ of a non-degenerate electronic state, and hence the total energy, is a unique functional of $\rho(r)$*"
>
> 2nd theorem: "*The ground state energy can be obtained variationally and the density that minimizes the energy is the exact ground state energy*"

The first theorem stablishes that the energy of the system can be calculated from the electron density from a unique external potential

$$E[\rho] = \int \rho\,(\vec{r})\, V_{ext}(\vec{r}) d\vec{r} + F_{HK}[\rho] \qquad (2.7)$$

where, $V_{ext}(\vec{r})$ is the unique external potential (in practice that provided by the nuclei) and $F_{HK}[\rho]$ is the Hohenberg-Kohn functional consisting of a kinetic energy term $T[\rho]$ and an interaction term $V_{ee}[\rho]$ accounting for the electron-electron repulsion. The Hohenberg-Kong functional is said to be universal as its form is independent of the number of electrons and the position and charge of the nuclei.

The second theorem uses the variational principle to determine the exact ground state energy. However, it is only true if the exact density functional is used. The problem is that in any real application of DFT we are forced to use an approximation of the functional since the real form of the functional, even proven to exist, is still unknown. We are then using an approximated rather than the exact functional so that the variational principle does not hold anymore. For that reason, when doing DFT calculations it is possible to obtain energies below the exact energy.

2.2.2. The Kohn-Sham equations

A year after Hohenberg and Kohn introduced the foundations of DFT, Kohn and Sham presented an approach that provides a practical way to compute the ground state energy from the electron density only.[4] They proposed that instead of using the real system of N interacting particles, one can use a system of N non-interacting particles moving in an

effective local potential ($V_{KS}(\vec{r})$) in such a way that the electron density matches that of the real system. Then, the wave function of the non-interacting system can be simply expressed as a single Slater determinant build up from one electron orbitals, referred as Kohn-Sham orbitals (ϕ_i^{KS}). These are obtained after solving the Kohn-Sham set of equations

$$\hat{h}^{KS}\phi_i^{KS}(\vec{r}) = \left[-\frac{1}{2}\nabla^2 + V_{KS}(\vec{r})\rho(\vec{r})\right]\phi_i^{KS}(\vec{r}) = \varepsilon_i^{KS}\phi_i^{KS}(\vec{r}) \quad (2.8)$$

which are similar to the Hartree-Fock equations but with $V_{KS}(\vec{r})$ providing the potential felt by the interacting set of electrons instead of an average one. Hence, the final electron density can be expressed as

$$\rho(\vec{r}) = \sum_{i=1}^{N}\left|\phi_i^{KS}(\vec{r})\right|^2 \quad (2.9)$$

Once the electron density is known, in the Kohn-Sham formalism, the system energy is expressed as

$$E_{KS}[\rho] = \sum_i^N \varepsilon_i^{KS} = T_{KS}[\rho] + \int \rho(\vec{r})V_{KS}(\vec{r})d\vec{r} \quad (2.10)$$

where $T_{KS}[\rho]$ stand for the Kohn-Sham kinetic energy (i.e., the electron kinetic energy of the non-interacting system) and $V_{KS}(\vec{r})$ is the Kohn-Sham effective potential that can be expressed as

$$V_{KS}(\vec{r}) = V_{ext}(\vec{r}) + V_{ee}(\vec{r}) + V_{XC}(\vec{r}) \quad (2.11)$$

where $V_{ext}(\vec{r})$, $V_{ee}(\vec{r})$ and $V_{XC}(\vec{r})$ represent the external potential, the classical Coulomb interaction between the electrons and the exchange-correlation potential, respectively. The last term is defined as the functional derivative of $E_{XC}[\rho]$ with respect to the electron density and accounts for the difference of kinetic and internal interaction energies of the true interacting many-body system from those of the non-interacting system. The exact expression of the exchange-correlation functional is still unknown and has to be approximated. As in the Hartree-Fock equations, the ground state energy needs equations to be solved self-consistently as the KS potential $V_{KS}(\vec{r})$ depends on the KS orbitals. As a matter of fact, $V_{KS}(\vec{r})$ is the functional derivative of $E_{XC}(\vec{r})$.

2.2.3. Exchange-correlation functionals

The central goal of modern DFT is to find an approximate enough form of the universal functional. Accounting to balance between complexity and accuracy the different functionals are classified by the so-called Jacob's Ladder[5] being the last step in the ladder the exact form of the universal exchange-correlation functional. The simplest approximation is the Local Density Approximation (LDA),[6] which assumes that the density can be described as a homogeneous electron gas and locally $E_{XC}[\rho]$ depends only on the electron density. This model is a fairly good approximation for metals but fails on atoms and molecules that are usually characterized by a rapid variation of densities across the space. The next logical step to improve the LDA model is to use not only the information about the density at a particular point, but also the gradient of the charge density in order to account for the non-homogeneity of the true electron density. This approximation is known as the Generalized Gradient Approximation (GGA),[7] which in general, gives more accurate results than LDA functionals. Growing in complexity the next family of functionals are named meta-GGA functionals. They are the second step to go beyond LDA in the sense that they use information of the density, the gradient of the density but they also introduce an approximate dependence on the Laplacian of the density. Finally, the next family is known as hybrid functionals and they are characterized by mixing some non-local Fock exchange into the DFT exchange and correlation functional.

In the present thesis, two different GGA functionals have been used namely the PBE[8] and BEEF-vdW functionals.[9] The former has been well tested and it is one of the most popular and used functionals in computational catalysis with very good balance between computational cost and accuracy. For adsorption energies, the latter has been shown to provide better agreement with the experimental data than other commonly used functionals. Moreover, it includes non-local correlation but at the same time is computationally more expensive and usually involves convergence problems.

2.2.4. Including dispersion

One of the most significant problems of modern DFT is the lack of dispersion forces also known as van der Waals (vdW) forces which originate from instantaneous electron-

electron interaction leading to terms involving induced dipole and higher order terms. Thus, dispersion can be seen as an attractive interaction from the response of dynamical correlations between fluctuating charge distributions. In order to account for such interactions within DFT, different approaches have emerged during the past decades as nicely reviewed by Klimes and Michaelides.[10] The simplest solution is to add a dispersion contribution to the conventional DFT energy

$$E_{tot} = E_{DFT} + E_{disp} \tag{2.12}$$

where E_{DFT} is the total DFT energy computed with the desired exchange correlation functional and E_{disp} stands for the dispersion interaction and can be empirically computed as

$$E_{disp} = -\sum_{A,B} f(r_{AB}, A, B) \frac{C_6^{AB}}{r_{AB}^6} \tag{2.13}$$

where C_6^{AB} are the dispersion coefficients that depend on the element pairs A and B, r_{AB} is the intermolecular distance between the element pairs A and B and $f(r_{AB}, A, B)$ is a damping function that is equal to one for large r and decreases E_{disp} to zero or to a constant for small r. Grimme and coworkers[11-13] following the above-mentioned scheme developed the DFT-D approach which after parametrization produces very reliable results with insignificant computational cost. Growing in complexity, there are other approaches that instead of using external input parameters directly use the electron density to compute the dispersion interactions.[14] The methods that applies this approach are called non-local correlation functionals as they add non-local correlations to local or semi-local correlation functionals. The non-local correlation energy E_c^{nl} is calculated from

$$E_c^{nl} = \iint d\vec{r_1} d\vec{r_2} \rho(\vec{r_1}) \varphi(\vec{r_1}, \vec{r_2}) \rho(\vec{r_2}) \tag{2.14}$$

where $\rho(\vec{r})$ is the electron density and $\varphi(\vec{r_1}, \vec{r_2})$ is some integration kernel with the integration kernel being analogous to the classical Coulomb interaction kernel $1/|r_1 - r_2|$ but with a more complicated formula used for $\varphi(\vec{r_1}, \vec{r_2})$ with $\mathcal{O}(1/|r_1 - r_2|^6)$ asymptotic behavior. Then, within this approach the exchange correlation energy is calculated as

$$E_{XC} = E_x^{GGA} + E_c^{LDA} + E_c^{nl} \tag{2.15}$$

where E_x^{GGA} and E_c^{LDA} vary depending on the explicit functional that one is using. This more complex approach is thought to be in general more accurate than the previous approaches for describing the dispersion energy although this remains to be proven. The beauty of this approach is that it does not need an a priori parametrization thus being more general. However, as it explicitly calculates the non-local interaction at each step it is also much more computationally demanding. In this doctoral thesis both the Grimme D3 correction and the BEEF-vdW functional that includes non-local correlation have been used.

2.2.5. Periodic DFT calculations

In DFT calculations to correctly describe the electron density a suitable basis set is needed and the choice of the type of basis set used commonly depends if the system is periodic or not. For non-periodic systems such as molecules the commonest basis functions used consist on Gaussian-type orbitals (GTO) or Slater-type orbitals (STO). Molecular orbitals are described as a linear combination of atomic orbitals (LCAO approximation) so that the *i*th molecular orbital, φ_i, is defined as

$$\varphi_i = \sum_\mu c_{\mu i}\eta_\mu \tag{2.16}$$

where η_μ is the μth atomic orbital of the set $\{\eta_\mu\}$ and $c_{\mu i}$ is the corresponding coefficient that represents the weight of the μth atomic orbital in the *i*th molecular orbital. Moreover, each atomic orbital η_μ, is expanded at the same time in a linear combination of nuclei centred functions such as GTO's or STO's. However, for periodic systems such as solids, a common choice is to use a basis set of plane waves (PW) that has the form

$$\eta^{PW} = e^{i\vec{k}\vec{\mathrm{T}}} \tag{2.17}$$

where the vector $\vec{k}$ is related to the momentum $\vec{p}$ of the plane wave through $\vec{p} = \hbar\vec{k}$ and $\vec{\mathrm{T}}$ is any translational vector leaving the Hamiltonian invariant. Plane waves are not centred at the nuclei but they expand throughout all the space, which makes it very interesting for periodic system calculations since they include implicitly the concept of periodic boundary conditions. However, a large number of plane waves is needed to properly describe the large oscillations observed in the core region.[15] Nonetheless, since many of the chemical and physical properties of atoms are determined by the valence

electrons while core electrons remain almost unmodified, a good approximation is to treat the core electrons as "frozen" electrons that are merely spectators making more affordable the DFT calculations. Therefore, the all-electron potential is replaced by a pseudopotential that mimics the effect of core electrons on the valence electron density, and the valence electrons are described by pseudo wavefunctions with significant fewer nodes, thus reducing the PW basis set size. One advantage of using pseudopotentials is that relativistic effects, which are important for heavy atoms, may be accounted for on the pseudopotentials without increasing the computational cost.

2.3. Transition State Theory

Chemical kinetics deals with the rates of chemical reactions and with how the rates depend on several factors, such as concentration and temperatures among others. Rates are essential to provide evidence on how reactions evolve and about the mechanisms of chemical processes at different working conditions. Different theories exist to study chemical kinetics with Transition State Theory being one of the most used approaches, with further improvements such as Variational TST. As catalysis is all about speeding up a reaction, there is a direct relation between catalysis, chemical kinetics and TST, which address how reaction rates can be obtained. The conventional Transition State Theory was published almost simultaneously by H. Eyring and M. G. Evans and M. Polanyi in 1935. According to TST, there is a special state between reactants and products called activated complex or transition state (TS). This TS represents a stationary (null gradient) saddle point (one and only one negative eigenvalue of the Hessian matrix) in the potential energy surface that connects reactants and products. The theory involves different assumptions and approximations:[16-18]

i) Molecular systems that have surmounted the transition state in the direction of products cannot turn back and form reactants again.
ii) Reactants are in chemical equilibrium with the transition state even the whole system is not at equilibrium.
iii) It is possible to separate the motion of the system over the energy barrier from the other motions associated with the transition state.
iv) A chemical reaction can be satisfactorily treated in terms of classical motion over the barrier, quantum effects being ignored.

Let suppose the following gas-phase reaction

$$A_{(g)} + B_{(g)} \rightleftarrows X^{\neq}_{(g)} \rightarrow Y_{(g)} + Z_{(g)} \tag{2.18}$$

where $X^{\neq}_{(g)}$ is the so-called activated complex or transition state, which after the development of quantum mechanics turns out to be a saddle point over the reaction path of the PES. Consider now the equilibrium between reactants and the activated complex so that the TS concentration can be derived from statistical mechanics

$$K_c^{\neq} = \frac{[X^{\neq}]}{[A][B]} = \frac{k_B T}{h\xi} \frac{{q^{\neq}}/{V}}{{q_A}/{V}\,{q_B}/{V}} e^{-{\Delta E_0^{\neq}}/{k_B T}} \tag{2.19}$$

where $K_c^{\neq}$ is the equilibrium constant between the TS and reactants, $q^{\neq}$, q_A and q_B are the total partition functions of the TS and reactants A and B, respectively, $\Delta E_0^{\neq}$ is the energy difference between the TS and reactants including the zero point energy correction, ξ is the imaginary frequency of vibration of the activated complex treated as a translational degree of freedom corresponding to its conversion into products, k_B is the Boltzmann constant, h is the Planck's constant and T is the absolute temperature. Rearranging the above equation

$$\xi[X^{\neq}] = [A][B]\ \frac{k_B T}{h} \frac{{q^{\neq}}/{V}}{{q_A}/{V}\,{q_B}/{V}} e^{-{\Delta E_0^{\neq}}/{k_B T}} \tag{2.20}$$

In this equation, the expression on the left-hand side represents the product of the activated complex concentration by their frequency of conversion into products, which is nothing but *r*, the rate of reaction,

$$r = [A][B] \frac{k_B T}{h} \frac{{q^{\neq}}/{V}}{{q_A}/{V}\,{q_B}/{V}} e^{-{\Delta E_0^{\neq}}/{k_B T}} \tag{2.21}$$

and therefore, knowing from classical kinetics that $r = k[A][B]$ the thermal rate constant is defined as

$$k(T) = \frac{k_B T}{h} \frac{{q^{\neq}}/{V}}{{q_A}/{V}\,{q_B}/{V}} e^{-{\Delta E_0^{\neq}}/{k_B T}} \tag{2.22}$$

In general, one can express a generic rate constant derived from transition state theory as

$$k(T) = \frac{k_B T}{h} \frac{{q^{\neq}}/{V}}{\left({q_{react(i)}}/{V}\right)_{react=i}} e^{-{\Delta E_0^{\neq}}/{k_B T}} \quad (2.23)$$

where $q^{\neq}$ is the TS partition function and $q_{react(i)}$ is the partition function of reactant i. Both partition functions depend on the type of reaction and the reactant nature. For instance, the partition functions used in Eq. 2.23 are not the same if one studies a unimolecular reaction, a bimolecular reaction or a surface reaction. Note that we have introduced the volume so that the units of the rate constant are consistent with the type of reaction. The derivation of the rates for the different types of reactions will be introduced in detail latter on. In this doctoral thesis TST has been used to calculate the rate constants from DFT results, which are latter adapted to transition probabilities that are used in the kinetic Monte Carlo simulations.

2.4. Kinetic Monte Carlo simulations

Quantum mechanical calculations are of paramount interest as they give useful information of the energetics of the system under study. Particularly, in computational heterogeneous catalysis, quantum mechanical calculations, most often in the framework of DFT, provide relevant information about the energetics of the adsorbates and transition states that can be formed during the catalytic process, which finally allow for the construction of the potential energy surface providing insights into the possible reaction mechanisms. Nevertheless, the information of the electronic structure calculations is a static picture that by itself cannot, in general, explain the dynamic evolution of the system and thus disclose the dominant reaction mechanism.

To bridge the gap between the static picture at the atomic level and the macroscopic regime, DFT calculations can be coupled with kinetic modelling techniques[19-23] such as microkinetic modelling (MM) or kinetic Monte Carlo. In both techniques the goal is to solve a master equation that defines the time evolution of the system. To do so, one has to define the different elementary reactions that can take place and, for each process, define and estimate the rate constant both in the forward and backward direction. In MM the master equation expresses the rate of change of each adsorbate coverage as a function of the instantaneous coverage of all species in the model, represented as a system of ordinary non-linear differential equations. This method relies on the mean-field

approximation (MFA) and assumes that the adsorbates are randomly distributed over the sites creating a mean coverage. This assumption may not hold as adsorbates interact with each other either attractively or repulsively leading to a correlation in the occupation of neighbouring sites. Moreover, these interactions may even result in island formation or ordered adlayers. One may think that if for instance islands of a specific species are formed only the species that are on the edges can actually react while this cannot be considered with the mean-field approach used in MM simulations.

In order to overcome the MM shortcomings, a more detailed and sophisticated approach can be used such as the kMC method. In this approach one has a detailed spatial resolution of the reaction system, represented by an appropriate lattice, and can capture different phenomena such as adsorbate mobility (diffusion), steric exclusion effects, complex reaction patterns involving adsorbates in specific binding configurations, spatial correlations arising from adsorbate lateral interactions and changes in the energy due to the presence of neighbouring spectator species. Moreover, kMC takes into account the discrete nature of the coverage for nanoparticles or clusters, which expose a small number of sites.

2.4.1. The Markovian master equation

In kMC simulations, the long-term time evolution of the catalytic system is said to be governed by successive state-to-state transitions. In this approach, one considers that transition between two stable states (i.e., two minima of the PES) are much slower than the fast rotations and vibrations so that the new state "forgets" how it got there and each transition becomes completely independent of any previous event. Then it is possible to assume that such state-to-state dynamics constitute a so-called Markov chain.[24] Therefore, the time evolution of the probability $P_i(t)$ of the system to actually be in state i at time t, is governed by a balancing equation, the so-called Markovian master equation

$$\frac{dP_i(t)}{dt} = \sum_{j \neq i} \omega_{ji} P_j(t) - \sum_{j \neq i} \omega_{ij} P_i(t) \qquad (2.24)$$

where ω_{ij} denotes the probability for a transition between the current state i into any other state j, and ω_{ji} denotes the probability for a transition between the state j into any other state i. The parameter ω_{ij} is essentially a stochastic rate constant that in the context

of chemical kinetics can be derived from TST considering the properties of the involved PES. Therefore, ω is the transition probability (or a pseudo rate constant) of an elementary process that change from one configuration to another. One should be aware that transition probabilities are not necessarily the same than thermal rate constants even though in the present context of chemical kinetics the former are derived from TST. In TST thermal rate constants have different units depending on the type of reaction— this is *e.g.* why the volume appears in Eqs (2.19) to (2.23)— while in the kMC framework transition probabilities have units of inverse of time as they define the rate of transition from one state to another. Nevertheless, one can relate the thermal rate constants with the transition probabilities for each specific process. For instance, for Eley-Rideal reactions, activated adsorptions and non-activated adsorptions $\omega_i = k_i/V$ where V stands for the volume. For a Langmuir-Hinshelwood type reaction $\omega_{L-H} = k_{L-H}/A$ where A stands for the surface area. Finally, for a desorption $\omega_{des} = k_{des}$. The explicit form of the transition probabilities used in the kMC simulations for the different processes can be found in section 2.4.4.

The idea behind kMC simulations[25,26] is to achieve a numerical solution of the master equation based on stochastic trajectories. These state-to-state trajectories are propagated until a converged time evolution of the probabilities $P_i(t)$ is achieved by ensemble averaging over these trajectories. When the steady-state is reached the ensemble average may be replaced by a time average over a singular sufficiently long trajectory. Due to the stochastic nature of the kMC method ideally several simulations (at the same conditions) must be run to have a large ensemble average or time average to obtain meaningful results.

2.4.2. kMC algorithms

As introduced above, the idea behind the kMC method is to stochastically obtain the solution of the master equation that is to find the correct time evolution of the probabilities $P_i(t)$ by ensemble averaging over the many trajectories. To do so, the kMC code needs to determine repeatedly the processes that occur (i.e., the state-to-state trajectories), the time at which they occur and the position at the surface in which they occur changing the occupation of the lattice correctly. Each of these different processes can be determined in many different ways which results in different algorithms. The three most popular

algorithms are the Random Selection Method (RSM), the First Reaction Method (FRM) and the Variable Step Size Method (VSSM). Lukkien et al.[27] have shown the equivalence in results of the three different methods so that the preference for one or the other emerges only out of computational efficiency considerations depending on the system. Among them, VSSM is probably the most widely used algorithm. The VSSM workflow is presented below and schematically sketched in Figure 2.1a.

1. **Initialize**

   Generate an initial configuration

   Set t = 0

   Make a list of all possible processes *j* according to the lattice

   Choose conditions when to stop the simulation

2. **Time**

   Draw two random numbers $\rho_1, \rho_2 \in (0,1]$

   Calculate $\omega_{tot} = \sum_j \omega_j$, the sum running over all the processes of the list

   Generate a time interval Δt following a Poisson distribution $\Delta t = -\frac{ln(\rho_1)}{\omega_{tot}}$

   Update time $t \longrightarrow t + \Delta t$

3. **Process**

   Extract a process, q, that satisfies $\sum_{j=1}^{q-1} \omega_j \leq \rho_2 \omega_{tot} \leq \sum_{j=1}^{q} \omega_j$

   Execute the ω_q selected process

4. **Update**

   Update the lattice according to the executed q process

   Update the list of events according to the new lattice configuration

5. **Continuation**

   If the stop conditions are satisfied then stop. If not, repeat at step 2

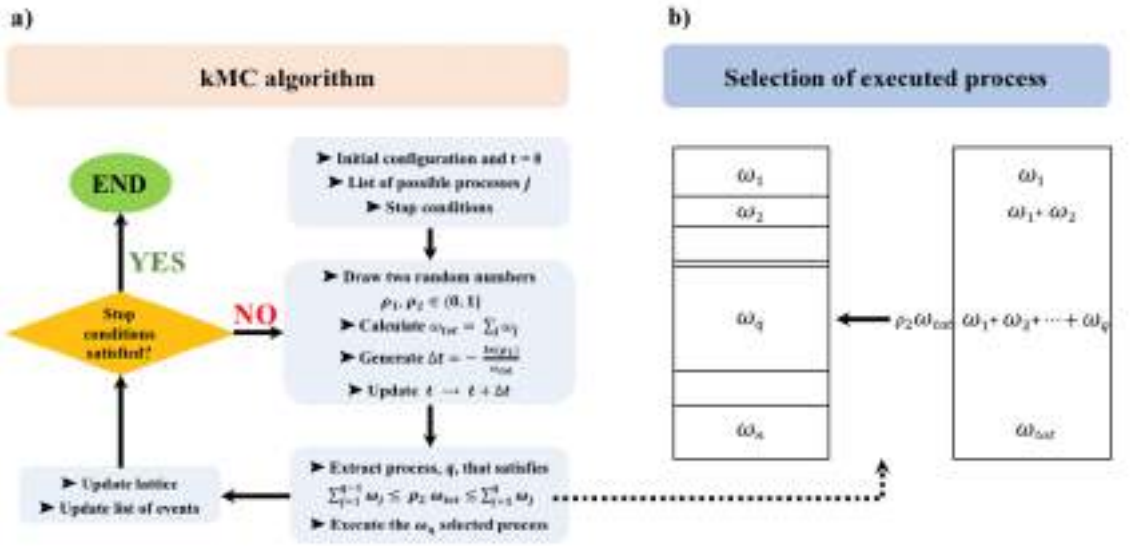

Figure 2.1. a) VSSM algorithm for the kMC method. b) Selection procedure of executed process.

It is important to highlight that the total escape time is governed by a Poisson distribution of the total transition probabilities but not by the actual transition probability of the selected process (ω_q). This actual process nevertheless needs to be identified since this is what determines to which new state the system propagates. To see how the event is selected (see Figure 2.1b) one can imagine a stack of segments, each segment having a height proportional to the transition probability ω_j and the sum of all segments being ω_{tot}. Therefore, by using a random number, ρ_2, between 0 and 1 and multiplying it by ω_{tot} a value will be obtained corresponding to one of the segments that involve a specific process. Then this process is executed. This selection procedure makes more probable those processes with higher transition probabilities. The main bottleneck of the VSSM algorithm is the step of updating the list and computing the new ω_{tot}, and different algorithms can be used in order to increase the efficiency.

2.4.3. Lattice-gas reaction model

To describe the time evolution in kMC simulations it is necessary to define a lattice-gas reaction model. This model defines the set of different elementary reactions that can take place and the lattice in which they can occur. The different lattice positions, hereon called sites, correspond to minima in the potential energy surface for the adsorbate-surface system. If the surface has two-dimensional translational symmetry, or when it can be

modeled as such, the sites form a regular grid or lattice. Moreover, periodic boundary conditions can be used to mimic real surfaces and avoid size effects. Note that the lattice can represent any catalytic system and the complexity of the real system represents the complexity of the lattice. Therefore, one can simulate very different lattices, ranging from simple models like *fcc* (111) or (100) metallic facets to more intricate structures like stepped surfaces, clusters anchored over some support featuring a variety of different sites or even nanoparticles. However, including all the sites into the lattice model can be very complex and computationally and intellectually demanding. Thus, it is common to use the concept of a generalized site (i.e., coarse-grained site) that represents the energetic of a specific site of the real system. For instance, for an *fcc* (111) surface —that features four different sites (i.e., fcc, hcp, bridge and top sites)— it is common to use a coarse-grained site that represent a unique site in which the species adsorb. Nevertheless, if desired, one can go as deeper in complexity as required. In order to indicate the lattice occupation, the different points of the lattice are labeled with different labels that define a free site or the type of species that occupies the site. The particular labelling of all sites is called the lattice configuration. Then, the evolution of the lattice is described by a set of possible elementary reactions (i.e., adsorption, desorption, diffusion and bond breaking/forming reactions) that can take place on the surface and change the lattice from one configuration to another configuration. In summary, the lattice-gas reaction model defines the lattice configuration and possible elementary processes that can take place at each step of the simulation. The lattice-gas reaction model depends on the lattice configuration and the initial mixture of gas species.

A simple example is presented below and schematically shown in Figure 2.2. Imagine we want to study the CO adsorption, desorption and diffusion over the Ni(100) facet. In order to represent the Ni(100) facet we chose a single coarse-grained site representing the four-fold hollow in which CO is adsorbed. Then we have a lattice with square symmetry that contains a variety of sites. Here for simplicity we will consider only a cell of four different sites each site having a connectivity of two (*i.e.* connected only to the nearest neighbors). The elementary reactions processes in the reaction model are

$$CO_{(g)} + * \xrightarrow{\omega_{ads}} CO^* \tag{2.25}$$

$$CO^* \xrightarrow{\omega_{des}} CO_{(g)} + * \tag{2.26}$$

$$CO^* + * \overset{\omega_{diff}}{\longleftrightarrow} * + CO^* \qquad (2.27)$$

where * represents a free adsorption site on the lattice while $CO_{(g)}$ and CO^* refer to gas-phase and adsorbed CO, respectively. The initial lattice configuration, *l*, consists in four empty sites and the list of possible events contains the four CO adsorptions. Since all the sites are equivalent also the transition probabilities for CO adsorption are the same and the probability of CO to adsorb on a specific site will be 1/4. Then CO adsorbs over let's say site 2 changing the configuration from *l* to *m* (*i.e.* from $l \equiv \{1{:}*, 2{:}*, 3{:}*, 4{:}*\}$ to $m \equiv \{1{:}*, 2{:}CO^*, 3{:}*, 4{:}*\}$). Now the lattice configuration is different with the concomitant change on the list of possible events. The new list of events based on the new configuration contains a total of 6 possible processes: the three remaining adsorptions over sites 1,3 and 4; the CO desorption from site 2 and two CO diffusions to adjacent sites (i.e., 2 → 1 and 2 → 4). As diffusions are generally fast processes, they have higher probability of being executed, and, in fact, the diffusion corresponds to the selected process that change configuration from *m* to *n*. In the new configuration CO occupies site 1. Note that in our example we have directly labeled the site occupation with * and CO* but in kMC algorithms these labels correspond to integer occupation values (i.e., 0 for free site and 1 for adsorbed CO).

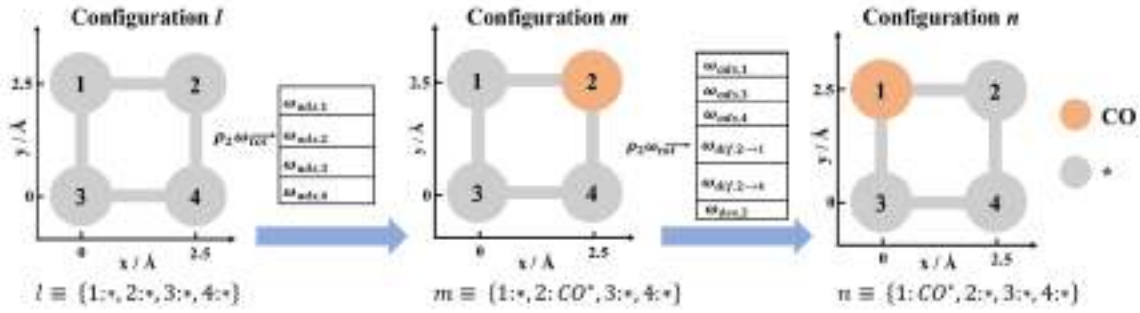

Figure 2.2. Representation of the lattice-gas reaction model.

2.4.4. Transition probabilities calculation

The transition probabilities used in kMC simulations are those introduced in the master equation (Eq. 2.24) that specify the rate of each process to take place and are used in the kMC algorithm to simulate the state-to-state trajectories. As already mentioned, one should be aware that these transition probabilities even derived from TST are not necessarily the same as the thermal rate constants that appear in macroscopic rate

equations. The transition probabilities of the different processes that can take place in the kMC simulations can be derived directly from the master equation in a way that resembles the original TST.[25] Depending on the reaction type the computed transition probability has a particular form which depends on the partition functions of the reactants and transition states involved.

For gas-phase species ($X_{(g)}$) the total partition function is composed by the rotational ($q_{rot,X_{(g)}}$), translational ($q_{trans3D,X_{(g)}}$), vibrational ($q_{vib,X_{(g)}}$) and electronic ($q_{elec,X_{(g)}}$) partition functions

$$Q_{X_{(g)}} = q_{rot,X_{(g)}} q_{trans3D,X_{(g)}} q_{vib,X_{(g)}} q_{elec,X_{(g)}} \tag{2.28}$$

Note that the electronic separations from the ground state are usually very large, so for most cases $q_{elec,X_{(g)}}$ = 1. However, in the case of atoms and molecules with electronically degenerated ground states $q_{elec,X_{(g)}} = g^E$, where g^E is the degeneracy of the electronic ground state. The rotational partition function $q_{rot,X_{(g)}}$ depends on the molecule geometry. For linear molecules the rotational partition function is

$$q_{rot,X_{(g)}} = \frac{8\pi^2 I k_B T}{\sigma h^2} \tag{2.29}$$

where I is the inertia moment and σ is the symmetry number of the molecule. For non-linear molecules, the rotational partition function takes the form

$$q_{rot,X_{(gas)}} = \frac{(\pi I_a I_b I_c)^{1/2}}{\sigma} \left(\frac{8\pi^2 k_B T}{h^2}\right)^{3/2} \tag{2.30}$$

where now it depends on the three principal moments of inertia (I_a, I_b and I_c). The translational partition function ($q_{trans3D,X_{(g)}}$) in the classical limit is

$$q_{trans3D,X_{(g)}} = V \left(\frac{2\pi m k_B T}{h^2}\right)^{3/2} \tag{2.31}$$

In the context of heterogeneous catalysis, the direction perpendicular to the surface can be used as a reaction coordinate, thereby motivating the decoupling of the z component of the translational partition function as follows

$$q_{trans3D,X_{(g)}} = q_{trans2D,X_{(g)}} l_z \frac{\sqrt{2\pi m k_B T}}{h} \tag{2.32}$$

where l_z is the length of the gas-phase pathway in the *z*-direction and $q_{trans2D,X_{(g)}}$ is the 2D translational partition function that reads

$$q_{trans2D,X_{(g)}} = A_{st}\frac{2\pi m k_B T}{h^2} \tag{2.33}$$

where A_{st} is the effective area of the site in which the reaction takes place and m is the mass of $X_{(g)}$. Finally, the vibrational partition function is expressed as a product of contributions from each vibrational mode of the species, commonly using the harmonic approximation

$$q_{vib,X_{(g)}} = \prod_k^{3N-6(5)} \frac{e^{-\left(\frac{h\nu_k}{2k_BT}\right)}}{1-e^{-\left(\frac{h\nu_k}{k_BT}\right)}} \tag{2.34}$$

where ν_k is the vibrational frequency of the *k*th vibrational mode and the product runs over all the $3N_{atoms}-6$ normal modes ($3N_{atoms}-5$ normal modes if the molecule is linear). If one chose the first vibrational level to be the zero of energy because the zero-point energy correction has been already included in the energy barrier ($\Delta E_0^{\neq}$), Eq. 2.34 reads as

$$q_{vib,X_{(g)}} = \prod_k^{3N-6(5)} \frac{1}{1-e^{-\left(\frac{h\nu_k}{k_BT}\right)}} \tag{2.35}$$

For adsorbed species it is considered that translational and rotational motions are frustrated and only vibrations are allowed; thus, only the vibrational partition function is considered. Note that for adsorbed species the product of Eq. 2.35 runs over the $3N_{atoms}$ normal modes as frustrated translations and rotations are now treated as vibrations. Moreover, one has also to consider that for transition states the product of Eq. 2.35 runs over $3N_{atoms}-1$ normal modes (i.e., all the normal modes except the one that corresponds to the imaginary frequency treated effectively as a translation).

Now, the transition probabilities for each process can be derived using the specific form of the reactants and transition state partitions functions. For a surface Langmuir-Hinshelwood type reaction $X^* + Y^* \rightarrow Z^* + *$, species have only vibrational contributions to the partition function and the transition probability takes the form

$$\omega_{L-H} = \frac{k_BT}{h}\frac{q_{vib}^{\neq}}{q_{vib,X^*}\,q_{vib,Y^*}}e^{-\Delta E_0^{\neq}/k_BT} \tag{2.36}$$

where $\Delta E_0^{\neq}$ is the energy barrier of the bond breaking/forming process including the zero-point energy correction. Diffusion processes can be treated similarly as surface reactions. The transition probability for a diffusion process of type $X^* + * \rightarrow * + X^*$ can be calculated as

$$\omega_{diff} = \frac{k_B T}{h} \frac{q_{vib}^{\neq}}{q_{vib,X^*}} e^{-\Delta E_0^{\neq} / k_B T} \tag{2.37}$$

and here $\Delta E_0^{\neq}$ is the ZPE corrected energy barrier for the diffusion process. For an activated adsorption process (i.e., an adsorption process occurring through a transition state), denoted as $X_{(g)} + * \rightarrow X^*$, the transition probability is given by the following expression

$$\omega_{Act.Ads} = \frac{q_{vib}^{\neq}}{q_{vib,X_{(g)}} q_{rot,X_{(g)}} q_{trans2D,X_{(g)}} q_{elec,X_{(g)}}} S_{st} \frac{P_x A_{st}}{\sqrt{2\pi m k_B T}} e^{-\Delta E_0^{\neq} / k_B T} \tag{2.38}$$

where P_x is the partial pressure of $X_{(g)}$ species and S_{st} is the so-called sticking coefficient, which is introduced to take into account the fact that only a fraction of the incoming molecules will be adsorbed due to the influence of their trajectories in the gas-phase. For a non-activated adsorption process, denoted as $X_{(g)} + * \rightarrow X^*$, the transition probability for adsorption is simplified to

$$\omega_{Non-Act.Ads} = S_{st} \frac{P_x A_{st}}{\sqrt{2\pi m k_B T}} \tag{2.39}$$

The transition probabilities for the desorption processes can be obtained from the equilibrium constant (K_{eq}) of the adsorption/desorption process

$$K_{eq} = \frac{\omega_{ads}}{\omega_{des}} = \frac{q_{vib,X^*}}{q_{vib,X_{(g)}}} e^{-\Delta E_{ads,0} / k_B T} \tag{2.40}$$

where $\Delta E_{ads,0}$ stands for the adsorption energy of the specific species including the zero-point energy correction. Note that this expression is completely independent of the TS since the equilibrium only depends on the thermodynamic properties of the initial and final states. Therefore, in order to maintain thermodynamic consistency and to not violate the micro reversibility principle one should include the sticking coefficient also in the desorption transition probabilities. Then, the transition probabilities for a non-activated desorption and an activated desorption read as

$$\omega_{Non-Act.Des} = S_{st}\ \frac{k_B T}{h}\frac{q_{vib,X_{(g)}} q_{rot,X_{(g)}}\ q_{trans2D,X_{(g)}} q_{elec,X_{(g)}}}{q_{vib,X^*}}\ e^{\Delta E_{ads,0}/k_B T} \quad (2.41)$$

$$\omega_{Act.Des} = S_{st}\frac{k_B T}{h}\frac{q^{\neq}_{vib}}{q_{vib,X^*}}\ e^{-\left(\Delta E_0^{\neq} - \Delta E_{ads,0}\right)/k_B T} \quad (2.42)$$

Finally, for an Eley-Rideal reaction of type $X_{(gas)} + Y^* \rightarrow Z^*$, the transition probability turns to be

$$\omega_{E-R} = \frac{q^{\neq}_{vib}}{q_{vib,X_{(g)}} q_{rot,X_{(g)}}\ q_{trans2D,X_{(g)}} q_{elec,X_{(g)}} q_{vib,Y^*}}\ S_{st}\frac{P_x A_{st}}{\sqrt{2\pi m_x k_B T}}\ e^{-\Delta E_0^{\neq}/k_B T} \quad (2.43)$$

Lastly, for processes involving hydrogen atom transfer, it is possible to introduce a one-dimensional tunneling correction factor ($\kappa \geq 1$) that is computed using the expression derived from a symmetrical Eckart barrier[28] as

$$\kappa(T) = 1 + \frac{1}{24}\left|\frac{h\nu_{img}}{k_B T}\right|^2\left(1 + \frac{k_B T}{\Delta E_0^{\neq}}\right) \quad (2.44)$$

where ν_{img} is the imaginary frequency associated to the transition state.

2.4.5. Including lateral interactions

A correct representation of the kinetics of complex surface reactions requires the inclusion of adsorbate-adsorbate interactions, also known as lateral interactions. These are interactions that adsorbates exert to each other when they are adsorbed and can change the stability of either the adsorbed intermediates and the transition states of a specific reaction. They can be either attractive or repulsive depending on the chemical nature of the involved species and the surface. In case of repulsive interactions, coadsorbed species in neighboring sites are less stable than when they are separated. For attractive interactions, the situation is the opposite and species are more stable when they are closer.

In DFT calculations of energy barriers it is common to compute the zero-coverage limit energy barrier in which only the reactants/products species are considered and no spectators are present. This, of course, is far from reality in which many different species can coexist during the catalytic process interacting between them, with the concomitant changes on the initial, final and transition state energies (see Figure 2.3). In principle, one can calculate from DFT the different energetics accounting for the possible local

configurations of adsorbates. However, this can only be done for simple systems that contain only few elementary steps and intermediates during the reaction. For real systems in which a considerable large number of elementary steps or intermediates are considered this procedure becomes unfeasible. Moreover, if there is no experimental data available one does not know a priory which will be the equilibrium structure of the adlayer; thus, all the possible adlayer configurations should be, in principle, considered.

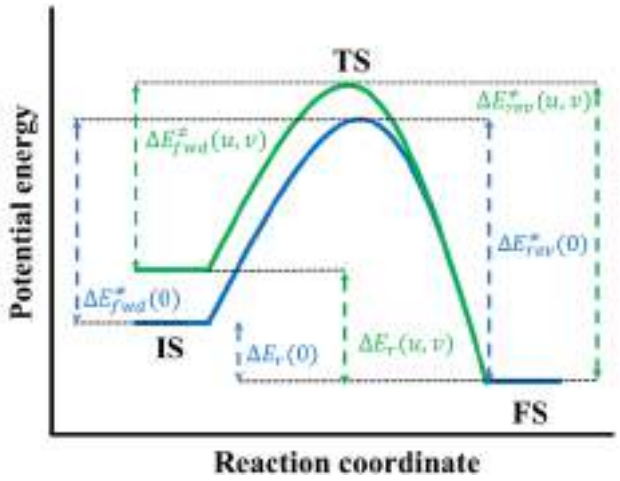

Figure 2.3. Potential energy diagram for a generic elementary step. Blue lines depict the energy profile in the zero-coverage limit (no lateral interactions effect). Green lines depict the situation in which repulsive interactions due to spectator species are considered shifting the initial state and transition state in energy.

To circumvent this problem, the coverage-dependent energy barriers can be linearly approximated by the so-called Brønsted-Evans-Polanyi (BEP) relations,[29,30] which assumes that the shape of the PES does not change. Instead, the initial and final states are shifted in energy due to the repulsive or attractive interactions that spectator species exert on the reactant/products. The coverage-dependent energy barrier due to the simultaneous presence of neighboring adsorbed species at the *u* and *v* states is then approximated as

$$\Delta E^{\neq}_{fwd}(u,v) = \Delta E^{\neq}_{fwd}(0) + \alpha\,[\Delta E_r(u,v) - \Delta E_r(0)] \tag{2.45}$$

where $\Delta E^{\neq}_{fwd}(0)$ and $\Delta E_r(0)$ are the zero-coverage limit (i.e., without spectator species) energy barrier and reaction energy, respectively, while $\Delta E^{\neq}_{fwd}(u,v)$ and $\Delta E_r(u,v)$ are the coverage-dependent (i.e., including the effect of lateral interactions) energy barrier and reaction energy, respectively, and α is the so-called proximity factor.[31] The latter is a value that defines the "nature" of the transition state and ranges from 0 for a reactants-like TS to 1 for a products-like TS. In that way, selecting a proximity factor of 0 keeps

the forward energy barrier fixed to the zero-coverage limit energy barrier and the reverse energy barrier is chosen to be thermodynamically consistent, whereas in the limit $\alpha = 1$ the reverse barrier is fixed to the zero-coverage limit and the forward barrier is adjusted. Therefore, in order to obtain the coverage-dependent energy barrier one needs to calculate the lateral interactions between the spectators and the reactants/products to obtain $\Delta E_r(u, v)$ and apply the BEP relations using a specific proximity factor.

A well-defined method to capture the lattice energetics is the cluster expansion (CE) of a lattice-gas Hamiltonian.[32-34] The use of cluster expansion Hamiltonians allows to properly represent the energetics of the system as a sum of single-, double- and multibody-terms called clusters or figures. Therefore, one can easily capture the adlayers energetics accounting for the different interactions that species exert to each other. A cluster can be a single adsorbed species or a group of two or more neighboring species with a certain lattice configuration. Therefore, the energy of a lattice configuration *u* expressed as a sum of the cluster energies is

$$E(u) = \sum_{k=1}^{N_C} n_k(u) \cdot CE_k \tag{2.46}$$

where $E(u)$ is the total energy of the system (i.e, the energy of the *u* lattice configuration), N_C is the total number of clusters included in the model, CE_k is the cluster energy of cluster *k* and $n_k(u)$ is the number of times that a pattern of cluster *k* appears in the lattice. Then, the $\Delta E_r(u, v)$ value on Eq. 2.45 is calculated as

$$\Delta E_r(u, v) = E(v) - E(u) \tag{2.47}$$

and finally, the coverage-dependent energy barrier used in the kMC simulations is calculated from Eq. 2.45 but applying a max operator that filters negative values, as well as values lesser than $\Delta E_r(u, v)$ if it is positive

$$\Delta E^{\neq}_{fwd,kMC}(u, v) = \max\left[0,\ \Delta E_r(u, v),\ \Delta E^{\neq}_{fwd}(u, v)\right] \tag{2.48}$$

In order to model the lattice energetics with a cluster expansion one needs to map all the DFT energies into energies that enters in Eq. 2.46. The cluster energies used in the cluster expansion can be calculated from the formation energies of the different structures (i.e., single adsorbates or multiple adsorbed species). Formation energies represent nothing but energy differences with respect to a reference set that has to be selected following the next rules:

i) The catalytic phase (i.e., the surface without adsorbed species) is included in the reference set.
ii) The rest of the reference species are gas-phase species and we need as many gas-phase species as the number of different atoms encountered in our species.
iii) The reference species must have linearly independent compositions, which means that we should not be able to write a reaction that produces a reference species from other reference species.

Consider for instance that we are studying the reverse water-gas shift reaction on TiC(001). In this case, we have C-, H- and O- containing species and our TiC surface as the catalyst. Therefore, a good reference set is {TiC (001), CO, H_2, H_2O}. The formation energy of an adsorbate i (E_i^f) is defined as

$$E_i^f = E_{i-slab} - E_{slab} - \sum_j (n_j R_j) \tag{2.49}$$

where E_{i-slab} is the raw DFT energy of the adsorbate i on the slab, E_{slab} is the raw DFT energy of the slab (i.e., TiC (001)), n_j is the number of atoms j in species i, and R_j is the reference energy of the atom j, defined in our reference set as:

$$R_H = 0.5 \left(E_{H_{2(g)}}\right) \tag{2.50}$$

$$R_O = E_{H_2O_{(g)}} - 2R_H \tag{2.51}$$

$$R_C = E_{CO_{(g)}} - R_c \tag{2.52}$$

where $E_{i\,(g)}$ is the raw DFT energy for the i gas-phase species. Within this definition the formation energy or cluster energy of a CO molecule adsorbed over TiC(001), E_{CO}^f, is expressed as

$$E_{CO}^f = E_{CO-TiC} - E_{TiC} - R_C - R_O \tag{2.53}$$

Let's now focus on the formation energy or cluster energy for two-body terms entering on the Eq. 2.46. For a pair of CO molecules adsorbed over TiC (001) this is nothing but an extension of the previous example

$$E_{CO+CO}^f = E_{CO+CO-TiC} - E_{TiC} - 2R_C - 2R_O \tag{2.54}$$

From the previous two magnitudes, one can easily compute the lateral interaction between two CO molecules. If these two molecules were located very far away from each other on the same surface, the E^f_{CO+CO} value should be twice the CO formation energy, E^f_{CO}. However, because of the interactions between them the energy of the two CO molecules is not twice the energy of one adsorbed CO and the magnitude of the pairwise interaction is

$$CE_{CO-CO} = E^f_{CO+CO} - 2E^f_{CO} \tag{2.55}$$

In the following, a simple example on how the CE formalism works and how coverage-dependent energy barriers are calculated for the CO_2 dissociation with neighboring spectator species is presented, as shown in Figure 2.4. Note that for single species the formation energy is the same as the cluster energy of the specific species while for multibody interactions the cluster energy that define such interaction is calculated from the formation energy of the multibody and single patterns.

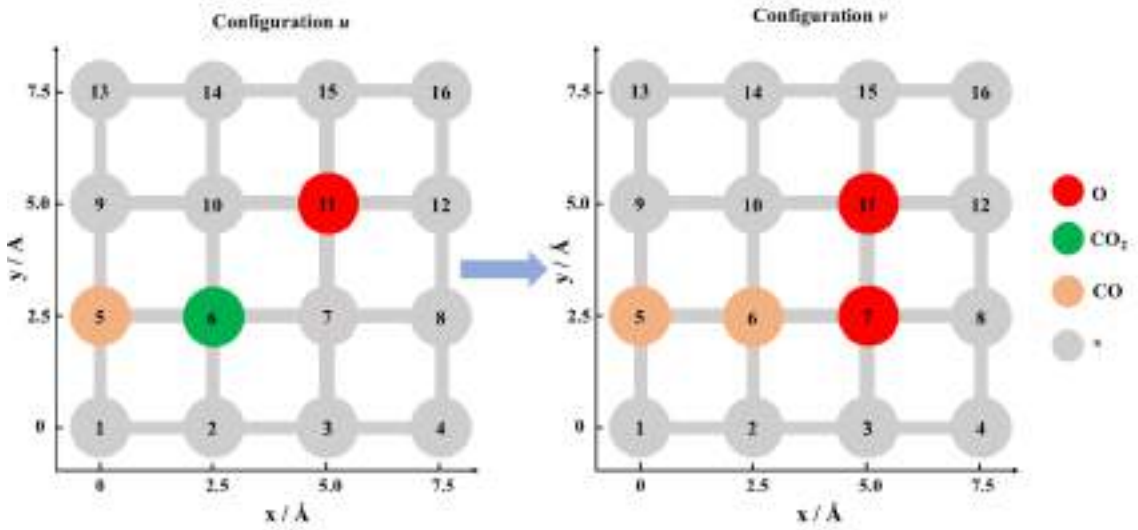

Figure 2.4. Graph-pattern of the CO_2 dissociation with neighboring spectator species.

This event is one of the possible elementary reactions to obtain CO in the reverse water-gas shift reaction. Let's now evaluate step by step how the cluster expansion and the BEP relations are used to calculate the coverage-dependent energy barrier. First of all, we will assume that the zero-coverage limit energy barrier is $\Delta E^{\neq}_{fwd}(0) = 0.80$ eV and that the cluster energies for the adsorbed species are $CE_{CO} = -1.2$ eV, $CE_O = -0.3$

eV and $CE_{CO_2} = -1.4$ eV. With this information it is possible to calculate the reaction energy at zero-coverage limit (i.e., without lateral interactions)

$$\Delta E_r(0) = E(v) - E(u) =$$

$$[2CE_O + 2CE_{CO}] - \left[CE_{CO_2} + CE_{CO} + CE_O\right] = -0.10 \text{ eV} \quad (2.56)$$

As shown in Figure 2.4 there are CO and O spectator species that interact with CO_2. Let's then include first nearest-neighbor pairwise lateral interactions in our model. Following the process outlined above we find that the two-body terms (i.e., the ones that account for pairwise lateral interactions) are $CE_{CO-CO} = 0.15$ eV, $CE_{CO-CO_2} = 0.05$ eV, $CE_{CO-O} = 0.10$ eV and $CE_{O-O} = 0.20$ eV. The coverage-dependent reaction energy is then

$$\Delta E_r(u,v) = E'(v) - E'(u) =$$

$$[2CE_O + 2CE_{CO} + CE_{CO-CO} + CE_{CO-O} + CE_{O-O}]$$

$$-\left[CE_{CO_2} + CE_{CO} + CE_O + CE_{CO-CO_2}\right]$$

$$= 0.30 \text{ eV} \quad (2.57)$$

Now, using the values obtained previously and assuming a proximity factor of 0.5 we can apply Eq. 2.45 to obtain the coverage-dependent energy barrier. The result is $\Delta E_{fwd}^{\neq}(u,v) = 1.0$ eV. This value is 0.2 eV larger than the zero-coverage limit energy barrier because the interactions with products are much repulsive than for reactants.

As shown, the use of lateral interactions become really important as under real working conditions a wide range of adsorbates can coexist modifying the energy barriers of the very different elementary processes. Therefore, relying only on zero-coverage limit energetics could give rise to misleading conclusions. Moreover, one has also to realize that lateral interaction can also affect the surface coverage.

2.4.6. Time scale disparity problem

kMC simulations are faster than ab initio molecular dynamics (AIMD) simulations as they avoid the explicit treatment of vibrations and rotations and instead considers only

rare events such as adsorption, desorption, diffusion and bond breaking and forming. However, these events that are happening over the catalyst occur at very different time scales. The slowest surface elementary steps are normally chemical reactions processes while adsorption/desorption and diffusion steps are normally faster. When this is the case, almost all the CPU time is spent simulating fast processes while other probably more important events such as the chemical reactions are difficult to sample. This implies that sometimes exceedingly large kMC simulations are needed in order to have some statistical meaningful evolution of the overall catalytic chemical process.

In order to deal with this time scale disparity problem, some solutions have been proposed. The main idea between all the proposed strategies is to somehow decrease the rate constants of the fast processes in order to reduce their propensity. The most straightforward solution is to multiply the rate constants of fast process by some scaling factor $\gamma < 1$. This solution has been successfully applied in many kMC studies.[35-39] A more sophisticated solution is to use accelerated algorithms in which fast processes are automatically scaled without the need of the user to previously specify the processes to be scaled. Chatterjee and Voter[40] developed the Accelerated Superbasin kinetic Monte Carlo (AS-kMC) method. In this method, the algorithm keeps track of how often processes are executed. If a specific process in the forward and reverse direction is executed a large number of times this might indicate that the system is trapped in these configurations (i.e., in the superbasin); then the algorithm applies a scaling factor of that process in order to reduce the rate constants and encourage the system to leave the current superbasin at an earlier time. The main drawback of this method is that for complex systems the total number of configurations can be exceedingly large and identifying the superbasin can be extremely slow. This latter problem was addressed by Dybeck et. al.[41] where instead of tracking the system configurations (superbasin) and processes, only some user-specified processes are tracked and scaled if the specified processes are quasi-equilibrated following the same criteria as Chatterjee and Voter method.

2.5. References

1. Schrödinger, E. Quantisierung als Eigenwertproblem. *Ann. Phys.*, **1926**, 84, 361–376.

2. Born, M.; Oppenheimer, J. R. Zur Quantentheorie der Molekeln. *Ann. Phys.*, **1927**, 84, 457.

3. Hohenberg, P.; Kohn, W. Inhomogeneous Electron Gas. *Phys. Rev.*, **1964**, 136, B864-B871.

4. Kohn, W.; Sham, L. J. Self-Consistent Equations Including Exchange and Correlation Effects. *Phys. Rev.*, **1965**, 140, A1133–A1138.

5. Perdew, J. P.; Schmidt, K. Jacob's Ladder of Density Functional Approximations for the Exchange-Correlation Energy. *AIP Conference Proceedings*, **2001,** 577, 1–20.

6. Perdew, J. P.; Zunger, A. Self-Interaction Correction to Density-Functional Approximations for Many-Electron Systems. *Phys. Rev. B*, **1981**, 23, 5048–5079.

7. Hua, X.; Chen, X.; Goddard, W. A. Generalized Gradient Approximation: An Improved Density-Functional Theory for Accurate Orbital Eigenvalues. *Phys. Rev. B*, **1997**, 55, 16103–16109.

8. Perdew, J. P.; Burke, K.; Ernzerhof, M. Generalized Gradient Approximation Made Simple. *Phys. Rev. Lett.*, **1996**, 77, 3865–3868.

9. Wellendorff, J.; Lundgaard, K. T.; Møgelhøj, A.; Petzold, V.; Landis, D. D.; Nørskov, J. K.; Bligaard, T.; Jacobsen, K. W. Density Functionals for Surface Science: Exchange-correlation Model Development with Bayesian Error Estimation. *Phys. Rev. B*, **2012**, 85, 235149-235172.

10. Klimeš, J.; Michaelides, A. Perspective: Advances and Challenges in Treating an der Waals Dispersion Forces in Density Functional Theory. *J. Chem. Phys.*, **2012**, 137, 120901-120913.

11. Grimme, S. Accurate Description of van der Waals Complexes by Density Functional Theory Including Empirical Corrections. *J. Comput. Chem.*, **2004**, 25, 1463–1473.

12. Grimme, S. Semiempirical GGA-type Density Functional Constructed with a Long-Range Dispersion Correction. *J. Comput. Chem*., **2006**, 27, 1787–1799.

13. Grimme, S.; Antony, J.; Ehrlich, S.; Krieg, H. A Consistent and Accurate Ab Initio Parametrization of Density Functional Dispersion Correction (DFT-D) for the 94 Elements H-Pu. *J. Chem. Phys.*, **2010**, 132, 154104-154123.

14. Dion, M.; Rydberg, H.; Schröder, E.; Langreth, D. C.; Lundqvist, B. I. Van der Waals Density Functional for General Geometries. *Phys. Rev. Lett.,* **2004**, 92, 246401-246405.

15. Schwerdtfeger, P. The Pseudopotential Approximation in Electronic Structure Theory. *Chem. Phys. Chem.,* **2011**, 12, 3143-3155.

16. Eyring, H. The Activated Complex in Chemical Reactions. *J. Chem. Phys*., **1935**, 3, 107–115.

17. Evans, M. G.; Polanyi, M. Some Applications of the Transition State Method to the Calculation of Reaction Velocities, Especially in Solution. *Trans. Faraday Soc*., **1935**, 31, 875–894.

18. Laidler, K. J. Chemical kinetics, Harper and Row, New York, **1987**.

19. Bruix, A.; Margraf, J.T.; Andersen, M.; Reuter, K. First-Principles-Based Multiscale Modeling of Heterogeneous Catalysis. *Nat. Catal.,* **2019**, 2, 659-670.

20. Pineda, M.; Stamatakis, M. Kinetic Monte Carlo Simulations for Heterogeneous Catalysis: Fundamentals, Current Status, and Challenges. *J. Chem. Phys.,* **2022**, 156, 120902-120931.

21. Grajciar, L.; Heard, J. C.; Bondarenko, A. A.; Polynski, M. V.; Meeprasert, J.; Pidko, E. A.; Nachtigall, P. Towards Operando Computational Modeling in Heterogeneous Catalysis. *Chem. Soc. Rev.*, **2018**, 47, 8307-8348.

22. Motagamwala, A. H.; Dumesic, J. A. Microkinetic Modeling: a Tool for Rational Catalyst Design. *Chem. Rev.,* **2021**, 121, 1049-1076.

23. Lozano-Reis, P.; Prats., H.; Sayos, R.; Illas, F. Limitations of Free Energy Diagrams to Predict the Catalytic Activity: The Reverse Water Gas Shift Reaction Catalyzed by Ni/TiC. *J. Catal.*, **2023**, 425, 203-211.

24. van Kampen, N. G. Stochastic Processes in Physics and Chemistry. Elsevier Science B. V. Amsterdam, North Holland, **2007**.

25. Jansen, A. P. J. An Introduction to Kinetic Monte Carlo Simulations of Surface Reactions, Springer-Verlag Berlin Heidelberg, **2012**.

26. Andersen, M.; Panosetti, C.; Reuter, K. A Practical Guide to Surface Kinetic Monte Carlo Simulations. *Front. Chem.,* **2019**, 202, 1-24.

27. Lukkien, J. J.; Segers, J. P. L.; Hilbers, P. A. J.; Gelten, R. J.; Jansen, A. P. J. Efficient Monte Carlo Methods for the Simulation of Catalytic Surface Reactions, *Phys. Rev. E*, **1998**, 58, 2598–2610.

28. Steinfeld, J.I.; Francisco, J. S.; Hase, W. L. Chemical kinetics and dynamics, Prentice Hall, Englewood Cliffs, USA, **1989**

29. Nørskov, J. K.; Bligaard, T.; Logadottir, A.; Bahn, S.; Hansen, L. B.; Bollinger, M.; Bengaard, H.; Hammer, B.; Sljivancanin, Z.; Mavrikakis, M.; Xu, Y.; Dahl, S.; Jacbsen, C. J. H. Universality in Heterogeneous Catalysis. *J. Catal.*, **2002**, 209, 275-278.

30. Michaelides, A.; Liu, Z. P.; Zhang, C. J.; Alavi, A.; King, D. A.; Hu, P. Identification of General Linear Relationships Between Activation Energies and Enthalpy Changes for Dissociation Reactions at Surfaces. *J. Am. Chem. Soc.* **2003,** 125, 3704–3705.

31. Grabow, L. C.; Gokhale, A. A.; Evans, S. T.; Dumesic J. A.; Mavrikakis, M. Mechanism of the Water Gas Shift Reaction on Pt: First Principles, Experiments, and Microkinetic modeling, *J. Phys. Chem. C*, **2008**, 112, 4608–4617.

32. Nielsen, J.; d'Avezac, M.; Hetherington, J.; Stamatakis, M.; Parallel Kinetic Monte Carlo Simulation Framework Incorporating Accurate Models of Adsorbate Lateral Interactions, *J. Chem. Phys*., **2013**, 139, 224706-2247019.

33. Stamatakis, M.; Vlachos, D. G. Unraveling the Complexity of Catalytic Reactions Via Kinetic Monte Carlo Simulation: Current Status and Frontiers, *ACS Catal*., **2012**, 2, 2648–2663.

34. Vignola, E.; Steinmann, S. N.; Vandegehuchte, B. D.; Curulla, D.; Stamatakis M.; Sautet, P. A Machine Learning Approach to Graph-Theoretical Cluster Expansions of the Energy of Adsorbate Layers, *J. Chem. Phys*., **2017**, 147, 054106-054119.

35. Prats, H.; Posada-Pérez, S.; Rodriguez, J. A.; Sayós, R.; Illas, F. Kinetic Monte Carlo Simulations Unveil Synergic Effects at Work on Bifunctional Catalysts. *ACS Catal.*, **2019**, 9, 9117-9126.

36. Lozano-Reis, P.; Prats, H.; Gamallo, P.; Illas, F.; Sayós, R.; Multiscale Study of the Mechanism of Catalytic CO_2 Hydrogenation: Role of the Ni(111) Facets. *ACS Catal.* **2020**, 10, 8077-8089.

37. Prats, H.; Álvarez, L.; Illas, F.; Sayós, R. Kinetic Monte Carlo Simulations of the Water Gas Shift Reaction on Cu(1 1 1) from Density Functional Theory Based Calculations. *J. Catal.*, **2016**, 333, 217–226.

38. Piccinin, S.; Stamatakis, M. CO Oxidation on Pd(111): A First-Principles-Based Kinetic Monte Carlo Study. *ACS Catal.*, **2014**, 4, 2143–2152.

39. Yang, L.; Karim, A.; Muckerman, J. T. Density Functional Kinetic Monte Carlo Simulation of Water Gas Shift Reaction on Cu/ZnO. *J. Phys. Chem. C.*, **2013**, 117, 3414–3425.

40. Chatterjee, A.; Voter, A. F. Accurate Acceleration of Kinetic Monte Carlo Simulations Through the Modification of Rate Constants, *J. Chem. Phys*., **2010**, 132, 194101-194113.

41. Dybeck, E. C.; Plaisance, C. P.; Neurock, M. Generalized Temporal Acceleration Scheme for Kinetic Monte Carlo Simulations of Surface Catalytic Processes by Scaling the Rates of Fast Reactions, *J. Chem. Theory Comput*., **2017**, 13, 1525–1538.

Chapter 3

CO_2 conversion over Ni(111)

3.1. Introduction

Carbon dioxide is one of the major contributors to global warming. It is mainly produced by burning carbon-rich fossil fuels, a process which is necessary to meet the energetic requirements of industrial processes. Although a switch from fossil fuels to green energies is desirable,[1,2] it is still not possible to cover the whole energy demands by using green energy only and it is expected that in the following decades the amounts of atmospheric CO_2 will still rise. Therefore, as a way to reverse this situation, many scientists have focused on CO_2 conversion into other valuable chemicals of industrial interest, thus taking benefit of the high amounts of CO_2 and using it as an economical C_1 carbon source. Among the different possible products in which CO_2 can be converted, CO, methane, methanol and formaldehyde are the most investigated options.[3-7] In this regard, just by modifying the type of metal and support, the working conditions and the structure and size of both the metal and the support one can tune the selectivity towards the desired product.

In the case of CO_2 hydrogenation, Ni-based catalysts are one of the most commonly used catalysts as they present a good compromise between catalytic activity and economic viability in comparison to other precious metals.[8,9] Regarding the different products that can be obtained after CO_2 hydrogenation over Ni-based catalysts, CH_4[10-22] and CO[17,20-26]—obtained via the Sabatier reaction and RWGS reaction, respectively—are by far the most common options and their selectivity depends on the morphology and size of the Ni nanoparticles or clusters, the type of support and the working conditions used. Note that most of the experimental studies deal with the CO_2 hydrogenation reaction on Ni cluster or nanoparticles anchored over some support while theoretical studies[27-33] usually focusses on extended surfaces and in particular on the Ni (111) surface as it is the most stable Ni surface, thus, most likely to be present in large nanoparticles. However, although many theoretical studies have dealt with the CO_2 hydrogenation reaction over Ni (111), there is still not a full consensus about the role of this surface on the overall

activity and selectivity that are experimentally observed. This is mainly due to the complexity of the reaction network for the CO_2 hydrogenation reaction. Moreover, most of the available theoretical studies rely on the pure static picture that DFT calculations provides. However, in such a complex system with many elementary reactions, kinetic simulations are required to clearly understand how the catalyst behaves under real working conditions.

The present chapter aims to compile the main results of the study of the CO_2 hydrogenation reaction over the Ni (111) surface by a multiscale approach coupling DFT calculations and kMC simulations, which allows us to unveil which is the role of the Ni (111) surface. A full description of the work done can be found in Ref 34.

3.2. Complexity of the reaction network

In the present study we have considered a quite large reaction network to study the CO_2 hydrogenation reaction over Ni (111) as shown in Figure 3.1. We have considered several elementary reactions and the possible formation of different products, namely: CO, CH_2O, CH_3OH and CH_4 as well as H_2O. The complexity of the studied reaction network lies on the large number of intermediate species, gas-phase species and elementary reactions that interconnect the different paths. The inclusion of all these species and reactions allows us to produce results as accurate as possible and to avoid to somehow bias the reaction to a given desired product. Moreover, including more reactions and intermediates increases the explored energetic landscape, avoids forgetting some possible relevant reactions and allows one to reach a better understanding of the mechanism behind the overall reaction. In total we have considered 86 elementary steps that include adsorption, desorption, diffusion, and bond breaking and forming processes.

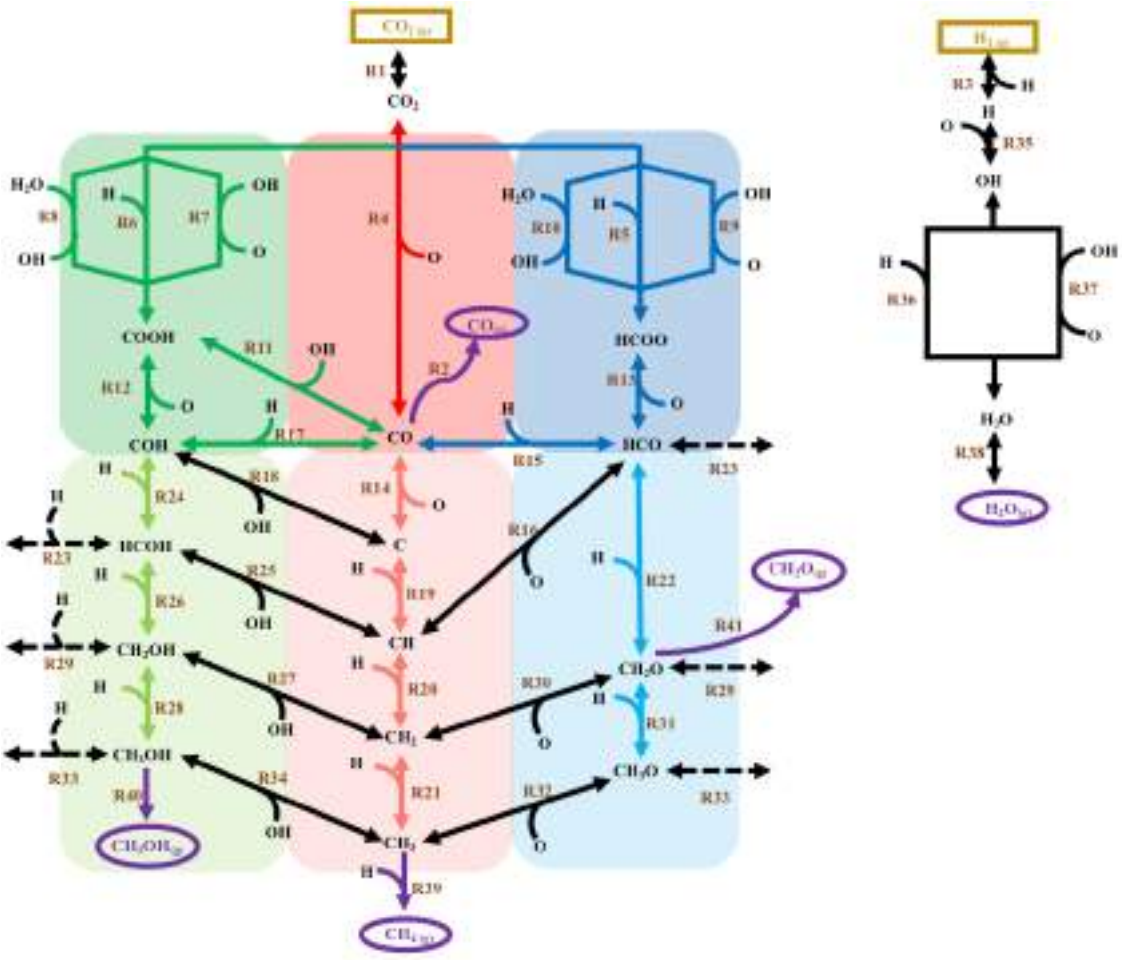

Figure 3.1. Reaction network proposed for the CO_2 hydrogenation (left) and H_2 oxidation (right). The redox pathway (red), formate pathway (dark blue) and carboxyl pathway (dark green) are considered for the RWGS reaction. The C hydrogenation pathway (salmon), HCO hydrogenation pathway (light blue) and COH hydrogenation pathway (light green) are considered for the Sabatier reaction. Black lines are for elementary steps that interconnect different pathways. Note that dashed lines are referred for those reactions that interconnect the COH and HCO hydrogenation pathways. Dark yellow and purple stands for reactants and products of the CO_2 hydrogenation reactions. Reversible steps are represented by double arrows. Picture adapted from the original picture in Ref 34.

3.3. Results

The main DFT and kMC results for the study of the CO_2 hydrogenation reaction over Ni (111) are presented below. The reader interested in more details is referred to ref 34.

3.3.1. DFT results

The DFT calculations provide the energetics of the gas-phase species, intermediate species and transition states. With this information one can calculate the reaction energies

($\Delta E_{0,r}$) and the energy barriers ($\Delta E_0^{\neq}$) of the different processes as summarized in Table 1, including the zero-point energy term.

Table 3.1. Reaction energies ($\Delta E_{0,r}$) and energy barriers ($\Delta E_0^{\neq}$) for the different considered elementary processes including the zero-point energy term. For the energy barriers the values in parentheses refer to the reverse energy barrier. Notation: free sites (*), adsorbed species (A) and gas-phase species (A(g)). Note that COOH, HCOO, CH_2OH and CH_3OH are bidentate species. Table adapted from the original table in Ref 34.

ID: surface process	$\Delta E_{0,r}$ / eV	$\Delta E_0^{\neq}$ / eV	ID: surface process	$\Delta E_{0,r}$ / eV	$\Delta E_0^{\neq}$ / eV
R1: $CO_{2(g)} + * \rightleftharpoons CO_2$	-0.14	0.0 (0.14)	**R26:** $HCOH + H \rightleftharpoons CH_2OH$	0.22	0.63 (0.41)
R2: $CO \rightarrow CO_{(g)} + *$	1.58	1.58 (0.0)	**R27**: $CH_2OH \rightleftharpoons CH_2 + OH$	-0.67	0.71 (1.38)
R3: $H_{2(g)} + 2* \rightleftharpoons 2H$	-0.60	0.26 (0.86)	**R28:** $CH_2OH + H \rightleftharpoons CH_3OH + *$	-0.29	0.74 (1.03)
R4: $CO_2 + * \rightleftharpoons CO + O$	-0.69	0.86 (1.55)	**R29**: $CH_2O + H \rightleftharpoons CH_2OH$	0.45	1.00 (0.55)
R5: $CO_2 + H \rightleftharpoons HCOO$	0.04	1.06 (1.02)	**R30**: $CH_2O + * \rightleftharpoons CH_2 + O$	-0.38	0.96 (1.34)
R6: $CO_2 + H \rightleftharpoons COOH$	0.51	1.35 (0.84)	**R31**: $CH_2O + H \rightleftharpoons CH_3O + *$	-0.33	0.52 (0.85)
R7: $CO_2 + OH + * \rightleftharpoons COOH + O$	0.35	0.47 (0.12)	**R32:** $CH_3O + * \rightleftharpoons CH_3 + O$	-0.14	1.36 (1.50)
R8: $CO_2 + H_2O + * \rightleftharpoons COOH + OH$	0.17	0.20 (0.03)	**R33**: $CH_3O + H \rightleftharpoons CH_3OH$	0.48	1.43 (0.95)
R9: $CO_2 + OH + * \rightleftharpoons HCOO + O$	-0.12	1.70 (1.82)	**R34:** $CH_3OH \rightleftharpoons CH_3 + OH$	-0.46	1.80 (2.26)
R10: $CO_2 + H_2O + * \rightleftharpoons HCOO + OH$	-0.31	1.61 (1.92)	**R35:** $O + H \rightleftharpoons OH + *$	0.16	1.28 (1.12)
R11: $COOH \rightleftharpoons CO + OH$	-1.04	0.50 (1.54)	**R36:** $OH + H \rightleftharpoons H_2O + *$	0.35	1.25 (0.90)
R12: $COOH \rightleftharpoons COH + O$	-0.08	1.28 (1.36)	**R37:** $OH + OH \rightleftharpoons O + H_2O$	0.19	0.42 (0.23)
R13: $HCOO \rightleftharpoons O + HCO$	0.53	1.39 (0.86)	**R38:** $H_2O \rightarrow * + H_2O_{(g)}$	0.20	0.20 (0.0)
R14: $CO + * \rightleftharpoons C + O$	1.43	2.98 (1.55)	**R39:** $CH_3 + H \rightarrow CH_{4(g)} + 2*$	-0.22	0.87 (1.09)
R15: $HCO + * \rightleftharpoons CO + H$	-1.26	0.21 (1.47)	**R40:** $CH_3OH \rightarrow CH_3OH_{(g)} + 2*$	0.31	0.31 (0.0)
R16: $HCO + * \rightleftharpoons CH + O$	-0.31	1.10 (1.41)	**R41:** $CH_2O \rightarrow CH_2O_{(g)} + *$	0.58	0.58 (0.0)
R17: $COH + * \rightleftharpoons CO + H$	-1.12	1.21 (2.33)	**D1:** $C_{fcc} + * \rightleftharpoons C_{hcp} + *$	-0.04	0.31 (0.35)
R18: $COH + * \rightleftharpoons C + OH$	0.47	1.81 (1.34)	**D2:** $O_{fcc} + * \rightleftharpoons O_{hcp} + *$	0.10	0.42 (0.32)
R19: $C + H \rightleftharpoons CH + *$	-0.49	0.78 (1.27)	**D3:** $H_{fcc} + * \rightleftharpoons H_{hcp} + *$	0.02	0.12 (0.10)
R20: $CH + H \rightleftharpoons CH_2 + *$	0.31	0.65 (0.34)	**D4:** $CO_{fcc} + * \rightleftharpoons CO_{hcp} + *$	-0.01	0.11 (0.12)
R21: $CH_2 + H \rightleftharpoons CH_3 + *$	-0.08	0.60 (0.68)	**D5:** $OH_{fcc} + * \rightleftharpoons OH_{hcp} + *$	0.09	0.19 (0.10)
R22: $HCO + H \rightleftharpoons CH_2O + *$	0.37	0.82 (0.45)	**D6:** $H_2O_{top} + * \rightleftharpoons H_2O_{top} + *$	0.00	0.08 (0.08)
R23: $HCO + H \rightleftharpoons HCOH + *$	0.60	1.13 (0.53)	**D7:** $CH_{fcc} + * \rightleftharpoons CH_{hcp} + *$	0.02	0.32 (0.31)
R24: $COH + H \rightleftharpoons HCOH + *$	0.73	0.88 (0.15)	**D8:** $CH_{2fcc} + * \rightleftharpoons CH_{2hcp} + *$	0.04	0.19 (0.15)
R25: $HCOH + * \rightleftharpoons CH + OH$	-0.75	0.72 (1.47)	**D9:** $CH_{3fcc} + * \rightleftharpoons CH_{3hcp} + *$	0.02	0.15 (0.13)

From the values reported in Table 3.1 it is possible to construct different potential energy diagrams (PED), which could give some insights about the mechanism governing the overall reaction. In this regard, we have distinguished three different pathways for the RWGS reaction and three different ones for the Sabatier reaction as shown in Figure 3.2.

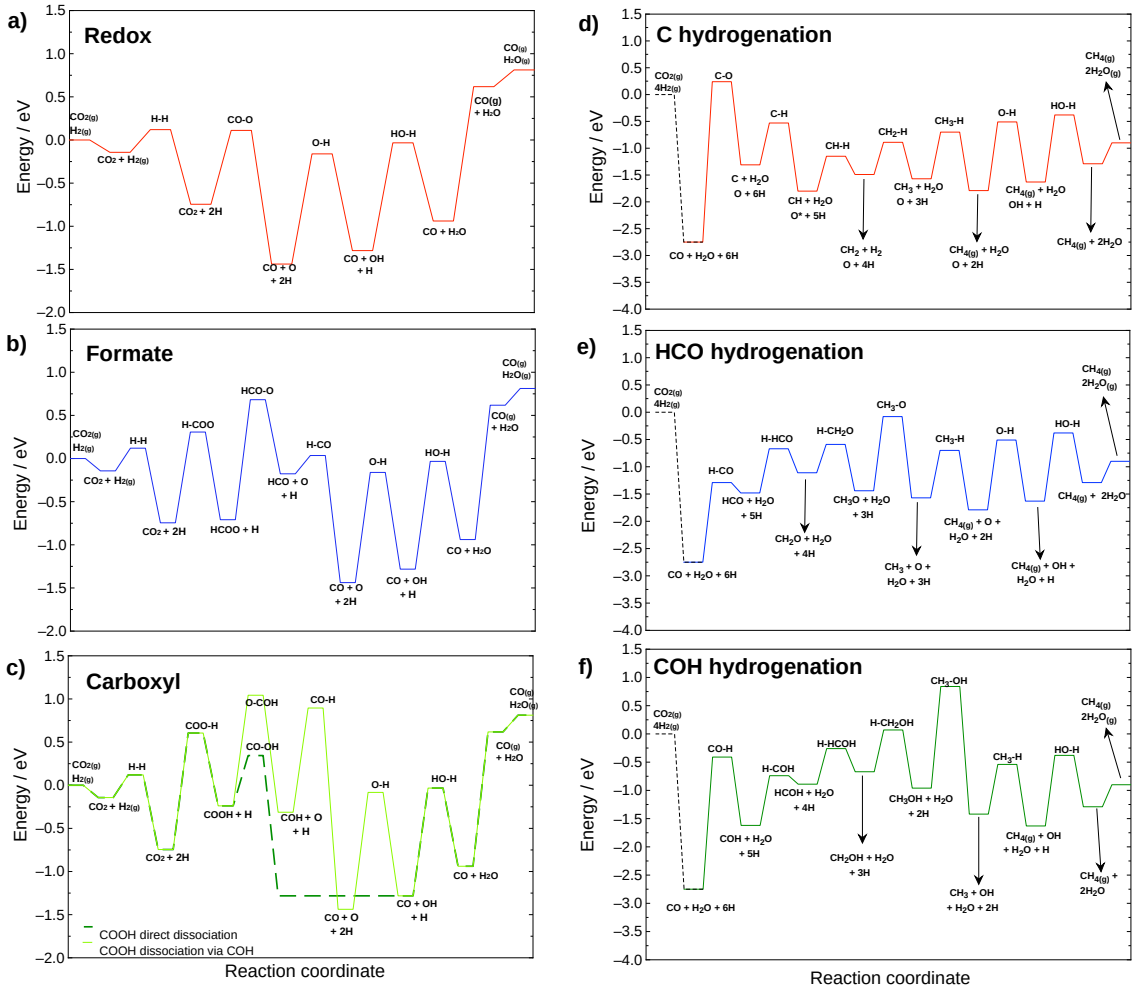

Figure 3.2. Potential energy diagrams for the RWGS reaction: a) redox, b) formate, and c) carboxyl pathways and for the Sabatier reaction d) C hydrogenation, e) HCO hydrogenation, and f) COH hydrogenation pathways. Adsorbed species are assumed to be at infinite distance and all the values include the zero-point energy term. Picture directly taken from Ref 34.

The three proposed pathways involved in the mechanisms of the RWGS reaction are depicted in the left side of Figure 3.2 and are the redox, formate and carboxyl pathways, (Figures 3.2a, 3.2b and 3.2c, respectively). For the redox route CO is produced after the direct CO_2 dissociation. However, both the formate and carboxyl pathways involve a first hydrogen-assisted step in which CO_2 is hydrogenated to HCOO or COOH, respectively. Next, these intermediate species follow successive dissociation steps to finally produce CO. Comparing the first step of the three pathways one can see that the

redox one involves a unimolecular step while both hydrogen-assisted pathways involve a bimolecular step, highly dependent on the H coverage and, in general, less likely to occur than the unimolecular one. Moreover, if one compares the energy barriers of these steps, namely, CO_2 dissociation, HCOO formation and COOH formation reactions (i.e., 0.86, 1.06 and 1.35 eV, respectively), it can be seen that the lowest energy barrier is for the CO_2 dissociation, which points directly to this pathway as dominant in the mechanism and, therefore, to be the most probable one. For the case of the formate and carboxyl pathways, it can be seen that the former has a lower hydrogenation energy barrier which in principle would favor the formation of HCOO rather than COOH. However, the following HCOO dissociation to HCO + O could compete with the dissociation to form CO_2 + H with energy barriers of 1.39 and 1.02 eV, respectively. For the case of the COOH formation, this intermediate will be certainly less probable to be formed but at the same time whenever COOH is formed it would probably prefer to dissociate to CO + OH ($\Delta E_0^{\neq}$= 0.50 eV) rather than go backward to CO_2 + H ($\Delta E_0^{\neq}$= 0.84 eV). Therefore, by looking at the potential energy diagrams for the HCOO and COOH mechanism only, it is not possible to firmly conclude which pathway dominates the mechanism. However, the PEDs clearly indicate that the redox pathway will be dominant, suggesting CO_2 dissociation as the rate determining step while both hydrogen-assisted pathways will be more important at high H coverages.

The three proposed mechanisms for the Sabatier reaction are shown in the right side of Figure 3.2 and are the carbon hydrogenation, HCO hydrogenation and COH hydrogenation pathways (Figures 3.2d, 3.2e and 3.2f, respectively). These three pathways start from CO as it is assumed that CO is formed from the redox one. As can be seen, they differ in the way CH_3 is formed which then is further hydrogenated to methane. Note that the different intermediates shown in the PEDs can be obtained from other elementary steps as there are many steps that interconnect the different pathways (see Figure 3.1). Let us start the analysis by comparing the initial step for each pathway, namely, CO dissociation, HCO formation and COH formation with energy barriers of 2.98, 1.47 and 2.33 eV, respectively. The lowest energy barrier is for the HCO formation followed by the COH formation, which suggest these reactions to be more probable than the CO dissociation reaction. Obviously, these reactions are H-assisted reactions; thus, highly dependent on the hydrogen coverage. However, the direct CO dissociation has an extremely high energy barrier which, even at very low hydrogen coverage, will be hardly

surmounted. Then, comparing the HCO and COH hydrogenation pathways one can readily see that HCO would be formed more easily than COH, suggesting the HCO hydrogenation pathway to be most likely. However, HCO formation is a very endothermic reaction, which implies that, whenever HCO is formed, it would dissociate again to form CO + H. The case of the COH formation involves a higher energy barrier but is less endothermic. Focusing now on the following hydrogenation steps of HCO and COH one can spot that, in general, all hydrogenation steps are endothermic, which will favor backward reactions. Moreover, the final CH_3O and CH_3OH dissociation reactions have quite high energy barriers of 1.36 and 1.80 eV, respectively. Therefore, among the three proposed reaction pathways the HCO hydrogenation pathway seems to be the most probable. However, only using DFT information is quite complicated to clearly define which will be the preferred pathway among the three suggested.

By inspecting the full reaction network shown in Figure 3.1, it is possible to suggest a possible alternative route more feasible for the CH_4 formation combining different pathways. First, CO is formed via the redox mechanism followed by its hydrogenation to HCO. Then HCO can either dissociate to CO + H or CH + O or be hydrogenated to CH_2O or HCOH with energy barriers of 0.21, 1.10, 0.82 and 1.13 eV, respectively. Among the different reactions the lowest energy barrier is the one for the CO formation. Regarding the other possible reactions that permit CH_4 formation, the most plausible mechanism at high hydrogen coverages would be the HCO hydrogenation to CH_2O and its further dissociation to CH_2 and hydrogenation to CH_4. On the contrary, at low H coverages an alternative route will be the HCO dissociation to CH and its further hydrogenation to methane. Therefore, one can suggest that the formation of CH_4 would involve the RWGS redox pathway followed by a combination of the HCO and C hydrogenation pathways. However, one must consider that intermediates can also desorb, which makes more complicated to firmly conclude if the proposed route will dominate the methane formation mechanism or if other side products would be preferred. To provide further insight, kMC simulations are performed to inspect how the system behaves at several working conditions.

3.3.2. kMC results

To study the mechanism and selectivity of the CO_2 hydrogenation reaction over Ni (111) we have run several kMC simulations under typical operating conditions for the Sabatier reaction on Ni-based catalysts; [4] thus, temperatures of 573.15 and 673.15 K and pressures of 1 and 10 bars with a CO_2/H_2 mixture ratio of 1:4 are considered. We then analyze the turnover frequency (TOF) and the event frequencies of the different executed events to unravel the dominant reaction mechanism and to provide estimates of activity and selectivity. The TOF and event frequencies at the four different conditions are shown in Figure 3.3.

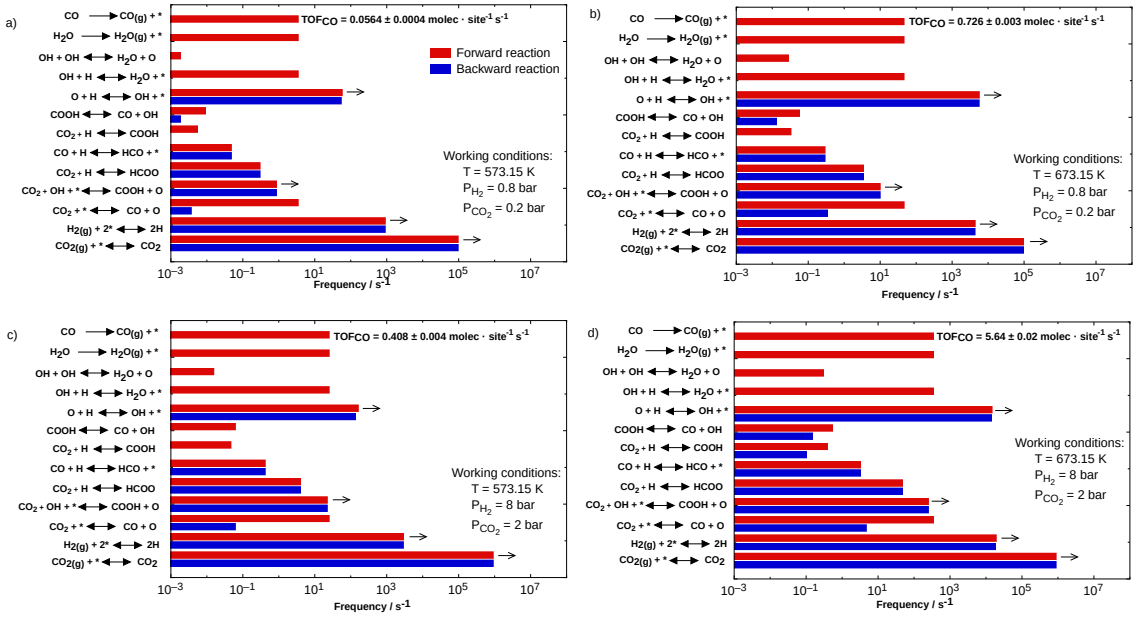

Figure 3.3. Event frequencies of the CO_2 hydrogenation reaction at four different working conditions. a) T= 573.15 K, P_{H_2} = 0.8 bar, P_{CO_2} = 0.2 bar, b) T= 573.15 K, P_{H_2} = 8 bar, P_{CO_2} = 2 bar, c) T= 673.15 K, P_{H_2} = 0.8 bar, P_{CO_2} = 0.2 bar, d) T= 673.15 K, P_{H_2} = 8 bar, P_{CO_2} = 2 bar. Picture directly taken from Ref 34.

From Figure 3.3 one can clearly see that for the four different working conditions no methane is formed and only CO is observed, hence showing that the CO_2 hydrogenation over Ni (111) follows the RWGS mechanism. The event frequencies indicate that CO is mainly formed via the redox mechanism as already inferred by the DFT calculations. Moreover, it can be seen that, to a lower extent, the carboxyl pathway is also a source of CO, something that only from the DFT calculations cannot be concluded. In fact, one can see that the HCOO formation is executed more times than the COOH formation as the energy barrier of the former reaction is lower than the latter one

(i.e., 1.06 and 1.35 eV, respectively). However, as HCOO dissociation to CO_2 + H has a lower energy barrier than the dissociation to produce HCO + O (i.e., 1.02 and 1.39 eV, respectively), whenever HCOO is formed it prefers to go backward and form CO_2 + H again, as shown in the event frequencies. On the contrary, although the COOH formation has a higher energy barrier, its dissociation to CO is kinetically less impeded, therefore being the carboxyl pathway also (in a lower extent) one of the dominant ones in the mechanisms for the RWGS reaction. In fact, CO is formed through the carboxyl pathway with a frequency of formation between 2 and 3 orders of magnitude smaller than through the redox pathway, which suggests that the CO_2 is the rate determining step as confirmed by calculating the Campbell degree of rate control.[35]

Regarding the main limitations for CH_4 formation, different conclusions can be extracted from the event frequency plots of Figure 3.3. From these plots, one can spot the lack of CO dissociation or COH formation reactions, as they present large energy barriers, which impedes two possible pathways for the CH_4 formation. On the contrary, the HCO formation is indeed observed, but as the DFT calculations suggest, whenever HCO is formed it prefers to dissociate to form CO + H again instead of dissociating to CH + O or being hydrogenated to form CH_2O. This, added to the very similar energy barrier for the CO desorption and HCO formation (i.e., 1.58 and 1.47 eV, respectively) make that CO normally prefers to desorb rather than being hydrogenated to HCO, and whenever HCO is formed it almost instantaneously dissociates to form CO + H with the further CO desorption. Finally, from the event frequencies it can be seen that increasing the temperature and pressure just increase the event frequencies in a fairly homogeneous way and that, as expected, the highest the temperature and pressure the highest the TOF.

Up to now we have shown that for the Ni (111) facet the CO_2 hydrogenation follows the RWGS reaction instead of the Sabatier reaction, which is in contradiction with some previous theoretical studies[27,30,31] and also with an experimental study[16] for the Ni(111) surface. However, the experimental study of Heine et al.[16] claims that the Ni (111) facet was able to produce methane but solely because of the presence of a XPS peak that was attributed to C. Nevertheless, the same study provides compelling evidence of CO being formed following the RWGS reaction. Regarding the theoretical studies, they suggested that, in general, methane was formed following the HCO mechanism but without considering the possible desorption of intermediate side products. Moreover, most of these studies rely on DFT calculations only, with conclusions extracted from the analysis

of the PEDs, which are extremely useful to gain insights about the reactivity but cannot completely explain how the system behaves under working conditions. To this end, it is required to couple DFT calculations with some type of kinetic simulations. Precisely, this is what Vogt et al.,[31] did in a recent work in which they studied the CO_2 hydrogenation reaction over a variety of Ni surfaces, including the Ni (111) facet, and concluded that some methane could be formed over all the Ni facets. However, their reaction network was quite incomplete, and the desorption of possible intermediate side products was neglected. As a result, they observed an extremely high CO coverage (~100%) and a very small CH_4 TOF. The effect of neglecting the desorption of possible side products and only allowing to desorb CH_4 could somehow bias the reaction through the desired product without knowing if other side products would prefer to desorb, as we have observed for the case of CO. Finally, the CO formation observed in our simulations could be apparently in contrast with the experimental evidence that Ni-based catalysts can be active towards the Sabatier reaction.[10-13] From our results, we conclude that the Ni (111) facet itself is not active for the CH_4 formation and that communication between other facets, the presence of undercoordinated sites, the role of the support, the metal-support interface and directly the presence of other Ni facets should play an important role in the overall CH_4 formation.

3.4. Summary and conclusions

To sum up, we have thoroughly studied the CO_2 hydrogenation reaction over Ni (111) by means of a multiscale approach coupling DFT calculations with kMC simulations. From the DFT data we have constructed different PEDs for the RWGS and Sabatier reaction in order to unravel which are the most plausible pathways dominating the molecular mechanisms of these two reactions. For the RWGS reaction we suggest that the redox pathway is the most favorable one, but we cannot firmly conclude whether the formate or carboxyl pathways will be preferred. Regarding the Sabatier reaction DFT calculations suggest that methane is formed following the redox pathway of the RWGS reaction and a subsequent combination of the HCO and C hydrogenation pathways. However, the possible desorption of intermediate side products and the endothermicity of the HCO formation reactions seem to hinder the CH_4 formation; thus, from DFT calculations only, one cannot firmly conclude which will be the preferred mechanism.

The kMC simulations have shown that, on the Ni(111) surface, no methane was observed at the different working conditions in contrast to what has been suggested in previous published DFT and microkinetic studies. kMC simulations show that CO is the unique product, which is formed following the redox mechanism of the RWGS reaction and through the carboxyl mechanism to a lesser extent. The limitations for CH_4 formation are mainly: (i) the very large CO dissociation and the COH formation energy barriers, which hinders the C and COH hydrogenation mechanisms, ii) the very large endothermicity of the HCO formation step, thus that whenever HCO is formed it goes backward to form CO + H again, and iii) the very similar energy barriers for the HCO formation and CO desorption processes, the latter guiding the selectivity towards CO. Therefore, we conclude that the methane production observed experimentally is not due to the Ni (111) facet itself but rather to a cooperative effect between the Ni (111) and other facets, the effect of the support and the interface or because of the presence of different Ni active facets.

3.5. Publications

ACS Catalysis

pubs.acs.org/acscatalysis Research Article

Multiscale Study of the Mechanism of Catalytic CO_2 Hydrogenation: Role of the Ni(111) Facets

Pablo Lozano-Reis, Hèctor Prats, Pablo Gamallo, Francesc Illas, and Ramón Sayós*

Cite This: *ACS Catal.* 2020, 10, 8077−8089 Read Online

ACCESS | Metrics & More | Article Recommendations | Supporting Information

ABSTRACT: The molecular mechanism of CO_2 hydrogenation on a Ni(111) surface has been thoroughly investigated by means of periodic density functional theory calculations, including dispersion interactions, along with accurate kinetic Monte Carlo simulations, including lateral interactions between the adsorbates. The present reaction model involves 25 different species and a total of 86 elementary processes, including adsorptions, desorptions, surface chemical steps, and diffusions. The reaction network accounts for three different mechanisms for the reverse water-gas shift reaction and three different mechanisms for methanation. The kinetic Monte Carlo simulations reveal that the reverse water-gas shift reaction dominates the CO_2 hydrogenation on Ni(111) with no evidence of methane formation. The reaction proceeds mainly through the redox route, with the carboxyl pathway also being active but to a lesser extent. Methane production is hindered by the H + CO → HCO endothermicity and the prohibitive energy barrier for CO dissociation, implying CO desorption rather than evolution through the Sabatier reaction. A detailed comparison to earlier theoretical studies supporting the methanation reaction shows that some unreliable assumptions along with limited theoretical approaches biased the former conclusion.

KEYWORDS: *reverse water-gas shift reaction, Sabatier reaction, nickel (111), density functional theory, kinetic Monte Carlo, catalytic activity*

INTRODUCTION

The continuous and drastic increase in the use of carbon-rich fossil fuels in response to the world energy demand has dangerously increased the amounts of atmospheric carbon dioxide with concomitant effects on the global warming of our climate system. Although a switch from fossil fuels toward different sources of green energies[1,2] would be desirable, these cannot yet cover all the global energy demands. In fact, it is expected that atmospheric CO_2 concentration will be still rising in upcoming years. Therefore, many efforts are being addressed toward the chemical conversion of CO_2 into new value-added chemicals of industrial interest, CO, CH_4, methanol, and formaldehyde being the more investigated options.[3−7] The common step for all of these processes is CO_2 capture from flue gases through the so-called carbon capture and storage (CCS) technologies.[8−10] Currently, this strategy seems to be suitable for industrial purposes that involves simultaneously reducing the environmental impact related to carbon dioxide emissions and generating chemicals that can be further used as energy carriers, thus creating a cyclic energy economy where appropriate heterogeneously catalyzed processes play an essential role.

In the last few decades, catalytic CO_2 hydrogenation has gained attraction toward the use of this greenhouse gas as an economical C_1 carbon source. Moreover, the power-to-gas (PtG) technology[11,12] has increased interest as a promising option to absorb and exploit surplus renewable energy. The PtG concept is based on using the excesses of renewable energies (i.e., excesses of solar power or wind power) for water splitting and then use the produced H_2 for CO_2 hydrogenation toward different chemicals. By a choice of the metal and type of support used for the heterogeneous catalyst for CO_2 hydrogenation, it is possible to tune the selectivity toward a specific product. Among the possible chemicals that can be obtained from the CO_2 hydrogenation, methanol,[13−23] methane,[24−36] and CO[28,37−41] have attracted increasing interest due to the various possible applications either as fuels or in syngas processes. Methanol is produced via CO_2 partial reduction using Au-,[13−15] Pd-,[16,17] or Cu-based catalysts,[18−20,22,23] methane is produced mostly using Ru-,[25−27] Ni-,[29−35] Pt-,[24] or Pd-based catalysts[28] via the well-known Sabatier reaction, and CO can be obtained through the reverse water-gas shift reaction (RWGS) using Pt-,[37] Rh-,[38] Fe-,[39] or Ni-based catalysts.[40,41]

In the case of CO_2 hydrogenation, Ni is one of the most commonly used catalysts because of its relatively high activity and its economic viability in comparison to the noble

Received: April 8, 2020
Revised: June 8, 2020
Published: June 18, 2020

https://dx.doi.org/10.1021/acscatal.0c01599
ACS Catal. 2020, 10, 8077−8089

metals.[42,43] It must be pointed out that, while most of the experimental works deal with CO_2 hydrogenation on Ni-based, usually supported catalysts,[29,35,40,41] theoretical studies have focused on the idealized Ni(111) surface.[44−52] The reason for this is that it constitutes the most stable extended Ni surface and, thus, Ni(111) facets would predominate in the large Ni nanoparticles that are present in the industrial catalysts. However, in spite of the many studies published on the mechanism of the CO_2 hydrogenation on Ni(111), the overall picture is not yet fully understood, with conflicting predictions regarding selectivity with respect to the RWGS or Sabatier reactions.

From an experimental point of view there has been only one study directly focusing on CO_2 hydrogenation on the Ni(111) surface. In this study, Heine et al.[35] used ambient-pressure X-ray photoelectron spectroscopy and identified OH and CO surface species, a clear indication that the RWGS reaction was occurring. Moreover, these authors also reported the presence of atomic C, hence indirectly suggesting that the Sabatier reaction would also take place on this surface through the reduction of CO to C and its later hydrogenation to CH_4. However, they did not provide direct evidence regarding methane formation and no information was given regarding either the turnover frequency (TOF) or the CO/CH_4 selectivity.

The number of theoretical studies dealing with CO_2 hydrogenation on Ni(111) is rather vast, with different models being used as well. For instance, a cluster model study proposed that the $2CO \rightarrow C + CO_2(g)$ disproportionation step constitutes the key process for atomic carbon formation that can be further hydrogenated to methane.[46] On the other hand, Ren et al.[47] suggested three different mechanisms for CO_2 methanation, concluding that the CO dissociation mechanism was the most likely to occur. It is interesting to mention that available studies regarding CO methanation on Ni(111) can provide additional information for CO_2 hydrogenation, as many elementary steps are coincident for both reactions. Thus, Zhou et al.[45] studied the competition between the water-gas shift (WGS) and CO methanation reactions on Ni(111), concluding that the WGS reaction was more likely than the methanation reaction. Similarly, Zhi et al.[44] investigated the CO methanation and proposed that the mechanisms through the HCO and HCOH species are the most favorable routes for methane formation. In a recent DFT study of the RWGS reaction on Ni(111) and Ni(311) surfaces, Zhang et al.[49] suggested that Ni(311) should be more active than Ni(111) for the surface redox mechanism in the RWGS reaction. There are also combined experimental and theoretical studies, although they seldom use the same models system. For instance, Vrijburg et al.[53] studied CO_2 hydrogenation on bimetallic catalysts, Ni/TiO_2 and $NiMn/TiO_2$ were used in the experiments, and $Mn_4O_4/Ni(111)$ and Ni(311) were used in the calculations. Both experiments and calculations suggest a higher activity for the bimetallic catalysts. Very recently, Vogt et al.[48] reported an experimental and theoretical study for CO_2 hydrogenation catalyzed by Ni. The experiments were performed over Ni catalyst supported on different metal oxides, whereas the calculations were carried out for several Miller low-index Ni ideal surfaces and included a rather limited microkinetic modeling. These authors provided experimental evidence that methane is formed over the supported Ni catalysts, a conclusion maintained by the theoretical study on the ideal surfaces.

In the present study we combine periodic DFT calculations including dispersion interactions with high-fidelity kinetic Monte Carlo (kMC) simulations to obtain an in-depth insight into the CO_2 hydrogenation mechanism on Ni(111) and to provide direct, unbiased predictions of activity and selectivity toward both the RWGS and Sabatier reactions under relevant operating conditions. Macroscopic modeling through kMC or microkinetic simulations are being increasingly used in theoretical studies of heterogeneously catalyzed reactions because they incorporate pressure and temperature effects beyond a purely thermodynamic picture. Indeed, temperature and pressure effects can have a decisive role in the catalytic performance. Even if both kMC and microkinetic simulations provide similar information regarding the macroscopic regime, we have chosen the former because they do not rely on the mean-field approximation and are spatially resolved, thus including adsorbate mobility and reaction dynamics in an explicit way.

COMPUTATIONAL METHODS AND MODELS

DFT Calculations. The DFT-based calculations have been carried out using the Vienna Ab Initio Simulation Package (VASP) code[54−56] with the frozen-core augmented wave (PAW) method[57] to describe the interaction between the atomic cores and the valence electron density. Since the exact universal functional remains unknown, the choice of the density functional is always an open issue and a matter of discussion. In view of recent benchmark studies[58−61] showing that the rather recently proposed BEEF-vdW functional[61] provides an agreement with the available experimental data better than other commonly used functionals, we decided to use this functional that includes nonlocal correlation effects as well. For the scrutinized systems this functional exhibits mean absolute deviations usually lower than 0.3 eV, although this is dependent on the training data considered.

Spin polarization has been considered to account for the magnetic properties of nickel. The optimized nickel lattice parameter is 3.54 Å, in good agreement with the experimental value of 3.52 Å.[62] The Ni(111) surface—featuring hcp, fcc, bridge, and top adsorption sites—has been modeled by a slab 3 × 3 supercell model containing four atomic layers with a 20 Å vacuum width between periodically repeated slabs, to avoid spurious interactions. The two bottom layers of the slab have been kept fixed at their bulk positions to provide an appropriate bulk environment to the two outermost surface atomic layers that have been allowed to fully relax in the geometry optimization calculations involving either the clean or adsorbate-covered surface. A cutoff energy for the plane wave expansion of 415 eV and a (7 × 7 × 1) Monkhorst−Pack[63] k-point mesh for sampling the first Brillouin zone have been used in all the calculations. A 10^{-5} eV threshold has been selected for the electronic energy optimization, while ionic relaxation has been allowed until the forces acting on the atoms were smaller than 0.01 eV $Å^{-1}$.

Transition states (TS) have been located by means of the climbing-image nudged elastic band method.[64,65] The initial guesses for the employed intermediate images have been generated by means of the Atomic Simulation Environment package[66] using the image dependent pair potential procedure.[67] The located TS structures have been properly characterized by pertinent frequency analyses, ensuring that they only exhibit one imaginary frequency. Frequency calculations have also been performed for all of the adsorbed

https://dx.doi.org/10.1021/acscatal.0c01599
ACS Catal. 2020, 10, 8077−8089

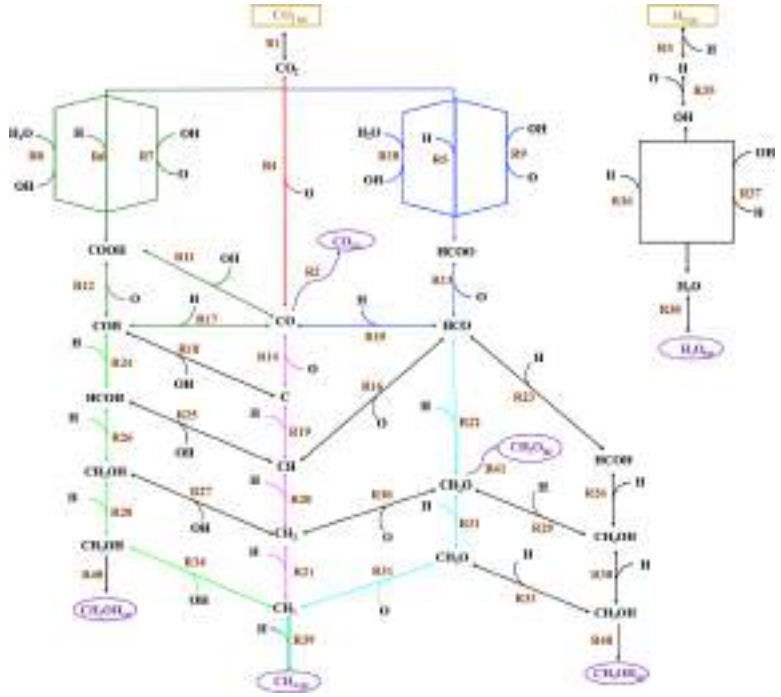

Figure 1. Reaction network proposed for the CO_2 hydrogenation (left) and H_2 oxidation (right). The redox pathway (red), formate pathway (dark blue), and carboxyl pathway (dark green) are considered for the RWGS reaction. The C hydrogenation pathway (magenta), HCO hydrogenation pathway (light blue), and COH hydrogenation pathway (light green) are considered for the Sabatier reaction. Black lines are for elementary steps that interconnect different pathways. Dark yellow and purple stand for reactants and products of the CO_2 hydrogenation reactions, respectively. Reversible steps are represented by double arrows.

species to ensure that they correspond to minima in the potential energy surface. In the calculation of reaction rates (*vide infra*), low-frequency modes below a cutoff value of 6.9 meV have been set to this cutoff value in order to approximate the entropy from a pseudotranslational/pseudorotational degree of freedom (see Section 1 in the Supporting Information for further details). The energy of an i gas-phase molecule ($E_{i(g)}$), has been calculated by placing a single molecule in an asymmetric box of dimensions $9 \times 10 \times 11$ Å^3 considering only the Γ point. We have used an asymmetric box to ensure convergence to the lowest energy state of the species. Then, the adsorption energy of any i of the considered 21 surface species ($E_{ads,i}$) has been calculated as

$$E_{ads,i} = E_{i\text{-slab}} - E_{slab} - E_{i(g)} \quad (1)$$

where $E_{(i\text{-slab})}$ is the energy of the i species adsorbed on the surface and E_{slab} is the energy of the relaxed pristine surface. With this definition, a negative value of $E_{ads,i}$ represents a favorable adsorption on the surface. The energy barriers and reaction energies are computed, as usual, taking the difference between the total energy of TS and reactant optimized structures and between the total energy of adsorbed products and reactants in their optimized structure. Both reaction energies ($\Delta E_{0,r}$) and energy barriers ($\Delta E_0^{\ddagger}$) reported in this work include also the contribution from the zero-point vibrational energies calculated within the harmonic oscillator approximation. This contribution is also taken into account on considering adsorption/desorption rates of reactants and products and involves both gas-phase and adsorbed species.

kMC Simulations. The present reaction model involves 25 different species (i.e., 6 gas-phase molecules and 19 adsorbed intermediates) and a total of 86 processes, as shown in Figure 1. The kMC method[68,69] simulates the system time evolution at the molecular level, in such a way that each elementary process has an associated transition rate (i.e., adsorption rate, diffusion rate, reaction rate, *etc.*). In this work, we have used the graph-theoretical kMC approach[70] combined with cluster expansion Hamiltonians[71,72] for the adlayer energetics as implemented in the Zacros code (version 1.01).[70,71] A lattice model consisting of a two-dimensional hexagonal periodic grid of $L \times L$ points has been used to mimic the hexagonal symmetry of the Ni(111) surface. Each point in the lattice model corresponds to a coarse-grained site that represents a catalytic site of the Ni(111) surface (i.e., fcc, hcp, bridge, or top sites). The convergence with respect

https://dx.doi.org/10.1021/acscatal.0c01599
ACS Catal. 2020, 10, 8077−8089

Table 1. Adsorption Energies (without ZPE) of Intermediate Species in Their Most Favorable Site[a]

		$E_{ads,i}$				
species i	site	this work	RPBE[51]	PBE[45]	PBE[52]	PW91[44]
C	hcp	−6.35	−6.00	−6.89	−6.61	
CH	fcc	−5.94	−5.90[c]	−6.41	−6.84	−6.47
CH_2	fcc	−3.64	−3.30	−4.03	−4.07	
CH_2O	fcc	−0.58	−0.20[c]			−0.84
CH_2OH	top-top	−1.47	−1.00[c]	−1.56[c]		−1.68[c]
CH_3	fcc	−1.64	−1.30	−1.89		−1.94
CH_3O	fcc	−2.59	−1.90			−2.75
CH_3OH	top-top	−0.36	−0.03[c]			−0.37[c]
CH_4	top	−0.13	0.13[c]			
CO	hcp	−1.61	−1.50	−1.93	−2.09	−1.91
CO_2	top	−0.16	0.03[c]	−0.01[c]	−0.12[c]	
COH	hcp	−4.02	−2.10	−4.39	−4.42[c]	−4.45
H	fcc	−2.75	−2.80	−2.80	−2.77	−2.78
H_2	fcc/hcp	−0.68[b]	−0.95[d]	−0.25[c]		
H_2O	top	−0.26	−0.02[c]	−0.27	−0.47	−0.33
HCO	fcc	−2.05	−1.80[c]	−2.27	−2.49[c]	−2.36[c]
HCOH	fcc	−2.65	−2.40	−3.88		−3.91[c]
HCOO	top-top	−2.93		−2.88	−3.02	
OH	fcc	−3.22	−2.50	−3.27	−3.34	−3.54
O	fcc	−5.30	−4.50	−5.39	−4.81	−5.76
t-COOH	top-top	−2.13	−2.30[c]	−2.25[c]	−2.54[c]	

[a]The adsorption sites in the literature are assumed to be the same unless it is specified. All values are in eV. [b]The calculated value corresponds to the dissociative adsorption of H_2 with an H on the fcc site and the other H on an hcp site. [c]The literature value corresponds to the CH_4 dissociative adsorption into CH_3 and H. [d]The literature value corresponds to the H_2 dissociative adsorption into two H. Both literature values are calculated at T = 800 K and P = 1 bar and consider species at infinite distance. [e]Adsorption energy corresponding to a adsorption site different from that presented in this study.

to the lattice size has been verified by computing the steady-state TOFs and coverages with different L = 8, 12, 16 values, concluding that the results from a 8 × 8 lattice virtually coincide with those obtained using larger surface models. Consequently, the 8 × 8 lattice has been used in the subsequent calculations; further details are given in Section 2 in the Supporting Information. In this 8 × 8 lattice model, each adsorbed species can interact with its six nearest neighbors in the hexagonal periodic grid. Species that occupy a single adsorption site in the DFT calculations are considered to occupy a single site in the kMC lattice, while species that occupy two neighboring adsorption sites in the DFT calculations are represented as bidentate adsorbates during the kMC simulations. For readers unfamiliar with the kMC method, we suggest the very recent tutorial from Andersen et al.[68]

In this study we have considered as a reaction model an ideal mixture of two gas-phase reactants (i.e., CO_2 and H_2 at given partial pressures and temperature) continuously impinging on an initially empty and thermalized Ni(111) surface, where a long list of surface processes can take place, and afterward, the formed products leave the surface region. Hence, the present model simulates a differential flow reactor with constant reactant flux and temperature. Therefore, reactants are allowed to adsorb and desorb, while products are only allowed to desorb. The reaction model involves the most relevant reaction mechanisms proposed in the literature, including three different reaction routes for the RWGS reaction and three different reaction routes for the Sabatier reaction. For completeness, we have also considered the possible formation of side products such as formaldehyde (CH_2O) and methanol (CH_3OH), although their formation is generally not observed on Ni-based catalysts. The total number of 86 processes included in our reaction model correspond to 36 reversible steps (i.e., adsorption, desorption, or surface chemical reaction), which include both forward and reverse processes plus 5 irreversible desorption steps and 9 reversible but symmetrical diffusion steps.

The expressions used to calculate the transition rates of all processes are described in detail in Section 3 if the Supporting Information. Mostly, transition state theory and DFT data were used. Due to the large number of species involved in our reaction model, we have truncated the cluster expansion to first-nearest-neighbor two-body terms. The cluster expansion includes pairwise lateral interactions for all of the reactants and product pairs as well as pairwise lateral interactions between the most relevant species during the simulations defined as species with significant coverage and key intermediate species. Overall, 19 different one-body terms and 50 different two-body terms are included in the cluster expansion, which are given in Tables S3 and S4 in the Supporting Information, respectively. The one-body terms were calculated as the formation energies of the adsorbed species, and the two-body terms were obtained as the difference between the formation energies of the coadsorbed species and the formation energies of the isolated species. Further details regarding the calculation of formation energies and the cluster expansion used are given in Sections 4 and 5 in the Supporting Information, respectively. Note that our reaction model involves processes with very dissimilar energy barriers, resulting in reaction rates differing by several orders of magnitude. The concomitant difference in time scales has been handled by manually scaling the reaction rates of fast processes by using a scaling factor (i.e., $\alpha < 1$) and ensuring that such scaling does not affect the final results; this is further described in Section 6 in the Supporting Information. This

https://dx.doi.org/10.1021/acscatal.0c01599
ACS Catal. 2020, 10, 8077−8089

Table 2. Reaction Energies ($\Delta E_{0,r}$) and Energy Barriers ($\Delta E_0^{\ddagger}$) for All of the Considered Processes Including the Zero-Point Energy Term along with Relevant Published Data[a]

	this work		literature value $\Delta E^{\ddagger}$		
ID: surface process	$\Delta E_{0,r}$	$\Delta E_0^{\ddagger}$	PBE[45]	PW91[44]	PBE[52]
R1: $CO_{2(g)} + * \rightleftharpoons CO_2$	−0.14	0.0 (0.14)	0.0 (0.01)		0.12 (0.0)
R2: $CO \rightarrow CO_{(g)} + *$	1.58	1.58 (0.0)	1.90 (0.0)	1.91 (0.0)	2.09 (0.0)
R3: $H_{2(g)} + 2* \rightleftharpoons 2H$	−0.60	0.26 (0.86)	0.01 (0.82)	0.13 (1.18)	0.08 (1.37)
R4: $CO_2 + * \rightleftharpoons CO + O$	−0.69	0.86 (1.55)	0.60 (1.56)		0.57 (1.53)
R5: $CO_2 + H \rightleftharpoons HCOO$	0.04	1.06 (1.02)	0.86 (0.99)		0.71 (1.05)
R6: $CO_2 + H \rightleftharpoons COOH$	0.51	1.35 (0.84)	1.11 (0.93)		0.80 (0.88)
R7: $CO_2 + OH \rightleftharpoons COOH + O$	0.35	0.47 (0.12)	0.19 (0.20)		1.06 (1.30)
R8: $CO_2 + H_2O \rightleftharpoons COOH + OH$	0.17	0.20 (0.03)	0.0 (0.0)		0.0 (0.0)
R9: $CO_2 + OH \rightleftharpoons HCOO + O$	−0.12	1.70 (1.82)	1.42 (1.75)		1.22 (1.62)
R10: $CO_2 + H_2O \rightleftharpoons HCOO + OH$	−0.31	1.61 (1.92)	1.33 (1.88)		1.22 (1.81)
R11: $COOH + * \rightleftharpoons CO + OH$	−1.04	0.50 (1.54)	0.44 (1.40)		0.50 (1.22)
R12: $COOH + * \rightleftharpoons COH + O$	−0.08	1.28 (1.36)			1.50 (1.41)
R13: $HCOO \rightleftharpoons O + HCO$	0.53	1.39 (0.86)	1.14 (0.73)		1.26 (0.74)
R14: $CO + * \rightleftharpoons C + O$	1.43	2.98 (1.55)	2.88 (1.60)	3.74 (2.32)	3.01 (1.59)
R15: $HCO + * \rightleftharpoons CO + H$	−1.26	0.21 (1.47)	0.19 (1.44)	0.21 (1.38)	0.20 (1.35)
R16: $HCO + * \rightleftharpoons CH + O$	−0.31	1.10 (1.41)	1.04 (1.54)	1.16 (1.44)	1.28 (1.43)
R17: $COH + * \rightleftharpoons CO + H$	−1.12	1.21 (2.33)	0.95 (1.91)	1.02 (1.94)	0.85 (1.81)
R18: $COH + * \rightleftharpoons C + OH$	0.47	1.81 (1.34)	1.86 (1.34)	2.01 (1.35)	2.07 (1.46)
R19: $C + H \rightleftharpoons CH + *$	−0.49	0.78 (1.27)	0.86 (1.39)	0.92 (1.38)	0.91 (1.32)
R20: $CH + H \rightleftharpoons CH_2 + *$	0.31	0.65 (0.34)	0.74 (0.36)	0.74 (0.40)	
R21: $CH_2 + H \rightleftharpoons CH_3 + *$	−0.08	0.60 (0.68)	0.63 (0.66)	0.77 (0.85)	
R22: $HCO + H \rightleftharpoons CH_2O + *$	0.37	0.82 (0.45)		0.53 (0.29)	
R23: $HCO + H \rightleftharpoons HCOH + *$	0.60	1.13 (0.53)	1.14 (0.71)	0.92 (0.58)	
R24: $COH + H \rightleftharpoons HCOH + *$	0.73	0.88 (0.15)	0.83 (0.10)		
R25: $HCOH + * \rightleftharpoons CH + OH$	−0.75	0.72 (1.47)	0.72 (1.45)	0.79 (1.26)	
R26: $HCOH + H \rightleftharpoons CH_2OH$	0.22	0.63 (0.41)	0.87 (0.53)	0.87 (0.62)	
R27: $CH_2OH \rightleftharpoons CH_2 + OH$	−0.67	0.71 (1.38)	0.65 (1.35)	0.85 (1.23)	
R28: $CH_2OH + H \rightleftharpoons CH_3OH + *$	−0.29	0.74 (1.03)			
R29: $CH_2O + H \rightleftharpoons CH_2OH$	0.45	1.00 (0.55)		1.06 (0.76)	
R30: $CH_2O + * \rightleftharpoons CH_2 + O$	−0.38	0.96 (1.34)		1.41 (1.57)	
R31: $CH_2O + H \rightleftharpoons CH_3O + *$	−0.33	0.52 (0.85)		0.65 (1.01)	
R32: $CH_3O + * \rightleftharpoons CH_3 + O$	−0.14	1.36 (1.50)		1.53 (1.57)	
R33: $CH_3O + H \rightleftharpoons CH_3OH$	0.48	1.43 (0.95)		1.31 (0.85)	
R34: $CH_3OH \rightleftharpoons CH_3 + OH$	−0.46	1.80 (2.26)			
R35: $O + H \rightleftharpoons OH + *$	0.16	1.28 (1.12)	1.17 (0.97)	1.21 (1.15)	1.16 (1.01)
R36: $OH + H \rightleftharpoons H_2O + *$	0.35	1.25 (0.90)	1.27 (0.86)	1.32 (1.02)	1.15 (0.90)
R37: $OH + OH \rightleftharpoons O + H_2O$	0.19	0.42 (0.23)	0.48 (0.27)		0.0 (0.0)
R38: $H_2O \rightarrow * + H_2O_{(g)}$	0.20	0.20 (0.0)	0.27 (0.0)	0.33 (0.0)	0.47 (0.0)
R39: $CH_3 + H \rightarrow CH_{4(g)} + 2*$	−0.22	0.87 (1.09)	0.0 (0.03)	0.96 (1.13)	
R40: $CH_3OH \rightarrow CH_3OH_{(g)} + 2*$	0.31	0.31 (0.0)		0.37 (0.0)	
R41: $CH_2O \rightarrow CH_2O_{(g)} + *$	0.58	0.58 (0.0)		0.83 (0.0)	
D1: $C_{fcc} + * \rightleftharpoons C_{hcp} + *$	−0.04	0.31 (0.35)			
D2: $O_{fcc} + * \rightleftharpoons O_{hcp} + *$	0.10	0.42 (0.32)			
D3: $H_{fcc} + * \rightleftharpoons H_{hcp} + *$	0.02	0.12 (0.10)			
D4: $CO_{fcc} + * \rightleftharpoons CO_{hcp} + *$	−0.01	0.11 (0.12)			
D5: $OH_{fcc} + * \rightleftharpoons OH_{hcp} + *$	0.09	0.19 (0.10)			
D6: $H_2O_{top} + * \rightleftharpoons H_2O_{top} + *$	0.00	0.08 (0.08)			
D7: $CH_{fcc} + * \rightleftharpoons CH_{hcp} + *$	0.02	0.32 (0.31)			
D8: $CH_{2fcc} + * \rightleftharpoons CH_{2hcp} + *$	0.04	0.19 (0.15)			
D9: $CH_{3fcc} + * \rightleftharpoons CH_{3hcp} + *$	0.02	0.15 (0.13)			

[a]Backward energy barriers are also shown in parentheses. Note that literature values (i.e., $\Delta E^{\ddagger}$) do not include The ZPE term. An asterisk represents a free adsorption Site. All values are in eV.

pragmatic solution has been successfully applied in several previous kMC studies.[73−76]

For each operating condition, we have carried out five kMC simulation runs over an initially pristine Ni(111) surface using different random seeds. In this way, a larger part of the configuration space is explored, in comparison to running one single very long simulation. To obtain the final results, the resulting steady-state macroscopic properties such as TOFs and coverages have been averaged, whereas the error bars have been taken as the standard deviation among the different kMC

https://dx.doi.org/10.1021/acscatal.0c01599
ACS Catal. 2020, 10, 8077−8089

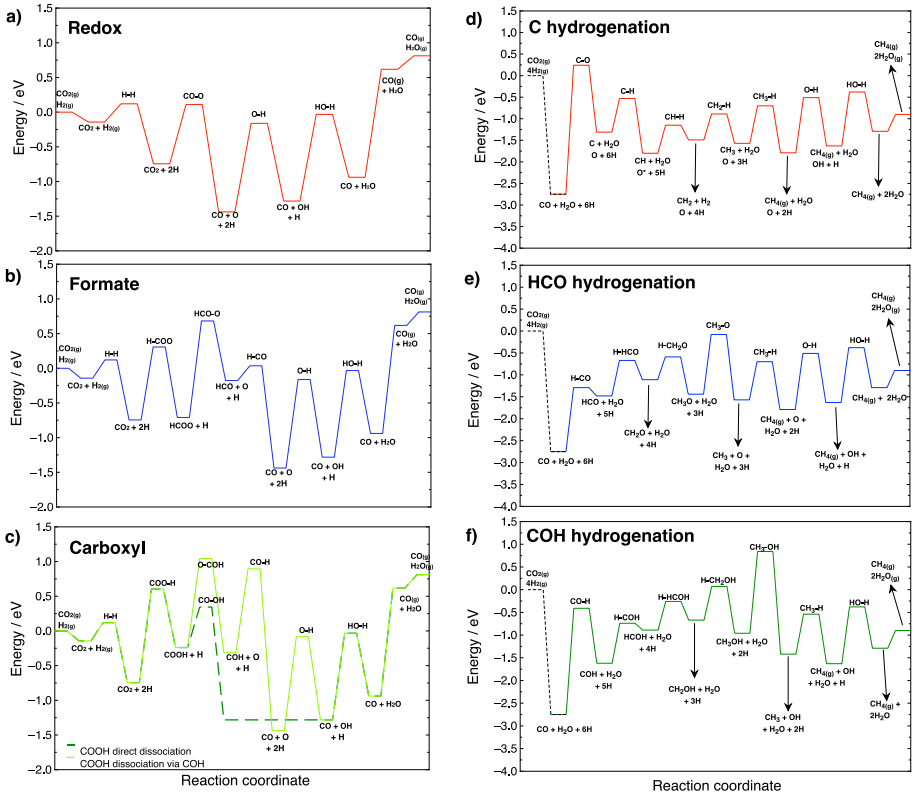

Figure 2. Potential energy diagrams corresponding to the RWGS reaction: (a) redox mechanism; (b) formate mechanism; (c) carboxyl mechanism and the Sabatier reaction; (d) C hydrogenation mechanism; (e) HCO hydrogenation mechanism; (f) COH hydrogenation mechanism. All values include the zero-point energy term, and coadsorbed species are assumed to be at infinite distance.

replicas. The total number of kMC steps was on the order of 10^8 for all working conditions. All of the simulations have been performed using an initial CO_2 and H_2 reactant mixture with a 1:4 ratio at total pressures of 1 and 10 bar and temperatures of 573.15 and 673.15 K, which are typical operating conditions.[4,48] Each simulation has been allowed to achieve a steady state in which no variations of the surface coverage for intermediate species are observed, with the exception of small fluctuations resulting from the stochastic nature of the method. Then, the TOF is calculated as the number of product species formed per site and unit time. Moreover, to unveil the dominant reaction mechanism that controls the reaction, the event frequency of the different processes has been analyzed.

Optimized structures (i.e., VASP CONTCAR files) of all relevant stationary points and Zacros input files for the kMC simulations have been made available on a public GitHub repository: https://github.com/plozanore/DFT_-_kMC_CO2_-_H2_Ni_111.

RESULTS AND DISCUSSION

DFT Results. We start by noting that a total of 21 adsorbed species and 7 gas-phase species are involved in the considered mechanisms for the RWGS and Sabatier reactions. The adsorption energies for all of the species have been calculated for each of the four possible high-symmetry adsorption sites (see Section 7 in the Supporting Information for further details). Table 1 summarizes the adsorption energies for all of the species in their optimized structures at the most favorable site along with already published data for comparison.[44,45,51,52] The present results are in close agreement with published data, even though some discrepancies are found, not only on the adsorption energy values but also on the reported most stable adsorption sites for some adsorbates, especially for the largest ones. In general, PBE[45,52] and PW91[44] functionals tend to overestimate adsorption energies with predicted values larger than those obtained from RPBE[51] or BEEF-vdW (Table 1). Moreover, there is a rather good agreement between the calculated CO heat

https://dx.doi.org/10.1021/acscatal.0c01599
ACS Catal. 2020, 10, 8077−8089

of adsorption (i.e., −1.55 eV at 300 K for 0.11 ML) and the experimental value of ∼−1.3 eV on hollow sites at 0.25 ML coverage and 300 ≤ T ≤ 425 K.[77,78] Note that the higher the coverage, the lower the adsorption energy, due to the repulsive CO−CO interaction. In addition, the present study nicely reproduces the experimental heat of adsorption hollow > bridge > ontop trend (see Table S7 in the Supporting Information).

For larger adsorbates such as CH_2OH, CH_3OH, HCOO and t-COOH, the PBE and PW91 adsorption energies are closer to the present BEEF-vdW-calculated values. However, this could be a result of error compensation in all previously reported DFT studies on this system, since PBE/PW91 overbinding is still present but the dispersion contributions are neglected. These interactions are especially important for the largest intermediates and physisorbed (nonpolar) molecules such as CO_2 or CH_4, and their inclusion can produce very large changes in the predicted reaction rates, as has been shown for the WGS reaction on Cu(321).[79]

To provide unambiguous insight regarding the mechanism that governs CO_2 hydrogenation on the Ni(111) surface, all possible relevant reaction mechanisms reported in the literature have been explicitly considered with the complete reaction network summarized in Figure 1. Table 2 reports the calculated reaction energies ($\Delta E_{0,r}$) and energy barriers ($\Delta E_0^{\ddagger}$) for all considered elementary steps, along with already published data to facilitate their comparison. Note that the present values include dispersion interactions and the zero-point energy (ZPE) term, while both are neglected in previous works. With this information at hand, three different mechanisms for the RWGS reaction and three different mechanisms for the Sabatier reaction can be distinguished, which are discussed on the basis of the corresponding calculated potential energy diagrams (PEDs). The possible desorption of some side species such as formaldehyde and methanol are also accounted for, although this is not included in the reported PEDs.

The three proposed mechanisms for the RWGS reaction are the reverse of the redox, formate, and carboxyl pathways in the WGS reaction, respectively (see Figure 2 for PEDs), which differ in the way CO is produced. In the redox pathway (Figure 2a), CO is directly produced by CO_2 dissociation (i.e., R4, $\Delta E_0^{\ddagger}$ = 0.86 eV) and water is formed by hydrogenation of adsorbed atomic O. The formate pathway (Figure 2b) involves the formation of HCOO by the reaction between CO_2 and H (R5, $\Delta E_0^{\ddagger}$ = 1.06 eV). Next, HCOO dissociates to produce adsorbed HCO and O species (R13, $\Delta E_0^{\ddagger}$ = 1.39 eV), with subsequent dissociation of the former species (R15, $\Delta E_0^{\ddagger}$ = 0.21 eV), leading to the formation of adsorbed CO. Again, water is formed by hydrogenation of adsorbed O. Finally, the carboxyl pathway (Figure 2c) is related to the formation of COOH. In this mechanism, adsorbed CO_2 and H react to produce COOH (R6, $\Delta E_0^{\ddagger}$ = 1.35 eV) and then CO can be produced either by direct COOH dissociation (R11, $\Delta E_0^{\ddagger}$ = 0.50 eV) or via the COH intermediate (R12, $\Delta E_0^{\ddagger}$ = 1.28 eV, and R17, $\Delta E_0^{\ddagger}$ = 1.21 eV, respectively).

Among the mechanisms proposed in the literature for the RWGS reaction, the redox pathway is by far the most favored route for CO production, since the energy barrier for CO_2 dissociation is lower than those for HCOO or COOH formation and it is a unimolecular step, which makes it more probable to occur than a bimolecular step, in agreement with previously reported results.[49,50,52] Both formate and carboxyl pathways involve hydrogen-assisted steps, and they will only be feasible at high H coverage. Among them, HCOO formation (R5) has a lower energy barrier than COOH formation (R6). However, after HCOO formation, the system can go backward because the reverse energy barrier for this process is lower than that for further dissociation to produce HCO (R13). Conversely, if COOH is formed, it will dissociate mainly to produce CO (R11) in comparison with the reverse R6 and R12 processes. Therefore, it is not clear which of these two mechanisms will dominate, although the current DFT calculations clearly suggest that both of them will be hardly relevant and that the redox mechanism should prevail, suggesting CO_2 dissociation as the rate-determining step.

The three proposed mechanisms for the Sabatier reaction are the carbon hydrogenation pathway, the HCO hydrogenation pathway, and the COH hydrogenation pathway, as also summarized in Figure 2. These mechanisms differ in the way CH_3 is produced, which is finally hydrogenated to methane. In all mechanisms it is assumed that CO is formed via the redox pathway and then it reacts to produce the key intermediate of each mechanism. Note that key intermediates could also be obtained from other elementary steps (see Figure 1) that are not included in the PEDs. The C hydrogenation pathway (Figure 2d) starts with the formation of atomic C species, either from CO dissociation (R14, $\Delta E_0^{\ddagger}$ = 2.98 eV) or from COH dissociation (R18, $\Delta E_0^{\ddagger}$ = 1.81 eV), and further hydrogenation to produce CH_3. The HCO hydrogenation pathway (Figure 2e) is related to the formation of the key intermediate HCO via the HCOO dissociation (R13, $\Delta E_0^{\ddagger}$ = 1.39 eV) or from H + CO hydrogenation (reverse R15, $\Delta E_0^{\ddagger}$ = 1.47 eV). Next, HCO is hydrogenated to CH_3O, which can dissociate to produce CH_3. Finally, the COH hydrogenation pathway (Figure 2f) involves the formation of the key intermediate COH via the COOH dissociation (R12, $\Delta E_0^{\ddagger}$ = 1.28 eV) or the CO + H hydrogenation (reverse R17, $\Delta E_0^{\ddagger}$ = 2.33 eV). Next, COH is further hydrogenated to methanol, which then dissociates to produce CH_3. Apart from these three main mechanisms, there are many elementary interconnecting steps, which are responsible for the high complexity of the CO_2 hydrogenation landscape on Ni(111), as shown in the reaction network in Figure 1. For instance, dehydroxylation of CH_xOH species leads to CH_x species, providing hybrid reaction routes combining the COH hydrogenation and C hydrogenation mechanisms. Similarly, CH_xO species can deoxygenate to produce CH_x species, providing connections between the HCO and C hydrogenation mechanisms. Note also that, in addition to the final products of the RWGS reaction (i.e., $CO_{(g)}$ and $H_2O_{(g)}$) and the Sabatier reaction (i.e., $CH_{4(g)}$ and $H_2O_{(g)}$), other intermediate species are present which can desorb, leading to side products. This is the case for methanol ($CH_3OH_{(g)}$) and formaldehyde ($CH_2O_{(g)}$).

By inspection of all the different possibilities provided by the full reaction network, the most feasible reaction route to $CH_{4(g)}$ production seems to be through CO formation via the redox mechanism, followed by its possible hydrogenation to HCO (reverse R15, $\Delta E_0^{\ddagger}$ = 1.47 eV). Then, in a H-dominated regime, HCO could be further hydrogenated to CH_2O (R22, $\Delta E_0^{\ddagger}$ = 0.82 eV), then deoxygenated to CH_2 (R30, $\Delta E_0^{\ddagger}$ = 0.96 eV), and finally hydrogenated to $CH_{4(g)}$. On the other hand, in a system with low H coverage and high availability of surface free sites, HCO could be deoxygenated to CH (R16, $\Delta E_0^{\ddagger}$ = 1.10 eV) and finally hydrogenated to $CH_{4(g)}$. Hence, the most favorable route for methane production would involve the RWGS redox mechanism to form CO, followed by a combination of the HCO and C hydrogenation mechanisms. However, there are

https://dx.doi.org/10.1021/acscatal.0c01599
ACS Catal. 2020, 10, 8077−8089

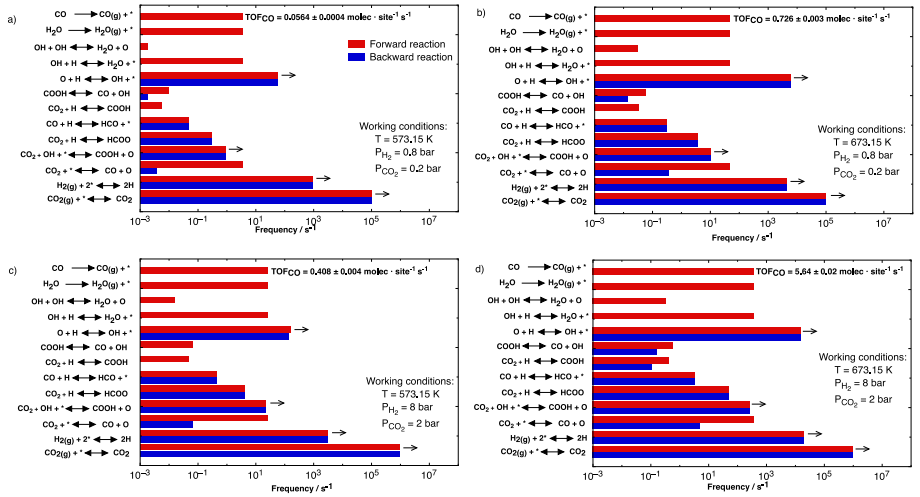

Figure 3. Event frequency of the CO_2 hydrogenation reaction under four different working conditions: (a) T = 573.15 K, P_{H_2} = 0.8 bar, P_{CO_2} = 0.2 bar; (b) T = 573.15 K, P_{H_2} = 8 bar, P_{CO_2} = 2 bar; (c) T = 673.15 K, P_{H_2} = 0.8 bar, P_{CO_2} = 0.2 bar; (d) T = 673.15 K, P_{H_2} = 8 bar, P_{CO_2} = 2 bar.

some thermodynamic and kinetic aspects that make $CH_{4(g)}$ production hardly achievable. The first challenge is the presence of bimolecular hydrogenation steps, which are obviously much slower than several unimolecular steps. Moreover, if CO is hydrogenated to HCO through reverse R15, the system will probably move backward, since the energy barrier in the backward direction for this elementary step is only 0.21 eV. Moreover, it is very likely that CO will desorb rather than follow the reaction path toward methane, methanol, or formaldehyde. The main reason is that, once a CO molecule is formed, it will desorb (R2, $\Delta E_{0,r} = \Delta E_0^{\ddagger}$= 1.58 eV) rather than react to form C, COH, or HCO. The first two processes are kinetically impeded due to extremely high energy barriers ($\Delta E_0^{\ddagger}$ = 2.98 and 2.33 eV, respectively). On the other hand, although the HCO formation process through reverse R15 has an energy barrier $\Delta E_0^{\ddagger}$ = 1.47 eV) similar to that of CO desorption, it is a bimolecular process, hence requiring a neighboring H adsorbate. Even in the case of a H-dominated regime, where the concentration of HCO could be significant, the system would again move backward, due to its very low energy barrier ($\Delta E_0^{\ddagger}$ = 0.21 eV).

Overall, a first inspection of the full DFT energy landscape seems to suggest that the RWGS reaction should dominate on Ni(111) with $CO_{(g)}$ being the main product through the redox mechanism. However, as mentioned in Section 1 in the Supporting Information, a more quantitative and rigorous description of the kinetics of such a complex reaction network requires the simultaneous consideration of all involved steps under the working conditions of pressures and temperatures; this is precisely the aim of the next section.

kMC Results. To gain further insight into the mechanism of CO_2 hydrogenation on Ni(111), kMC simulations have been carried out under the typical operating conditions for the Sabatier reaction on Ni-based catalysts;[4] thus, pressures of 1 and 10 bar and temperatures of 573.15 and 673.15 K are considered. These simulations involved a CO_2/H_2 mixture with a 1:4 ratio, although additional runs with a 1:1 CO_2/H_2 mixture lead to the same results. We start by analyzing the TOF and the event frequencies of the main elementary steps, which will allow us to provide estimations of catalyst activity and selectivity and also to unveil the dominant mechanism that controls the reaction.

The TOFs and event frequencies of the main elementary steps under the four different operating conditions are shown in Figure 3. Clearly, no methane formation is observed under any of the studied conditions, as implied also by the DFT calculations. Even if the simulations show that some HCO is produced through CO hydrogenation, which could be an important intermediate toward methane production, the energy barrier for HCO dissociation is very small, thus evolving back to CO and hence hindering the CH formation and subsequently the hydrogenation to methane. Figure 3 clearly shows that CO_2 hydrogenation on Ni(111) is dominated by the RWGS through the redox route (R4 step in Figure 1), also in agreement with what is inferred from the analysis of the DFT energy profiles. Interestingly, the carboxyl pathway is also active, with COOH being produced by reaction of CO_2 with either H (R6) or OH (R7). Nevertheless, COOH dissociates to produce CO through the R11 step. In any case, the frequency of CO formation through the carboxyl pathway is between 2 and 3 orders of magnitude smaller than that through the redox pathway. This clearly suggests that the CO_2 dissociation step is the rate-determining step. This has been confirmed by calculating the Campbell degree of rate control[80] for the three competing processes starting from CO_2 (i.e., R4, R5, and R6) at several temperatures (see Table S8 in the Supporting Information for further details).

With regard to the formate pathway, Figure 3 shows that indeed HCOO is formed but evolves backward to CO_2, meaning that this third mechanism does not contribute at all toward the

https://dx.doi.org/10.1021/acscatal.0c01599
ACS Catal. 2020, 10, 8077−8089

Table 3. Coverage Value of Some Species during the Simulations under Different Working Conditions

	coverage (θ)			
	T = 573.15 K, P_{H_2} = 0.8 bar, P_{CO_2} = 0.2 bar	T = 573.15 K, P_{H_2} = 8 bar, P_{CO_2} = 2 bar	T = 673.15 K, P_{H_2} = 0.8 bar, P_{CO_2} = 0.2 bar	T = 673.15 K, P_{H_2} = 8 bar, P_{CO_2} = 2 bar
θ_H	12.69 ± 0.08	17.33 ± 0.06	7.69 ± 0.06	12.36 ± 0.09
θ_{CO}	0.031 ± 0.004	0.140 ± 0.019	0.007 ± 0.003	0.020 ± 0.004
θ_O	0.170 ± 0.011	0.227 ± 0.011	0.675 ± 0.028	0.810 ± 0.024
θ_{CO_2}	0.769 ± 0.008	0.926 ± 0.018	0.695 ± 0.011	0.775 ± 0.023
θ_{OH}	0.007 ± 0.004	0.023 ± 0.006	0.055 ± 0.004	0.076 ± 0.004

RWGS reaction. Figure 3 also shows that, despite the scaling down of the adsorption/desorption step rates, the system spends most of the simulation time precisely adsorbing and desorbing CO_2. This result agrees with the low desorption energy of CO_2 (0.14 eV including ZPE correction), significantly lower that the energy barriers for other CO_2-related processes such as R4−R10 and also much less accessible because they are mainly bimolecular. At 573 K, the second most time consuming process is H_2 dissociative adsorption and its subsequent H recombination back to $H_{2(g)}$. Although the energy barrier for this recombination is quite high (i.e., reverse R3, $\Delta E_0^{\ddagger}$ = 0.86 eV), it is lower than other energy barriers for steps involving H (e.g., with O, OH, CO_2, or CO, the species with the highest coverages; *vide infra*). Moreover, it is more likely that neighboring H−H pairs are found in the lattice due to the dissociative $H_{2(g)}$ adsorption, in comparison to other pairs such as H−O, H−CO_2, and H−CO. These event frequency diagrams also show that, when a diffusing H atom finds an O atom arising from CO_2 dissociation, the system spends a considerable amount of time forming OH (R35) and going backward. In comparison to the others, the relative event frequency for this step increases with temperature because it is an endothermic process.

Water is mainly formed through OH hydrogenation (i.e., R36, $\Delta E_0^{\ddagger}$ = 1.25 eV), although to a lesser extent it is also formed by the disproportionation of two neighboring OH species (i.e., R37, $\Delta E_0^{\ddagger}$ = 0.42 eV). The energy barrier for the latter process is much lower, but its event frequency is 2−3 orders of magnitude lower because of the very low OH coverage (*vide infra*). Finally, the kMC simulations evidence that changes either in the reaction temperature or in the partial pressure of reactants have no significant effect, other than affecting the event frequency of all processes in a fairly homogeneous way. Obviously, as the temperature or pressure is increased, the overall TOF also increases (see Figure 3).

The steady-state (final) coverages of the main surface species are reported in Table 3. Under all studied reaction conditions, the coverage of all the intermediate species is below 1%, with the sole exception of atomic H, which has a coverage of around 7−17% depending on the T and P values. These results are a consequence of the adsorption of reactants, intermediates, and products over Ni(111) being too weak. According to the Le Sabatier principle, catalysts that present binding which is too weak or too strong for adsorbed species exhibit low activity. This is precisely what is observed; the TOF values reported in Figure 3 under different reaction conditions are all very low. These low values could be seemingly in contrast with the experimental evidence that Ni-based catalysts are active toward the RWGS and Sabatier reactions.[29−32,40,41] Therefore, one can conclude that the active sites are not located on the Ni(111) facets and that the role of the Ni support and the size and morphology of Ni nanoparticles are likely to play important roles in the overall process.

We have also computed the partial orders of reaction with respect to both reactants and the apparent activation energy of the overall reaction by performing different simulations at varying temperatures and pressures. The calculated partial orders at 673.15 K for CO_2 and H_2 are 0.82 and 0.21, respectively (see Section S9 in the Supporting Information for further details). The calculated apparent activation energies at 1 and 10 bar are 0.82 and 0.85 eV, respectively (see Section S10 in the Supporting Information). Note that these values are very similar to the energy barrier of the CO_2 dissociation step (i.e., 0.86 eV), thus confirming that this is indeed the rate-determining step. Unfortunately, to our knowledge, the experimental apparent activation energy and partial orders of reaction have not been reported.

Several theoretical studies[44,47,48] and one experimental work[35] have claimed that CO_2 hydrogenation on Ni(111) should produce methane. It is important to point out that the experimental study supports this claim solely by the presence of a peak at 283.3 eV attributed to adsorbed C, which is then taken as an indication that methanation could follow. However, the same study provides compelling evidence that CO_2 leads to CO through the RWGS, which is in agreement with the present results. The analysis of the present kMC simulations shows that, under the scrutinized conditions, methanation will not take place on Ni(111). The main bottleneck for methanation is that CO desorption is much more favorable than any other competing process evolving to methane such as HCO formation (reverse R15, $\Delta E_0^{\ddagger}$ = 1.47 eV) or CO dissociation (R14, $\Delta E_0^{\ddagger}$ = 2.98 eV) (see also Figure 2d,e). That CO desorption blocks methane formation is also supported by accurate measurements of the heat of adsorption of CO on Ni(111) of ∼−1.3 eV,[77,78] even lower than the value predicted by the present or previous DFT calculations (see Table 1). Nevertheless, since CO adsorption energies that are too strong could be obtained as a consequence of the selected functional, we have done a sensitivity analysis of the CO desorption process. We concluded that, even when the CO desorption rate is slowed by 2 orders of magnitude (corresponding to a 0.26 eV stronger CO adsorption energy), no methane is formed, and only CO is produced (see Section S11 in the Supporting Information for further details).

Additional support for the present findings comes from the work of Catapan et al.[52] on the WGS reactions over both flat Ni(111) and stepped Ni(211) surfaces which share the reverse R15 and R14 elementary steps. These authors report energy barriers and reaction energies similar to those reported in the present study, thus supporting that methanation on Ni(111) and Ni(211) surfaces is unlikely to occur. For the Ni(111) case, they proposed the redox pathway involving the route through direct CO_2 dissociation as the most plausible mechanism for the

https://dx.doi.org/10.1021/acscatal.0c01599
ACS Catal. 2020, 10, 8077−8089

RWGS reaction, in agreement with the present findings. Note that Zhang et al.[49] also reported the redox pathway as the most plausible mechanism for the RWGS reaction on the Ni(111) and Ni(311) surfaces, but from their data it is not possible to predict whether Ni(311) will be active for methanation. However, the study of Vrijburg et al.[53] that couples DFT calculations with microkinetic modeling shows that the Ni(311) surface is active for methane formation. They found that for the Ni(311) surface the COH intermediate is a possible source of atomic C, which is further hydrogenated to methane, although this would not be possible for Ni(111) or Ni(211) surfaces, indicating that not all stepped surfaces may exhibit methanation activity.

Regarding earlier theoretical studies on CO_2 hydrogenation, Choe et al.[46] claimed that CO disproportionation is a possible source of methane formation. However, their result is an artifact arising from excessively large adsorption energies for CO and CO_2. In our reaction network, this unusual CO disproportionation step has not been included, precisely because the energy barrier for CO disproportionation is higher[44−46] than that required for CO desorption. Ren et al.[47] proposed an optimal mechanism for methane production from CO_2 via a route involving CO_2 and CO consecutive dissociations. However, they did not consider the much more favorable CO desorption process and other important and competing processes for CO reactions, which should notably affect the final reaction products. In a recent experimental and theoretical study, Vogt et al.[48] presented a microkinetic modeling for CO_2 conversion over several Ni facets, concluding that some methanation could occur over these unsupported Ni facets. However, their reaction network was quite incomplete and involved several important limitations. For instance, their DFT study relied on the PBE functional, a robust and broadly used functional, but neglected dispersion energies and lateral interactions. Moreover, even more critical was neglecting the CO desorption step in the microkinetic modeling. As a result, an artificially too large CO coverage was obtained which favored the H-assisted CO dissociation process and hence the CH_4 formation.

Additional studies involving CO methanation and the WGS reaction on Ni(111) could give valuable additional information for understanding the CO_2 hydrogenation reaction much better. Zhou et al.[45] suggested that the HCO route was the most favorable pathway for methane production, although this intermediate was more likely to undergo the WGS reaction rather than the methanation reaction. However, these authors neglected the HCO hydrogenation step to CH_2O, which at high H coverages would be more feasible than the HCO dissociation to CH + O. Additionally, and more significantly, they also neglected the possible HCO dissociation to CO + H, which clearly hinders the Sabatier reaction, as shown in the present work. Similarly, Zhi et al.[44] proposed HCO and HCOH dissociation steps as the most favorable routes for methane formation from CO hydrogenation, but they did not consider the possible CH_2O formation or the low-energy barrier of HCO dissociation to form CO + H, which plays an important role. Moreover, since their energy barrier for CO hydrogenation to HCO was lower than that for CO desorption, they also neglected the CO desorption process. The present results clearly confirm that CO desorption is a key step that cannot be neglected, as it drives the CO_2 hydrogenation on Ni(111) to the RWGS reaction rather than to the Sabatier reaction. The importance of both CO desorption and HCO formation in tuning the selectivity from CO to CH_4 has been also shown in CO_2 hydrogenation over Pt, Pt/SiO_2 ,and Pt/TiO_2.[37]

CONCLUSIONS

DFT calculations along with kMC simulations have been performed to unravel the molecular mechanism of CO_2 hydrogenation on Ni(111), to determine the main products and to provide unbiased meaningful insights regarding the elementary steps governing the reaction. The reaction energies and energy barriers for a total of 86 elementary processes, conforming to a complete reaction network, have been obtained. These correspond to three possible mechanisms for the RWGS reaction and three possible mechanisms for the Sabatier reaction. Among all of the proposed mechanisms for the RWGS reaction, the redox pathway is by far the most favored route to $CO_{(g)}$ production. This is because the energy barrier for CO_2 dissociation is lower than those for HCOO or COOH formation and it corresponds to a unimolecular process. For the case of the HCOO and COOH routes, an analysis of the PEDs alone is not sufficient to provide a conclusive idea regarding which pathway is preferred. We have also analyzed the most feasible route for methane production, which involves the RWGS redox mechanism to form CO species, followed by a combination of the HCO and C hydrogenation mechanisms. However, the results show that several thermodynamic and kinetic aspects make $CH_{4(g)}$ production hardly achievable. In particular, we mention the presence of bimolecular hydrogenation steps, the very low energy barrier for the HCO → CO + H process, and the very likely CO desorption.

The present accurate kMC simulations have confirmed that no methane is formed on Ni(111) under any of the operating conditions studied, in contrast to what has been suggested in some earlier DFT and microkinetic studies based on some unreliable assumptions. kMC simulations also show that the RWGS reaction dominates mainly through the redox mechanism but also through the carboxyl mechanism to a lesser extent. We have also confirmed that the CO_2 dissociation step is clearly the only rate-determining step. Therefore, we conclude that methane production observed experimentally on Ni-based catalysts is not due to the large presence of Ni(111) facets of the Ni nanoparticles and it should be likely a result of other contributions involving a possible synergic effect between the Ni particle and the support and also the existence of other sites that may be present, depending on the particle morphology. This calls for subsequent studies on the effect of the support and low-coordinated sites on the CO_2 hydrogenation reaction.

ASSOCIATED CONTENT

Supporting Information

The Supporting Information is available free of charge at https://pubs.acs.org/doi/10.1021/acscatal.0c01599.

Information about the frequency scaling, the lattice model used, the reaction rates, and the formation energy calculations, the cluster expansion Hamiltonians used, how fast processes have been scaled, the adsorption energies of the species at different adsorption sites, how the Campbell degree of rate control is calculated, the reactants' partial orders of reaction, the apparent activation energies, a CO sensitivity analysis, details about the kMC simulations, and the structure of all minima and transition states (PDF)

https://dx.doi.org/10.1021/acscatal.0c01599
ACS Catal. 2020, 10, 8077−8089

AUTHOR INFORMATION

Corresponding Author

Ramón Sayós − *Departament de Ciència de Materials i Química Física & Institut de Química Teòrica i Computacional (IQTCUB), Universitat de Barcelona, 08028 Barcelona, Spain*; orcid.org/0000-0001-6627-7844; Email: r.sayos@ub.edu

Authors

Pablo Lozano-Reis − *Departament de Ciència de Materials i Química Física & Institut de Química Teòrica i Computacional (IQTCUB), Universitat de Barcelona, 08028 Barcelona, Spain*

Hèctor Prats − *Departament de Ciència de Materials i Química Física & Institut de Química Teòrica i Computacional (IQTCUB), Universitat de Barcelona, 08028 Barcelona, Spain*

Pablo Gamallo − *Departament de Ciència de Materials i Química Física & Institut de Química Teòrica i Computacional (IQTCUB), Universitat de Barcelona, 08028 Barcelona, Spain*; orcid.org/0000-0002-8531-8063

Francesc Illas − *Departament de Ciència de Materials i Química Física & Institut de Química Teòrica i Computacional (IQTCUB), Universitat de Barcelona, 08028 Barcelona, Spain*; orcid.org/0000-0003-2104-6123

Complete contact information is available at: https://pubs.acs.org/10.1021/acscatal.0c01599

Notes

The authors declare no competing financial interest.

ACKNOWLEDGMENTS

This research was supported by the Spanish Ministry of Science, Innovation and Universities through grants RTI2018-094757-B-I00, RTI2018-095460-B-I00, MCIU/AEI/FEDER, UE, and MDM-2017-0767 and in part by the *Generalitat de Catalunya* (2017SGR13 and XRQTC). P.L.-R. acknowledges the *Generalitat de Catalunya* for a predoctoral 2019 FI-B 00061 grant. P.G. is indebted to the *Serra Hunter* programme for supporting his professorship, and F.I. acknowledges additional support from the 2015 ICREA Academia Award for Excellence in University Research. Computational resources provided by *Consorci de Serveis Universitaris de Catalunya* (CSUC, former CESCA) are gratefully acknowledged.

REFERENCES

(1) Barbir, F. Transition to Renewable Energy Systems with Hydrogen as an Energy Carrier. *Energy* **2009**, *34*, 308−312.

(2) Dincer, I. Renewable Energy and Sustainable Development: a Crucial Review. *Renewable Sustainable Energy Rev.* **2000**, *4*, 157−175.

(3) Jalama, K. Carbon Dioxide Hydrogenation over Nickel-, Ruthenium-, and Copper-based Catalysts: Review of Kinetics and Mechanism. *Catal. Rev.: Sci. Eng.* **2017**, *59*, 95−164.

(4) Kattel, S.; Liu, P.; Chen, J. G. Tuning Selectivity of CO_2 Hydrogenation Reactions at the Metal/Oxide Interface. *J. Am. Chem. Soc.* **2017**, *139*, 9739−9754.

(5) Li, W.; Wang, H.; Jiang, X.; Zhu, J.; Liu, Z.; Guo, X.; Song, C. A Short Review of Recent Advances in CO_2 Hydrogenation to Hydrocarbons over Heterogeneous Catalysts. *RSC Adv.* **2018**, *8*, 7651−7669.

(6) Wang, W.; Wang, S.; Ma, X.; Gong, J. Recent Advances in Catalytic Hydrogenation of Carbon Dioxide. *Chem. Soc. Rev.* **2011**, *40*, 3703−3727.

(7) Nie, X.; Li, W.; Jiang, X.; Guo, X.; Song, C. Recent Advances in Catalytic CO_2 Hydrogenation to Alcohols and Hydrocarbons. *Adv. Catal.* **2019**, *65*, 121−133.

(8) Pirngruber, G. D.; Raybaud, P.; Belmabkhout, Y.; Čejka, J.; Zukal, A. The Role of the Extra-framework Cations in the Adsorption of CO_2 on Faujasite Y. *Phys. Chem. Chem. Phys.* **2010**, *12*, 13534−13546.

(9) Yang, H.; Xu, Z.; Fan, M.; Gupta, R.; Slimane, R. B.; Bland, A. E.; Wright, I. Progress in Carbon Dioxide Separation and Capture: A Review. *J. Environ. Sci.* **2008**, *20*, 14−27.

(10) Lv, Y. X.; Yan, G. H.; Xu, C. Q.; Xu, M.; Sun, L. Review on Membrane Technologies for Carbon Dioxide Capture from Power Plant Flue Gas. *Adv. Mater. Res.* **2012**, *602*−*604*, 1140−1144.

(11) Centi, G.; Quadrelli, E. A.; Perathoner, S. Catalysis for CO_2 Conversion: a Key Technology for Rapid Introduction of Renewable Energy in the Value Chain of Chemical Industries. *Energy Environ. Sci.* **2013**, *6*, 1711−1731.

(12) Götz, M.; Lefebvre, J.; Mörs, F.; Koch, A. M.; Graf, F.; Bajohr, S.; Reimert, R.; Kolb, R. Renewable Power-to-Gas: A Technological and Economic Review. *Renewable Energy* **2016**, *85*, 1371−1390.

(13) Hartadi, Y.; Widmann, D.; Behm, R. J. CO_2 Hydrogenation to Methanol on Supported Au Catalysts under Moderate Reaction Conditions: Support and Particle Size Effects. *ChemSusChem* **2015**, *8*, 456−465.

(14) Yang, X.; Kattel, S.; Senanayake, S. D.; Boscoboinik, J. A.; Nie, X.; Graciani, J.; Rodriguez, J. A.; Liu, P.; Stacchiola, D. J.; Chen, J. G. Low Pressure CO_2 Hydrogenation to Methanol over Gold Nanoparticles Activated on a CeO_x /TiO_2 Interface. *J. Am. Chem. Soc.* **2015**, *137*, 10104−10107.

(15) Sakurai, H.; Haruta, M. Synergism in Methanol Synthesis from Carbon Dioxide over Gold Catalysts Supported on Metal Oxides. *Catal. Today* **1996**, *29*, 361−365.

(16) Qu, J.; Zhou, X.; Xu, F.; Gong, X. Q.; Tsang, S. C. E. Shape Effect of Pd-promoted Ga_2O_3 Nanocatalysts for Methanol Synthesis by CO_2 Hydrogenation. *J. Phys. Chem. C* **2014**, *118*, 24452−24466.

(17) Bahruji, H.; Bowker, M.; Hutchings, G.; Dimitratos, N.; Wells, P.; Gibson, E.; Jones, W.; Brookes, C.; Morgan, D.; Lalev, G. Pd/ZnO Catalysts for Direct CO_2 Hydrogenation to Methanol. *J. Catal.* **2016**, *343*, 133−146.

(18) Kuld, S.; Thorhauge, M.; Falsig, H.; Elkjær, C. F.; Helveg, S.; Chorkendorff, I.; Sehested, J. Quantifying the Promotion of Cu Catalysts by ZnO for Methanol Synthesis. *Science* **2016**, *352*, 969−974.

(19) Studt, F.; Behrens, M.; Kunkes, E. L.; Thomas, N.; Zander, S.; Tarasov, A.; Schumann, J.; Frei, E.; Varley, J. B.; Abild-Pedersen, F.; Nørskov, J. K.; Schlögl, R. The Mechanism of CO and CO_2 Hydrogenation to Methanol over Cu-Based Catalysts. *ChemCatChem* **2015**, *7*, 1105−1111.

(20) Kattel, S.; Ramírez, P. J.; Chen, J. G.; Rodriguez, J. A.; Liu, P. Active Sites for CO_2 Hydrogenation to Methanol on Cu/ZnO Catalysts. *Science* **2017**, *355*, 1296−1299.

(21) Martin, O.; Mondelli, C.; Cervellino, A.; Ferri, D.; Curulla-Ferré, D.; Pérez-Ramírez, L. Operando Synchrotron X-ray Powder Diffraction and Modulated-excitation Infrared Spectroscopy Elucidate the CO_2 Promotion on a Commercial Methanol Synthesis Catalyst. *Angew. Chem., Int. Ed.* **2016**, *55*, 11031−11036.

(22) van den Berg, R.; Prieto, G.; Korpershoek, G.; van der Wal, L. I.; van Bunningen, A. J.; Lægsgaard-Jørgensen, S.; de Jongh, P. E.; de Jong, K. P. Structure Sensitivity of Cu and CuZn Catalysts Relevant to Industrial Methanol Synthesis. *Nat. Commun.* **2016**, *7*, 13057.

(23) Lei, H.; Nie, R.; Wu, G.; Hou, Z. Hydrogenation of CO_2 to CH_3OH over Cu/ZnO Catalysts with Different ZnO Morphology. *Fuel* **2015**, *154*, 161−166.

(24) Yu, K. P.; Yu, W. Y.; Kuo, M. C.; Liou, Y. C.; Chien, S. H. Pt/titania-nanotube: A Potential Catalyst for CO_2 Adsorption and Hydrogenation. *Appl. Catal., B* **2008**, *84*, 112−118.

(25) Falbo, L.; Martinelli, M.; Visconti, C. G.; Lietti, L.; Bassano, C.; Deiana, P. Kinetics of CO_2 Methanation on a Ru-based Catalyst at Process Conditions Relevant for Power-to-Gas Applications. *Appl. Catal., B* **2018**, *225*, 354−363.

(26) Jiménez, V.; Sánchez, P.; Panagiotopoulou, P.; Valverde, J. L.; Romero, A. Methanation of CO, CO_2 and Selective Methanation of CO, in Mixtures of CO and CO_2, over Ruthenium Carbon Nanofibers Catalysts. *Appl. Catal., A* **2010**, *390*, 35−44.

(27) Eckle, S.; Anfang, H. G.; Behm, R. J. Reaction Intermediates and Side Products in the Methanation of CO and CO_2 over Supported Ru catalysts in H_2 -rich Reformate Gases. *J. Phys. Chem. C* **2011**, *115*, 1361−1367.
(28) Park, J. N.; McFarland, E. W. A Highly Dispersed Pd−Mg/SiO_2 Catalyst Active for Methanation of CO_2. *J. Catal.* **2009**, *266*, 92−97.
(29) Chang, F. W.; Kuo, M. S.; Tsay, M. T.; Hsieh, M. C. Hydrogenation of CO_2 over Nickel Catalysts on Rice Husk Ash-alumina Prepared by Incipient Wetness Impregnation. *Appl. Catal., A* **2003**, *247*, 309−320.
(30) Aziz, M. A. A.; Jalil, A. A.; Triwahyono, S.; Mukti, R. R.; Taufiq-Yap, Y. H.; Sazegar, M. R. Highly Active Ni-promoted Mesostructured Silica Nanoparticles for CO_2 Methanation. *Appl. Catal., B* **2014**, *147*, 359−368.
(31) Tada, S.; Shimizu, T.; Kameyama, H.; Haneda, T.; Kikuchi, R. Ni/CeO_2 Catalysts with High CO_2 Methanation Activity and High CH_4 Selectivity at Low Temperatures. *Int. J. Hydrogen Energy* **2012**, *37*, 5527−5531.
(32) Ocampo, F.; Louis, B.; Kiwi-Minsker, L.; Roger, A. C. Effect of Ce/Zr Composition and Noble Metal Promotion on Nickel Based CexZr1−xO_2 Catalysts for Carbon Dioxide Methanation. *Appl. Catal., A* **2011**, *392*, 36−44.
(33) Zhou, G.; Liu, H.; Cui, K.; Xie, H.; Jiao, Z.; Zhang, G.; Xiong, K.; Zheng, X. Methanation of Carbon Dioxide over Ni/CeO_2 catalysts: Effects of Support CeO_2 Structure. *Int. J. Hydrogen Energy* **2017**, *42*, 16108−16117.
(34) Hwang, S.; Hong, U. G.; Lee, J.; Baik, J. H.; Koh, D. J.; Lim, H.; Song, I. K. Methanation of Carbon Dioxide over Mesoporous Nickel−M−alumina (M = Fe, Zr, Ni, Y, and Mg) Xerogel Catalysts: Effect of Second Metal. *Catal. Lett.* **2012**, *142*, 860−868.
(35) Heine, C.; Lechner, B. A. J.; Bluhm, H.; Salmeron, M. Recycling of CO_2: Probing the Chemical State of The Ni(111) Surface During the Methanation Reaction with Ambient-pressure X-ray Photoelectron Spectroscopy. *J. Am. Chem. Soc.* **2016**, *138*, 13246−13252.
(36) Muroyama, H.; Tsuda, Y.; Asakoshi, T.; Masitah, H.; Okanishi, T.; Matsui, T.; Eguchi, K. Carbon Dioxide Methanation over Ni Catalysts Supported on Various Metal Oxides. *J. Catal.* **2016**, *343*, 178−126.
(37) Kattel, S.; Yan, B.; Chen, J. G.; Liu, P. CO_2 Hydrogenation on Pt, Pt/SiO_2 and Pt/TiO_2: Importance of Synergy between Pt and Oxide Support. *J. Catal.* **2016**, *343*, 115−126.
(38) Kusama, H.; Bando, K. K.; Okabe, K.; Arakawa, H. CO_2 Hydrogenation Reactivity and Structure of Rh/SiO_2 Catalysts Prepared from Acetate, Chloride and Nitrate Precursors. *Appl. Catal., A* **2001**, *205*, 285−294.
(39) Kharaji, A. G.; Shariati, A.; Takassi, M. A. A Novel γ-alumina Supported Fe-Mo Bimetallic Catalyst for Reverse Water Gas Shift Reaction. *Chin. J. Chem. Eng.* **2013**, *21*, 1007−1014.
(40) Yang, L.; Pastor-Pérez, L.; Gu, S.; Sepúlveda-Escribano, A.; Reina, T. R. Highly Efficient Ni/CeO_2-Al_2O_3 Catalysts for CO_2 Upgrading Via Reverse Water-gas Shift: Effect of Selected Transition Metal Promoters. *Appl. Catal., B* **2018**, *232*, 464−471.
(41) Sun, F.; Yan, C.; Wang, Z.; Guo, C.; Huang, S. Ni/Ce−Zr−O Catalyst for High CO_2 Conversion During Reverse Water Gas Shift Reaction (RWGS). *Int. J. Hydrogen Energy* **2015**, *40*, 15985−15993.
(42) Aziz, M. A. A.; Jalil, A. A.; Triwahyono, S.; Ahmad, A. CO_2 Methanation over Heterogeneous Catalysts: Recent Progress and Future Prospects. *Green Chem.* **2015**, *17*, 2647−2663.
(43) Wei, W.; Jinlong, G. Methanation of Carbon Dioxide: an Overview. *Front. Chem. Sci. Eng.* **2011**, *5*, 2−10.
(44) Zhi, C.; Wang, Q.; Wang, B.; Li, D.; Zhang, R. Insight into the Mechanism of Methane Synthesis from Syngas on a Ni(111) Surface: a Theoretical Study. *RSC Adv.* **2015**, *5*, 66742−66756.
(45) Zhou, M.; Liu, B. DFT Investigation on the Competition of the Water-gas Shift Reaction ersus Methanation on Clean and Potassium-modified Nickel(111) Surfaces. *ChemCatChem* **2015**, *7*, 3928−3935.
(46) Choe, S. J.; Kang, H. J.; Kim, S. J.; Park, S. B.; Park, D. H.; Huh, D. S. Adsorbed Carbon Formation and Carbon Hydrogenation for CO_2 Methanation on the Ni(111) Surface: ASED-MO Study. *Bull. Korean Chem. Soc.* **2005**, *26*, 1682−1688.
(47) Ren, J.; Guo, H.; Yang, J.; Qin, Z.; Lin, J.; Li, Z. Insights into the Mechanisms of CO_2 Methanation on Ni(111) Surfaces by Density Functional Theory. *Appl. Surf. Sci.* **2015**, *351*, 504−516.
(48) Vogt, C.; Monai, M.; Sterk, E. B.; Palle, J.; Melcherts, A. E. M.; Zijlstra, B.; Groeneveld, E.; Berben, P. H.; Boereboom, J. M.; Hensen, E. J. M.; Meirer, F.; Filot, I. A. W.; Weckhuysen, B. M. Understanding Carbon Dioxide Activation and Carbon−carbon Coupling over Nickel. *Nat. Commun.* **2019**, *10*, 5330.
(49) Zhang, M.; Zijlstra, B.; Filot, I. A. W.; Li, F.; Wang, H.; Li, J.; Hensen, E. J. M. A theoretical Study of the Reverse Water-gas Shift Reaction on Ni(111) and Ni(311) Surfaces. *Can. Can. J. Chem. Eng.* **2020**, *98*, 740−748.
(50) Dietz, L.; Piccinin, S.; Maestri, M. Mechanistic Insights into CO_2 Activation Via Reverse Water-gas shift on Metal Surfaces. *J. Phys. Chem. C* **2015**, *119*, 4959−4966.
(51) Blaylock, D. W.; Ogura, T.; Green, W. H.; Beran, G. J. O. Computational Investigation of Thermochemistry and Kinetics of Steam Methane Reforming on Ni(111) under Realistic Conditions. *J. Phys. Chem. C* **2009**, *113*, 4898−4908.
(52) Catapan, R. C.; Oliveira, A. M. M.; Chen, Y.; Vlachos, D. G. DFT Study of the Water−gas shift Reaction and Coke Formation on Ni(111) and Ni(211) surfaces. *J. Phys. Chem. C* **2012**, *116*, 20281−20291.
(53) Vrijburg, W. L.; Moioli, E.; Chen, W.; Zhang, M.; Terlingen, B. J. P.; Zijlstra, B.; Filot, I. A. W.; Züttel, A.; Pidko, E. A.; Hensen, E. J. M. Efficient Base-metal NiMn/TiO_2 Catalyst for CO_2 Methanation. *ACS Catal.* **2019**, *9*, 7823−7839.
(54) Kresse, G.; Hafner, J. Ab Initio Molecular Dynamics for Liquid Metals. *Phys. Rev. B: Condens. Matter Mater. Phys.* **1993**, *47*, 558−561.
(55) Kresse, G.; Furthmüller, J. Efficient Iterative Schemes for Ab Initio Total-energy Calculations Using a Plane-wave Basis Set. *Phys. Rev. B: Condens. Matter Mater. Phys.* **1996**, *54*, 11169−11186.
(56) Kresse, G.; Furthmüller, J. Efficiency of Ab-initio Total Energy Calculations for Metals and Semiconductors Using a Plane-wave Basis Set. *Comput. Mater. Sci.* **1996**, *6*, 15−50.
(57) Kresse, G.; Joubert, D. From Ultrasoft Pseudopotentials to the Projector Augmented-wave Method. *Phys. Rev. B: Condens. Matter Mater. Phys.* **1999**, *59*, 1758−1775.
(58) Wellendorff, J.; Silbaugh, T. L.; Garcia-Pintos, D.; Nørskov, J. K.; Bligaard, T.; Studt, F.; Campbell, C. T. A Benchmark Database for Adsorption Bond Energies to Transition Metal Surfaces and Comparison to Selected DFT Functionals. *Surf. Sci.* **2015**, *640*, 36−44.
(59) Campbell, C. T. Energies of Adsorbed Catalytic Intermediates on Transition Metal Surfaces: Calorimetric Measurements and Benchmarks for Theory. *Acc. Chem. Res.* **2019**, *52*, 984−993.
(60) Gautier, S.; Steinmann, S. N.; Michel, C.; Fleurat-Lessard, P.; Sautet, P. Molecular Adsorption at Pt(111). How Accurate are DFT functionals? *Phys. Chem. Chem. Phys.* **2015**, *17*, 28921−28930.
(61) Wellendorff, J.; Lundgaard, K. T.; Møgelhøj, A.; Petzold, V.; Landis, D. D.; Nørskov, J. K.; Bligaard, T.; Jacobsen, K. W. Density Functionals for Surface Science: Exchange-correlation Model Development with Bayesian Error Estimation. *Phys. Rev. B* **2012**, *85*, 235149.
(62) Kittle, C. *Introduction to Solid State Physics*, 6th ed.; Wiley: 1986.
(63) Monkhorst, H. J.; Pack, J. D. Special Points for Brillouin-zone Integrations. *Phys. Rev. B* **1976**, *13*, 5188−5192.
(64) Jónsson, H.; Mills, G.; Jacobsen, K. W. Nudged Elastic Band Method for Finding Minimum Energy Paths of Transitions. In *Classical and Quantum Dynamics in Condensed Phase Simulations*; World Scientific: Lerici, Villa Marigola, 1998; pp 385−404.
(65) Henkelman, G.; Uberuaga, B. P.; Jónsson, H. A Climbing Image Nudged Elastic Band Method for Finding Saddle Points and Minimum Energy Paths. *J. Chem. Phys.* **2000**, *113*, 9901−9904.
(66) Hjorth Larsen, A.; Jørgen Mortensen, J.; Blomqvist, J.; Castelli, I. E.; Christensen, R.; Dułak, M.; Friis, J.; Groves, M. N.; Hammer, B.; Hargus, C.; Hermes, E. D.; Jennings, P. C.; Bjerre Jensen, P.; Kermode, J.; Kitchin, J. R.; Leonhard Kolsbjerg, E.; Kubal, J.; Kaasbjerg, K.; Lysgaard, S.; Bergmann Maronsson, J.; Maxson, T.; Olsen, R.;

https://dx.doi.org/10.1021/acscatal.0c01599
ACS Catal. 2020, 10, 8077−8089

Pastewka, L.; Peterson, A.; Rostgaard, C.; Schiøtz, J.; Schütt, O.; Strange, M.; Thygesen, K. S.; Vegge, T.; Vilhelmsen, L.; Walter, M.; Zeng, Z.; Jacobsen, K. W. The Atomic Simulation Environment—a Python Library for Working with Atoms. *J. Phys.: Condens. Matter* **2017**, *29*, 273002.
(67) Smidstrup, S.; Pedersen, A.; Stokbro, K.; Jónsson, H. Improved Initial guess for Minimum Energy Path Calculations. *J. Chem. Phys.* **2014**, *140*, 214106.
(68) Andersen, M.; Panosetti, C.; Reuter, K. A Practical Guide to Surface Kinetic Monte Carlo Simulations. *Front. Chem.* **2019**, *7*, 202.
(69) Prats, H.; Illas, F.; Sayós, R. General Concepts, Assumptions, Drawbacks and Misuses in Kinetic Monte Carlo and Microkinetic Modelling Simulations Applied to Computational Heterogeneous Catalysis. *Int. J. Quantum Chem.* **2018**, *118*, e25518.
(70) Stamatakis, M.; Vlachos, D. G. A Graph-theoretical Kinetic Monte Carlo Framework for on-lattice Chemical Kinetics. *J. Chem. Phys.* **2011**, *134*, 214115.
(71) Stamatakis, M.; Vlachos, D. G. Unraveling the Complexity of Catalytic Reactions Via kinetic Monte Carlo Simulation: Current Status and Frontiers. *ACS Catal.* **2012**, *2*, 2648−2663.
(72) Nielsen, J.; d'Avezac, M.; Hetherington, J.; Stamatakis, M. Parallel kinetic Monte Carlo Simulation Framework Incorporating Accurate Models of Adsorbate Lateral Interactions. *J. Chem. Phys.* **2013**, *139*, 224706.
(73) Yang, L.; Karim, A.; Muckerman, J. T. Density Functional Kinetic Monte Carlo Simulation of Water−gas Shift Reaction on Cu/ZnO. *J. Phys. Chem. C* **2013**, *117*, 3414−3425.
(74) Prats, H.; Álvarez, L.; Illas, F.; Sayós, R. Kinetic Monte Carlo Simulations of the Water Gas Shift reaction on Cu(1 1 1) From Density Functional Theory Based Calculations. *J. Catal.* **2016**, *333*, 217−226.
(75) Piccinin, S.; Stamatakis, M. CO Oxidation on Pd(111): a First-principles-based Kinetic Monte Carlo Study. *ACS Catal.* **2014**, *4*, 2143−2152.
(76) Prats, H.; Posada-Perez, S.; Rodriguez, J. A.; Sayos, R.; Illas, F. Kinetic Monte Carlo Simulations Unveil Synergic Effects at Work on Bifunctional Catalysts. *ACS Catal.* **2019**, *9*, 9117.
(77) Stuckless, J. T.; AlSarraf, N.; Wartnaby, C.; King, D. A. Calorimetric Heats of Adsorption for CO on Nickel Single Crystal Surfaces. *J. Chem. Phys.* **1993**, *99*, 2202−2212.
(78) Beniya, A.; Isomura, N.; Hirata, H.; Watanabe, Y. Low Temperature Adsorption and Site-conversion Process of CO on the Ni(111) Surface. *Surf. Sci.* **2012**, *606*, 1830−1836.
(79) Prats, H.; Gamallo, P.; Sayos, R.; Illas, F. Unexpectedly Large Impact of Van der Waals Interactions on the Description of Heterogeneously Catalyzed Reactions: the Water Gas Shift Reaction on Cu(321) as a Case Example. *Phys. Chem. Chem. Phys.* **2016**, *18*, 2792−2801.
(80) Campbell, C. T. The Degree of Rate Control: a Powerful Tool for Catalysis Research. *ACS Catal.* **2017**, *7*, 2770−2779.

https://dx.doi.org/10.1021/acscatal.0c01599
ACS Catal. 2020, 10, 8077−8089

3.6. References

1. Barbir, F. Transition to Renewable Energy Systems with Hydrogen as an Energy Carrier. *Energy*, **2009**, 34, 308−312.

2. Dincer, I. Renewable Energy and Sustainable Development: a Crucial Review. *Renewable Sustainable Energy Rev*., **2000**, 4, 157−175.

3. Jalama, K. Carbon Dioxide Hydrogenation over Nickel-, Ruthenium-, and Copper-based Catalysts: Review of Kinetics and Mechanism. *Catal. Rev.: Sci. Eng.*, **2017**, 59, 95−164.

4. Kattel, S.; Liu, P.; Chen, J. G. Tuning Selectivity of CO_2 Hydrogenation Reactions at the Metal/Oxide Interface. *J. Am. Chem. Soc.*, **2017**, 139, 9739−9754.

5. Li, W.; Wang, H.; Jiang, X.; Zhu, J.; Liu, Z.; Guo, X.; Song, C. A Short Review of Recent Advances in CO_2 Hydrogenation to Hydrocarbons over Heterogeneous Catalysts. *RSC Adv.*, **2018**, 8, 7651−7669.

6. Wang, W.; Wang, S.; Ma, X.; Gong, J. Recent Advances in Catalytic Hydrogenation of Carbon Dioxide. *Chem. Soc. Rev.*, **2011**, 40, 3703−3727.

7. Nie, X.; Li, W.; Jiang, X.; Guo, X.; Song, C. Recent Advances in Catalytic CO_2 Hydrogenation to Alcohols and Hydrocarbons. *Adv. Catal.*, **2019**, 65, 121−133.

8. Aziz, M. A. A.; Jalil, A. A.; Triwahyono, S.; Ahmad, A. CO_2 Methanation over Heterogeneous Catalysts: Recent Progress and Future Prospects. *Green Chem.*, **2015**, 17, 2647−2663.

9 .Wei, W.; Jinlong, G. Methanation of Carbon Dioxide: an Overview. *Front. Chem. Sci. Eng.*, **2011**, 5, 2−10.

10. Chang, F. W.; Kuo, M. S.; Tsay, M. T.; Hsieh, M. C. Hydrogenation of CO_2 over Nickel Catalysts on Rice Husk Ash- alumina Prepared by Incipient Wetness Impregnation. *Appl. Catal. A*, **2003**, 247, 309−320.

11. Aziz, M. A. A.; Jalil, A. A.; Triwahyono, S.; Mukti, R. R.; Taufiq- Yap, Y. H.; Sazegar, M. R. Highly Active Ni-promoted Mesostructured Silica Nanoparticles for CO_2 Methanation. *Appl. Catal. B*, **2014**, 147, 359−368.

12. Tada, S.; Shimizu, T.; Kameyama, H.; Haneda, T.; Kikuchi, R. Ni/CeO_2 Catalysts with High CO_2 Methanation Activity and High CH_4 Selectivity at Low Temperatures. *Int. J. Hydrog. Energy*, **2012**, 37, 5527−5531

13. Ocampo, F.; Louis, B.; Kiwi-Minsker, L.; Roger, A. C. Effect of Ce/Zr Composition and Noble Metal Promotion on Nickel Based CexZr1−xO_2 Catalysts for Carbon Dioxide Methanation. *Appl. Catal. A*, **2011**, 392, 36−44.

14. Zhou, G.; Liu, H.; Cui, K.; Xie, H.; Jiao, Z.; Zhang, G.; Xiong, K.; Zheng, X. Methanation of Carbon Dioxide over Ni/CeO_2 catalysts: Effects of Support CeO_2 Structure. *Int. J. Hydrog. Energy*, **2017**, 42, 16108−16117.

15. Hwang, S.; Hong, U. G.; Lee, J.; Baik, J. H.; Koh, D. J.; Lim, H.; Song, I. K. Methanation of Carbon Dioxide over Mesoporous Nickel− M−alumina (M = Fe, Zr, Ni, Y, and Mg) Xerogel Catalysts: Effect of Second Metal. *Catal. Lett.*, **2012**, 142, 860−868.

16. Heine, C.; Lechner, B. A. J.; Bluhm, H.; Salmeron, M. Recycling of CO_2: Probing the Chemical State of The Ni(111) Surface During the Methanation Reaction with Ambient-pressure X-ray Photoelectron Spectroscopy. *J. Am. Chem. Soc.*, **2016**, 138, 13246−13252

17. Zheng, H.; Liao, W.; Ding, J.; Xu, F.; Jia, A.; Huang, W.; Zhang, Z. Unveiling the Key Factors in Determining the Activity and Selectivity of CO_2 hydrogenation over Ni/CeO_2 Catalysts. *ACS. Catal.*, **2022**, 12, 15451-5462.

18. Vogt, C.; Groeneveld, E.; Kamsma, G.; Nachtegaal, M.; Lu, L.; Kiely, J. C.; Berben. H. P.; Meirer, F.; Weckhuysen. B. M. Unravelling Structure Sensitivity in CO_2 Hydrogenation over Nickel. *Nat. Catal.*, **2018**, 1, 127-134.

19. Feng, K.; Tian, J.; Guo, M.; Wang, Y.; Wang, S.; Wu, Z.; Zhang, J.; He, L.; Yan. B. Experimentally Unveiling the Origin of Tunable Selectivity for CO_2 Hydrogenation over Ni-based Catalysts. *Appl. Catal. B*, **2021**, 292, 120191-120198.

20. Villagra-Soza, F.; Godoy, S.; Karelovic, A.; Jimenez, R. Scrutinizing the Mechanism of CO_2 Hydrogenation over Ni, Co and bimetallic NiCo Surfaces: Isotopic Measurements, Operando-FTIR Experiments and Kinetics Modelling. *J. Catal*, **2022**, 414, 1-15.

21. Martin, M. N.; Velin, P.; Skoglundh, M.; Bauer, M.; Carlsson, P. Catalytic Hydrogenation of CO_2 to Methane over Supported Pd, Rh and Ni Catalysts. *Catal. Sci. Technol.*, **2017**, 7, 1086-1094.

22. Galhardo, S. T.; Braga, H. A.; Arpini, H. B.; Szanyi, J.; Gonçalves, V. R.; Zornio, F. B., Miranda, R. C.; Rossi, M. L. Optimizing Active Sites for High CO Selectivity during CO_2 Hydrogenation over Supported Nickel Catalysts. *J. Am. Chem. Soc.*, **2021**, 143, 4268−4280.

23. Yang, L.; Pastor-Peŕez, L.; Gu, S.; Sepulveda-Escribano, A.; Reina, T. R. Highly Efficient Ni/CeO_2-Al_2O_3 Catalysts for CO_2 Upgrading Via Reverse Water-gas Shift: Effect of Selected Transition Metal Promoters. *Appl. Catal. B*, **2018**, 232, 464−471.

24. Sun, F.; Yan, C.; Wang, Z.; Guo, C.; Huang, S. Ni/Ce−Zr−O Catalyst for High CO_2 Conversion During Reverse Water Gas Shift Reaction (RWGS). *Int. J. Hydrog. Energy*, **2015**, 40, 15985−15993.

25. Rodriguez, J. A.; Evans, J.; Feria, L.; Vidal, A. B.; Liu, P.; Nakamura, K.; Illas, F. CO_2 Hydrogenation on Au/TiC, Cu/TiC, and Ni/TiC Catalysts: Production of CO, Methanol, and Methane. *J. Catal.*, **2013**, 307, 162−169.

26. D, L.; Ai, X.; Xie, F.; Zhou, G. Efficient Ni-based Catalysts for Low-temperature Reverse Water-gas Shift (RWGS) Reaction. *Chem. Asian J.*, **2021**, 16, 949-958.

27. Zhi, C.; Wang, Q.; Wang, B.; Li, D.; Zhang, R. Insight into the Mechanism of Methane Synthesis from Syngas on a Ni(111) Surface: a Theoretical Study. *RSC Adv.*, **2015,** 5, 66742−66756.

28. Zhou, M.; Liu, B. DFT Investigation on the Competition of the Water-gas Shift Reaction ersus Methanation on Clean and Potassium- modified Nickel(111) Surfaces. *ChemCatChem*, **2015**, 7, 3928−3935.

29. Choe, S. J.; Kang, H. J.; Kim, S. J.; Park, S. B.; Park, D. H.; Huh, D. S. Adsorbed Carbon Formation and Carbon Hydrogenation for CO_2 Methanation on the Ni(111) Surface: ASED-MO Study. *Bull. Korean Chem. Soc.*, **2005**, 26, 1682−1688.

30. Ren, J.; Guo, H.; Yang, J.; Qin, Z.; Lin, J.; Li, Z. Insights into the Mechanisms of CO_2 Methanation on Ni(111) Surfaces by Density Functional Theory. *Appl. Surf. Sci.*, **2015**, 351, 504−516.

31. Vogt, C.; Monai, M.; Sterk, E. B.; Palle, J.; Melcherts, A. E. M.; Zijlstra, B.; Groeneveld, E.; Berben, P. H.; Boereboom, J. M.; Hensen, E. J. M.; Meirer, F.; Filot, I. A. W.; Weckhuysen, B. M. Understanding Carbon Dioxide Activation and Carbon−carbon Coupling over Nickel. *Nat. Commun.*, **2019**, 10, 5330-5340.

32. Zhang, M.; Zijlstra, B.; Filot, I. A. W.; Li, F.; Wang, H.; Li, J.; Hensen, E. J. M. A theoretical Study of the Reverse Water-gas Shift Reaction on Ni(111) and Ni(311) Surfaces. *Can. J. Chem. Eng.*, **2020**, 98, 740−748.

33. Dietz, L.; Piccinin, S.; Maestri, M. Mechanistic Insights into CO_2 Activation Via Reverse Water-gas shift on Metal Surfaces. *J. Phys. Chem. C*, **2015**, 119, 4959−4966.

34. Lozano-Reis, P.; Prats, H.; Gamallo, P.; Illas, F.; Sayós, R. Multiscale Study of the Mechanism of Catalytic CO_2 Hydrogenation: Role of the Ni (111) facets. *ACS Catal.*, **2020**, 10, 8077-8089.

35. Campbell, C. T. The Degree of Rate Control: a Powerful Tool for Catalysis Research. *ACS Catal.*, **2017**, 7, 2770−2779.

Chapter 4

RWGS on Ni_4/TiC and TiC(001) surfaces

4.1. Introduction

Heterogeneous catalytic processes are of paramount importance in keeping the welfare of nowadays societies, as almost 90 % of the chemical manufacturing processes over the world are based on this technology.[1] Moreover, catalysis constitutes one of the most important strategies to mitigate the climate change emergency. To this end, considerable attention has been paid to find suitable catalytic processes that are able to efficiently convert greenhouse gases such as CO_2 into new value-added chemicals of industrial interest—such as CO, methane or methanol—creating a C_1 cyclic energy economy.[2-7] Therefore, the exploration of new catalysts with superior activity and selectivity at a low economic and environmental cost is of high interest. In this regard, a deep understanding on how catalysts behave and why they are (in)active or selective towards a specific product is fundamental for a rational design of novel catalysts, as inefficient and costly trial and error procedures continue to be largely used as a research strategy.

Most common industrial catalysts consist of small-to-medium size metallic clusters or nanoparticles anchored to some support, usually zeolites, sulfides or metal oxides.[1] Depending on the metal and the support, on the size and morphology of both constituents, and on the working conditions used, it is possible to tune the catalytic activity and selectivity towards the desired product. In the past decades, it was generally believed that the role of the support was merely to efficiently disperse the metallic clusters or nanoparticles, hence increasing their effective surface area with the concomitant enhancement of the system catalytic activity. However, there is increasing evidence that the role of the support goes well beyond this simplified picture and that the interaction between the metal and the support could be crucial for the new reactivity observed. This interaction, also known as strong metal-support interaction (SMSI) was introduced by Tauster and coworkers in the late seventies.[8-10] In their seminal works, these authors found that the SMSI is detrimental for the activity, but the origin of these effects was not clear. Nevertheless, this was finally understood as a capping of the metal nanoparticles

by support islands during the experiments, which induced a reduction of the metal active sites with the concomitant decrease of the catalytic activity. However, there is also strong evidence that SMSI can be beneficial and enhances the catalytic activity as reported by many authors.[11-16] Moreover, it has also been shown that the support plays an important role, which adds importance to the SMSI as a possible way to tune the catalytic activity and selectivity.[17] Therefore, a complete understanding on how strong metal-support interactions affect the way intermediate species interact with the catalyst is of paramount interest for rational catalyst design.

In order to take benefit of metal-support interactions it is necessary to use supports that truly bind metal atoms. Among the very different supports used in catalysis, transition metal carbides (TMCs)[18] have emerged as exceptional alternatives to oxide surfaces. TMCs have gained increasing interest as they combine physical properties of three different classes of materials; these are: (i) the extreme hardness that covalent solids present, (ii) the excellent thermal and electric conductivity of metals and (iii) the high melting points, in particular for ionic crystals.[18,19] For olefin selective hydrogenation, TMCs have been shown to present catalytic activities similar or even better than Pt-group metals,[20-22] hence being proposed as alternative catalysts to noble metals. Moreover, TMCs are not only interesting because of the good catalytic activity they present by itself, but as mentioned above, they can be used as supports for metals, displaying excellent activities and selectivity. For instance, Au nanoparticles supported on TiC and Cu and Ni nanoparticles supported on TiC and other TMCs (i.e., MoC and Mo_2C) have been shown to present exceptional catalytic activity for CH_4 dissociation,[23] desulfurization processes,[24-28] CO_2 hydrogenation,[29,30] O_2 dissociation[31-33] and the water-gas shift reaction.[13] In particular, Ni nanoparticles and clusters supported on TiC have been shown to display outstanding CO_2 hydrogenation activity with respect to the bare TiC surface.[34] However, details explaining why Ni/TiC systems are more active than the bare TiC surface are still unknown. This is mainly because of the complexity of the Ni/TiC system featuring three very different regions, namely: the Ni nanoparticle/cluster, the TiC surface and the interface that lies in the middle of the metal and the support, each one interacting differently with the income mixture and intermediate species formed during the reaction.

From an experimental point of view, understanding why a catalyst is active or selective towards a specific product is extremely challenging, which is a hurdle for proper rational design of novel catalysts. The main drawback that experimentalists face up is the

high complexity of industrial catalysts with many different active sites and the large number of intermediate species and elementary reactions that can take place for many reactions of industrial interest. Even if notable progresses have been done in the past years in the use of experimental *operando* techniques,[35-41] a detailed description of the mechanism that drives the reaction and the role of the different active sites are still out of be reached from an experimental perspective alone. To tackle this problem, theoretical modeling is paramount as it allows to obtain information from the atomistic scale, which in the best case is coupled to some kinetic simulation techniques to predict macroscopic magnitudes. Regarding quantum mechanical calculations, most often in the framework of DFT, they are extensively used as they provide useful insights about the energetics and chemical bonding of the adsorbed species and of the transition states. With this information, it is possible to construct potential energy diagrams that are commonly used to unveil which are the most plausible reaction mechanisms, at least from a static point of view. Nevertheless, for most real heterogeneously catalyzed processes, the information obtained solely from the electronic structure calculations is generally insufficient to correctly describe the system behavior under real working conditions, although it could be sufficient, perhaps, for simple model systems. Therefore, to bridge the gap between the atomic static picture and the macroscopic regime, DFT calculations must be coupled to kinetic modeling techniques,[42-45] such as microkinetic modeling or kinetic Monte Carlo simulations. In this way, by means of such type of multiscale approaches, one can clearly understand and rationalize the role of the different active sites and intermediate species, and define which are the most probable pathways that govern the reaction mechanism, which in the end could be very useful for proper rational design of novel catalysts.

The present chapter aims to understand the boost of the catalytic activity experimentally observed for Ni/TiC with respect to TiC for the RWGS reaction.[34] To do so, we grow in complexity going from DFT calculations of different Ni/TiC models to propose a representative model that can be mimic the experimental systems and that can explain the increase of activity observed for Ni/TiC with respect to the bare TiC surface. Then, we finally perform kMC simulations to clearly understand the experimental observations. Summing up, we start by studying the metal-support interactions of several Ni clusters supported on the TiC surface.[46] Then, we analyze the H_2 and CO_2 adsorption and activation on a variety of the abovementioned systems as these two species are the reactants of the RWGS reaction.[47] Finally, based on the results of the two previous studies

we chose a proper model system and we study the RWGS reaction over the Ni_4/TiC and TiC systems from a kMC perspective.[48]

4.2. Models

For the overall study of the RWGS reaction catalyzed by Ni/TiC and TiC we have used different surface models as shown in Figure 4.1.

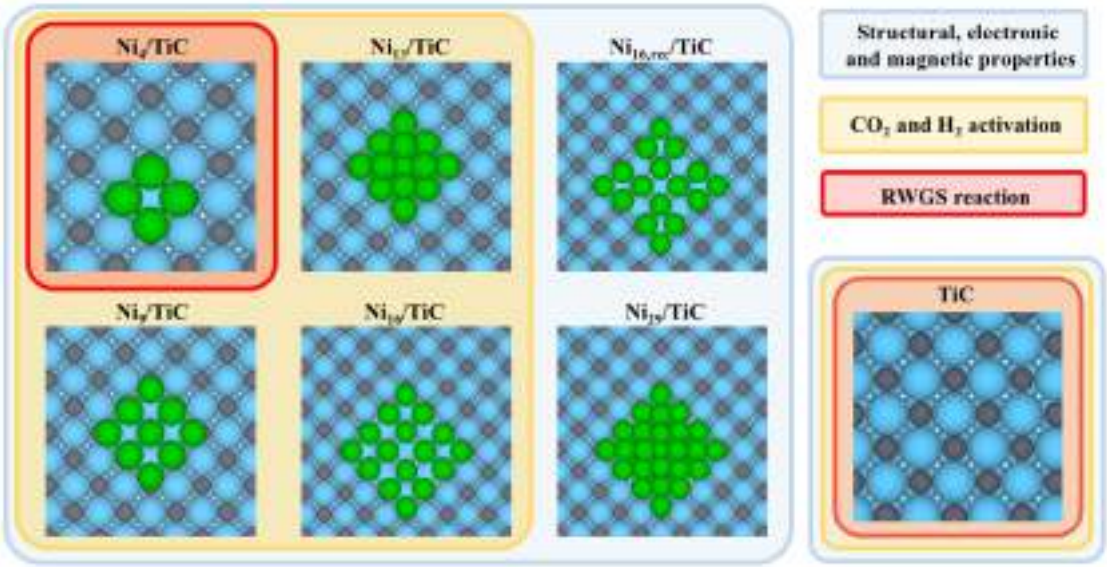

Figure 4.1. Ni_n clusters supported on the TiC (001) surface. Light blue, grey and green colors denote titanium, carbon and nickel atoms, respectively. Note that the Ni_{13}/TiC and Ni_{29}/TiC systems involve 3D clusters. Shadow colored boxes show the systems that have been used in the different studies. The blue box stands for the study of the structural, electronic and magnetic properties. The yellow box refers to the systems used in the CO_2 and H_2 activation study and the red box denotes the systems used for the RWGS study.

The different systems differ in the size and morphology of the Ni cluster. A set of five (six considering the reconstructed structure of the Ni_{16} cluster) Ni_n/TiC structures featuring 2D and 3D Ni clusters supported on the TiC(001) surface have been chosen to study their electronic, magnetic and structural properties. From the results obtained we have restricted the following study to four different Ni_n/TiC systems and studied the CO_2 and H_2 activation. Again, the Ni clusters used feature different sizes and morphologies. The particular choice of CO_2 and H_2 is because they are the reactants of the RWGS reaction. Finally, from the results of both abovementioned studies we have found that the Ni_4/TiC system was a good model to explain the boost of catalytic activity observed for the Ni/TiC system with respect to the bare TiC surface. Therefore, we have restricted the

calculations of the overall reactivity for the RWGS reaction for the Ni_4/TiC and TiC systems.

4.3. Results

The main results for the different studies of the Ni/TiC and TiC systems are presented below. The reader interested in more details is referred to Refs.46-48

4.3.1. Structural, magnetic and electronic properties of Ni_n/TiC systems

The interaction of several Ni clusters of different sizes and morphologies supported on TiC have been studied to rationalize how metal-support interactions can affect the final reactivity of the Ni/TiC system as well as finding a reliable model for the final study of the RWGS reaction over Ni/TiC. To this end, we start by choosing five different Ni clusters, namely: Ni_4, Ni_9, Ni_{13}, Ni_{16} and Ni_{29}. In Figure 4.2 we show the most stable gas-phase structures of the aforementioned Ni_n clusters.

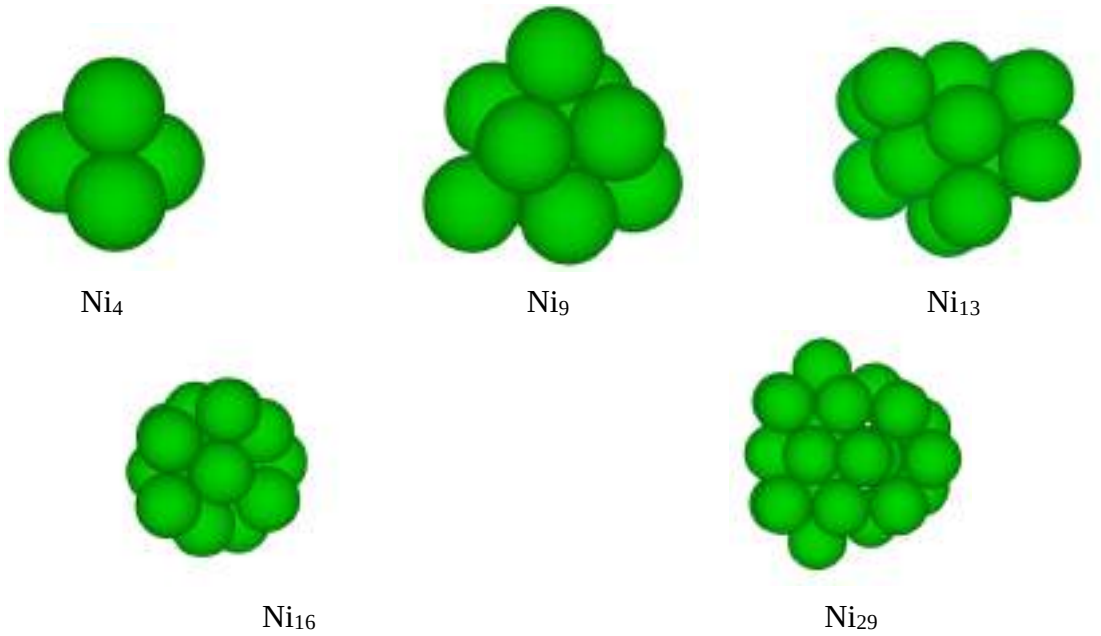

Figure 4.2. Structures of the most stable Ni_n gas-phase clusters. Figure directly taken from Ref. 46.

Generally, supports can induce modifications of the metal particles behavior after their adsorption over the support due to the metal-support interactions. We then have studied the metal-support interactions for the five different clusters mentioned above after

adsorption over the TiC surface. We have considered different small to medium size clusters featuring 2D and 3D morphologies. This special choice is because experimental evidence shows that at low coverages metal particles supported over TMCs tend to adopt planar structures to maximize the metal-support contact, while at higher coverages they tend to aggregate and form 3D structures. [28,33] The structure of the studied Ni_n/TiC systems is the one shown in Figure 4.1. For all the structures the Ni clusters adsorb with the metal atoms interacting directly with the C atoms of the TiC surface exhibiting a (001) facet morphology. Note that for the Ni_{16} system two metastable structural configurations have been obtained, one exhibiting the square shape of the (001) facet while the other seems to display an aggregation of four Ni_4 clusters, the latter one hereafter denoted as $Ni_{16,rec}$. Interestingly, the structures adopted by the Ni cluster when adsorbed over TiC are different to the ones observed over metal oxides, where 3D structures have been reported.[49-55]

In order to quantify the interaction between the cluster and the support and the availability of the cluster to actually be formed, we have calculated the adsorption, adhesion and deformation energies per atom in contact with the TiC surface, as reported in Table 4.1. We have considered the adsorption energy and adhesion energy as descriptors for the formation and interaction of the clusters with the support, respectively. Note that, the more negative the value for the adsorption and adhesion energies the strongest the interaction between the Ni cluster and the TiC surface while the more positive the deformation energy the stronger the deformation. The reader interested in how these magnitudes are calculated is referred to Ref 46.

Table 4.1. Adsorption (E_{ads}), adhesion (E_{adh}) and deformation (E_{def}) energies in eV per atom of nickel in direct contact for the different Ni_n clusters. The total number of nickel atoms in direct contact with the surface is given in parentheses. For the sake of simplicity, $Ni_{16,rec}$ values have not been included. Table directly taken from Ref 46.

	E_{ads}	E_{adh}	E_{def}
Ni_4 (4)	-1.76	-2.07	0.31
Ni_9 (9)	-1.16	-1.85	0.69
Ni_{13} (9)	-1.58	-1.99	0.41
Ni_{16} (16)	-0.88	-1.92	1.04
Ni_{29} (16)	-1.41	-2.00	0.59

From Table 4.1 different conclusion can be extracted. For instance, comparing the 2D and 3D clusters separately, the larger the size of the Ni cluster the smaller the adsorption energy. This lowering of the energy when growing in size is more pronounced for the 2D particles than for their 3D counterparts. This first observation can be rationalized because the larger the gas-phase cluster the most stable it is, thus less likely to reorganize and to attach to the surface, which is also evidenced by the higher deformation energy for the larger clusters. The second observation, related with the higher lowering in adsorption energy for the 2D clusters, can be understood as the energy required to reorganize the cluster upon adsorption should be larger for the 2D clusters than for the 3D ones because of the 3D nature of the gas-phase particles. This is confirmed by looking at the deformation energy which is larger for the 2D clusters with the solely exception of the Ni_4 cluster which has not to reorganize that much its structure. Comparing the adsorption energy per atom for similar Ni clusters with previous reported values, it can be seen that Ni clusters adsorbed over non-reducible[51-53] and reducible oxides[55,56] present smaller adsorption energies than the ones we have obtained, which suggest that TiC interact much more strongly with the Ni clusters than other metal oxide supports. Regarding the adhesion energies, it can be seen that the values are very similar for all the Ni_n/TiC systems, which infers that all the clusters interact very similarly with the TiC surface, although the Ni_4 cluster presents a slightly higher adhesion energy, thus interacting strongly with the surface. Interestingly, comparing the 2D clusters with their 3D counterparts, the latter present slightly larger adhesion energies, which suggest that the uppermost Ni atoms also add a small contribution for the interaction with the surface. Compiling all the information from Table 4.1, we suggest that the Ni_4 cluster should be the most stable and easy to form among all the studied systems as it has the largest adhesion and adsorption energies. Similarly, for the cases in which the Ni contact atoms are the same, the 3D clusters should be more stable and easier to form than the 2D counterparts, while stability should be more or less similar regarding the very analogous adhesion energies.

Next, we focus on the effect of the support on the magnetic and electronic properties, which are of great interest for catalysis. We first start by analyzing the spin densities taken as an estimate of the magnetic moment as shown in Table 4.2. In order to disentangle which effects produce the metal-support interaction and the structure reconstruction on the magnetic moment thus obtained, we evaluate the magnetic moment

of three distinct structures, namely, the gas-phase cluster ($\mu_{Ni,g}$), the Ni cluster in the gas-phase but at the equilibrium adsorbed geometry ($\mu_{Ni,eq}$) and the adsorbed Ni cluster ($\mu_{Ni,ads}$).

Table 4.2. Total magnetic moment of Ni_n clusters at the gas-phase nickel ($\mu_{Ni,g}$), at the adsorbed geometry but without being adsorbed ($\mu_{Ni,eq}$) and when adsorbed ($\mu_{Ni,ads}$). Results in parentheses correspond to the average magnetic moment per Ni atom. All results are in Bohr magneton units (μ_B). The calculated value for bulk Ni is 0.65 μ_B, which is close to the experiment value of 0.6 μ_B.[57] Table directly taken from Ref 46.

	$\mu_{Ni,g}$	$\mu_{Ni,eq}$	$\mu_{Ni,ads}$
Ni_4	4.00 (1.00)	5.14 (1.29)	1.85 (0.46)
Ni_9	8.00 (0.89)	8.00 (0.89)	3.52 (0.39)
Ni_{13}	10.00 (0.77)	11.43 (0.88)	4.58 (0.35)
Ni_{16}	12.00 (0.75)	16.06 (1.00)	2.29 (0.14)
$Ni_{16\ rec}$	12.00 (0.75)	16.03 (1.00)	5.50 (0.34)
Ni_{29}	20.00 (0.69)	22.22 (0.77)	10.38 (0.36)

From Table 4.2 one should mention that, for the gas-phase clusters, as expected, the magnetic moment nicely converges to the experimental value of 0.6 μ_B[57] when growing in size. Also, one can spot that, in general, the magnetic moments for the Ni clusters at the adsorbed equilibrium positions are larger than the ones for the gas-phase clusters. This is rationalized as a support structural related effect because after Ni adsorption the Ni clusters adopt conformations in which the coordination number of the Ni clusters are smaller than the ones for the same cluster at the gas-phase. Remarkably the supported Ni clusters exhibit the lowest magnetic moments, which is a clear indication of the significant chemical interaction between the Ni atoms and the TiC support. In fact, this interaction involving a covalent bond between the Ni_{3d} and C_{2p} orbital mixing, is such strong that it is able to quench the increase of magnetic moment induced by the structural change upon adsorption. Interestingly, for the 3D clusters, the atoms that are in direct contact with the support present lower magnetic moments than the uppermost Ni atoms. This is another indication about that the metal-support interactions induces a quenching of the magnetization of the cluster.

Last but not least, to further understand the metal-support interactions we have carried out a Bader charge analysis[58], which enables one to estimate the net charge of both the Ni atoms and the support atoms. Interestingly, we do not find any relevant change on the charges of the atoms indicating that there is not a relevant charge transfer between the cluster and the support. In order to better understand the interaction between the Ni clusters and the TiC support we have computed the density of states and the charge density differences. Particularly, we have calculated the local density of states (LDOS) and the partial density of states (PDOS) for the bare TiC surface and the Ni_n/TiC systems. We have focused on the upper layer of TiC and the overall clusters focusing on the Ti_{3d}, C_{2p} and Ni_{3d} states as shown in Figure 4.3. From Figure 4.3 one can spot that the region near the Fermi level is flatter for the bare TiC surface than for the Ni_n/TiC systems. This increase for the Ni_n/TiC systems is a result of the mixing of the C_{2p}, Ti_{3d} and Ni_{3d} states, which suggests a chemical interaction between the surface and the cluster. Moreover, it can be seen that for the 3D clusters the uppermost nickel layers also mix with the C_{2p} and Ti_{3d} states, although to a lesser extent than the atoms that are in direct contact, which suggest that the highest adhesion energy observed for the 3D clusters is due to an interaction (to a lower extent) of the uppermost layers with the TiC surface.

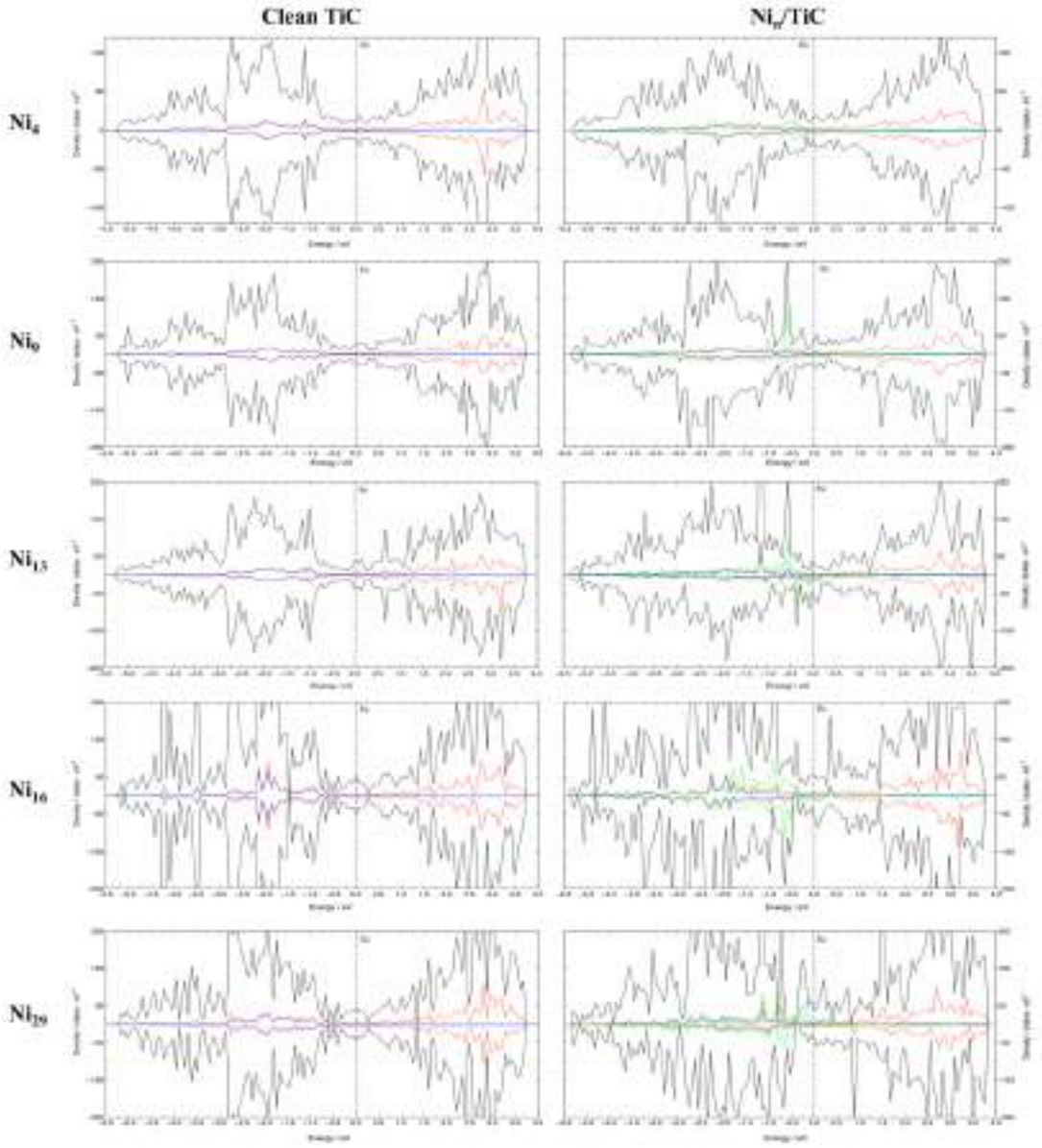

Figure 4.3. Density of states diagram (DOS) for the clean TiC surface and the Ni_n/TiC clusters. Black colour represents the total DOS contribution and red, blue and green colours represent the contribution of the Ti_{3d}, C_{2p} and Ni_{3d} states, respectively. For the 3D clusters light blue and orange colours represent Ni_{3d} states of the second and third layer, respectively. The dashed line represents the Fermi level. Note that we have only considered the contribution of the outermost TiC layer and all the nickel atoms. Figure directly taken from Ref 46.

Finally, in Figure 4.4 we show the charge density difference plot for the different systems, which allows us to further evaluate the metal-support interaction. From Figure 4.4 a clear chemical interaction between the support and the clusters can be seen that polarizes the electron density. It can also be seen a charge accumulation on top of the Ni atoms while there is a charge depletion on the hollow sites. Interestingly, for the 3D structures the uppermost layers have lower charge density accumulation since they interact less with the TiC surfaces as already shown in the DOS analysis. This indicate

that probably the most active clusters are the 2D small clusters as suggested by the experiments.

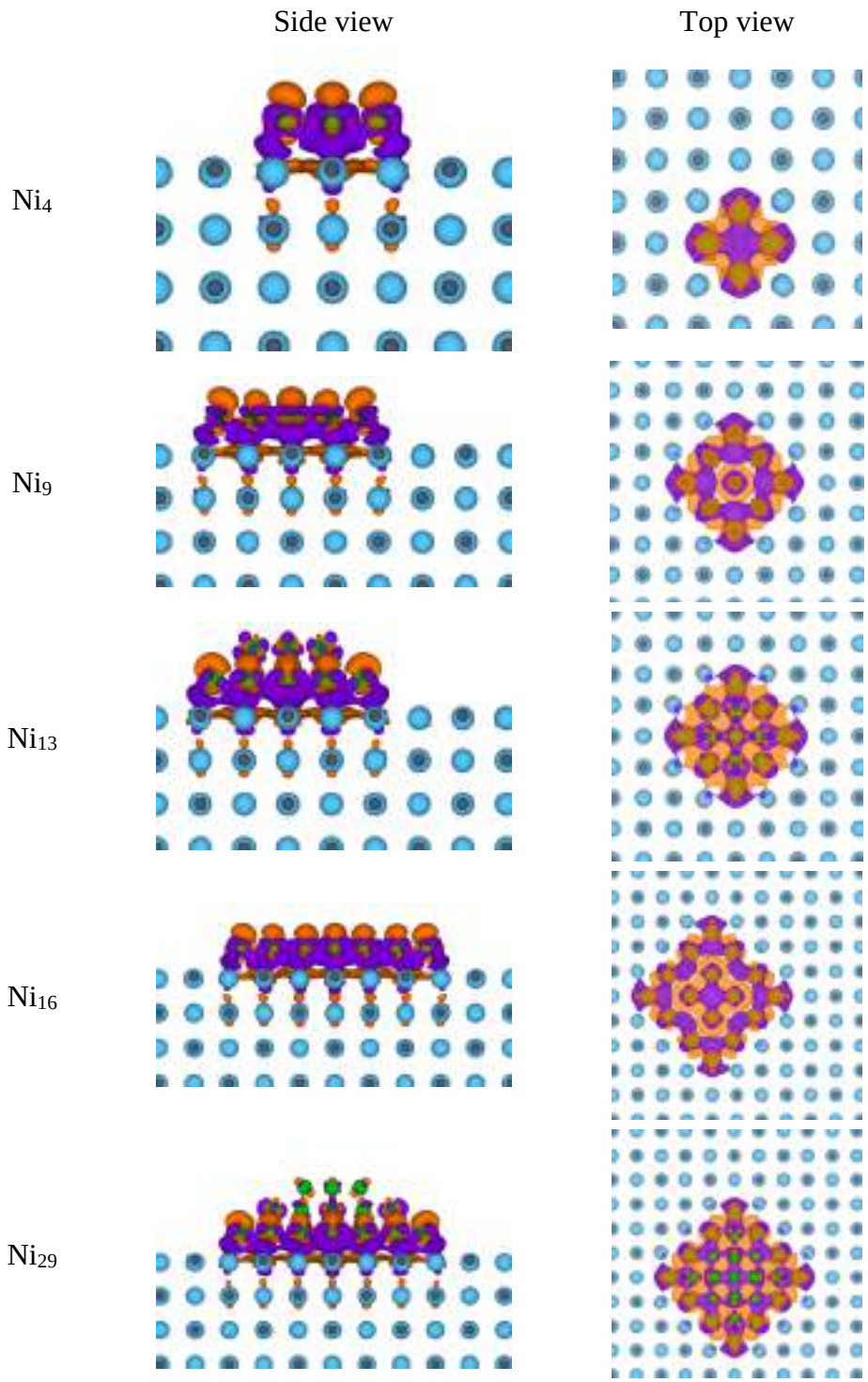

Figure 4.4. Charge density difference maps for Ni_n-TiC. Light blue, grey and green colours are used for titanium, carbon and nickel, respectively. The isosurface is taken as 0.0033 e^-/bohr^3. Orange regions denote accumulation of charge density, while purple regions denote charge density depletion. Figure directly taken from Ref 46.

To sum up, we have investigated the structural, electronic and magnetic properties of several Ni clusters supported over TiC in order to understand how metal-support interactions can affect these systems. From our results, different conclusions have been extracted. We have shown that the smallest Ni_4 cluster exhibit the largest adsorption and adhesion energies, which suggest that this cluster is the easiest to form and the most stable one among the different studied systems. Also, we have seen that the 3D clusters present stronger adsorption energies than their 2D counterparts, which suggest that these clusters should be easier to form due to the lower energy penalty that has to be paid for the deformation of the small clusters upon adsorption. Moreover, we have shown that all the clusters present similar adhesion energies, suggesting a similar stability while the 3D systems feature slightly higher energies due to the interaction of the uppermost Ni layers. Regarding other systems, our results show that Ni clusters supported on TiC present higher adsorption energies than Ni clusters anchored over metal oxides. Last but not least, we have observed a quenching of the magnetic moment of the Ni clusters after adsorption over the TiC surface that suggests a clear interaction between the metal and the support. Finally, the DOS and the density charge difference analysis clearly point to an interaction between the metal and the support, which greatly polarizes the electron density of the Ni cluster, which in the end, could be beneficial for catalysis purposes. In this regard, the atoms in direct contact with the support present higher interactions, which suggest 2D clusters to be more active for catalysis.

4.3.2. CO_2 and H_2 activation on Ni_n/TiC

In the previous section, the formation and stability as well as the metal-support interaction of several Ni clusters supported over TiC have been described. It has been clearly shown that metal-support interactions induce an electron density polarization that can be beneficial for catalysis. Here, we study CO_2 and H_2 activation on four Ni_n/TiC model systems of different sizes and morphologies, namely, Ni_4/TiC, Ni_9/TiC, Ni_{13}/TiC and Ni_{16}/TiC, with results for the bare TiC(001) and Ni (111) surfaces included for comparison. For the different systems we inspect CO_2 and H_2 activation at several adsorption sites. The particular choice of CO_2 and H_2 is because these two molecules are the reactants of the RWGS reaction. The main results for the CO_2 and H_2 adsorption and dissociation are summarized below. The reader interested in more details is referred to ref 47.

4.3.2.1. CO_2 and H_2 adsorption

The calculated H_2 and CO_2 adsorption energies for the most stable configuration of each adsorbate on the Ni_n/TiC, TiC(001) and Ni(111) systems along with structural data are shown in Table 4.3.

Table 4.3. CO_2 and H_2 adsorption energies (including the ZPE term), C-O bond lengths (d_{C-O}), H-H bond lengths (d_{H-H}) and O-C-O bond angles (θ_{O-C-O}), for the most stable adsorbed sites for H_2 and CO_2 over the different surface models. Note that except in Ni_{13}/TiC(001), the Ni supported clusters have a 2D atomic structure. Table directly taken from Ref 47.

	CO_2			
Model	site	E_{ads} / eV	d_{C-O} / Å	θ_{O-C-O} / º
Ni(111)	tNi	-0.15	1.18, 1.18	180
TiC(001)	tC	-0.58	1.29, 1.29	128
Ni_4/TiC(001)	hNi	-1.37	1.35, 1.28	122
Ni_9/TiC(001)	hNi_2	-1.41	1.36, 1.29	119
Ni_{13}/TiC(001)	tNi_3	-0.48	1.24, 1.26	138
Ni_{16}/TiC(001)	hNi_1	-1.49	1.36, 1.29	117
	H_2			
Model	site	E_{ads} / eV	d_{H-H} / Å	
Ni(111) [a]	bNi	-0.02	0.74	
TiC(001)	tM	-0.01	0.74	
Ni_4/TiC(001)	tNi	-0.34	0.83	
Ni_9/TiC(001)	tNi_2	-0.35	0.85	
Ni_{13}/TiC(001)	tNi_1	-0.12	0.83	
Ni_{16}/TiC(001)	tNi_3	-0.42	0.83	

From Table 4.3 it appears that both CO_2 and H_2 molecules adsorb, in general, stronger on the Ni_n/TiC systems than over the bare Ni(111) and TiC(001) surface. CO_2, physisorbs on Ni(111) but chemisorbs on the TiC(001) surface, with adsorption energies of -0.15 and -0.58 eV, respectively. The CO_2 molecule adsorbs on the TiC surface interacting with the C surface atoms, in such a way that it is activated as shown by the increase of the C-O bond lengths and the significant O-C-O bending as shown in Table 4.3. Similar structural patterns have been previously observed for the CO_2 adsorption over TiC[59] and TiC-doped[60],[61] systems. For the case of H_2, physisorption is predicted on both Ni(111) and TiC(001) surfaces with small adsorption energies of -0.02 and -0.01 eV, respectively. Regarding the Ni_n/TiC systems, the electron density polarization induced by

the metal-support interactions appears to be beneficial for the adsorption of both CO_2 and H_2 molecules. This is clearly evidenced from the noticeable increase of the C-O and H-H bond lengths as well as O-C-O bending upon adsorption on the supported Ni clusters (see Table 4.3). Interestingly, as shown in Table 4.3, 2D supported clusters strongly adsorb both molecules. This can be rationalized as for the 2D clusters all the Ni atoms are in direct contact with the surface; thus, suffering a large electron density polarization, which is not the case for the 3D supported clusters. Remarkably, neither CO_2 nor H_2 adsorb at the topmost hollow site of the Ni_{13}/TiC system. Focusing now on the size effect, it can be seen that, in general, all the structures have similar adsorption energies with slightly higher adsorption energies for the largest clusters. This can be understood as the larger the cluster, the better it can adapt its structure after CO_2 or H_2 adsorption with the concomitant system stabilization.

Let us now compare the values we have obtained with previously reported values on similar systems. Before starting the discussion, we want to stress that we have used the BEEF-vdW functional while other studies have used another functionals, either PW91 or PBE. Therefore, we do not aim at a quantitative discussion but rather a qualitative comparison. Regarding the H_2 adsorption, Florez et al.,[62] using the PW91 functional without including dispersion studied the H_2 adsorption over Au_4/TiC and Au_9/TiC and reported adsorption energies of 0.01 and -0.04 eV, respectively. This small interaction contrast with our values of -0.34 and -0.35 eV for the Ni_4/TiC and Ni_9/TiC systems, respectively. In a subsequent work, Gomez et al., [63] also using the PW91 functional without including dispersion studied the H_2 activation on a variety of M_4/TiC systems (M = Pd, Pt, Cu, Ag and Au). They found an almost negligible H_2 adsorption over the Au_4/TiC, Cu_4/TiC and Ag_4/TiC systems but higher values for the Pd_4/TiC and Pt_4/TiC systems, with adsorption energies of -0.70 and -0.87 eV, respectively. In comparison with the value we have calculated for the Ni_4/TiC system it can be seen that our value (i.e., -0.34 eV) lies in between the reported values for the coinage and Pt-group metals, which may suggest that Ni_4/TiC is more active than coinage metal but less active than Pt-group metals. However, for a fair comparison one has also to consider the H_2 dissociation energy barrier (vide infra). Finally, comparing the PBE reported values of Mohsenzadeh et al.[64] for the H_2 adsorption on Ni(111), Ni(100) and Ni(110), with adsorption energies of -0.17, -0.22 and -0.33 eV, respectively, it can be seen that Ni_n/TiC clusters present slightly higher adsorption energies.

For CO_2 adsorption, Vogt et al.,[65] using the PBE functional, studied the Ni(111), Ni(100), Ni(110) and Ni(211) surfaces and found CO_2 adsorption energies of, 0.25, -0.27, -0.43 and -0.41 eV, respectively. Their values are slightly smaller than the ones we have obtained for the TiC(001) and for the 3D supported Ni cluster and far from the ones obtained for the 2D supported Ni clusters, suggesting higher CO_2 activation for the Ni_n/TiC systems. Interestingly, Lopez et al.,[60,61] studied in two different works CO_2 adsorption on doped-TiC(001) surfaces in which a Ti atom was replaced by another metal atom. In their last work they found the largest adsorption energies for the TiC-doped systems, being of -1.10 and -1.22 eV for the Ce- and Sr-doped systems, respectively. Even if their values clearly show the dopant effect on the CO_2 adsorption energy, their values are still slightly lower than the ones we have obtained for the 2D Ni_n/TiC systems, suggesting a higher interaction with the clusters supported on TiC(001). Finally, Rodriguez et al.,[34] using the PBE functional reported CO_2 adsorption energies of -1.11, -0.59, -0.68 and -0.36 eV for the Cu_4/TiC, Au_4/TiC, Cu_9/TiC and Au_9/TiC, respectively, which are also smaller than the ones we have obtained for the 2D Ni_n/TiC systems. This indicate that Ni clusters supported over TiC are more active for the CO_2 adsorption than Cu and Au clusters supported over TiC.

4.3.2.2. CO_2 and H_2 dissociation

Results in the previous section showed that both CO_2 and H_2 are strongly adsorbed over the supported Ni_n clusters. Nevertheless, although a notable adsorption is a necessary step for CO_2 and H_2 conversion, strong adsorption energies do not necessarily correlate with an increased activity and, in fact, too strong adsorption energies can be undesirable. In that sense, one need species that bound with the surface but that at the same time dissociate easily enough, thus involving a small dissociation energy barrier. In Table 4.4 the dissociation energy barriers for both the CO_2 and H_2 molecules on the different systems of interest are summarized.

Table 4.4. CO_2 and H_2 reaction energy ($\Delta E_{r,0}$) and forward and reverse energy barriers ($\Delta E^{\neq}_{fw,0}$ and $\Delta E^{\neq}_{rev,0}$, respectively) over the most probable sites for reaction of the different considered Ni_n/TiC models with Ni(111) and TiC(001) included for comparison. Note that excepting Ni_{13}/TiC(001), the Ni supported clusters have a 2D atomic structure. All energy values were obtained with the BEEF-vdW functional and include the ZPE contribution. C-O and H-H breaking/forming distance of the transition state structure (d_{C-O} and d_{H-H}, respectively). Table adapted from Ref 47.

CO_2					
Model	Reaction	$\Delta E_{r,0}$ / eV	$\Delta E^{\neq}_{fw,0}$ / eV	$\Delta E^{\neq}_{rev,0}$ / eV	d_{C-O} / Å
Ni_4/TiC(001)	$CO_{2,hNi} \rightleftharpoons CO_{hNi} + O_{tTi1}$	0.03	0.55	0.52	1.75
Ni_9/TiC(001)	$CO_{2,hNi} \rightleftharpoons CO_{hNi} + O_{tTi1}$	0.25	0.52	0.27	1.74
Ni_{13}/TiC(001)	$CO_{2,tNi2} \rightleftharpoons CO_{tNi2} + O_{tTi1}$	-0.39	0.83	1.22	1.53
Ni_{16}/TiC(001)	$CO_{2,hNi1} \rightleftharpoons CO_{hNi1} + O_{hNi2}$	-0.68	0.35	1.03	1.92
Ni(111)	$CO_{2,top} \rightleftharpoons CO_{hcp} + O_{fcc}$	-0.57	0.86	1.43	1.84
TiC(001)	$CO_{2,tC} \rightleftharpoons CO_{tC} + O_{hMMC}$	-0.06	1.03	1.08	1.84
H_2					
Model	Reaction	$\Delta E_{r,0}$ / eV	$\Delta E^{\neq}_{fw,0}$ / eV	$\Delta E^{\neq}_{rev,0}$ / eV	d_{H-H} / Å
Ni_4/TiC(001)	$H_{2,tNi} \rightleftharpoons H_{bNi} + H_{bNi}$	-0.60	0.08	0.68	1.36
Ni_9/TiC(001)	$H_{2,tNi1} \rightleftharpoons H_{hNi} + H_{hNi}$	-0.95	0.02	0.97	1.14
Ni_{13}/TiC(001)	$H_{2,tNi1} \rightleftharpoons H_{tNi1} + H_{tNi3}$	-0.51	0.11	0.62	1.11
Ni_{16}/TiC(001)	$H_{2,tNi3} \rightleftharpoons H_{bNi4} + H_{bNi4}$	-0.44	0.07	0.52	1.32
Ni(111)	$H_{2,bNi} \rightleftharpoons H_{fcc} + H_{hcp}$	-0.31	0.28	0.59	0.94
TiC(001)	$H_{2\ tM} \rightleftharpoons H_{tC} + H_{tC}$ [a]	-0.50	1.07	1.57	1.27

[a] Note that this process occurs in two steps, as shown in Ref. [66]. Thus, the energy barrier is calculated with respect to the TS with the highest energy. See Table S3 in the SI for information about the energetics of each of the two-steps.

From Table 4.4 it is clear that the highest dissociation energy barriers for both the CO_2 and H_2 molecules correspond to their dissociation over the clean TiC(001) and Ni(111) surfaces. Moreover, comparing both extended surfaces it can be seen that Ni(111)

presents lower energy barriers than the TiC(001), particularly for the H_2 dissociation, suggesting a higher activity for the Ni(111) surface. Note however, that H_2 dissociation will be limited by the very weak adsorption over both surfaces implying that, for practical purposes, a relatively high H_2 partial pressure is needed. Regarding CO_2 activation, from the DFT results only it is difficult to determine which of the two extended surfaces will be more active, as CO_2 adsorbs strongly over the TiC(001) surface but it has a higher dissociation energy barrier in comparison to the weaker adsorption and lower dissociation energy barrier on the Ni(111) surface.

Focusing on the Ni_n/TiC systems, Table 4.4 shows that the induced electron density polarization due to the metal-support interactions clearly affects the dissociation energy barriers for both H_2 and CO_2, compared to the clean, extended surfaces. The low dissociation energy barriers together to the noticeable adsorption energies make these systems suitable candidates for CO_2 conversion and H_2 hydrogenation reactions. Regarding CO_2 dissociation, it will be preferred on the 2D clusters rather than on the 3D ones with energy barriers of 0.35-0.55 eV vs. 0.83 eV, respectively. Results in Table 4.4 also show that the CO_2 dissociation energy barrier slightly decreases with increasing the cluster size. This energy barrier lowering is rationalized as larger clusters can better adapt its atomic structure with the concomitant stabilization of the system. For the case of H_2, the dissociation energy barrier is very small for all the studied systems with values ranging from 0.02 eV to 0.11 eV, without any drastic change neither for the 2D and the 3D clusters nor when growing in size. These findings suggest that 2D supported clusters are a better option for CO_2 activation while both 2D and 3D supported clusters are equally good candidates for H_2 activation, the 2D ones being preferred due to the higher H_2 adsorption.

Next, we present a comparison of our data with previous studies over similar systems. For instance, Florez et al.[62] using the PW91 functional without including dispersion, studied the H_2 dissociation over Au_4, Au_9 and Au_{13} clusters supported over TiC and reported energy barriers of 0.08, 0.20 and 0.99 eV, respectively. Their reported energy barriers for the 2D systems (i.e., Au_4 and Au_9) are small, like the ones we have reported for these 2D clusters (i.e., 0.08 eV and 0.02 eV, for the Ni_4 and Ni_9 clusters, respectively), pointing to these systems to be good candidates for hydrogenation reactions. However, the lower energy barrier we have found for the Ni_{13}/TiC, contrast with the larger energy barrier they reported for the Au_{13}/TiC (0.11 eV vs. 0.99 eV,

respectively). This suggests that for hydrogenation reactions Ni clusters supported over TiC should be preferred rather than Au clusters as at medium-high coverages 3D clusters are expected to be abundant. In a latter work, Gomez et al.[63] using the PW91 functional, studied the H_2 dissociation on several M_4/TiC (M = Pd, Pt, Cu, Ag and Au) clusters. They reported that the H_2 dissociation energy barrier follows the order Pt > Ag > Pd > Cu > Au with values of 1.16, 0.79, 0.53, 0.37 and 0.08 eV, respectively. From their reported values, we suggest that the Ni_4/TiC system should be more active for hydrogenation reactions as it presents a H_2 dissociation energy barrier as small as the one reported for the Au_4/TiC system, while Ni_4/TiC adsorbs H_2 stronger than Au_4/TiC. Mohsenzadeh et al.[64] using the PBE functional, reported the H_2 dissociation energy barriers on the Ni(111), Ni(100) and Ni(110) surfaces to be 0.03, 0.02 and 0.06 eV, respectively. Their values are very small and like the ones observed for the Ni_n/TiC systems although we suggest that the larger H_2 adsorption over Ni_n/TiC make the latter systems more attractive for hydrogenation reactions.

Regarding the CO_2 activation, Vogt el al.[65] using the PBE functional, studied CO_2 dissociation on the Ni(111), Ni(100), Ni(110) and Ni(211) surfaces and reported values of 0.52, 0.16, 0.40 and 0.93 eV, respectively. Except for the Ni(100) surface, 2D supported clusters present similar or even lower energy barriers than the extended surfaces, and, since Ni_n/TiC systems adsorb CO_2 stronger, we suggest that they are likely to be better catalysts for CO_2 conversion than the extended Ni surfaces, with the exception of the Ni(100) surface in which firm conclusions cannot be extracted. Finally, Rodriguez et al.[34] using the PW91 functional, studied the CO_2 dissociation over the Cu_4/TiC system and reported an energy barrier of 0.81 eV, which is higher than the value of 0.55 eV for the Ni_4/TiC system. Moreover, CO_2 adsorbs stronger on Ni_4/TiC than on Cu_4/TiC with adsorption energies of -1.37 and -1.11 eV, respectively. Therefore, Ni/TiC systems are predicted to be more active towards CO_2 conversion than Cu/TiC systems.

To sum up, we have shown how the electron density polarization that the Ni clusters exhibit upon adsorption over the TiC surface, due to the metal-support interactions, can be beneficial for catalysis purposes. We have shown that Ni_n/TiC systems, in general, adsorb stronger and dissociates easily CO_2 and H_2 than the bare TiC(001) and Ni(111) surfaces. This suggest that Ni_n/TiC systems should be more active than the bare TiC(001) and Ni(111) surfaces for CO_2 and H_2 activation. The present results also point to the supported 2D clusters to be more active than the 3D ones as; in general, 2D clusters

present higher adsorption energies and smaller dissociation energy barriers. We have also shown that larger 2D clusters present slightly higher CO_2 adsorption energies and slightly lower CO_2 dissociation energy barriers while no noticeable differences are observed for the H_2 molecule. These small differences have been rationalized as a better reorganization of large clusters that stabilize the system. Finally, a comparison with previous studies on similar systems suggests that Ni_n/TiC should be more active towards CO_2 and H_2 dissociation. This indeed point to Ni_n/TiC systems to be excellent catalysts for CO_2 conversion and hydrogenation reactions.

4.3.3. Study of the RWGS reaction on the Ni_4/TiC and TiC systems

In Section 4.3.1, for a variety of Ni_n clusters supported over TiC(001), we have studied how their size and morphology affect their stability, formation and metal-support interactions. We have concluded that for all the studied systems there is a metal-support interaction that induces an electron density polarization of the Ni clusters that could be beneficial for catalytic purposes. We have also observed that all supported Ni_n clusters present a similar stability, but the 3D clusters seem to be easier to form than the 2D ones. Nevertheless, among the different studied systems, Ni_4/TiC is the most stable and easiest to form and presents large metal-support interactions. In Section 4.3.2 we have selected some of the previous Ni_n/TiC systems and studied the size and morphology effects on the CO_2 and H_2 activation. We have found that 2D clusters are more active than 3D clusters for the activation of both CO_2 and H_2. From the conclusions extracted from the two previous sections we have decided to use the Ni_4/TiC system as our model system to study the RWGS reaction over Ni/TiC by a multiscale approach. Summing up, we choose this model as the Ni_4 cluster can be easily formed, it is stable and presents good catalytic activity towards the CO_2 and H_2 dissociation reactions. Thus, this can be a good model to explain the experimental observations. The main results of the study for the RWGS reaction on Ni_4/TiC and TiC systems are depicted below and this is organized as follows: first the analysis of the DFT results are presented, then, the discussion of the kMC results for the Ni_4/TiC system is given, and finally, an explanation of why Ni_4/TiC is more active than the TiC system is proposed. The reader interested in more details is referred to Ref 48.

4.3.3.1. DFT results

In order to understand the boost of catalytic activity experimentally observed for the Ni/TiC system with respect to the bare TiC surface for the RWGS reaction, we have calculated the energetics of the different elementary steps that can be involved in the RWGS reaction for the Ni_4/TiC and TiC model systems as shown in Figure 4.5. Note that the Ni_4/TiC system has three distinct regions, namely: the Ni region, the TiC region and the interface region that lies in between these two other regions, with different energetics. In order to clearly understand the experimental observations, we have explicitly calculated the adsorption energy of the different intermediates and the energy barriers for all the considered elementary steps at the three distinct regions. With the energetic of all the different elementary steps, it is possible to construct Gibbs free energy diagrams for the different considered pathways at specific working conditions, and in principle by analyzing them, it is possible to rationalize which could be the most probable mechanism and try to understand the experimental observations.

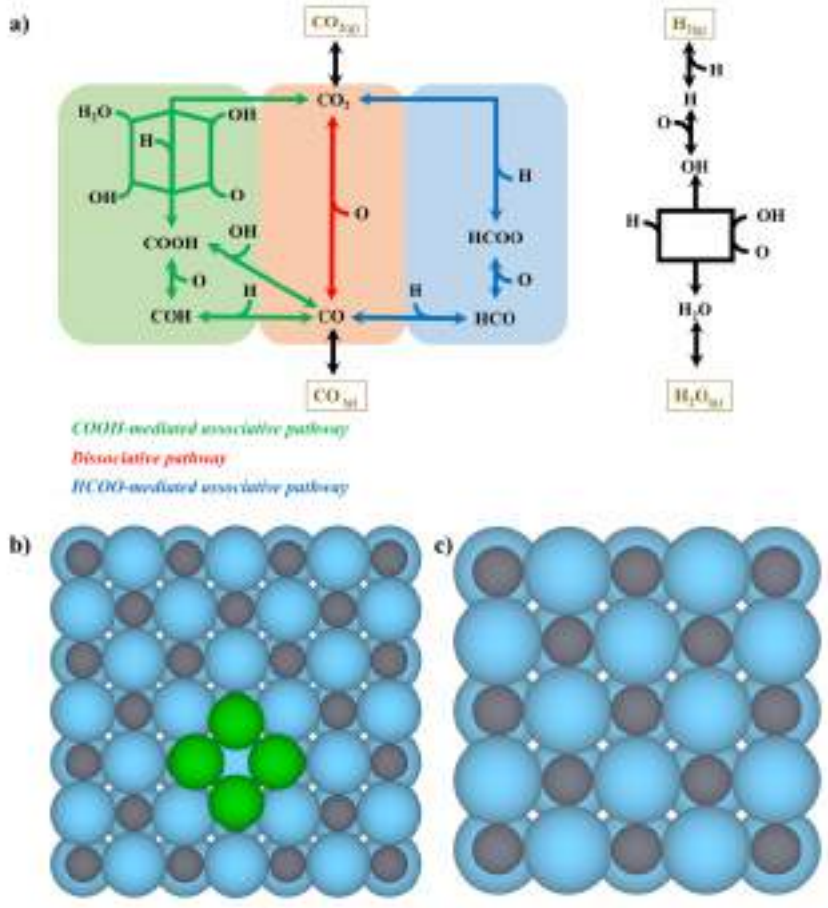

Figure 4.5. a) Possible reaction pathways for the RWGS reaction. b) Unit cell for the Ni_4/TiC surface model used on the DFT calculations. c) Unit cell for the TiC surface model used on the DFT calculations. Grey, light blue and green colors represent C, Ti and Ni atoms, respectively. Figure adapted from ref 48.

From figure 4.5a it can be seen that the RWGS reaction can advance via three different pathways, namely, the dissociative pathway (i.e., CO_2 direct dissociation), the COOH-mediated associative pathway (i.e., COOH formation) and the HCOO-mediated associative pathway (i.e., HCOO formation). The reaction energies and energy barriers of some relevant steps at the three distinct regions are summarized in Table 4.5.

Table 4.5. Reaction energies ($\Delta E_{0,r}$) and forward and reverse energy barriers ($\Delta E_{0,f}^{\neq}$, $\Delta E_{0,r}^{\neq}$) in eV for some processes including the ZPE correction term for the Ni_4/TiC system. Note that reactions have been considered at the different Ni/TiC regions. Table adapted from Ref 48.

Name (Region)	$\Delta E_{0,r}$	$\Delta E_{0,f}^{\neq}$	$\Delta E_{0,r}^{\neq}$
CO_2 dissociation (Ni)	0.03	0.55	0.52
CO_2 dissociation (interface)	-0.15	0.77	0.93
CO_2 dissociation (TiC)	-0.06	1.03	1.08
COOH formation (Ni)	0.44	1.32	0.88
COOH formation (interface)	0.63	0.97	0.34
COOH formation (TiC)	0.51	0.77	0.26
HCOO formation (Ni)	-0.29	0.84	1.13
HCOO formation (interface)	0.41	2.19	1.77
HCOO formation (TiC)	0.37	2.15	1.78
COOH dissociation to CO (Ni)	-0.36	0.27	0.62
COOH dissociation to CO (interface)	-0.47	0.51	0.99
COOH dissociation to CO (TiC)	0.01	0.50	0.49

Let's analyze Table 4.5 and focus first on the two associative mechanisms. From the reported values it appears that one can consider the COOH-mediated mechanism instead of the HCOO-mediated mechanism. This is because, in general, COOH can be formed easily than the HCOO intermediate as the formation of the first is favored over the TiC and interface regions while the formation of the latter is only favored on the Ni region. Now, for each region of the Ni_4/TiC system we focus on the dissociative pathway ($CO_2 \rightarrow CO + O$) and the COOH-mediated associative pathway ($CO_2 + H \rightarrow COOH \rightarrow CO + OH$) as shown in Figure 4.6.

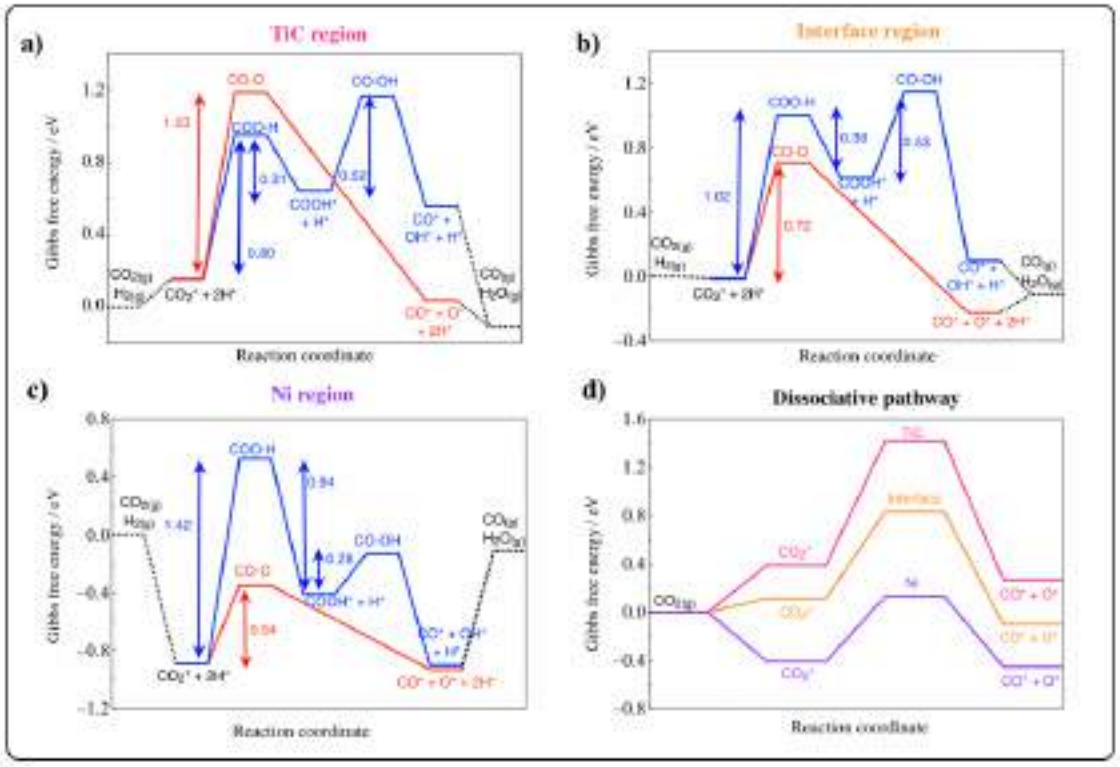

Figure 4.6. Gibbs free energy diagrams at T = 550 K and P(CO_2) = 0.5 bar, P(H_2) = 4.5 bar, P(CO) = 0.001 bar and P(H_2O) = 0.001 bar for the dissociative (red) and the COOH-mediated associative (blue) pathways in a) the TiC region; b) the interface region; and c) the Ni cluster. d) Gibbs free energy profiles for CO_2 adsorption and dissociation over the Ni cluster, the interface region and TiC region (purple, orange, and pink lines, respectively). Figure directly taken from Ref 48.

In the TiC region (see Figure 4.6a) both the dissociative and associative pathway can compete. The dissociative pathway has an energy barrier of 1.03 eV and is a unimolecular reaction. The COOH formation step, despite having a lower energy barrier of 0.80 eV is quite an endothermic reaction with a reverse energy barrier of 0.31 eV, that would favor the COOH dissociation to CO_2 + H rather than dissociation to CO + OH, the latter with an energy barrier of 0.52 eV. Moreover, COOH formation is a bimolecular step, highly dependent on the reactant coverage and in general less likely to occur than unimolecular ones. Overall, we suggest that for the TiC region, the dissociative pathway that involves only a unimolecular reaction will be preferred rather than the COOH-mediated pathway involving a first bimolecular reaction and the subsequent COOH dissociation. For the interface region, the Gibbs free energy diagram (see Figure 4.6b) clearly shows that the dissociative pathway is the dominant one, with an energy barrier of 0.72 eV in contrast with the energy barrier of 1.02 eV for the COOH formation. Similarly, the dissociative pathway is also dominant in the Ni region with an energy

barrier of 0.54 eV compared to the COOH formation energy barrier of 1.42 eV (see Figure 4.6c). From all this information, one would conclude that the dissociative pathway will be the dominant for all the three distinct regions and that the activity will increase in the order TiC < interface < Ni, following the trend of the CO_2 dissociation energy barriers of 1.03, 0.72, and 0.54 eV for the TiC, interface and Ni regions, respectively, as shown in Figure 4.6d. Therefore, from this information one would suggest that the highest activity experimentally observed for the Ni/TiC system compared to TiC is mainly because of the superior ability of the Ni cluster and, to a lower extent of the interface, to dissociate CO_2 compared to the TiC region. Nevertheless, in the next section we will show that this is a largely oversimplified picture.

4.3.3.2. kMC simulations

At first sight one may think that the results of kinetic simulations just complement the DFT results and bring additional details concerning conversion at working conditions of temperatures and pressures. While this may be the case for simple model systems with only one type of active sites and few elementary steps, this is not at all the case for model systems that closely resemble a real catalyst as the one we are studying here. In fact, the present kMC simulations show that almost all CO is produced at the TiC region mainly following the COOH-mediated associative pathway, and the remaining CO is formed at the interface region while no CO is observed on the Ni region as shown in Figure 4.7. These results are in clear contradiction with the dominant reaction mechanism and activity order that arises from the DFT predictions only. These discrepancies between DFT and kMC results are due to coverage effects and site availability as explained in detail below.

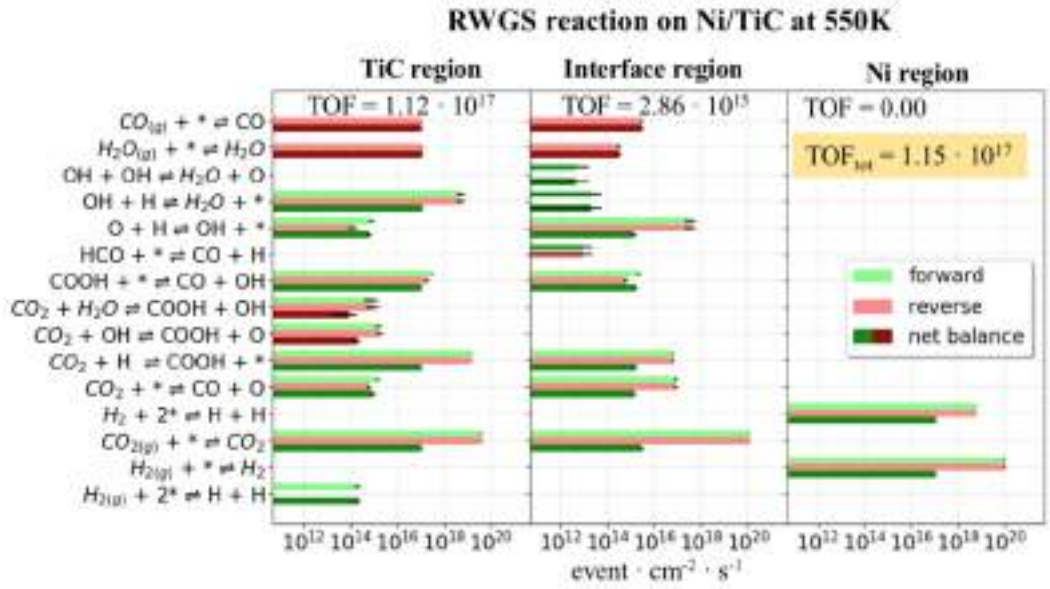

Figure 7. Event frequencies of the RWGS reaction on Ni_4/TiC at T = 550 K and $P(H_2)$ = 4.5 bar and $P(CO_2)$ = 0.5 bar at the different regions. Figure adapted from ref 48.

The main reasons that make the TiC region to be the most active region at steady state conditions is because of the poisoning of both the interface and Ni regions at the initial stage of the simulations as shown in Figure 4.8.

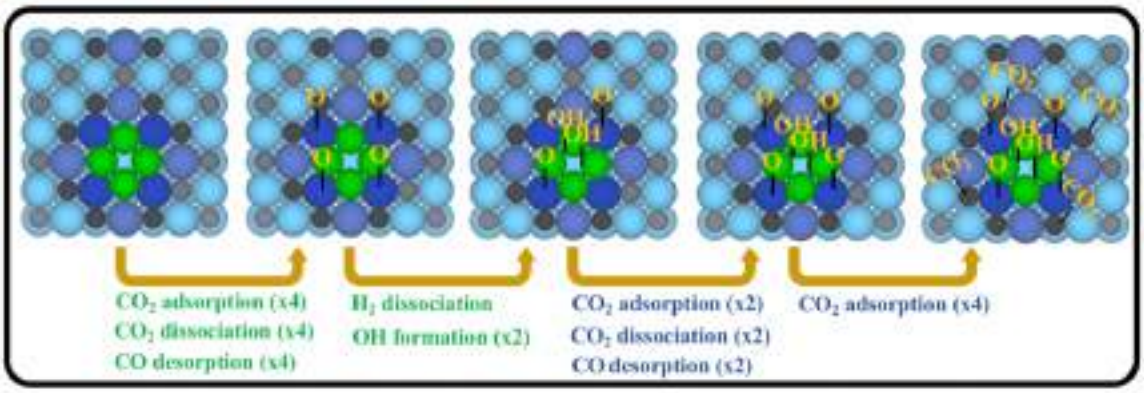

Figure 4.8. Cluster and interface poisoning at the initial stages of the kMC simulations. Figure adapted from ref 48.

At the beginning of the simulations CO_2 adsorbs and dissociates over the Ni cluster, producing O adatoms on the interfacial region and CO on the cluster that further desorbs. Next, H_2 adsorbs and dissociates on the supported Ni cluster to produce H species that hydrogenate the O interfacial atoms to final produce OH species on the Ni cluster. Then, attractive adsorbate-adsorbate interactions between the OH species on the cluster and

neighboring H, CO_2 and O species make the OH + OH → H_2O + O very endothermic, hence extremely difficult to happen with the concomitant cluster poisoning with OH species and, at the same time, hindering the possible adsorption of other species on the cluster. Meanwhile, CO_2 adsorbs and dissociates on the interface region to produce O and CO species at the interface. While the produced CO desorbs, the O adatoms remain at the interface creating a partial poisoning of the interface region. Finally, CO_2 can adsorb over the remaining sites of the interface but it cannot dissociate as the O adatoms are blocking the sites needed for CO_2 dissociation at the interface. The steady state coverages over the different sites are shown in Table 4.6.

Table 4.6. Percentage of site occupancy for the different species that are adsorbed on the surface of the Ni_4/TiC model catalyst at 550 K under steady state conditions. Values of 0.0 represent an occupation lower than 0.05 % while dashes (-) means that these species cannot adsorb at those sites. Table directly taken from Ref 48.

T = 550 K	**Site occupancy (%)**							
Species	**tC**	**tTi**	**tC_{in}**	**$tTi_{in\text{-}1NN}$**	**$tTi_{in\text{-}2NN}$**	**Ni**	**h**	**h_{Ni}**
H_2O*	-	0.1	-	-	0.0	0.0	-	-
COOH*	0.0	0.0	0.0	-	0.0	0.0	-	-
CO*	1.7	-	0.0	-	0.0	0.0	-	-
O*	12.8	-	5.0	89.0	0.1	0.0	-	-
CO_2*	11.9	59.6	49.3	-	98.5	0.0	-	-
OH*	-	0.8	-	-	0.0	0.0	-	-
OH*+OH*	-	-	-	-	-	100.0	-	-
H*	-	-	-	-	-	-	34.8	50.2
H_2*	-	-	-	-	-	-	-	2.4
Total	26.4	60.5	54.3	89.0	98.6	100.0	34.8	52.6

Just by looking at Table 4.6 one can clearly see that at steady state conditions the supported Ni cluster is completely poisoned by OH species while the interfacial sites are partially poisoned by O and CO_2 species. This poisoning is the reason why at steady state conditions the RWGS reaction occurs almost completely at the TiC region contrary to what can be inferred from the DFT results. Interestingly, this phenomenon can only be captured by kMC simulations that naturally accounts for the effect of surface coverage and site availability while cannot be captured only from DFT calculations. One may argue that coverage effects can also be included on the DFT calculations improving the

accuracy of the DFT results. Nevertheless, this becomes unfeasible when the adlayer structure under operating conditions is unknown as the number of combinations of possible adsorbates at different sites is very high.

From a deeper analysis of the event frequency plot under steady state conditions shown in Figure 4.7 it is possible to unravel which is the main mechanism that governs the overall reaction, and which the role of the different regions is, as sketched in Figure 4.9a.

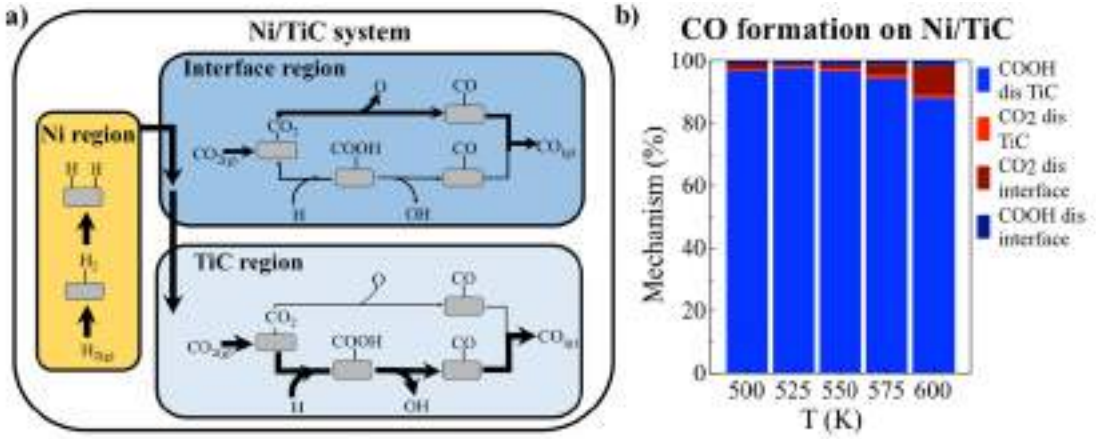

Figure 4.9. a) Scheme of the observed mechanism for Ni_4/TiC model with the role of each region of the catalyst. b) Percentage of the dissociative and COOH-mediated pathways on the final CO production at five different temperatures. Figure adapted from Ref 48.

From Figure 4.9a it can be seen that the role of the Ni region is to adsorb and dissociate H_2 to produce H species that further spillover to the TiC region where the reactivity happens. The interface region produces some CO—either via the dissociative pathway and the COOH-mediated associative pathway—but to a lesser extent than the TiC region where almost all CO is produced, mainly because of the high coverage at the interface region that block available sites as explained above. As shown in Figure 4.9b, at high temperatures the interface region starts to become a little bit more active. This is because the higher the temperature the lower the coverage; thus, less interfacial species blocking available sites with the concomitant increase of the activity in that region. Last but not least, the TiC region is the main contributor of CO, mainly via the COOH-mediated associative pathway due to the high H coverage that facilitates the COOH formation. Moreover, CO_2 species need a free neighboring tC site to dissociate, an unlikely situation due to the high coverage that also favors the COOH-mediated associative pathway. This observation again shows the importance of free available sites

as one must consider free sites as actual reactants involved in the reaction. Finally, it can be seen that most of the water formed during the simulations comes from the hydrogenation of OH formed after COOH dissociation at the TiC region. At this point, one might wonder why Ni_4/TiC is more active than the clean TiC surface if the most active region is the TiC region. This is precisely the aim of the next section.

4.3.3.3. Comparing Ni_4/TiC and TiC activity for the RWGS reaction

From the previous section, it is clear that the most active region of the Ni_4/TiC system is the TiC region, which raises the question of why Ni_4/TiC is then two orders of magnitude more active than TiC. To clearly understand where the differences come from, we have performed kMC simulations for the TiC system as well. In Figure 4.10 one can spot the turnover frequencies for both systems and the experimental ones[34] at different temperatures.

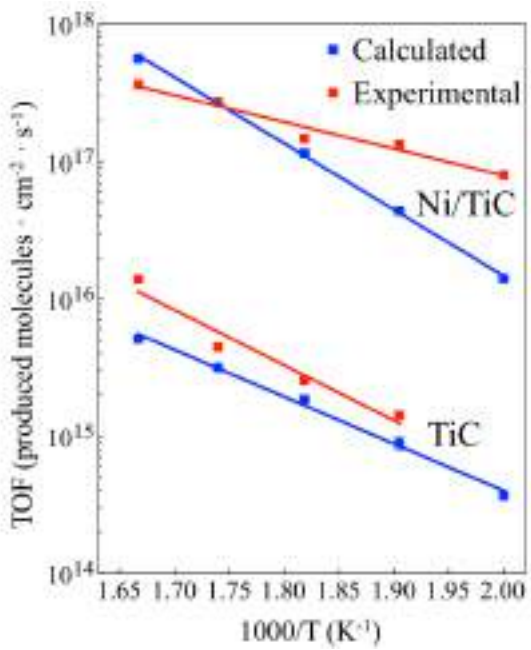

Figure 4.10. Calculated and experimental (from ref. 34) turn over frequencies for the CO production at different temperatures for the TiC and Ni_4/TiC systems. Picture adapted from ref 48.

From Figure 4.10 it can be seen that the calculated and experimental values are in remarkable agreement, meaning that the chemistry of both systems is correctly captured by the present kMC simulations. However, some differences exist between the theoretical model and the experimental system that one may note when aiming at a quantitative comparison. First, the Ni_4/TiC model that we have used in our calculations correspond to

a Ni coverage of 0.14 ML instead of the 0.10 ML used in the experiments. Moreover, in our model all clusters are flat and correspond to a 4 Ni atoms cluster while experimentally it is likely that an ensemble of Ni clusters with different sizes and morphologies exists. Furthermore, additional deviations may arise from the limitation of the kMC method itself, errors in the computed DFT data and the truncation to two-body terms in the cluster expansion, among other limitations. This explain why the agreement between the kMC simulations and the experimental values is just qualitatively correct for the Ni/TiC system while it is excellent for the TiC system. Nevertheless, the agreement is remarkable for both systems and the kMC simulations can properly predict the boost of activity of two orders of magnitude for Ni/TiC with respect to TiC. The reasons of the boost of activity are explained below and the data supporting these conclusions are sketched in Figure 4.11.

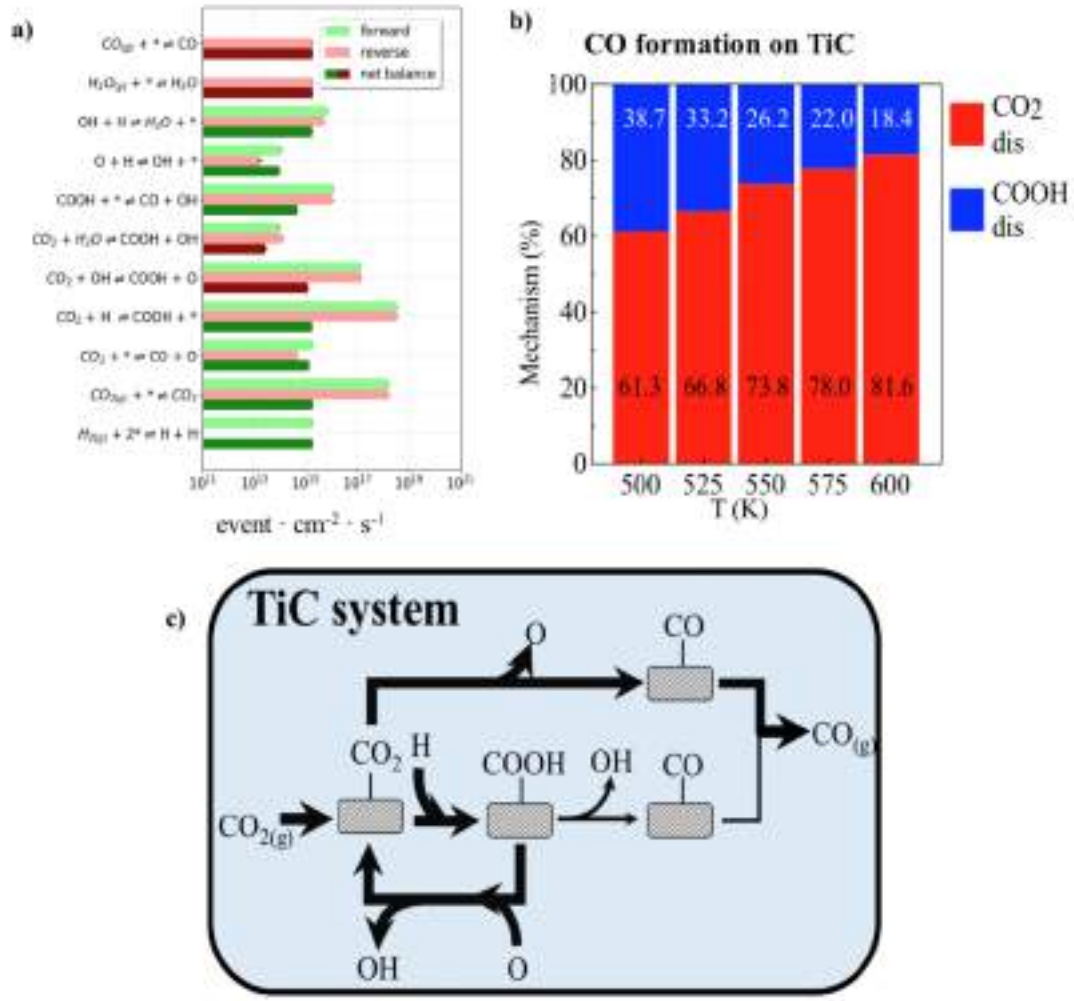

Figure 4.11. a) Event frequencies of the RWGS reaction on the TiC model at T = 550 K and P(H_2) = 4.5 bar and P(CO_2) = 0.5 bar. b) Percentage of the dissociative and COOH-mediated pathways on the final CO production at five different temperatures. c) Scheme of the observed mechanism for the TiC model. Picture adapted from ref 48.

From the event frequency plot shown in Figure 4.11a one can readily see that the dissociative pathway is responsible for most of the CO molecules formed over TiC being even more important as temperature rises (see Figure 4.11b). This agrees with the DFT predictions, and it is in contrast with the TiC region of Ni_4/TiC, in which most of the CO is produced following the COOH-mediated associative pathway. Since the same energy barriers are used for the elementary steps for the clean TiC surface and for the TiC region of Ni_4/TiC, the question is where the calculated and experimental observed differences in catalytic activity come from. The answer again lies in the catalyst surface coverage (see Table 4.7), which plays a fundamental role.

Table 4.7. Percentage of site occupancy for the different species that are adsorbed on the TiC surface at 550 K under steady state conditions. Values of 0.0 represent an occupation lower than 0.05 % while dashes (-) means that these species cannot adsorb at those sites. Table directly taken from Ref 48.

T = 550 K	**Site occupancy (%)**		
Species	**tC**	**tTi**	**h**
CO*	0.0	-	-
O*	46.1	-	-
OH*	-	0.1	-
H_2O*	-	0.1	-
CO_2*	10.0	19.9	-
COOH*	0.2	0.4	-
H*	-	-	0.9
Total	**56.3**	**20.5**	**0.9**

From Table 4.7 it appears that for the bare TiC surface the only species that have a significant coverage are O and CO_2. Comparing the values for the bare TiC surface and the ones for the TiC region of Ni_4/TiC (see Table 4.6) one can spot a similar CO_2 coverage but very different O and H coverages. At 550 K, the O coverage over tC sites decreases from 46 % for TiC to 13 % for Ni_4/TiC, while the H site occupancy on h sites increases from 1 % for TiC to 35 for Ni_4/TiC. These coverages are directly related to the boost of activity observed for the Ni_4/TiC system and the change in the mechanism that drives the overall reaction. The low H coverages on the bare TiC surfaces hinders the COOH formation with the concomitant decrease on the contribution of the COOH-mediated pathway and lowering the total turnover frequency. In spite of this, one can clearly see in Figure 4.11a that the COOH formation step still occurs more times than the CO_2

dissociation step, but in the vast majority of cases it goes backward, while higher H coverage will enhance the probability of COOH to be formed and finally push the COOH dissociation to CO. Moreover, the higher O coverage on the bare TiC surface also contributes to more COOH going backwards to CO_2 due to its reaction with O (i.e., $COOH + O \rightarrow CO_2 + OH$), reducing the amounts of COOH that dissociates and produces CO, and spending time in a side reaction, with the concomitant decrease on the CO production. The direct CO_2 dissociation occurs less frequently (see Figure 4.11a) but it is a much more irreversible reaction, and the net balance is higher for the dissociative pathway than the COOH-mediated pathway. Therefore, as schematically shown in Figure 4.11c, the dominant mechanism that governs the RWGS reaction on the bare TiC surface is the dissociative pathway as already inferred by the DFT calculations. Interestingly, the contribution that each pathway has on the overall mechanism can change with the temperature as shown in Figure 4.11b. For instance, the contribution of the dissociative pathway increases from 61 % at 500 K to 82 % at 600 K. This change is directly related to the coverages as at lower temperatures the coverages of CO_2 and H are higher, hence increasing the contribution of the COOH-mediated associative pathway.

To sum up, we have performed a multiscale study coupling DFT calculations with kinetic Monte Carlo simulations to unravel the boost of activity experimentally observed for the RWGS reaction on Ni/TiC compared to TiC systems. In this regard, we have found a remarkable agreement between the calculated values and the experimental ones and extracted some conclusions for the increase of activity observed for the Ni_4/TiC system. Moreover, we have shown that, to a large extent, the conclusions from the DFT calculations coincide with the results of the kMC simulations for the bare TiC surface. However, for the more complex Ni_4/TiC system we have encountered a completely opposite situation. For the Ni_4/TiC system the DFT predictions suggest that the activity will increase in the order TiC < interface < Ni with the dissociative pathway being the dominant one. Nevertheless, spatially resolved kMC simulations point to the opposite direction, the activity increasing in the order Ni < interface < TiC via the COOH-mediated pathway. The reason of this discrepancy is mainly due to coverage effects not included and not easily to include in the DFT calculations as those change during the course of the reaction. Moreover, kMC simulations show that the boost of activity is because of a synergic effect between the Ni cluster in which H_2 adsorbs and dissociates to produce H that further spillover to the TiC region in which the overall reactivity occurs. This is a

consequence of the poisoning of the Ni and interface regions at the initial stages of the simulations that blocks these sites and forbids the reactivity over the Ni and interface regions, something that cannot be extracted solely from the analysis of the Gibbs free energy profiles. Moreover, we have shown that the surface coverage is key for the boost of activity of the Ni_4/TiC system with respect to the TiC surface. Even though the TiC region for the Ni_4/TiC system is the most active region, the higher H coverage in that region with respect to the clean TiC surface favors the COOH formation with the concomitant increase on the final CO production, also changing the reaction mechanism.

4.4. Summary and conclusions

To summarize, we have thoroughly studied the RWGS reaction over suitable models of the Ni_4/TiC and TiC systems with the goal to understand the experimental observations of the boost of catalytic activity observed for the bifunctional catalyst. In this regard, we have divided our research in three distinct parts going from the most atomistic picture to the macroscopic observables. We have then studied the metal-support interaction of different Ni clusters supported over the TiC(001) surface. We have concluded that 2D clusters present higher metal-support interactions while 3D clusters seem to be easier to form and slightly more stable. Nevertheless, the most stable and easy to form cluster was the Ni_4 clusters which also present large metal-support interactions. Then, in the following study we have analyzed how metal-support interactions, that induce an electron density polarization of the Ni clusters, can affect the CO_2 and H_2 activation. We have found that 2D clusters can adsorb and dissociate easily both molecules; thus, being good candidates for catalytic purposes. In that sense, and with the conclusions extracted from the two previous works, we have decided to use the Ni_4/TiC system as our model system as this cluster is stable, easy to form and very active towards the CO_2 and H_2 dissociation, which are requirements for a system that can explain the experimental observations for the boost of activity observed for the Ni/TiC system. To this end, we have performed a multiscale study coupling DFT calculations to kMC simulations to unravel the increase of catalytic activity experimentally observed. From our DFT results we are not only able to understand why Ni/TiC is more active than TiC but we also stress the importance of performing multiscale studies to clearly understand how the system behaves under working conditions. In this regard, we have shown that DFT predictions for the catalytic activity of the different Ni_4/TiC regions are opposite to the outcome of the kMC

simulations. From the kMC simulations we have understood that the boost of activity is due to a synergic effect between the Ni cluster and the TiC surface. The first, is responsible of the H_2 adsorption and dissociation to produce H that further spillover to the TiC region. Then, in the TiC region the overall reactivity happens, in which CO_2 is hydrogenated to COOH, which finally dissociates to produce CO. We have shown that the inactivity of both the Ni and the interface regions is due to the poisoning of these two regions at the initial stages of the simulation, which shows the importance of coverage and the necessity of preforming kinetic simulations, at least for complex systems, as these conclusions cannot be extracted only from the DFT calculations. We have also shown that the large H coverage is the main responsible for the increase of activity for the Ni_4/TiC system, again something that solely from the DFT calculations it is not possible to know.

4.5. Publications

PCCP

ROYAL SOCIETY OF CHEMISTRY

PAPER

Cite this: *Phys. Chem. Chem. Phys.*, 2020, **22**, 26145

Structural, electronic, and magnetic properties of Ni nanoparticles supported on the TiC(001) surface†

Pablo Lozano-Reis,[a] Ramón Sayós,[a] José A. Rodriguez[b] and Francesc Illas*[a]

Received 15th September 2020,
Accepted 23rd October 2020

DOI: 10.1039/d0cp04884d

rsc.li/pccp

Metals supported on transition metal carbides are known to exhibit good catalytic activity and selectivity, which is interpreted in terms of electron polarization induced by the support. In the present work we go one step further and investigate the effect that a titanium carbide (TiC) support has on the structural, electronic, and magnetic properties of a series of Ni nanoparticles of increasing size exhibiting a two- or three-dimensional morphology. The obtained results show that three-dimensional nanoparticles are more stable and easier to form than their homologous two-dimensional counterparts. Also, comparison to previous results indicates that, when used as the support, transition metal carbides have a marked different chemical activity with respect to oxides. The analysis of the magnetic moments of the supported nanoparticles evidences a considerable quenching of the magnetic moment that affects mainly the Ni atoms in close contact with the TiC substrate indicating that these atoms are likely to be responsible for the catalytic activity reported for these systems. The analysis of the electronic structure reveals the existence of chemical interactions between the Ni nanoparticles and the TiC support, even if the net charge transfer between both systems is negligible.

Introduction

Heterogeneous catalytic processes play an essential role in the chemical industry as over 90% of the chemical manufacturing processes of the world are based on this technology.[1] Catalysis is also at the heart of strategies aimed to mitigate the climate change-emergency that calls for a switch from fossil fuels towards green energies.[2,3] Unfortunately, covering the global energy demand through these new energy sources is still out of reach. Consequently, considerable attention is paid to the catalytic chemical conversion of greenhouse gases such as CO_2 and CH_4 to value-added chemicals of industrial interest, thus creating a cyclic energy economy. Here new heterogeneously catalysed processes are necessary and they are currently the focus of considerable research endeavours.

The most common industrial catalysts are constituted of small to medium size metallic nanoparticles, often from scarce precious elements, anchored on some type of support, usually on metal oxides, sulphides or zeolites.[1] Due to its relatively high activity and low cost compared to noble metals, Ni-based catalysts are extensively used for CO_2 hydrogenation reactions leading to CO, CH_4 or methanol.[4–9] Ni catalysts are also used in the steam and dry reforming reaction of methane.[10–15] These catalysts usually involve nickel nanoparticles supported over different metal oxides.[4–15] In principle, the role of the support goes to disperse the metallic nanoparticles and thus to increase the effective surface area. However, there is increasing evidence that the role of the support goes well beyond this simple picture. There is compelling evidence that the metal support interactions can be detrimental as in the so-called strong metal support interactions (SMSI) introduced by Tauster.[16–18] These were finally understood as capping of the metal nanoparticles by support islands as a result of prolonged exposure at high temperature thus leading to a concomitant decrease in the number of active sites. There is also evidence that the metal–support interactions can be beneficial as shown by Bruix *et al.*[19] for the water gas shift reaction (WGSR) on a model catalyst consisting of Pt nanoparticles supported on ceria and by Klyushin *et al.*[20] for the CO oxidation on Au supported catalyst. However, one must advert that carbides interact with metals much stronger than oxides with the direct formation of a strong bond between the Ni particle and the TiC support (see below) that produces noticeable electronic perturbations on the supported particle. Precisely, the intricate interplay between the metal and the support has been recently shown through extensive kinetic Monte Carlo simulations on the water gas shift reaction on Au nanoparticles supported on MoC that

[a] *Departament de Ciència de Materials i Química Física & Institut de Química Teòrica i Computacional (IQTCUB), Universitat de Barcelona, C. Martí i Franquès 1, Barcelona 08028, Spain. E-mail: francesc.illas@ub.edu*
[b] *Department of Chemistry, Brookhaven National Laboratory, Upton, New York, 11973-5000, USA*

† Electronic supplementary information (ESI) available. See DOI: 10.1039/d0cp04884d

highlighted the role played by every part of the catalyst.[21] The number of cases evidencing a possible active role of the support is increasingly growing and it is now clear that metal support interactions can be used to tune a specific activity and selectivity.[22] Clearly, this requires a detailed description of the mechanism of the catalytic reaction that includes both metal and support. In this sense, a complete understanding of the metal–support interactions is necessary to fully exploit this phenomenon and many research articles focus precisely on the properties of nickel nanoparticles supported on metal oxides.[23–31]

In principle, when designing novel catalysts, metal–support interactions can be used to modify the chemical properties and the dispersion of a metal, but it is necessary to use supports which are truly active in the binding of the metal. Among the possible materials that can be used as supports in catalysis, transition metal carbides (TMCs)[32] have emerged as a good alternative (*vide infra*) to oxide surfaces, which usually need defects or O vacancies to interact well with a dispersed metal. TMCs have long attracted the attention of the catalysis community, since these materials combine physical properties of three different classes of materials. They present the extreme hardness particular to covalent solids, the excellent electric and thermal conductivities of a metal and the high melting points usual of ionic crystals.[32,33] TMCs have been proposed as alternative catalysts to noble metals because they display catalytic activities similar to or even better than Pt-group metals.[34–37] These materials are also increasingly investigated in electrocatalysis, both in the hydrogen evolution[38–41] and oxygen reduction[42] reactions. As mentioned above, TMCs have been rather recently introduced as possible supports for metallic nanoparticles displaying good activity and selectivity. In particular, Au nanoparticles supported on TiC, but also Cu and Ni supported on TiC and on other TMCs such as MoC and Mo_2C have been shown to possess excellent activity in desulfurization processes,[43–47] O_2 dissociation,[48–50] H_2 dissociation,[51] CH_4 dissociation,[52] CO_2 hydrogenation[53,54] and WGSR.[21] It is worth emphasizing that Ni nanoparticles on TiC have shown good activity for CO_2 conversion,[55] although many details of the mechanism remain unknown, starting with the effect of the TiC support on the atomic and electronic properties of the Ni nanoparticles. This, at variance with other cases that have been previously studied,[56–58] introduces new aspects related to the magnetic properties arising from incomplete 3d shells. Ni nanoparticles are attracting a lot of attention for the hydrogenation of CO_2 because, in addition to being non-expensive, depending on their size and interaction with the support they can yield CO, CH_4, higher alkanes or methanol as the main reaction product. Thus, one has a system which can be catalytically tuned in terms of activity and selectivity.

In the present work, we investigate the interaction between nickel nanoparticles and a TiC support and compare the previous studies focusing on other metallic nanoparticles on the same TiC support. We also compare the present results with those reported previously for nickel nanoparticles supported on metal oxides. From this comparison, new features emerge that may help to develop new and more efficient catalysts for greenhouse gas conversion. In particular, the choice of magnetic nanoparticles turns out to be especially useful as it is revealed that the metal atoms at the interface are likely to be responsible for the catalytic activity that has been reported for these systems.

Computational details and surface models

The interaction between different types of two-dimensional (2D) and three-dimensional (3D) Ni nanoparticles and the TiC(001) surface has been investigated by means of density functional theory (DFT)-based calculations applied to suitable periodic models that are described in detail below.

All calculations have been performed using the Vienna ab initio simulation package (VASP) code[59–61] where the valence electron density is expanded in a plane wave basis set and the atomic cores are represented by the projector augmented wave (PAW) method.[62] The BEEF–vDW exchange correlation functional,[63] which includes non-local correlation and dispersion effects, has been chosen since several benchmark studies[63–65] have shown that it provides a better agreement with the available experimental data than other typical functionals. Except for the bare TiC surface model, spin-polarization is always taken into account, a requirement due to the existence of magnetic moments in the nickel atoms arising from its incomplete occupation of the 3d shell.

The TiC(001) surface has been modelled by a slab supercell model including four atomic layers. In the past, a slab of this thickness has been shown to be useful for studying the interaction of metals and molecules with the TiC(001) substrate.[49,66] Depending on the size of the supported Ni nanoparticles, different supercell sizes have been used to avoid interactions between periodically repeated nickel nanoparticles. In a similar way, a vacuum width of at least 12 Å has been used to minimize spurious interactions between periodically repeated slabs in the perpendicular direction to the surface. In all calculations, a cut-off energy of 415 eV has been used for the plane wave expansion, while the size of the Monkhorst–Pack[67] *k*-point mesh used for sampling the first Brillouin zone has been varied, adapting to the size of the slab supercell as explained below. The electronic energy convergence criterion has been selected to be 10^{-5} eV, while the geometry optimization (ionic relaxation) has been iterated until all forces acting on atoms were smaller than 0.01 eV $Å^{-1}$. For all the calculations nickel nanoparticles were allowed to fully relax in the geometry optimization calculations, while the number of titanium carbide layers able to relax varied depending on the surface size.

Five different slab models consisting of a titanium carbide surface with adsorbed nickel nanoparticles have been considered. These include three 2D nickel nanoparticles (Ni_4, Ni_9 and Ni_{16}) and two 3D (Ni_{13} and Ni_{29}) nickel nanoparticles; for, the smallest (Ni_4), medium (Ni_9 and Ni_{13}) and largest (Ni_{16} and Ni_{29}) supported nickel nanoparticles are considered in the present work. Several sites were explored for the supported particles with Ni atoms on top of Ti, on top of Ti–Ti bridge sites and on top of C, the latter being the most stable, as expected, with the final structures obtained being

in line with other theoretical and experimental observation for Au nanoparticles supported on TiC.[46,47] Note that the focus here is on the electronic properties of the supported clusters similar to those that are observed by STM, thus neglecting dynamic aspects that can lead to sintering. This is no doubt an important issue that is out of the scope of the present work.

The TiC(001) surface has been modelled with 3×3, 4×4 and 5×5 TiC supercells, respectively. The Monkhorst–Pack[67] k-point meshes used in the calculations were $(5 \times 5 \times 1)$, $(3 \times 3 \times 1)$ and $(1 \times 1 \times 1)$ for the small, medium and large supercells, respectively. For the small and medium size models the two bottom layers have been kept fixed in their bulk positions, while for the larger slabs the three bottom layers have been kept fixed. This is justified as the calculations for the small and medium supercells do not show significant relaxation of the subsurface atomic layers. The remaining outermost layers and the nickel nanoparticles have been allowed to fully relax during the geometry optimization calculations. The calculations for the isolated Ni_n nanoparticles were carried out placing the nanoparticles in an asymmetric box at the Γ-point. The dimensions of the boxes are $(11 \times 12 \times 13)$ Å^3, $(13 \times 14 \times 15)$ Å^3 and $(17 \times 18 \times 19)$ Å^3 for the smallest, medium and the largest nanoparticles, respectively. The choice of an asymmetric box is to ensure that the orbital filling does not involve dealing with near degeneracies. Yet, one must be aware that switching occupied and virtual orbitals can lead to a nearly degenerate electronic state. The initial geometries used for the gas-phase nickel nanoparticles are those reported as the most stable in previous works.[68,69] Note that whenever two different geometries are reported for a given nanoparticle, two calculations have been carried out to obtain the most stable nanoparticle. For a better rationalization of the metal–support interactions, pertinent density of states (DOS) calculations have been done using the smearing method proposed by Methfessel–Paxton[70] with a denser k-point mesh. Finally, a charge density difference analysis has been carried out by means of the VESTA software;[71] this turns out to be an excellent way to quantify charge transfer between the metal and the support.

Several different properties related to the gas-phase and adsorbed nanoparticles have been investigated. First, we consider the cohesive energy (E_{coh}) of the gas-phase Ni_n nanoparticles defined as in eqn (1),

$$E_{coh} = \frac{E_{Ni_n}}{n} - E_{Ni} \quad (1)$$

where E_{Ni_n} is the energy of the gas-phase Ni_n nanoparticle and E_{Ni} is the energy of the isolated nickel atom in the gas-phase. The adsorption energy (E_{ads}) of the Ni_n nanoparticles has been calculated as in eqn (2),

$$E_{ads} = E_{Ni_n\text{–}TiC} - E_{Ni_n} - E_{TiC} \quad (2)$$

where $E_{Ni_n\text{–}TiC}$ is the energy of the supercell containing the nickel nanoparticle adsorbed on the TiC surface and E_{TiC} is the energy of the relaxed pristine TiC(001) surface. Note that with this definition, the more negative E_{ads}, the stronger the interaction. Finally, the adhesion energy (E_{adh}) is calculated as follows:

$$E_{adh} = E_{Ni_n\text{–}TiC} - E_{Ni_n,optgeom} - E_{TiC,optgeom} \quad (3)$$

where $E_{Ni_n,optgeom}$ and $E_{TiC,optgeom}$ are the energies of the isolated nickel nanoparticle and of the isolated surface both at the optimized geometry upon adsorption, respectively. Here, as for E_{ads}, the more negative E_{adh}, the stronger the interaction. It is worth pointing out that the adhesion energy is normally reported per unit area assuming that the interaction is merely due to the atoms in direct contact with the surface. Here, we report the adhesion energy per number of nickel atoms in direct contact; thus, representing the same magnitude. Note that the adhesion energy could be described also as

$$E_{adh} = E_{ads} - E^{def}_{Ni_n} - E^{def}_{TiC} = E_{ads} - E^{def} \quad (4)$$

where $E^{def}_{Ni_n}$ and E^{def}_{TiC} are the deformation energy of the Ni_n nanoparticle and the deformation energy of the TiC carbide surface upon adsorption; the sum of the two contributions is denoted as E^{def}. For comparison, the adsorption, adhesion and deformation energies will be reported normalized per atom in contact with the surface.

Results and discussions

Gas-phase Ni_n nanoparticles were optimized using previously available data as initial guesses[68,69] and whenever two different structures were reported, optimization of both structures was done to obtain the optimum structure. The most stable gas-phase nanoparticles are presented in Fig. 1 and structural details are given in the ESI.† The results show that even the smallest gas-phase nickel nanoparticles adopt a 3D conformation. This is not always observed for all the transition metals as it is known that small Cu and Au clusters exhibit a planar conformation.[56,68] The cohesive energies of all gas-phase nickel nanoparticles are summarized in Table 1, where values for fcc bulk Ni are included for comparison. In fact, the calculated bulk cohesive energy agrees with the experimental value,[72]

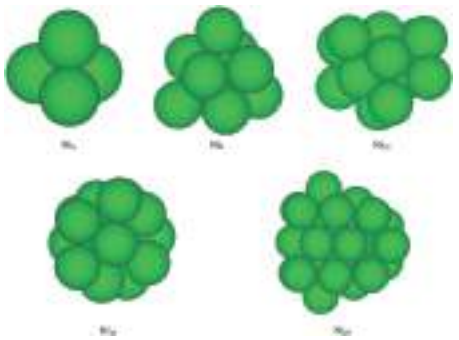

Fig. 1 Atomic structures of the most stable gas-phase Ni_n nanoparticles.

Table 1 Calculated cohesive energy (E_{coh}) of gas-phase Ni_n nanoparticles, Ni bulk and experimental Ni bulk value

Structure	E_{coh}, eV per atom
Ni_4	−1.88
Ni_9	−2.56
Ni_{13}	−2.75
Ni_{16}	−2.85
Ni_{29}	−3.13
Ni bulk	−4.28
Ni bulk, experimental[72]	−4.44

Table 2 Total magnetic moment of Ni_n nanoparticles at the gas-phase nickel ($\mu_{Ni,g}$), at the adsorbed geometry but without being adsorbed ($\mu_{Ni,eq}$) and when adsorbed ($\mu_{Ni,ads}$). Results in parentheses correspond to the average magnetic moment per Ni atom. All results are in bohr magneton units (μ_B). The calculated value for bulk Ni is 0.65 μ_B, which is close to the experimental figure of 0.6 μ_B.[72]

	$\mu_{Ni,g}$	$\mu_{Ni,eq}$	$\mu_{Ni,ads}$
Ni_4	4.00 (1.00)	5.14 (1.29)	1.85 (0.46)
Ni_9	8.00 (0.89)	8.00 (0.89)	3.52 (0.39)
Ni_{13}	10.00 (0.77)	11.43 (0.88)	4.58 (0.35)
Ni_{16}	12.00 (0.75)	16.06 (1.00)	2.29 (0.14)
$Ni_{16,reconstructed}$	12.00 (0.75)	16.03 (1.00)	5.50 (0.34)
Ni_{29}	20.00 (0.69)	22.22 (0.77)	10.38 (0.36)

which is in line with previous results obtained using the GGA, meta-GGA and hybrid density functionals.[73,74] Moreover, as expected, the cohesive energy nicely converges to the bulk value with the nanoparticles increasing in size. Another important property of the Ni nanoparticles is their magnetic moment, which is reported in the leftmost column of Table 2. The total magnetic moment increases with the number of Ni atoms, as expected. A more interesting magnitude is the magnetic moment per Ni atom; this is the largest for the smallest Ni_4 cluster but converges quite fast towards the bulk values. The convergence to the bulk value is because the larger the average coordination number, the lower the average magnetic moment, and as the gas-phase nanoparticle grows, the average coordination number increases. As expected, the calculated magnetic moments are in good agreement with previous studies[68,69] since the gas-phase geometries were already very similar.

In general, the deposition of a metal particle on a support could induce modifications in its structure as a consequence of strong metal–support interactions, which might overcome the effects of metal–metal bonding. In our study, the metal–support interaction has been studied for the five different nickel nanoparticles already described, which ranges from small to medium experimental sizes, adopting 2D and 3D morphologies. The reason for this particular choice is that experimental evidence shows that at low coverage, transition metal nanoparticles adsorbed over TMCs tend to acquire planar structures, while for larger coverage they become 3D.[47,50] The structure of the adsorbed nanoparticles is displayed in Fig. 2 and reported in the ESI.† In all cases the Ni nanoparticles adsorb with the metal atoms above the C atoms of the TiC support, acquiring a distorted morphology but exhibiting clearly (001) facets. The smallest nanoparticles are flat, in line with the shape observed for small Au–TiC and Cu–TiC,[45,47,48,56,57] and as the size increases they become 3D as observed for the Au–TiC system.[47,50] In particular, the Ni_{16} nanoparticle has two metastable atomic configurations with a difference of 0.05 eV in the total energy difference only. One of the isomers exhibits a square shape and (001) facets and the structure of the second one can be

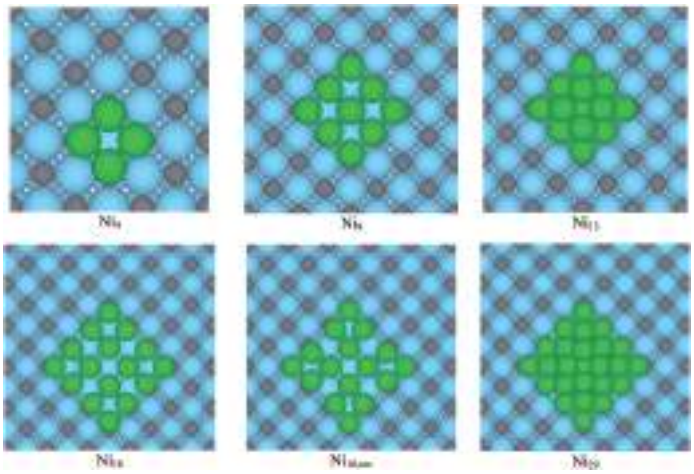

Fig. 2 Ni_n nanoparticles adsorbed over the (001) titanium carbide surface. Light blue, grey and green colours are used for titanium, carbon and nickel, respectively. Note that Ni_{13} and Ni_{29} are 3D nanoparticles.

understood as the aggregation of four Ni_4 nanoparticles; hereafter this second structure will be denoted as $Ni_{16,rec}$. Therefore, the structures of Ni nanoparticles supported on TiC do not follow the trend observed for metal oxide supports such as ZrO_2, TiO_2, CeO_2 and MgO, where 3D structures have been reported even for small nanoparticles,[23–25,28–31] with the bottom nickel atoms interacting mostly with the oxygen atoms of the surface. Nevertheless, Mao *et al.*[31] did not find remarkable stability differences for the Ni_4 flat and Ni_4 3D nanoparticles adsorbed over CeO_2, though the 3D nanoparticle was found to be the most stable.

Next, we discuss the adsorption, adhesion and deformation energies per atom in contact with the surface as defined in the previous section and summarized in Table 3. Note that with this definition we consider that the Ni atoms in direct contact with the TiC surface are those contributing mainly to the adsorption and adhesion of the overall nanoparticle. From Table 3 it can be seen that the greater the number of Ni atoms in similar structures (2D or 3D), the lower the adsorption energy. Besides, a more pronounced change in the adsorption energy when increasing the size of the nanoparticles is found for the 2D structures than for the 3D structures. The first observation could be rationalized because the larger the gas-phase nanoparticle, the more stable it is with a concomitant decrease on the bonding capability. On the contrary, the smaller the nanoparticle, the larger its bonding capability. The second observation could be understood as the energy required to reorganize the nanoparticle structures being larger for the 2D nanoparticles than that for the 3D. Compared to other metals on TiC, the calculated adsorption energy per atom for the Ni_4 nanoparticle is lower than those of Pd_4 and Pt_4 on TiC but higher than those of Cu_4, Ag_4 and Au_4 on TiC reported by Gomez *et al.*,[75] which nicely follows the trend that Pt-group metals adsorb stronger on TiC than Au-group elements. Note that the adsorption energies calculated by Gomez *et al.*[75] using the GGA (PW91) functional are relative to the gas-phase rhombus structure, while our calculations are with respect to the tetrahedral structure. This could lead to a slightly lower Pd_4–TiC adsorption energy, since the most stable structure in the gas-phase is also tetrahedral.[68] It is also interesting to compare the effects of the substrates. To this end, we compare our calculated adsorption energies for nickel nanoparticles on TiC with those reported for similar Ni nanoparticles supported on metal oxides. A first noticeable difference is that the interaction of Ni nanoparticles with the TiC support is stronger than those reported for non-reducible oxides such as MgO. Giordano *et al.*[28] reported an adsorption energy of the tetrahedral Ni_4 nanoparticle on MgO(001) of −1.17 eV per atom; somewhat smaller values were reported by Di Valentin *et al.*[29] for the square planar Ni_4 and the 3D Ni_9 nanoparticles adsorbed over MgO(001), −0.28 and −0.48 eV per atom, respectively. The same trend is found for the tetrahedral Ni_4 nanoparticle adsorbed over ZrO_2, which is also a non-reducible oxide; the reported adsorption energy was −0.47 eV per atom.[25] Not surprisingly, the adsorption energy becomes larger for a reducible oxide since charge-transfer between the particle and the adsorbate becomes chemically favoured. Thus, Mao *et al.*[31] and Wang *et al.*[26] found that the adsorption energies of the flat and tetrahedral Ni_4 nanoparticles adsorbed over CeO_2 and TiO_2 were −1.34 and −1.00 eV per atom, and −1.43 and −1.02 eV per atom, respectively. Note that, for a better comparison, all the literature values discussed above have been normalized with respect to the number of Ni atoms that are in contact with the oxide surface. As can be seen from Table 3, the interaction between Ni nanoparticles and TiC per Ni atom in contact with the surface is even larger than for reducible oxides.

Regarding the adhesion energy values presented in Table 3, no marked differences are observed for the different nanoparticle sizes, meaning that the different nanoparticles interact similarly with the surface, although Ni_4 is the one that has the strongest interaction, and hence the highest adhesion energy. Interestingly, for the cases where the Ni nanoparticle has the same number of contact atoms with the surface, namely Ni_9 and Ni_{13} or Ni_{16} and Ni_{29}, the larger nanoparticle has a slightly higher adhesion energy, which could be explained because the uppermost atoms add a small contribution to the interaction with the surface. Concerning the deformation energies, note also that, according to eqn (4), it contains two contributions. The major contribution to the deformation energy is mostly related to the gas-phase nickel nanoparticle, while the TiC surface is almost not deformed. The differences in the deformation energy contribution of the Ni nanoparticles with respect to the nanoparticle size are larger than for the adhesion energies. From Table 3 it appears that the Ni_4 nanoparticle is the one with the smallest deformation energy. This is because, when going from the gas-phase tetrahedral conformation to the adsorbed rhombohedral conformation, the structural change implies one atom only. For the larger nanoparticles the number of atoms that have to be reorganized is also larger, and hence the deformation energy increases. Comparing the nanoparticles with the same number of contact atoms, the 3D nanoparticles have lower deformation energies. Again, this is because the number of atoms that have to be reorganized is smaller than in the 2D nanoparticles. Compiling all the information from Table 3 it is concluded that the Ni_4 nanoparticles should be the most stable and the easiest to form nanoparticles on top of the TiC surface because they exhibit the largest adhesion and adsorption energies. Similarly, for those nanoparticles, which are different in size but contain the same number of atoms in contact with the surface, the 3D ones are more stable and easier to form because of the highest adhesion and adsorption energies. This has implications for the modelling and also to understand the results of the experiments for CO_2

Table 3 Adsorption (E_{ads}), adhesion (E_{adh}) and deformation (E_{def}) energies per atom of nickel in direct contact for the different Ni_n nanoparticles. The total number of nickel atoms in direct contact with the surface is given in parentheses. For the sake of simplicity, $Ni_{16,rec}$ values have not been included

	E_{ads}, eV per atom	E_{adh}, eV per atom	E_{def}, eV per atom
Ni_4 (4)	−1.76	−2.07	0.31
Ni_9 (9)	−1.16	−1.85	0.69
Ni_{13} (9)	−1.58	−1.99	0.41
Ni_{16} (16)	−0.88	−1.92	1.04
Ni_{29} (16)	−1.41	−2.00	0.59

hydrogenation on Ni nanoparticles supported on TiC.[55] The variations in the structural properties of the Ni particles open the possibility of different ways to bind and activate CO_2, which could lead to different reaction products in the hydrogenation process (*e.g.*, CO, CH_4, higher alkanes or methanol).

To complete the study, we focus now on the effect that the support has on the magnetic properties of the Ni nanoparticles. The interest here is because, in principle, any catalytic reaction involving radical species can be affected by a change in the spin alignment and magnetic properties of a metal centre. To disentangle

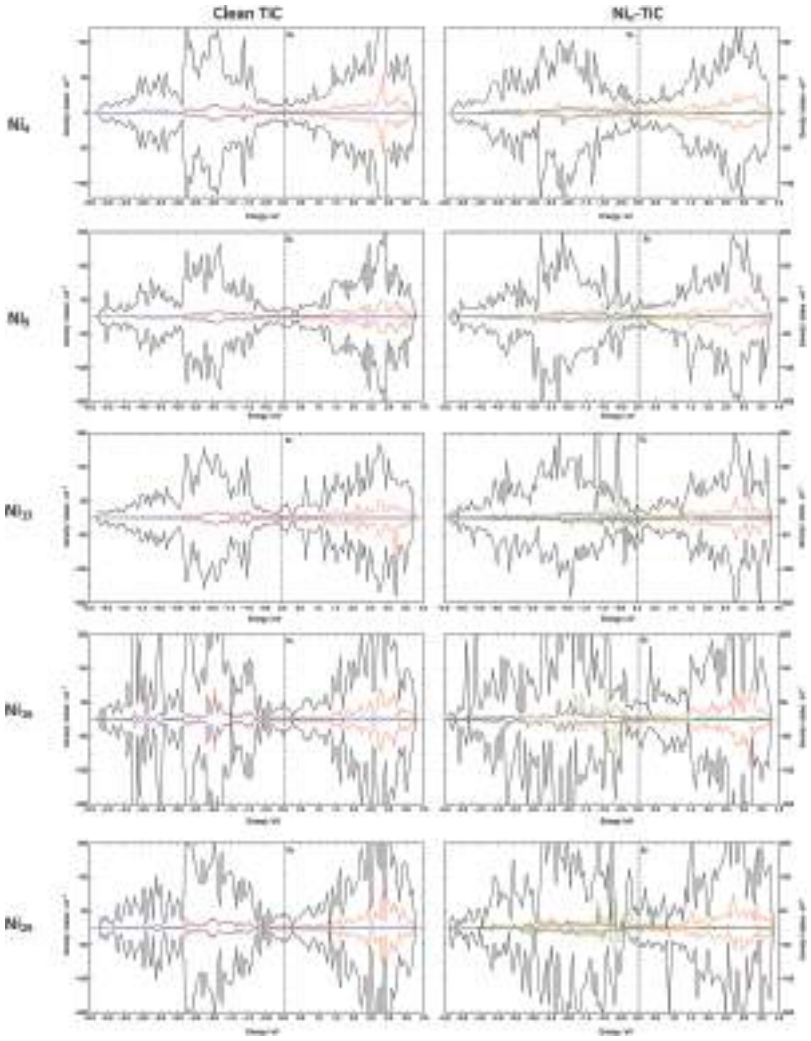

Fig. 3 Density of states diagram for the clean TiC surface and the Ni_n–TiC systems. Black colour represents the total DOS contribution and red, blue and green colours represent the contributions of the Ti_{3d}, C_{2p} and Ni_{3d} states, respectively. For the 3D nanoparticles light blue and orange colours represent Ni_{3d} states of the second and third layers, respectively. The dashed line represents the Fermi level. Note that we have only considered the contribution of the outermost TiC layer and all the nickel atoms.

the support and structural effects we consider the magnetic moments of three different structures; the gas-phase Ni nanoparticle ($\mu_{Ni,g}$), the Ni nanoparticle in the gas-phase but at the adsorbed geometry ($\mu_{Ni,eq}$), and the Ni nanoparticle adsorbed over the surface ($\mu_{Ni,ads}$). The trend for the gas-phase nanoparticles has already been discussed and we just recall that the magnetic moment per atom converges quite rapidly to the calculated bulk value, which is also close to the experimental value of 0.6 μ_B.[72] Table 2 shows that, in general, the magnetic moments of the Ni nanoparticles at the equilibrium adsorption structures ($\mu_{Ni,eq}$) are quite high compared with the corresponding values in the gas-phase equilibrium geometry ($\mu_{Ni,g}$). This support-effect can be easily rationalized because the coordination number of the Ni nanoparticles at the supported geometry is smaller than for the gas-phase structure. Remarkably, the supported Ni nanoparticles exhibit the lowest magnetic moments ($\mu_{Ni,ads}$). This is a clear indication of a chemical interaction between the Ni nanoparticle and the support. This interaction, involving covalent bonding through Ni(3d) and C(2p) orbital mixing, is strong enough to quench the increase of magnetic moment induced by the structural change upon adsorption. As seen for the other cases, the larger the adsorbed nanoparticle, the lower the magnetic moment per atom as the average coordination number of the nickel atoms increases. Note also that the Ti and C surface atoms of the TiC substrate do not exhibit any magnetic moment, and this does not change upon adsorption of the nickel nanoparticles. Interestingly, the coordination number effect is also observed when comparing the Ni_{16} and $Ni_{16,rec}$ nanoparticles, the former exhibiting a higher average coordination number and also a lower magnetic moment. Finally, it is also interesting to point out that for the 3D nanoparticles, the uppermost atoms have a larger magnetic moment, while for the atoms in direct contact this is lower. This is in agreement with the above mentioned conclusion that the metal–support interaction induces a quenching of the magnetization of the supported nanoparticle. This conclusion contrasts with the findings of previous studies for Ni nanoparticles supported on MgO(001). Giordano *et al.*[28] found that the magnetic moment per atom of the tetrahedral Ni_4 nanoparticle supported over MgO was 1.0 μ_B, the same observed for the gas-phase species. Later on, Di Valentin *et al.*[29] reported a magnetic moment for the flat Ni_4 and 3D Ni_9 nanoparticles adsorbed over MgO to be 1.40 and 0.89 μ_B, again the same as in the gas-phase nanoparticles. The fact that the values reported for Ni nanoparticles supported on MgO are higher than the present ones for similar nanoparticles supported on TiC is a clear indication of the existence of a chemical interaction between the Ni nanoparticles and the TiC surface, which is not present when the support is MgO, where the leading interactions are electrostatic with an expected contribution of dispersion.

To further understand the metal–support interaction we have carried out a Bader analysis[76] and computed the net charge for the Ni atoms in the nanoparticle as well as for the atoms in the support. Interestingly, there are no relevant changes in the net charges indicating that there is no noticeable charge transfer between the Ni nanoparticles and the TiC. A similar result was encountered long ago for the interaction of Au nanoparticles with the TiC surface; no clear sign of charge transfer but a clear polarization of the Au nanoparticle electron density produced by the support that has a clear fingerprint in the C(1s) X-ray photoemission spectra.[56] To further analyse the nature of the interaction between the Ni nanoparticles and the TiC support we have also obtained the density of states (DOS) and charge density difference plots. In particular, a local density of states (LDOS) and partial density of states (PDOS) have been carried out for the clean TiC surface and the Ni_n–TiC systems.

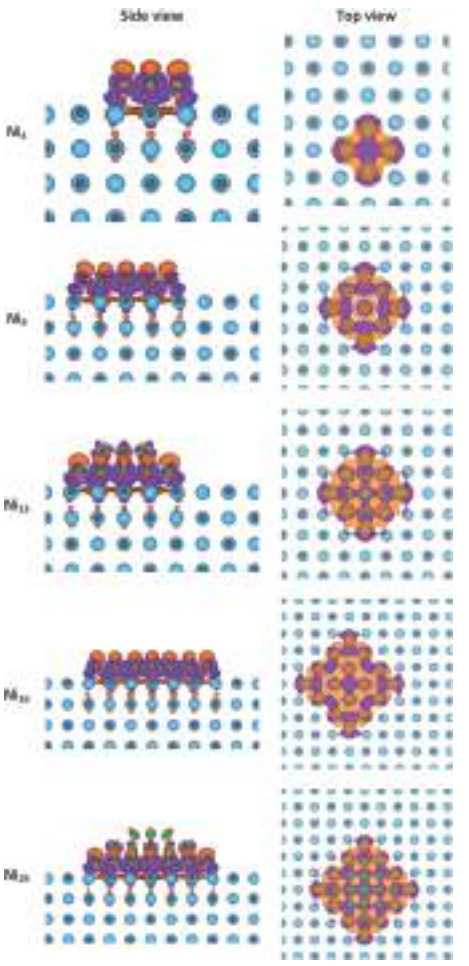

Fig. 4 Charge density difference maps for Ni_n–TiC. Light blue, grey and green colours are used for titanium, carbon and nickel, respectively. The isosurface is taken as 0.0033 e^- $bohr^{-3}$. Orange regions denote accumulation of charge density, while purple regions denote charge density depletion.

On the calculations we have considered the upper layer of the titanium carbide surface and the overall nickel nanoparticles focus on the Ti_{3d}, C_{2p} and Ni_{3d} states, as summarized in Fig. 3. From Fig. 3 the region near the Fermi level for the clean TiC is flatter than when the nanoparticle is adsorbed because there are some Ni_{3d} populated states around this region. Moreover, for the Ni_n–TiC systems there are some pronounced peaks near the Fermi level, which are related to a mixing of the C_{2p}, Ti_{3d} and Ni_{3d} states; thus showing a chemical interaction between the nanoparticles and the surface. Furthermore, for the 3D nanoparticles it could be seen that the uppermost nickel atoms also mix with the C_{2p} and Ti_{3d} states, although to a lesser extent than the interfacial atoms. This confirms that the higher interaction in the 3D nanoparticles is due to the additional contribution of Ni atoms in the uppermost atomic layers.

Finally, we have performed a charge density difference analysis to evaluate the metal–support interaction, which is reported in Fig. 4. The charge difference is defined as

$$\rho = \rho_{Ni_n\text{-TiC}} - \rho_{Ni_n,\text{optgeom}} - \rho_{TiC,\text{optgeom}} \quad (5)$$

where $\rho_{Ni_n\text{-TiC}}$, $\rho_{Ni_n,\text{optgeom}}$ and $\rho_{TiC,\text{optgeom}}$ are the electron densities of the adsorbed nanoparticle over the surface, the isolated nanoparticle at the optimum adsorption geometry and the titanium carbide surface at the optimum adsorption geometry, respectively. From Fig. 4 it could be seen that for all the nanoparticles there is an accumulation of charge density on top of the nickel atoms, while there is charge depletion on the hollow sites. There is a clear chemical interaction even if the net charge transfer is negligible. Moreover, for the 3D structures the uppermost layers have lower charge density accumulation, since they interact less with the surface as shown in the DOS diagrams. As a matter of fact, it could be seen that the third layer of the Ni_{29} structure is almost non-perturbed by the titanium carbide surface. This is in agreement with previous works indicating that the catalytic activity of metals on TiC is due to the presence of flat and small supported nanoparticles.[44–52]

Conclusions

Metals supported on transition metal carbides are known to exhibit good catalytic activity and selectivity in a rather large list of reactions. For metals such as Cu and Au, the increased catalytic activity has been attributed to the polarization of their electron densities in response to the presence of the underlying carbide.[47,51,77] However, in the case of magnetic nanoparticles the available information is almost nonexistent. To fill this gap in our understanding of catalysts based on metals supported on transition metal carbides we investigated in detail the effect that a TiC support has on the structural, electronic, and magnetic properties of Ni nanoparticles. By means of periodic DFT calculations using suitable supercells, three two-dimensional (Ni_4, Ni_9 and Ni_{16}) and two three-dimensional (Ni_{13} and Ni_{29}) nanoparticles of increasing size have been selected as representative examples.

The obtained results plus a detailed comparison to earlier studies involving other metals on the TiC support or Ni nanoparticles on other supports allowed us to reach a series of firm conclusions. First, the smallest Ni_4 nanoparticles exhibit the largest adsorption and adhesion energies. The great stability of these supported nanoparticles together with the large adsorption energies indicates that these are likely to be abundant in Ni/TiC systems prepared by vapor deposition;[55] a conclusion which is in agreement with the prediction that such small Ni nanoparticles supported on TiC are active for methane dissociation even at room temperature.[52] Second, the three-dimensional nanoparticles are more stable and easier to form than their homologous two-dimensional counterparts. Third, Ni_4 and Ni_9 appear to interact with the TiC substrate stronger than, as reported for, non-reducible and reducible oxides such as MgO and CeO_2, respectively. Additionally, for the Ni_4–TiC nanoparticle we have confirmed the trend that Pt-group nanoparticles adsorb stronger than Au-group nanoparticles over TiC surfaces. Finally, we presented evidence that, while the distortion of the structure of the supported nanoparticles induced by the support increases the average magnetic moment per Ni atom, the overall result is a considerable quenching of the magnetic moment. This is a feature not observed in nickel nanoparticles supported on MgO and a clear indication of the presence of chemical interaction between the Ni nanoparticles and the TiC support. This is confirmed by the analysis of the three-dimensional nanoparticles, where the largest magnetic moment corresponds to atoms in the uppermost layers. The fact that the magnetic moment in the uppermost layers remains as in the isolated nanoparticle indicates that the chemical activity of these atoms is almost not affected by the presence of the TiC support and that the active sites will be those at the interface, thus giving support to previous studies focusing on this type of model. The DOS and the charge density difference analysis also reveal the existence of chemical interactions between the Ni nanoparticles and the TiC support, even if the net charge transfer between the two systems is negligible.

The reported results have been obtained for a TiC support but, in view of the similarity in the electronic structures of other transition metal carbides with 1:1 stoichiometry and rock-salt crystal structure, it is likely that the present findings will apply to systems composed of other magnetic nanoparticles and different transition metal carbides, which also have implications in the catalytic properties of the resulting systems. Furthermore, from these results, it is clear that a carbide support can be quite useful to modify the chemical properties and the dispersion of a metal, while designing novel catalysts.

Conflicts of interest

There are no conflicts of interest to declare.

Acknowledgements

The research at the Universitat de Barcelona has been supported by the Spanish Ministry of Science, Innovation and Universities (MICIUN) through grants RTI2018-094757-B-I00,

RTI2018-095460-B-I00, MCIU/AEI/FEDER, UE and MDM-2017-0767, and in part, by the Generalitat de Catalunya (grant 2017SGR13). The work carried out at the Brookhaven National Laboratory (BNL) was supported by the U.S. Department of Energy, Office of Science and Office of Basic Energy Sciences under contract No. DE-SC0012704. P. L.-R. acknowledges MICIUN for a predoctoral FPU18/02313 grant. F. I. acknowledges additional support from the 2015 ICREA Academia Award for Excellence in University Research. Computational resources provided by Consorci de Serveis Universitaris de Catalunya (CSUC, former CESCA) and Red Española de Supercomputación at the Barcelona Supercomputing Center (grants QS-2020-1-0003 and QS-2020-2-0009) are gratefully acknowledged.

References

1 J. M. Thomas and W. J. Thomas, *Principles and Practice of Heterogeneous Catalysis*, VCH, Weinheim, 1997.
2 F. Barbir, *Energy*, 2009, **34**, 308–312.
3 I. Dincer, *Renewable Sustainable Energy Rev.*, 2000, **4**, 157–175.
4 M. A. A. Aziz, A. A. Jalil, S. Triwahyono, R. R. Mukti, Y. H. Taufiq-Yap and M. R. Sazegar, *Appl. Catal., B*, 2014, **147**, 359–368.
5 F. Ocampo, B. Louis, L. Kiwi-Minsker and A.-C. Roger, *Appl. Catal., A*, 2011, **392**, 36–44.
6 G. Zhou, H. Liu, K. Cui, H. Xie, Z. Jiao, G. Zhang, K. Xiong and X. Zheng, *Int. J. Hydrogen Energy*, 2017, **42**, 16108–16117.
7 S. Hwang, U. G. Hong, J. Lee, J. H. Baik, D. J. Koh, H. Lim and I. K. Song, *Catal. Lett.*, 2012, **142**, 860–868.
8 L. Yang, L. Pastor-Pérez, S. Gu, A. Sepúlveda-Escribano and T. R. Reina, *Appl. Catal., B*, 2018, **232**, 464–471.
9 F. Sun, C. Yan, Z. Wang, C. Guo and S. Huang, *Int. J. Hydrogen Energy*, 2015, **40**, 15985–15993.
10 Y. Wang, L. Yao, Y. Wang, S. Wang, Q. Zhao, D. Mao and C. Hu, *ACS Catal.*, 2018, **8**, 6495–6506.
11 S. Ali, M. M. Khader, M. J. Almarri and A. G. Abdelmoneim, *Catal. Today*, 2020, **343**, 26–37.
12 K. Delgado, L. Maier, S. Tischer, A. Zellner, H. Stotz and O. Deutschmann, *Catalysts*, 2015, **5**, 871–904.
13 M. M. Barroso-Quiroga and A. E. Castro-Luna, *Int. J. Hydrogen Energy*, 2010, **35**, 6052–6056.
14 K. Lertwittayanon, W. Youravong and W. J. Lau, *Int. J. Hydrogen Energy*, 2017, **42**, 28254–28265.
15 M. García-Diéguez, I. S. Pieta, M. C. Herrera, M. A. Larrubia and L. J. Alemany, *J. Catal.*, 2010, **270**, 136–145.
16 S. J. Tauster, S. C. Fung and R. L. Garten, *J. Am. Chem. Soc.*, 1978, **100**, 170–175.
17 S. J. Tauster, S. C. Fung, R. T. K. Baker and J. A. Horsley, *Science*, 1981, **211**, 1121–1125.
18 S. J. Tauster, *Acc. Chem. Res.*, 1987, **20**, 389–394.
19 A. Bruix, J. A. Rodriguez, P. J. Ramírez, S. D. Senanayake, J. Evans, J. B. Park, D. Stacchiola, P. Liu, J. Hrbek and F. Illas, *J. Am. Chem. Soc.*, 2012, **134**, 8968–8974.
20 A. Y. Klyushin, T. E. Jones, T. Lunkenbein, P. Kube, X. Li, M. Hävecker, A. Knop-Gericke and R. Schlögl, *ChemCatChem*, 2018, **10**, 3985–3989.
21 H. Prats, S. Posada-Pérez, J. A. Rodriguez, R. Sayós and F. Illas, *ACS Catal.*, 2019, **9**, 9117–9126.
22 T. W. van Deelen, C. H. Mejía and K. P. de Jong, *Nat. Catal.*, 2019, **2**, 955–970.
23 A. Cadi-Essadek, A. Roldan and N. H. de Leeuw, *Faraday Discuss.*, 2018, **208**, 87–104.
24 A. Cadi-Essadek, A. Roldan and N. H. de Leeuw, *Fuel Cells*, 2017, **17**, 125–131.
25 J. Yang, J. Ren, H. Guo, X. Qin, B. Han, J. Lin and Z. Li, *RSC Adv.*, 2015, **5**, 59935–59945.
26 Y. Wang, Y. Su, M. Zhu and L. Kang, *RSC Adv.*, 2015, **5**, 16582–16591.
27 A. Markovits, M. K. Skalli, C. Minot, G. Pacchioni, N. López and F. Illas, *J. Chem. Phys.*, 2001, **115**, 8172–8177.
28 L. Giordano, G. Pacchioni, A. M. Ferrari, F. Illas and N. Rösch, *Surf. Sci.*, 2001, **473**, 213–226.
29 C. Di Valentin, L. Giordano, G. Pacchioni and N. Rösch, *Surf. Sci.*, 2003, **522**, 175–184.
30 J. Carrasco, L. Barrio, P. Liu, J. A. Rodriguez and M. V. Ganduglia-Pirovano, *J. Phys. Chem. C*, 2013, **117**, 8241–8250.
31 Z. Mao, P. G. Lustemberg, J. R. Rumptz, M. V. Ganduglia-Pirovano and C. T. Campbell, *ACS Catal.*, 2020, **10**, 5101–5114.
32 H. H. Hwu and J. G. Chen, *Chem. Rev.*, 2005, **105**, 185–212.
33 L. E. Toth, *Transition Metal Carbides and Nitrides*, Academic, New York, 1971.
34 R. B. Levy and M. Boudart, *Science*, 1973, **181**, 547–549.
35 I. Kojima, E. Miyazaki, Y. Inoue and I. Yasumori, *J. Catal.*, 1979, **59**, 472–474.
36 C. Jimenez-Orozco, E. Flórez, F. Viñes, J. A. Rodriguez and F. Illas, *ACS Catal.*, 2020, **10**, 6213–6222.
37 J. A. Rodriguez, P. J. Ramírez and R. A. Gutierrez, *Catal. Today*, 2017, **289**, 47–52.
38 W.-F. Chen, J. T. Muckerman and E. Fujita, *Chem. Commun.*, 2013, **49**, 8896.
39 F. Harnisch, G. Sievers and U. Schröder, *Appl. Catal., B*, 2009, **89**, 455–458.
40 D. Ham, R. Ganesan and J. Lee, *Int. J. Hydrogen Energy*, 2008, **33**, 6865–6872.
41 S. Wirth, F. Harnisch, M. Weinmann and U. Schröder, *Appl. Catal., B*, 2012, **126**, 225–230.
42 A. Ignaszak, C. Song, W. Zhu, J. Zhang, A. Bauer, R. Baker, V. Neburchilov, S. Ye and S. Campbell, *Electrochim. Acta*, 2012, **69**, 397–405.
43 P. Liu and J. A. Rodriguez, *J. Chem. Phys.*, 2003, **119**, 10895–10903.
44 J. A. Rodriguez, P. Liu, Y. Takahashi, F. Viñes, L. Feria, E. Florez, K. Nakamura and F. Illas, *Catal. Today*, 2011, **166**, 2–9.
45 L. Feria, J. A. Rodriguez, T. Jirsak and F. Illas, *J. Catal.*, 2011, **279**, 352–360.
46 J. A. Rodriguez, P. Liu, Y. Takahashi, K. Nakamura, F. Viñes and F. Illas, *J. Am. Chem. Soc.*, 2009, **131**, 8595–8602.
47 J. A. Rodriguez, P. Liu, F. Viñes, F. Illas, Y. Takahashi and K. Nakamura, *Angew. Chem.*, 2008, **120**, 6787–6791.
48 J. A. Rodriguez, P. Liu, J. Dvorak, T. Jirsak, J. Gomes, Y. Takahashi and K. Nakamura, *J. Chem. Phys.*, 2004, **121**, 465–474.

49 F. Viñes, C. Sousa, F. Illas, P. Liu and J. A. Rodriguez, *J. Phys. Chem. C*, 2007, **111**, 16982–16989.
50 J. A. Rodríguez, L. Feria, T. Jirsak, Y. Takahashi, K. Nakamura and F. Illas, *J. Am. Chem. Soc.*, 2010, **132**, 3177–3186.
51 E. Florez, T. Gomez, P. Liu, J. A. Rodriguez and F. Illas, *ChemCatChem*, 2010, **2**, 1219–1222.
52 H. Prats, R. A. Gutiérrez, J. J. Piñero, F. Viñes, S. T. Bromley, P. J. Ramírez, J. A. Rodriguez and F. Illas, *J. Am. Chem. Soc.*, 2019, **141**, 5303–5313.
53 J. A. Rodriguez, P. Liu, D. J. Stacchiola, S. D. Senanayake, M. G. White and J. G. Chen, *ACS Catal.*, 2015, **5**, 6696–6706.
54 A. B. Vidal, L. Feria, J. Evans, Y. Takahashi, P. Liu, K. Nakamura, F. Illas and J. A. Rodriguez, *J. Phys. Chem. Lett.*, 2012, **3**, 2275–2280.
55 J. A. Rodriguez, J. Evans, L. Feria, A. B. Vidal, P. Liu, K. Nakamura and F. Illas, *J. Catal.*, 2013, **307**, 162–169.
56 J. A. Rodriguez, F. Viñes, F. Illas, P. Liu, Y. Takahashi and K. Nakamura, *J. Chem. Phys.*, 2007, **127**, 211102.
57 E. Florez, L. Feria, F. Viñes, J. A. Rodriguez and F. Illas, *J. Phys. Chem. C*, 2009, **113**, 19994–20001.
58 S. Posada-Pérez, F. Viñes, J. A. Rodríguez and F. Illas, *J. Chem. Phys.*, 2015, **143**, 114704.
59 G. Kresse and J. Hafner, *Phys. Rev. B: Condens. Matter Mater. Phys.*, 1993, **47**, 558–561.
60 G. Kresse and J. Furthmüller, *Phys. Rev. B: Condens. Matter Mater. Phys.*, 1996, **54**, 11169–11186.
61 G. Kresse and J. Furthmüller, *Comput. Mater. Sci.*, 1996, **6**, 15–50.
62 G. Kresse and D. Joubert, *Phys. Rev. B: Condens. Matter Mater. Phys.*, 1999, **59**, 1758–1775.
63 J. Wellendorff, K. T. Lundgaard, A. Møgelhøj, V. Petzold, D. D. Landis, J. K. Nørskov, T. Bligaard and K. W. Jacobsen, *Phys. Rev. B: Condens. Matter Mater. Phys.*, 2012, **85**, 235149.
64 J. Wellendorff, T. L. Silbaugh, D. Garcia-Pintos, J. K. Nørskov, T. Bligaard, F. Studt and C. T. Campbell, *Surf. Sci.*, 2015, **640**, 36–44.
65 C. T. Campbell, *Acc. Chem. Res.*, 2019, **52**, 984–993.
66 F. Viñes, C. Sousa, P. Liu, J. A. Rodriguez and F. Illas, *J. Chem. Phys.*, 2005, **122**, 174709.
67 H. J. Monkhorst and J. D. Pack, *Phys. Rev. B: Solid State*, 1976, **13**, 5188–5192.
68 A. S. Chaves, M. J. Piotrowski and J. L. F. Da Silva, *Phys. Chem. Chem. Phys.*, 2017, **19**, 15484–15502.
69 W. Song, W.-C. Lu, C. Z. Wang and K. M. Ho, *Comput. Theor. Chem.*, 2011, **978**, 41–46.
70 M. Methfessel and A. T. Paxton, *Phys. Rev. B: Condens. Matter Mater. Phys.*, 1989, **40**, 3616–3621.
71 K. Momma and F. Izumi, *J. Appl. Crystallogr.*, 2011, **44**, 1272–1276.
72 C. Kittle, *Introduction to Solid State Physics*, John Wiley & Sons, Inc., Hoboken, NJ, 8th edn, 2005.
73 P. Janthon, S. M. Kozlov, F. Viñes, J. Limtrakul and F. Illas, *J. Chem. Theory Comput.*, 2013, **9**, 1631–1640.
74 P. Janthon, S. Luo, S. M. Kozlov, F. Viñes, J. Limtrakul, D. G. Truhlar and F. Illas, *J. Chem. Theory Comput.*, 2014, **10**, 3832–3839.
75 T. Gomez, E. Florez, J. A. Rodriguez and F. Illas, *J. Phys. Chem. C*, 2011, **115**, 11666–11672.
76 R. F. W. Bader, *Chem. Rev.*, 1991, **91**, 893–928.
77 J. A. Rodriguez and F. Illas, *Phys. Chem. Chem. Phys.*, 2012, **14**, 427–438.

THE JOURNAL OF PHYSICAL CHEMISTRY C
A JOURNAL OF THE AMERICAN CHEMICAL SOCIETY

pubs.acs.org/JPCC Article

Assessing the Activity of Ni Clusters Supported on TiC(001) toward CO_2 and H_2 Dissociation

Pablo Lozano-Reis, Hector Prats, Ramón Sayós, José A. Rodriguez, and Francesc Illas*

Cite This: J. Phys. Chem. C 2021, 125, 12019−12027 Read Online

ACCESS | Metrics & More | Article Recommendations | Supporting Information

ABSTRACT: Small Ni particles supported on TiC(001) were shown to display a very high activity for the catalytic hydrogenation of CO_2 but the underlying chemistry is, to a large extent, unknown. Here, by means of periodic density functional theory (DFT) calculations with the BEEF−vdW functional, we explore the adsorption and subsequent dissociation of CO_2 and H_2 on several Ni_n clusters (n = 4, 9, 13, and 16) supported on TiC(001) and compare the results to those obtained for the bare Ni(111) and TiC(001) surfaces using exactly the same computational approach. The calculations reveal that the Ni_n/TiC system exhibits stronger adsorption energies and lower dissociation energy barriers for CO_2 and H_2 than the bare Ni(111) and TiC(001) surfaces. This is in line with the experimental finding evidencing that the Ni/TiC system has a catalytic activity higher than that of the separated Ni and TiC constituents. In addition, the calculated results show that two-dimensional (2D) supported clusters adsorb CO_2 and H_2 stronger than the three-dimensional (3D) supported clusters and also the 2D clusters exhibit lower energy barriers for CO_2 dissociation. Within the 2D supported clusters, larger particles feature slightly stronger adsorption energies and lower CO_2 dissociation energy barriers. Finally, H_2 dissociation proceeds with a very low energy barrier on all of the studied models, which makes these novel systems potential good candidates for hydrogenation reactions.

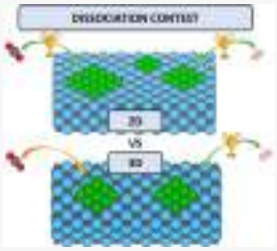

1. INTRODUCTION

Excessive emissions of greenhouse gases are producing a devastating effect on the Earth's environment leading to phenomena such as the global warming with direct impact on the overall climate system. Among the different greenhouse gases, carbon dioxide (CO_2) is the major contributor to global warming and sea acidification.[1,2] The increase of atmospheric CO_2 is directly associated with the use of carbon-rich fossil fuels for covering the ever-growing world energy demand. Unfortunately, satisfying the whole current world energy requirements with green energies is still remote[3,4] and significant efforts are being addressed toward the CO_2 catalytic chemical conversion. This strategy involves simultaneously reducing the environmental impact related to CO_2 emissions and generating energy carriers, thus creating a cyclic energy economy. In the last decades, CO_2 hydrogenation has gained interest in generating new value-added chemicals of industrial significance. Among the different chemicals of industrial interest, CO, methane, methanol, and formaldehyde are the most investigated options[5−8] and all require appropriate active and selective catalysts.

The most common heterogeneous catalysts used in industrial applications consist of small-to-medium-sized metallic nanoparticles anchored on some type of support, usually an oxide or sulfide.[9] The nature of both, metal and support, controls the catalytic activity and, more importantly, the selectivity toward a specific product. Normally, precious metals like Pd and Pt are highly active, but they are scarce and expensive. Therefore, metals that could be active, abundant, and cheap attract considerable attention. In that sense, Ni-based catalysts are widely used for the CO_2 hydrogenation reaction due to their relatively high activity and low cost compared to noble metals.[10−17] In these catalysts, nickel nanoparticles are often supported over different metal oxides although transition-metal carbides (TMCs) were also proposed as supports,[18−20] the resulting systems exhibiting high activity and selectivity. The enhanced activity was attributed to the polarization that the TMC surface provokes on the supported particle electronic density.[21] This type of positive interaction between the metal cluster and the TMC support is different from the so-called strong metal−support interactions (SMSIs) introduced by Tauster, a term used in the 1970−1990s, that had a detrimental effect on the catalytic activity.[22−24] In the last 15 years, a large number of studies have shown a positive active role of the support and it is now clear that metal−support interactions in many cases can be used to tune a specific activity and selectivity.[25] For instance, Klyushin et al.[26] evidenced the benefits of metal−support

Received: April 9, 2021
Revised: May 18, 2021
Published: May 28, 2021

https://doi.org/10.1021/acs.jpcc.1c03219
J. Phys. Chem. C 2021, 125, 12019−12027

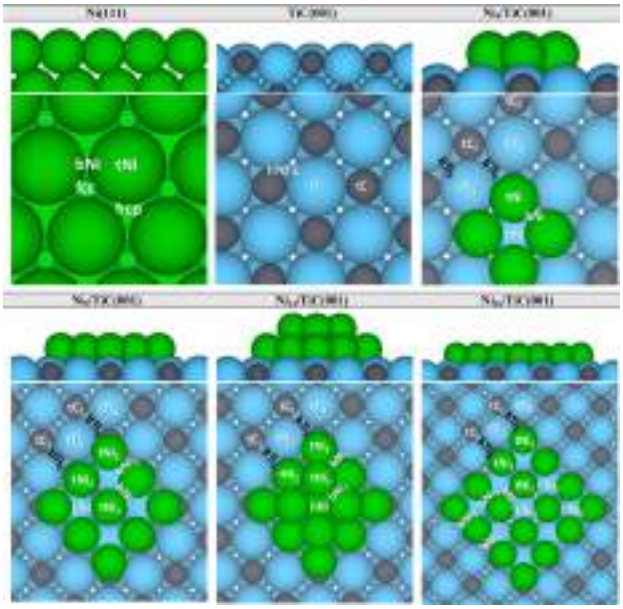

Figure 1. Side and top views of the six different surface models studied. The top view contains the label of the different considered adsorption sites. Light blue, gray, and green colors are used for titanium, carbon, and nickel, respectively.

interactions for the CO oxidation reaction catalyzed by Au nanoparticles supported on TiO_2. Similarly, Bruix et al.[27] showed an activity enhancement for the water gas shift reaction (WGSR) on Pt clusters anchored over a ceria support that was due to metal−support interactions. Moreover, in a recent study, Prats et al.[28] showed the interplay between the metal and the support for the WGSR on Au clusters supported on molybdenum carbide using a multiscale approach. Clearly, catalysis design can benefit from the use of metal−support interactions that open new opportunities for the generation of tailor-made materials.

Coming back to the case of CO_2 activation, experiments under well-controlled conditions showed that Ni clusters supported on titanium carbide (TiC) exhibit a high activity toward CO_2 hydrogenation[20] with a noted selectivity toward CO production, although the underlying chemistry is essentially unknown. In part, this is due to the complex network of reactions that are involved in this apparently simple reaction where direct dissociation of CO_2 and H_2 competes with hydrogen-assisted CO_2 dissociation to CO and COOH formation that eventually leads to a small amount of methanol. On extended surfaces of nickel, the products of the hydrogenation of CO_2 can be CO, methanol, methane, other light alkanes, and coke. Thus, the high selectivity seen on Ni/TiC(001) for the production of CO is remarkable.[20]

Recent work has shown that TiC(001) and TiC powders can store large amounts of hydrogen that are available for any hydrogenation process.[29] Thus, in Ni/TiC(001), one has a catalyst in which the properties of the carbide and metal−support interactions may be responsible for the high selectivity seen during CO_2 hydrogenation.[20] Furthermore, in this system, the reactivity also depends on the size of the supported metal particle, small two-dimensional (2D) supported clusters being more active than larger three-dimensional (3D) clusters.[20] This is likely due to differences in the electronic distribution of the 2D and 3D supported Ni clusters induced by the TiC support. Precisely, a recent study has shown that Ni clusters bind stronger over TiC than over different reducible and non-reducible metal oxides.[30] This study also revealed that 3D clusters should be easier to form and are more stable, which can be beneficial for catalysis, provided the morphology of the supported clusters can be controlled. The clear influence of the particle size and morphology further complicates the situation and calls for modeling studies where the different effects can be studied separately. To contribute to disentangling this problem, we have studied the size and morphology effect of supported nickel clusters on the adsorption and dissociation of CO_2 and H_2. This is a necessary step before selecting an appropriate catalytic model to thoroughly study the CO_2 hydrogenation reaction by a multiscale approach.

2. COMPUTATIONAL METHODS AND MATERIAL MODELS

The adsorption and dissociation of CO_2 and H_2 on a series of models representing a variety of Ni clusters supported on TiC (vide infra) were studied by means of density functional theory (DFT)-based calculations using periodic models. All calculations described in the present work were carried out by

https://doi.org/10.1021/acs.jpcc.1c03219
J. Phys. Chem. C 2021, 125, 12019−12027

means of the Vienna ab initio simulation package (VASP) code,[31−33] where the valence electron density is expanded in a plane-wave basis set, as indicated below, while the effect of the core electrons on the valence electron density is represented by the projector-augmented wave (PAW) method.[34] Spin polarization has been considered for all of the systems containing Ni to account for its magnetic properties arising from its incomplete occupation of the 3d shell. All DFT calculations were carried out using the nonlocal BEEF−vdW exchange−correlation functional[35] that includes dispersion effects. The reason for this particular choice comes from several benchmark studies showing that it provides better agreement with available experimental data than other commonly used functionals.[35−37]

The different systems representing Ni clusters supported on the TiC(001) surface were modeled by a (N × M) supercell containing four TiC atomic layers plus the Ni_4, Ni_9, Ni_{13}, and Ni_{16} clusters, as shown in Figure 1. In these systems, we change the number of atoms in the cluster and consider configurations in which all of the nickel atoms are in contact with the carbide substrate (maximizing metal−support interactions) or have a 3D configuration where some of its atoms do not touch the support. For comparison, the interaction of CO_2 and H_2 with the Ni(111) and TiC(001) surfaces was also considered, with data calculated here using the same computational approach and compared to previous values in the literature.[20,38] Regarding the models for the supported clusters, one should be aware that several near-degenerate structural isomers may be present, especially at operating conditions.[39,40] However, the focus of the present work is on the effect of cluster size and shape (2D versus 3D atomic structures) rather than a complete study of the reactivity of different isomers for each supported cluster. This will shed light on important aspects of a complex reaction network by guiding appropriate catalyst models that, even if not perfect, are realistic enough to provide physically meaningful insights into the molecular process by subsequent multiscale simulations.

The size of the supercell was large enough to avoid spurious interactions between periodically repeated species. Similarly, a vacuum width of at least 12 Å was used to minimize spurious interactions between periodically repeated slabs in the vertical direction. In all calculations, at least the outermost TiC atomic layer, the nickel cluster and the adsorbed species were allowed to fully relax, while the other TiC layers were fixed to provide a bulk environment to the surface region. A cutoff energy of 415 eV was set for the plane-wave expansion, while the Monkhorst−Pack[41] k-point mesh was varied depending on the surface model used. The specific values used for each surface model are summarized in Table S1 in the Supporting Information (SI). The electronic energy convergence criterion was set to 10^{-5} eV, while atomic positions were allowed to relax until the forces acting on the atoms were smaller than 0.01 eV $Å^{-1}$. Note that for calculations in which convergence problems have aroused, we have ensured that the electronic energy does not vary more than 10^{-3} eV.

Transition-state (TS) structures were located using the climbing-image nudged elastic band method (CI-NEB).[42,43] The initial guesses for the employed intermediate images were generated using the image-dependent pair potential procedure,[44] as implemented in the atomic simulation environment (ASE) package.[45] Vibrational frequency analysis was carried out to ensure that all TS have only one imaginary frequency, whereas, for adsorbed species, all frequencies were positive, thus corresponding to real minima on the potential energy surface. The calculated frequencies were also used to compute the zero-point energy (ZPE) contribution to the energy of all adsorbed species. The energy of gas-phase molecules was calculated by placing a single molecule in a box of dimensions 9 × 10 × 11 $Å^3$ and considering the Γ point only. Then, the adsorption energy of the considered i species was calculated as follows

$$E_{\mathrm{ads},i} = E_{i,\mathrm{slab}} - E_{\mathrm{slab}} - E_{i,\mathrm{g}} \quad (1)$$

where $E_{i,\mathrm{slab}}$ is the energy of the i species adsorbed over the surface, E_{slab} is the energy of the relaxed pristine surface, and $E_{i,\mathrm{g}}$ is the i gas-phase energy. With this definition, favorable adsorption corresponds to negative $E_{\mathrm{ads},i}$ values. Reaction energies (ΔE_r) and energy barriers ($\Delta E^{\neq}$) were calculated as

$$\Delta E_r = E_{\mathrm{FS}} - E_{\mathrm{IS}} \quad (2)$$

$$\Delta E^{\neq} = E_{\mathrm{TS}} - E_{\mathrm{IS}} \quad (3)$$

where E_{IS}, E_{FS}, and E_{TS} are the total energy of the initial, final, and transition states, respectively. Note that for the final states, the coadsorbed configuration (i.e., CO + O or H + H) was always considered. Unless otherwise specified, all energy values reported in the present work include the ZPE contribution. Before starting the following section, it is important to point out that the density functional used in the present work differs from that used in previous works. Nevertheless, to ensure that a proper comparison is well suited and qualitative interpretations could be extracted, we have also calculated the H_2 and CO_2 adsorption energies on the Ni_4/TiC system using the Perdew−Burke−Ernzerhof (PBE)[46] and PW91[47] functionals without including the dispersion contribution. We have observed that, not surprisingly, these functionals predict adsorption energies of H_2 and CO_2 0.30−0.34 eV larger than BEEF−vdW (see Table S2 in the SI for further information). Although this functional dependence on the adsorption energies does not affect the general conclusions obtained from the comparison between our BEEF−vdW results and previous results in the literature, it should be taken into account when comparing the absolute values of adsorption energies with literature data.

3. RESULTS AND DISCUSSION

3.1. CO_2 and H_2 Adsorption on Ni_n/TiC Models. The adsorption energies for CO_2 and H_2 on the different sites of the four Ni_n/TiC different model systems as well as on bare TiC(001) and Ni(111) are shown in Table 1; the most stable configurations are schematically displayed in Figure 2. As shown in Figure 2, a similar pattern emerges for both CO_2 and H_2 adsorbed molecules. On the bare TiC(001) and Ni(111) surfaces, the CO_2 adsorption energies calculated with the BEEF−vdW functional are of −0.58 and −0.15 eV, indicating chemisorption and physisorption, respectively. It is known that CO_2 interacts weakly with Ni(111) and with other surfaces of late transition metals.[48,49] For CO_2 adsorption on TiC(001), the reported BEEF−vdW value is close to the PBE ones reported by Kunkel et al.[50] (−0.57 eV) and by López et al.[51,52] (−0.61) and slightly smaller than the PBE-D3 values reported by the same authors (−0.83 and −0.85 eV, respectively). The small difference is clearly due to the different treatments of dispersion in the BEEF−vdW and PBE-D3 approaches, the latter known to overestimate the adsorption energy. Apart from this small discrepancy, all studies point to the formation

https://doi.org/10.1021/acs.jpcc.1c03219
J. Phys. Chem. C 2021, 125, 12019−12027

Table 1. CO_2 and H_2 Adsorption Energies (Including the ZPE Term), C−O Bond Lengths (d_{C-O}), H−H Bond Lengths (d_{H-H}), and O−C−O Bond Angles (θ_{O-C-O}), for the Most Stable Adsorbed Sites for H_2 and CO_2 over the Different Surface Models[a]

	CO_2			
model	site	E_{ads}/eV	d_{C-O}/Å	θ_{O-C-O}/°
Ni(111)[b]	tNi	−0.15	1.18, 1.18	180
TiC(001)	tC	−0.58	1.29, 1.29	128
Ni_4/TiC(001)	hNi	−1.37	1.35, 1.28	122
Ni_9/TiC(001)	hNi_1	−1.36	1.36, 1.29	119
Ni_9/TiC(001)	hNi_2	−1.41	1.36, 1.29	119
Ni_{13}/TiC(001)	tNi_2	−0.47	1.28, 1.28	130
Ni_{13}/TiC(001)	tNi_3	−0.48	1.24, 1.26	138
Ni_{16}/TiC(001)	hNi_1	−1.49	1.36, 1.29	117
Ni_{16}/TiC(001)	hNi_2	−1.45	1.37, 1.29	118
Ni_{16}/TiC(001)	hNi_3	−1.45	1.35, 1.28	120
	H_2			
model	site	E_{ads}/eV	d_{H-H}/Å	
Ni(111)[b]	bNi	−0.02	0.74	
TiC(001)	tM	−0.01	0.74	
TiC(001)	tC	−0.01	0.74	
Ni_4/TiC(001)	tNi	−0.34	0.83	
Ni_9/TiC(001)	tNi_1	−0.30	0.86	
Ni_9/TiC(001)	tNi_2	−0.35	0.85	
Ni_9/TiC(001)	tNi_3	−0.33	0.83	
Ni_{13}/TiC(001)	tNi_2	−0.01	0.82	
Ni_{13}/TiC(001)	tNi_3	−0.12	0.82	
Ni_{13}/TiC(001)	tNi_1	−0.12	0.83	
Ni_{16}/TiC(001)	tNi_1	−0.40	0.84	
Ni_{16}/TiC(001)	tNi_2	−0.40	0.84	
Ni_{16}/TiC(001)	tNi_3	−0.42	0.83	

[a]Note that except in Ni_{13}/TiC(001), the Ni supported clusters have a 2D atomic structure. [b]The Ni(111) values were taken from ref 38.

of a C_{surf}−CO_2 bond giving an adsorption configuration in which the molecule is activated with a concomitant increase of the C−O bond lengths and appearance of significant O−C−O bending (see Table 1). On the other hand, H_2 has a similar interaction with both TiC(001) and Ni(111), as expected since it is physisorbed on both surfaces.

For the Ni cluster supported on TiC(001), the strong metal−support interaction[30] generates a charge redistribution over the Ni atoms that results in much larger adsorption energies for both CO_2 and H_2 (see Figure 2). On the Ni_n/TiC systems, adsorption induces a strong activation of both molecules evidenced by increased bond lengths and, in the case of CO_2, a large deviation from linearity (see Table 1). As a curiosity, the C−O bond length nicely correlates with the CO_2 adsorption energy, so, the largest the bond length, the largest the adsorption energy, as shown in Figure 3. Regarding the

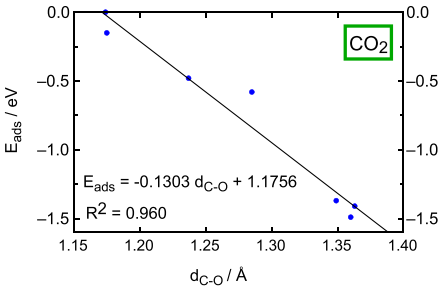

Figure 3. Correlation between the adsorption energy for CO_2 and C−O bond length.

effect of the supported morphology, those clusters with a 2D atomic structure adsorb CO_2 and H_2 strongly than the 3D one. The reason for this behavior is simply that the Ni atoms in the 2D clusters are more affected by the underlying TiC support than those of the supported 3D clusters where there are Ni atoms that are not in direct contact with the support and, consequently, much less affected. This is a general trend already observed for other metallic particles supported on TMCs.[21,53] Within 2D clusters, adsorption energies slightly increase with particle sizes, which can be attributed to the lower energy penalty for structure reconstruction upon adsorption on Ni_{16}/TiC compared to that on Ni_4/TiC and Ni_9/TiC.[21] Interestingly, the topmost hollow site of Ni_{13}/TiC does not adsorb CO_2 nor H_2, as this site closely resembles the fourfold hollow site of the Ni(100) surface that is known to interact poorly with CO_2, but it can interact significantly with H_2.[54]

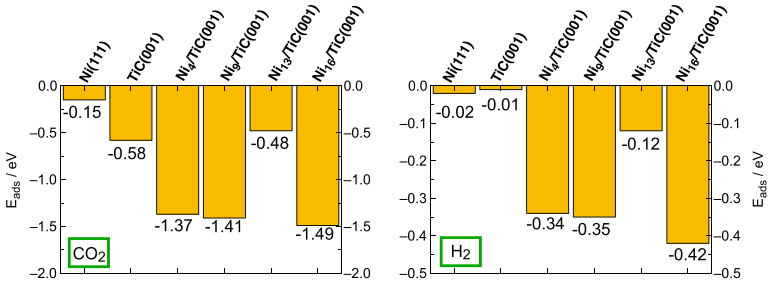

Figure 2. H_2 and CO_2 adsorption energies over different surface models. The ZPE term is included. The adsorption energies on Ni(111) were taken from ref 38.

https://doi.org/10.1021/acs.jpcc.1c03219
J. Phys. Chem. C 2021, 125, 12019−12027

Table 2. CO_2 and H_2 Reaction Energies ($\Delta E_{r,0}$) and Forward and Reverse Energy Barriers ($\Delta E^{\neq}_{fw,0}$ and $\Delta E^{\neq}_{rev,0}$, Respectively) over the Most Probable Sites for Reaction of the Different Considered Ni_n/TiC Models with Ni(111) and TiC(001) Included for Comparison[a]

CO_2					
model	reaction	$\Delta E_{r,0}$/eV	$\Delta E^{\neq}_{fw,0}$/eV	$\Delta E^{\neq}_{rev,0}$/eV	d_{C-O}/Å
Ni_4/TiC(001)	$CO_{2,hNi} \rightleftharpoons CO_{hNi} + O_{tTi1}$	0.03	0.55	0.52	1.75
Ni_9/TiC(001)	$CO_{2,hNi} \rightleftharpoons CO_{hNi} + O_{tTi1}$	0.25	0.52	0.27	1.74
Ni_{13}/TiC(001)	$CO_{2,tNi2} \rightleftharpoons CO_{tNi2} + O_{tTi1}$	−0.39	0.83	1.22	1.53
Ni_{16}/TiC(001)	$CO_{2,hNi1} \rightleftharpoons CO_{hNi1} + O_{hNi2}$	−0.68	0.35	1.03	1.92
Ni(111)	$CO_{2,top} \rightleftharpoons CO_{hcp} + O_{fcc}$	−0.57	0.86	1.43	1.84
TiC(001)	$CO_{2,tC} \rightleftharpoons CO_{tC} + O_{hMMC}$	−0.06	1.03	1.08	1.84
H_2					
model	reaction	$\Delta E_{r,0}$/eV	$\Delta E^{\neq}_{fw,0}$/eV	$\Delta E^{\neq}_{rev,0}$/eV	d_{H-H}/Å
Ni_4/TiC(001)	$H_{2,tNi} \rightleftharpoons H_{bNi} + H_{bNi}$	−0.60	0.08	0.68	1.36
Ni_9/TiC(001)	$H_{2,tNi1} \rightleftharpoons H_{hNi} + H_{hNi}$	−0.95	0.02	0.97	1.14
Ni_{13}/TiC(001)	$H_{2,tNi1} \rightleftharpoons H_{bNi1} + H_{tNi3}$	−0.51	0.11	0.62	1.11
Ni_{16}/TiC(001)	$H_{2,tNi3} \rightleftharpoons H_{bNi4} + H_{bNi4}$	−0.44	0.07	0.52	1.32
Ni(111)	$H_{2,bNi} \rightleftharpoons H_{fcc} + H_{hcp}$	−0.31	0.28	0.59	0.94
TiC(001)	$H_{2\ tM} \rightleftharpoons H_{tC} + H_{tC}$[b]	−0.50	1.07	1.57	1.27

[a]Note that except Ni_{13}/TiC(001), the Ni supported clusters have a 2D atomic structure. All energy values were obtained with the BEEF−vdW functional and include the ZPE contribution. C−O and H−H breaking/forming distance of the transition-state structure (d_{C-O} and d_{H-H}, respectively). [b]Note that this process occurs in two steps, as shown in ref 61. Thus, the energy barrier is calculated with respect to the TS with the highest energy. See Table S3 in the SI for information about the energetics of each of the two steps.

To have a better perspective of the different interactions involved in the H_2 and CO_2 adsorption with the different Ni_n clusters supported on TiC, it is interesting to compare with other studies of similar systems either involving TiC(001) surfaces doped with metals,[51,52] other supported metals on TiC(001),[20,55,56] or even other low Miller index Ni surfaces.[57,58] A comparison with these previous works shows that Ni_n/TiC(001) systems are really attractive as they interact stronger with H_2 and CO_2. For instance, for H_2 adsorption, Florez et al.[55] reported adsorption energy values of 0.01 and −0.04 eV for the Au_4/TiC and Au_9/TiC systems, respectively. These values were obtained using a different but quite similar functional, PW91 without including dispersion, but, in any case, are significantly smaller than the BEEF−vdW calculated values for the Ni_4/TiC and Ni_9/TiC systems (−0.34 and −0.35 eV, respectively). Note that Florez et al.[55] also reported a H_2 adsorption energy of −0.48 eV on the bare TiC(001) surface, which is larger than the present calculated value (−0.01 eV). An analysis of the involved structures shows that the value reported by Florez et al.[55] corresponds to a nearly dissociated structure with a H−H distance of 1.73 Å, as specified by the authors, whereas the present calculations clearly find a physisorbed H_2 molecule. Clearly, the lack of dispersion in the PW91 functional used by Florez et al.[55] is the reason why the physisorbed species was not detected in the calculations. In a subsequent work, Gomez et al.[56] studied the adsorption of H_2 on a series of M_4/TiC systems (M = Pd, Pt, Cu, Ag, and Au). They used the same PW91 functional, again without including dispersion, and found an almost negligible H_2 adsorption energy on the Cu_4/TiC, Ag_4/TiC, and Au_4/TiC systems. Oppositely, they found a stronger adsorption energy for the Pd_4/TiC and Pt_4/TiC systems (−0.70 and −0.87 eV, respectively). In spite of the use of a density functional neglecting dispersion, the trends are physically sound and can be safely compared to the present BEEF−vdW values. The present value for the H_2 adsorption energy on Ni_4/TiC of −0.34 eV is clearly in between the values for coinage and Pt-group metals. Moreover, both Pd_4/TiC and Pt_4/TiC exhibit a rather large energy barrier for dissociation (vide infra), which makes Ni_4/TiC more attractive for H_2 dissociation, as discussed more in detail in the next section. Comparing the H_2 adsorption energy with that on different Ni surfaces, Mohsenzadeh et al.[57] found H_2 adsorption energies of −0.17, −0.22, and −0.33 eV for the Ni(111), Ni(100), and Ni(110) surfaces, respectively, using the PBE functional. Their reported values are larger than those reported for both naked surfaces but slightly lower than that of the Ni_n/TiC systems. Therefore, the supported Ni clusters appear to be more active than the corresponding extended surfaces.

Regarding CO_2 adsorption, as mentioned above, it is known that the molecule interacts weakly with Ni(111) and with other surfaces of late transition metals.[48,49] For instance, Vogt et al.[58] using the PBE functional found CO_2 adsorption energies of 0.25, −0.17, −0.43, and −0.41 eV for the Ni(111), Ni(100), Ni(110), and Ni(211) surfaces, respectively. Their results show that stepped surfaces adsorb CO_2 stronger than flat surfaces, which comes from low-coordination metal atoms at the step sites, but are still far away from the adsorption strength observed on the 2D supported Ni_n/TiC clusters. It is also interesting to compare to the results reported by López et al.,[51,52] who studied the effect of doping the TiC(001) surface with different kinds of metals. In particular, these authors first considered the situation where one surface Ti atom is replaced by another transition-metal atom chosen from the list of those that are commonly present in TMCs such as Zr, Hf, V, Nb, Mo, Cr, Ta, and W. They found that the highest CO_2 adsorption energy corresponded to the Hf- and Zr-doped systems, with PBE adsorption energies of −0.96 and −0.93 eV, respectively. In both cases, CO_2 adsorbs via a C_{surf}−CO_2 bond, with one of the oxygen atoms pointing to the dopant. In the following study, these authors increased the set of doping atoms so as to include Mg, Ca, Sr, Al, Ga, In, Si, Sn, Pd, Pt, Rh, Ir, La, and Ce and found that, among all dopants studied, the Sr- and Ce-doped systems exhibited the largest adsorption

https://doi.org/10.1021/acs.jpcc.1c03219
J. Phys. Chem. C 2021, 125, 12019−12027

energy. However, they also found significant differences in the bonding mechanism; CO_2 interacts directly with Ce dopant resulting in a PBE adsorption energy of −1.10 eV, but in the case of Sr, the bonding mode does not involve such direct interaction and the reported PBE adsorption energy was −1.22 eV. However, these values are still slightly smaller than those of the 2D Ni_n/TiC systems of −1.37, −1.41, and −1.49 eV for the Ni_4/TiC, Ni_9/TiC, and Ni_{16}/TiC systems, respectively, although these include dispersion through the BEEF−vdW functional. Note that in the present calculations the bonding mode implies a clear direct interaction between the CO_2 molecule and the Ni atoms of the nickel clusters. Finally, Rodriguez et al.[20] reported CO_2 adsorption energies of −1.11, −0.59, −0.68, and −0.37 eV over Cu_4/TiC, Au_4/TiC, Cu_9/TiC, and Au_9/TiC, respectively, also lower than 2D Ni_n/TiC systems. Even if these values have been obtained with the PW91 functional and, hence, neglect dispersion, it is clear that the Ni clusters supported on TiC are more active to adsorb CO_2 than those of Cu and Au on the same support. It is also worth noting that for the 3D coinage clusters supported on TiC, the interaction of CO_2 with the uppermost layer was negligible as we have observed for Ni_{13}/TiC. Note that previous studies do not include the ZPE contribution term although its contribution to the adsorption energy is on the order of 0.02 eV or less.

3.2. CO_2 and H_2 Dissociation on Ni_n/TiC Models. The dissociation of CO_2 and H_2 on the present models is rather complex since both adsorbates interact with a rather similar strength on different sites. Thus, we have considered all possible reaction pathways, which are listed in Table S3 in the SI. Table 2 reports the reaction energies and energy barriers for the pathways exhibiting the lowest energy barrier. The highest dissociation energy barriers for both CO_2 and H_2 correspond to the bare TiC(001) and Ni(111) surfaces with Ni(111) predicted to be slightly more active than TiC(001) for CO_2 and H_2 dissociation. Note that the Ni(111) surface activity will be limited by the weak CO_2 and H_2 adsorption, in agreement with experimental trends.[49] Likewise, one must point out that, during the hydrogenation process, the dissociation of the CO_2 molecule can occur either spontaneously or assisted by hydrogen adatoms arising from a previous H_2 dissociation step. These constitute the initial steps of a complex reaction network (see ref 38), ultimately determining the selectivity of the process, with the possible products being CO, methanol, CH_4 or other light alkanes, and coke. Therefore, to better understand the underlying chemistry, it is convenient to focus first on the adsorption and dissociation of CO_2 and H_2, and this is precisely the aim of the present work.

For the Ni_n/TiC models, the strong metal−support interactions result in moderately low energy barriers for CO_2 direct dissociation with values in the 0.35−0.83 eV range. Moreover, the process is clearly favored over the 2D supported clusters and, as these adsorb CO_2 stronger, they are suitable candidates for CO_2 conversion. Note also that CO_2 dissociates with a similar energy barrier on all of the considered different sites of the 2D supported clusters, but this is not the case of 3D clusters (see Table S3 in the SI). Results in Table 2 also indicate that, for the 2D clusters, the CO_2 dissociation energy barrier slightly decreases with cluster size. These minor differences are also observed for the adsorption strength and are rationalized as a smaller reorganization of the supported cluster atomic structure in the largest ones. The energy barriers are even smaller for H_2 dissociation, with values as low as 0.02−0.11 eV. Contrarily to what is observed for H_2 adsorption, there is no clear trend relating the Ni_n/TiC atomic structure and the corresponding energy barrier for H_2 dissociation. However, 2D clusters emerge as excellent candidates for hydrogenation reactions given their very low energy barriers and rather strong H_2 adsorption. Note that the H_2 dissociation mechanism on all supported clusters is very similar irrespectively on the adsorption site (see Table S3 in the SI). As a final remark, one should mention that the good H_2 dissociation capacity and the ability of TiC(001) to pack large coverages of hydrogen make Ni_n/TiC systems really attractive for hydrogenation reactions. Note that H_2 dissociates preferably leading both H atoms on the supported Ni cluster, but as investigated for the Ni_4/TiC system, the final state, in which one H atom sits on the supported cluster while the other spills over to a Ti−Ni interface site, is only ∼0.30 eV less stable but still exothermic, and the transition state is supposed to be very similar. Therefore, under regular pressures of H_2, one could expect that some H atoms could spill over from Ni_n clusters to the TiC(001) surface, producing a large H reservoir that could be useful for hydrogenation reactions. Nevertheless, it is important to point out that this spillover effect is strongly dependent on the H coverage,[59,60] although a more detailed study is out of the scope of the present study.

It is interesting to compare the present results with other studies for different metal clusters on the same support[20,55,56] and for different Ni surfaces. Clearly, the Ni_n/TiC(001) systems are more attractive for CO_2 hydrogenation as the small energy barrier for H_2 dissociation is accompanied by a rather strong CO_2 adsorption although a systematic study is needed involving all possible intermediates, typically COOH and HCOO, and the subsequent evolution either to CO or methanol. This study is out of the scope of the present work but will be the focus of future studies. Regarding the comparison to previous works, Florez et al.[55] studied the H_2 dissociation reaction over Au_4, Au_9, and Au_{13} clusters supported on the TiC(001) surface and considered also the pristine TiC(001) surface. They used the PW91 exchange−correlation functional and did not include dispersion meaning that, as for many of the preceding discussions, a meaningful comparison should focus on trends rather than absolute values. Similar to the present results for the 2D supported Ni clusters, H_2 dissociation on the 2D supported Au cluster was found to involve very small energy barriers (0.08 and 0.20 eV for Au_4/TiC and Au_9/TiC, respectively). However, for the 3D Au_{13}/TiC system, the energy barrier was found to be much higher than that reported here for Ni_{13}/TiC, 0.99 and 0.11 eV, respectively. Therefore, while both 2D Au and Ni clusters anchored over TiC(001) are very attractive for hydrogenation reactions, Ni_n/TiC appears as a more robust candidate because, in practice, a control of the supported cluster morphology can be extremely challenging and, at high metal coverage, 3D clusters become predominant. It is also interesting to compare the present results with those reported by Gomez et al.[56] for the catalytic activity of M_4/TiC (M = Pd, Pt, Cu, Ag, and Au) systems toward H_2 dissociation. Their calculations with the PW91 functional found that the H_2 dissociation energy barrier follows the order Pt > Ag > Pd > Cu > Au; again, the absolute values of 1.16, 0.79, 0.53, 0.37, and 0.08 eV, respectively, should not be compared, while the trend is for sure meaningful. Thus, among the different M_4 supported clusters studied, Ni_4/TiC and Au_4/TiC exhibit the lowest energy barriers. Regarding different extended nickel

https://doi.org/10.1021/acs.jpcc.1c03219
J. Phys. Chem. C 2021, 125, 12019−12027

surfaces, Mohsenzadeh et al.[57] reported a H_2 dissociation energy barrier calculated with the PBE functional for the Ni(111), Ni(100), and Ni(110) surfaces of 0.03, 0.02, and 0.06 eV, respectively. Their values are similar to those calculated for the Ni_n/TiC systems although the larger adsorption energy for the Ni_n/TiC will facilitate dissociation with respect to desorption. Concerning CO_2 dissociation, Vogt et al.[58] using the PBE functional found a CO_2 dissociation energy barrier of 0.52, 0.16, 0.40, and 0.93 eV for the Ni(111), Ni(100), Ni(110), and Ni(211) surfaces, respectively. Except for the Ni(100) surface, 2D supported Ni clusters have similar or even lower CO_2 dissociation energy barriers than the extended surfaces. As Ni_n supported clusters adsorb the CO_2 molecule rather strongly, they are likely to be better catalysts for CO_2 conversion than the extended nickel surfaces with exception of the Ni(100) surface in which firm conclusions cannot be obtained. Finally, Rodriguez et al.[20] reported a PW91 dissociation energy barrier of 0.81 eV on Cu_4/TiC, which is significantly larger than our BEEF−vdW calculated value of 0.55 eV for Ni_4/TiC. In addition, the adsorption energy of CO_2 on Cu_4/TiC (−1.11 eV) is smaller than on Ni_4/TiC (−1.37 eV). Therefore, Ni_n/TiC systems are predicted to be more active than the Cu_n/TiC and Au_n/TiC systems, which nicely agrees with experimental findings.[20]

4. CONCLUSIONS

The adsorption and subsequent dissociation of CO_2 and H_2 have been studied for a series of 2D and 3D Ni clusters supported on TiC(001), using suitable periodic models and density functional calculations with the BEEF−vdW exchange−correlation functional including dispersion. The 2D clusters contained 4, 9, and 16 Ni atoms, whereas Ni_{13} was selected as representative of the 3D ones. For comparison, bare Ni(111) and TiC(001) surfaces were also considered so that all systems have been studied using exactly the same computational approach. The present study allowed us to reach firm conclusions regarding the effect of the cluster size and of metal−support interactions on the catalytic activity of these novel systems.

The present systematic study shows that both CO_2 and H_2 molecules adsorb in general on Ni_n/TiC(001) stronger than on the bare Ni(111) and TiC(001) surfaces, with dissociation energy barriers that are quite low and smaller than for these two extended surfaces. The present results also indicate that the 2D supported clusters adsorb CO_2 and H_2 stronger and dissociate CO_2 easier than the 3D supported clusters. In all studied Ni_n/TiC(001) models, H_2 dissociates with very low energy barriers with no clear trend. We also show that, for the 2D supported clusters, the larger particles feature slightly stronger adsorption energies and lower CO_2 energy barriers, although the differences are minimal. These minor differences are attributed to the fact that the larger clusters exhibit a smaller atomic reorganization when the molecule adsorbs and, eventually, dissociates. A comparison with previous studies on similar systems shows that Ni_n/TiC(001) systems are more attractive for CO_2 and H_2 dissociation than metal-doped TiC(001) surfaces and other metal clusters supported on TiC(001) and extended Ni surfaces.

■ ASSOCIATED CONTENT

Supporting Information

The Supporting Information is available free of charge at https://pubs.acs.org/doi/10.1021/acs.jpcc.1c03219.

Information about specific values used for each of the studied surface models (Section S1), the CO_2 and H_2 adsorption energy on the Ni_4/TiC system using different exchange−correlation functionals (Section S2), and the CO_2 and H_2 dissociation energy barriers and the initial, final, and transition-state structures of each reaction (Section S3); and optimized structures (i.e., VASP CONTCAR files) of all relevant structures have also been made available on a public GitHub repository: https://github.com/plozanore/Nin-TiC_CO2_H2_dissociation (PDF)

■ AUTHOR INFORMATION

Corresponding Author

Francesc Illas − *Departament de Ciència de Materials i Química Física & Institut de Química Teòrica i Computacional (IQTCUB), Universitat de Barcelona, 08028 Barcelona, Spain;* orcid.org/0000-0003-2104-6123; Email: francesc.illas@ub.edu

Authors

Pablo Lozano-Reis − *Departament de Ciència de Materials i Química Física & Institut de Química Teòrica i Computacional (IQTCUB), Universitat de Barcelona, 08028 Barcelona, Spain*

Hector Prats − *Department of Chemical Engineering, University College London, London WC1E 7JE, U.K.;* orcid.org/0000-0003-4991-253X

Ramón Sayós − *Departament de Ciència de Materials i Química Física & Institut de Química Teòrica i Computacional (IQTCUB), Universitat de Barcelona, 08028 Barcelona, Spain;* orcid.org/0000-0001-6627-7844

José A. Rodriguez − *Department of Chemistry, Brookhaven National Laboratory, Upton, New York 11973-5000, United States;* orcid.org/0000-0002-5680-4214

Complete contact information is available at: https://pubs.acs.org/10.1021/acs.jpcc.1c03219

Notes

The authors declare no competing financial interest.

■ ACKNOWLEDGMENTS

The research at the Universitat de Barcelona has been supported by the Spanish Ministry of Science, Innovation and Universities (MICIUN) through grants RTI2018-094757-B-I00, RTI2018-095460-B-I00, and MDM-2017-0767 and includes funds from MCIUN/AEI/FEDER and UE and, in part, by the Generalitat de Catalunya grant 2017SGR13. The work carried out at the Brookhaven National Laboratory (BNL) was supported by the U.S. Department of Energy, Office of Science and Office of Basic Energy Sciences under contract No. DE-SC0012704. P.L-R. acknowledges MICIUN for a predoctoral FPU18/02313 grant. Computational resources provided by Consorci de Serveis Universitaris de Catalunya (CSUC, former CESCA) with financial support from the Universitat de Barcelona and Red Española de Supercomputación (grants QS-2020-1-0003 and QS-2020-2-0009) are gratefully acknowledged.

https://doi.org/10.1021/acs.jpcc.1c03219
J. Phys. Chem. C 2021, 125, 12019−12027

REFERENCES

(1) Seneviratne, S. I.; Donat, M. G.; Pitman, A. J.; Knutti, R.; Wilby, R. L. Allowable CO2 Emissions Based on Regional and Impact-Related Climate Targets. *Nature* **2016**, *529*, 477−483.

(2) Licker, R.; Ekwurzel, B.; Doney, S. C.; Cooley, S. R.; Lima, I. D.; Heede, R.; Frumhoff, P. C. Attributing Ocean Acidification to Major Carbon Producers. *Environ. Res. Lett.* **2019**, *14*, No. 124060.

(3) Barbir, F. Transition to Renewable Energy Systems with Hydrogen as an Energy Carrier. *Energy* **2009**, *34*, 308−312.

(4) Dincer, I. Renewable Energy and Sustainable Development: A Crucial Review. *Renewable Sustainable Energy Rev.* **2000**, *4*, 157−175.

(5) Jalama, K. Carbon Dioxide Hydrogenation over Nickel-, Ruthenium-, and Copper-Based Catalysts: Review of Kinetics and Mechanism. *Catal. Rev.* **2017**, *59*, 95−164.

(6) Kattel, S.; Liu, P.; Chen, J. G. Tuning Selectivity of CO_2 Hydrogenation Reactions at the Metal/Oxide Interface. *J. Am. Chem. Soc.* **2017**, *139*, 9739−9754.

(7) Li, W.; Wang, H.; Jiang, X.; Zhu, J.; Liu, Z.; Guo, X.; Song, C. A Short Review of Recent Advances in CO_2 Hydrogenation to Hydrocarbons over Heterogeneous Catalysts. *RSC Adv.* **2018**, *8*, 7651−7669.

(8) Wang, W.; Wang, S.; Ma, X.; Gong, J. Recent Advances in Catalytic Hydrogenation of Carbon Dioxide. *Chem. Soc. Rev.* **2011**, *40*, 3703.

(9) Thomas, J. M.; Thomas, W. J. *Principles and Practice of Heterogeneous Catalysis*; VCH: Weinheim, 1997.

(10) Chang, F.-W.; Kuo, M.-S.; Tsay, M.-T.; Hsieh, M.-C. Hydrogenation of CO_2 over Nickel Catalysts on Rice Husk Ash-Alumina Prepared by Incipient Wetness Impregnation. *Appl. Catal., A* **2003**, *247*, 309−320.

(11) Aziz, M. A. A.; Jalil, A. A.; Triwahyono, S.; Mukti, R. R.; Taufiq-Yap, Y. H.; Sazegar, M. R. Highly Active Ni-Promoted Mesostructured Silica Nanoparticles for CO_2 Methanation. *Appl. Catal., B* **2014**, *147*, 359−368.

(12) Tada, S.; Shimizu, T.; Kameyama, H.; Haneda, T.; Kikuchi, R. Ni/CeO_2 Catalysts with High CO_2 Methanation Activity and High CH_4 Selectivity at Low Temperatures. *Int. J. Hydrogen Energy* **2012**, *37*, 5527−5531.

(13) Ocampo, F.; Louis, B.; Kiwi-Minsker, L.; Roger, A.-C. Effect of Ce/Zr Composition and Noble Metal Promotion on Nickel Based $Ce_xZr_{1-x}O_2$ Catalysts for Carbon Dioxide Methanation. *Appl. Catal., A* **2011**, *392*, 36−44.

(14) Zhou, G.; Liu, H.; Cui, K.; Xie, H.; Jiao, Z.; Zhang, G.; Xiong, K.; Zheng, X. Methanation of Carbon Dioxide over Ni/CeO_2 Catalysts: Effects of Support CeO_2 Structure. *Int. J. Hydrogen Energy* **2017**, *42*, 16108−16117.

(15) Hwang, S.; Hong, U. G.; Lee, J.; Baik, J. H.; Koh, D. J.; Lim, H.; Song, I. K. Methanation of Carbon Dioxide Over Mesoporous Nickel−M−Alumina (M = Fe, Zr, Ni, Y, and Mg) Xerogel Catalysts: Effect of Second Metal. *Catal. Lett.* **2012**, *142*, 860−868.

(16) Yang, L.; Pastor-Pérez, L.; Gu, S.; Sepúlveda-Escribano, A.; Reina, T. R. Highly Efficient Ni/CeO_2-Al_2O_3 Catalysts for CO_2 Upgrading via Reverse Water-Gas Shift: Effect of Selected Transition Metal Promoters. *Appl. Catal., B* **2018**, *232*, 464−47.

(17) Sun, F.-m.; Yan, C.; Wang, Z.; Guo, C.; Huang, S. Ni/Ce−Zr−O Catalyst for High CO_2 Conversion during Reverse Water Gas Shift Reaction (RWGS). *Int. J. Hydrogen Energy* **2015**, *40*, 15985−15993.

(18) Rodriguez, J. A.; Liu, P.; Stacchiola, D. J.; Senanayake, S. D.; White, M. G.; Chen, J. G. Hydrogenation of CO_2 to Methanol: Importance of Metal−Oxide and Metal−Carbide Interfaces in the Activation of CO_2. *ACS Catal.* **2015**, *5*, 6696−6706.

(19) Vidal, A. B.; Feria, L.; Evans, J.; Takahashi, Y.; Liu, P.; Nakamura, K.; Illas, F.; Rodriguez, J. A. CO_2 Activation and Methanol Synthesis on Novel Au/TiC and Cu/TiC Catalysts. *J. Phys. Chem. Lett.* **2012**, *3*, 2275−2280.

(20) Rodriguez, J. A.; Evans, J.; Feria, L.; Vidal, A. B.; Liu, P.; Nakamura, K.; Illas, F. CO_2 Hydrogenation on Au/TiC, Cu/TiC, and Ni/TiC Catalysts: Production of CO, Methanol, and Methane. *J. Catal.* **2013**, *307*, 162−169.

(21) Rodriguez, J. A.; Illas, F. Activation of Noble Metals on Metal-Carbide Surfaces: Novel Catalysts for CO Oxidation, Desulfurization and Hydrogenation Reactions. *Phys. Chem. Chem. Phys.* **2012**, *14*, 427−438.

(22) Tauster, S. J. Strong Metal-Support Interactions. *Acc. Chem. Res.* **1987**, *20*, 389.

(23) Tauster, S. J.; Fung, S. C.; Garten, R. L. Strong Metal-Support Interactions. Group 8 Noble Metals Supported on Titanium Dioxide. *J. Am. Chem. Soc.* **1978**, *100*, 170−175.

(24) Tauster, S. J.; Fung, S. C.; Baker, R. T. K.; Horsley, J. A. Strong Interactions in Supported-Metal Catalysts. *Science* **1981**, *211*, 1121−1125.

(25) van Deelen, T. W.; Hernández Mejía, C.; de Jong, K. P. Control of Metal-Support Interactions in Heterogeneous Catalysts to Enhance Activity and Selectivity. *Nat. Catal.* **2019**, *2*, 955−970.

(26) Klyushin, A. Yu.; Jones, T. E.; Lunkenbein, T.; Kube, P.; Li, X.; Hävecker, M.; Knop-Gericke, A.; Schlögl, R. Strong Metal Support Interaction as a Key Factor of Au Activation in CO Oxidation. *ChemCatChem* **2018**, *10*, 3985−3989.

(27) Bruix, A.; Rodriguez, J. A.; Ramírez, P. J.; Senanayake, S. D.; Evans, J.; Park, J. B.; Stacchiola, D.; Liu, P.; Hrbek, J.; Illas, F. A New Type of Strong Metal−Support Interaction and the Production of H_2 through the Transformation of Water on Pt/CeO_2 (111) and $Pt/CeO_x/TiO_2$ (110) Catalysts. *J. Am. Chem. Soc.* **2012**, *134*, 8968−8974.

(28) Prats, H.; Posada-Pérez, S.; Rodriguez, J. A.; Sayós, R.; Illas, F. Kinetic Monte Carlo Simulations Unveil Synergic Effects at Work on Bifunctional Catalysts. *ACS Catal.* **2019**, *9*, 9117−9126.

(29) Piñero, J. J.; Ramírez, P. J.; Bromley, S. T.; Illas, F.; Viñes, F.; Rodriguez, J. A. Diversity of Adsorbed Hydrogen on the TiC(001) Surface at High Coverages. *J. Phys. Chem. C* **2018**, *122*, 28013−28020.

(30) Lozano-Reis, P.; Sayós, R.; Rodriguez, J. A.; Illas, F. Structural, Electronic, and Magnetic Properties of Ni Nanoparticles Supported on the TiC(001) Surface. *Phys. Chem. Chem. Phys.* **2020**, *22*, 26145−26154.

(31) Kresse, G.; Hafner, J. *Ab Initio* Molecular Dynamics for Liquid Metals. *Phys. Rev. B* **1993**, *47*, 558−561.

(32) Kresse, G.; Furthmüller, J. Efficient Iterative Schemes for *Ab Initio* Total-Energy Calculations Using a Plane-Wave Basis Set. *Phys. Rev. B* **1996**, *54*, 11169−11186.

(33) Kresse, G.; Furthmüller, J. Efficiency of Ab-Initio Total Energy Calculations for Metals and Semiconductors Using a Plane-Wave Basis Set. *Comput. Mater. Sci.* **1996**, *6*, 15−50.

(34) Kresse, G.; Joubert, D. From Ultrasoft Pseudopotentials to the Projector Augmented-Wave Method. *Phys. Rev. B* **1999**, *59*, 1758−1775.

(35) Wellendorff, J.; Lundgaard, K. T.; Møgelhøj, A.; Petzold, V.; Landis, D. D.; Nørskov, J. K.; Bligaard, T.; Jacobsen, K. W. Density Functionals for Surface Science: Exchange-Correlation Model Development with Bayesian Error Estimation. *Phys. Rev. B* **2012**, *85*, No. 235149.

(36) Wellendorff, J.; Silbaugh, T. L.; Garcia-Pintos, D.; Nørskov, J. K.; Bligaard, T.; Studt, F.; Campbell, C. T. A Benchmark Database for Adsorption Bond Energies to Transition Metal Surfaces and Comparison to Selected DFT Functionals. *Surf. Sci.* **2015**, *640*, 36−44.

(37) Campbell, C. T. Energies of Adsorbed Catalytic Intermediates on Transition Metal Surfaces: Calorimetric Measurements and Benchmarks for Theory. *Acc. Chem. Res.* **2019**, *52*, 984−993.

(38) Lozano-Reis, P.; Prats, H.; Gamallo, P.; Illas, F.; Sayós, R. Multiscale Study of the Mechanism of Catalytic CO_2 Hydrogenation: Role of the Ni(111) Facets. *ACS Catal.* **2020**, *10*, 8077−8089.

(39) Zhai, H.; Alexandrova, A. N. Local Fluxionality of Surface-Deposited Cluster Catalysts: The Case of Pt_7 on Al_2O_3. *J. Phys. Chem. Lett.* **2018**, *9*, 1696−1702.

(40) Sun, G.; Fuller, J. T.; Alexandrova, A. N.; Sautet, P. Global Activity Search Uncovers Reaction Induced Concomitant Catalyst Restructuring for Alkane Dissociation on Model Pt Catalysts. *ACS Catal.* **2021**, *11*, 1877−1885.

https://doi.org/10.1021/acs.jpcc.1c03219
J. Phys. Chem. C 2021, 125, 12019−12027

(41) Monkhorst, H. J.; Pack, J. D. Special Points for Brillouin-Zone Integrations. *Phys. Rev. B* **1976**, *13*, 5188−5192.
(42) Jónsson, H.; Mills, G.; Jacobsen, K. W. Nudged Elastic Band Method for Finding Minimum Energy Paths of Transitions. In *Classical and Quantum Dynamics in Condensed Phase Simulations*; World Scientific: LERICI, Villa Marigola, 1998; pp 385−404.
(43) Henkelman, G.; Uberuaga, B. P.; Jónsson, H. A Climbing Image Nudged Elastic Band Method for Finding Saddle Points and Minimum Energy Paths. *J. Chem. Phys.* **2000**, *113*, 9901−9904.
(44) Smidstrup, S.; Pedersen, A.; Stokbro, K.; Jónsson, H. Improved Initial Guess for Minimum Energy Path Calculations. *J. Chem. Phys.* **2014**, *140*, No. 214106.
(45) Hjorth Larsen, A.; Jørgen Mortensen, J.; Blomqvist, J.; Castelli, I. E.; Christensen, R.; Dułak, M.; Friis, J.; Groves, M. N.; Hammer, B.; Hargus, C.; et al. The Atomic Simulation Environment—a Python Library for Working with Atoms. *J. Phys.: Condens. Matter* **2017**, *29*, No. 273002.
(46) Perdew, J. P.; Burke, K.; Ernzerhof, M. Generalized Gradient Approximation Made Simple. *Phys. Rev. Lett.* **1996**, *77*, 3865−3868.
(47) Perdew, J. P.; Chevary, J. A.; Vosko, S. H.; Jackson, K. A.; Pederson, M. R.; Singh, D. J.; Fiolhais, C. Atoms, Molecules, Solids, and Surfaces: Applications of the Generalized Gradient Approximation for Exchange and Correlation. *Phys. Rev. B* **1992**, *46*, 6671−6687.
(48) Liu, X.; Sun, L.; Deng, W.-Q. Theoretical Investigation of CO_2 Adsorption and Dissociation on Low Index Surfaces of Transition Metals. *J. Phys. Chem. C* **2018**, *122*, 8306−8314.
(49) Freund, H.-J.; Roberts, M. W. Surface Chemistry of Carbon Dioxide. *Surf. Sci. Rep.* **1996**, *25*, 225−273.
(50) Kunkel, C.; Viñes, F.; Illas, F. Transition Metal Carbides as Novel Materials for CO_2 Capture, Storage, and Activation. *Energy Environ. Sci.* **2016**, *9*, 141−144.
(51) López, M.; Broderick, L.; Carey, J. J.; Viñes, F.; Nolan, M.; Illas, F. Tuning Transition Metal Carbide Activity by Surface Metal Alloying: A Case Study on CO_2 Capture and Activation. *Phys. Chem. Chem. Phys.* **2018**, *20*, 22179−22186.
(52) López, M.; Viñes, F.; Nolan, M.; Illas, F. Predicting the Effect of Dopants on CO_2 Adsorption in Transition Metal Carbides: Case Study on TiC (001). *J. Phys. Chem. C* **2020**, *124*, 15969−15976.
(53) Posada-Pérez, S.; Viñes, F.; Rodríguez, J. A.; Illas, F. Structure and electronic properties of Cu nanoclusters supported on Mo_2C-(001) and MoC(001) surfaces. *J. Chem. Phys.* **2015**, *143*, No. 114704.
(54) He, Y.; Wang, W. H_2 Dissociation on H-Precovered Ni(100) Surface: Physisorbed State and Coverage Dependence. *J. Phys. Chem. C* **2019**, *123*, 5365−5377.
(55) Florez, E.; Gomez, T.; Liu, P.; Rodriguez, J. A.; Illas, F. Hydrogenation Reactions on Au/TiC(001): Effects of Au↔C Interactions on the Dissociation of H_2. *ChemCatChem* **2010**, *2*, 1219−1222.
(56) Gomez, T.; Florez, E.; Rodriguez, J. A.; Illas, F. Reactivity of Transition Metals (Pd, Pt, Cu, Ag, Au) toward Molecular Hydrogen Dissociation: Extended Surfaces versus Particles Supported on TiC(001) or Small Is Not Always Better and Large Is Not Always Bad. *J. Phys. Chem. C* **2011**, *115*, 11666−11672.
(57) Mohsenzadeh, A.; Richards, T.; Bolton, K. DFT Study of the Water Gas Shift Reaction on Ni(111), Ni(100) and Ni(110) Surfaces. *Surf. Sci.* **2016**, *644*, 53−63.
(58) Vogt, C.; Monai, M.; Sterk, E. B.; Palle, J.; Melcherts, A. E. M.; Zijlstra, B.; Groeneveld, E.; Berben, P. H.; Boereboom, J. M.; Hensen, E. J. M.; et al. Understanding Carbon Dioxide Activation and Carbon−Carbon Coupling over Nickel. *Nat. Commun.* **2019**, *10*, No. 5330.
(59) Chen, H.-Y. T.; Tosoni, S.; Pacchioni, G. Hydrogen Adsorption, Dissociation, and Spillover on Ru 10 Clusters Supported on Anatase TiO 2 and Tetragonal ZrO 2 (101) Surfaces. *ACS Catal* **2015**, *5*, 5486−5495.
(60) Sihag, A.; Xie, Z.-L.; Thang, H. V.; Kuo, C.-L.; Tseng, F.-G.; Dyer, M. S.; Chen, H.-Y. T. DFT Insights into Comparative Hydrogen Adsorption and Hydrogen Spillover Mechanisms of Pt_4/Graphene and Pt_4/Anatase (101) Surfaces. *J. Phys. Chem. C* **2019**, *123*, 25618−25627.
(61) Prats, H.; Piñero, J. J.; Viñes, F.; Bromley, S. T.; Sayós, R.; Illas, F. Assessing the Usefulness of Transition Metal Carbides for Hydrogenation Reactions. *Chem. Commun.* **2019**, *55*, 12797−12800.

https://doi.org/10.1021/acs.jpcc.1c03219
J. Phys. Chem. C 2021, 125, 12019−12027

Journal of Catalysis 425 (2023) 203–211

Contents lists available at ScienceDirect

Journal of Catalysis

journal homepage: www.elsevier.com/locate/jcat

Research article

Limitations of free energy diagrams to predict the catalytic activity: The reverse water gas shift reaction catalyzed by Ni/TiC

Pablo Lozano-Reis [a,*], Hector Prats [b,*], Ramón Sayós [a], Francesc Illas [a]

[a] Departament de Ciència de Materials i Química Física & Institut de Química Teòrica i Computacional (IQTCUB), Universitat de Barcelona, C. Martí i Franquès 1, 08028 Barcelona, Spain
[b] Department of Chemical Engineering, University College London, Roberts Building, Torrington Place, London WC1E 7JE, UK

ARTICLE INFO

Article history:
Received 10 March 2023
Revised 24 May 2023
Accepted 27 May 2023
Available online 1 June 2023

Keywords:
Surface coverage
kinetic Monte Carlo
Density Functional Theory
Kinetic modeling
Mechanistic analysis
Rational design
Reverse water-gas shift reaction

ABSTRACT

The temporal evolution at the catalyst surface is a result of an intricate interplay between all involved microscopic events such as adsorption, desorption, diffusion, and bond breaking/formation steps, and the interaction with the surrounding environment. By properly including these effects, kinetic Monte Carlo (kMC) simulations can accurately describe the complexity of real catalysts, unravel the dominant reaction mechanisms and provide fundamental understanding towards the rational design of novel catalysts. In this work, we combine density functional theory (DFT) calculations, statistical thermodynamics and kMC simulations to study the reverse water–gas shift (RWGS) reaction on Ni/TiC, a bifunctional catalyst. The predictions from DFT energy profiles do not coincide with the outcome of the kMC simulations, evidencing the limitations of the former, especially in including the effect of coverage of surface species, which plays a crucial role. The kMC simulations results are in remarkable agreement with the experimental data, proving that the kMC simulations are able to describe the complex chemistry of the RWGS reaction on a bifunctional catalyst.

1. Introduction

Experimentally, it is extremely challenging to understand why a given material can be highly active towards a particular reaction, which is crucial for a rational design of novel catalysts. This is, in part, because of the high complexity of real industrial catalysts, which typically involves metal clusters or nanoparticles supported over some substrate with many active regions that are exposed to the incoming reactants [1]. Moreover, many industrial reactions encompass a large number of adsorbed species and elementary steps that take place simultaneously. Despite notable progress in the use of experimental *operando* techniques [2–8], a detailed description of the active sites and dominant reaction path is still out of reach. The rational design of efficient catalysts is generally unfeasible without a clear guidance from theoretical modeling, ideally going from the atomic and molecular level to the macroscopic scale. Quantum mechanical calculations, most often in the framework of Density Functional Theory (DFT), provide useful insights into the molecular reaction mechanism, such as the energetics of the different adsorbates and transition states involved, which allow for the construction of the potential energy surfaces (PES), usually approximated investigating each elementary step separately, or Gibbs free energy diagrams at temperature and pressure conditions of interest. The obtained profiles are often used to unveil the most plausible path, at least from a static point of view. Note, however, that rigorously speaking one should consider pre-exponential factors as relying on energy barriers only can be misleading. Nevertheless, the information provided from the electronic structure calculations, hereafter assumed to rely on DFT, is generally insufficient to correctly determine the time evolution and thus to disclose the dominant reaction mechanism [9,10]. This is particularly the case for reactions involving many elementary steps and/or complex catalysts facing different active regions. In fact, the coverage of different species involved in a heterogeneously catalyzed reaction can be extremely important in determining the time evolution under working conditions to the point that it may not be possible to predict the catalytic activity or unveil the dominant reaction pathway along time from solely DFT calculations, except perhaps for simple systems.

To bridge the gap between the static picture at the atomic level and the macroscopic regime, DFT calculations must be coupled with kinetic modelling techniques [11–14] that capture adsorbate mobility (diffusion), steric exclusion effects, complex reaction patterns involving adsorbates in specific binding configurations,

* Corresponding authors.
E-mail addresses: p.lozano@ub.edu (P. Lozano-Reis), h.garcia@ucl.ac.uk (H. Prats).

https://doi.org/10.1016/j.jcat.2023.05.026
0021-9517/

spatial correlations arising from adsorbate lateral interactions and changes in the energy barriers due to the presence of neighboring spectator species. These effects can be modelled by means of kinetic Monte Carlo (kMC) simulations and used in this work to illustrate that the conclusions extracted from DFT energy diagrams are in complete disagreement with the outcome of kMC simulations. This is illustrated taking the case of the reverse water–gas shift (RWGS) reaction ($CO_2 + H_2 \rightarrow CO + H_2O$) on Ni/TiC. The choice of this system comes from a series of recent works, where transition metal carbides (TMCs) have been shown to be active supports for small metal clusters, presenting a catalytic activity and selectivity much superior to the same particles dispersed on more traditional oxide supports [15], a result of the strong polarization of the electron density of the supported particles [16,17]. For instance, small Ni particles dispersed on TiC are able to dissociate CH_4 at room temperature [18] and displays a catalytic activity towards the RWGS reaction that is two orders of magnitude higher compared to that of the clean TiC(001) surface [19]. Preliminary DFT calculations suggested that the overall CO production was dominated by the Ni cluster [20], but the underlying chemistry responsible for this boost of catalytic activity is, however, not totally understood, as it involves a network of elementary steps taking place in three distinct regions: the supported Ni cluster, the bare TiC region, and the interface region that lies in the middle.

Here, we combine DFT calculations with kMC simulations to study the RWGS reaction on the complex Ni/TiC catalyst. The DFT derived PES suggests that the catalytic activity decreases in the order Ni > interface > TiC. However, the kMC simulations show a completely opposite trend, with the TiC region being the most active one, and the Ni region almost acting as a mere spectator. This surprising result is directly related to the key role of surface coverage and site blocking, an aspect that cannot be captured from DFT calculations only. Even more, the kMC simulations explain why the Ni/TiC catalyst is more active than the bare TiC surface, even if the TiC region is the active one which, again, is attributed to coverage effects. Remarkably, the present kMC simulations not only correctly capture the relative increase in turnover frequency (TOF) between Ni/TiC and TiC but predict a TOF absolute value in close agreement with experiment [19]. This work reaffirms the importance of kinetic studies beyond the analysis of DFT energy barriers or (free) energy profiles, and highlights the fundamental role played by the surface coverage of the different adsorbates, which tends to be ignored.

2. Methods

DFT Calculations. To characterize the energetics of the RWGS reaction on Ni/TiC, spin polarized periodic DFT calculations using the BEEF-vdW functional [21] have been carried out by means of the Vienna Ab Initio Simulation Package (VASP) code [22–24]. An appropriate supercell (Fig. 1a) has been used to represent the three different regions of the TiC system: the supported Ni cluster (Ni region), the interface between the Ni cluster and the TiC support (interface region), and the bare TiC surface (TiC region). Because all three regions are catalytically active, we have computed the formation energies for the different adsorbates and properly characterized transition states, which are needed for the subsequent kMC simulations, as well as quantifying the energy barriers for diffusion steps and the lateral interactions between adsorbates. In addition, Gibbs free energy profiles are presented which permit to account for temperature and pressure effects. The free energy profiles are obtained following the procedure outlined by Nørskov *et al.* [25]. Further details on the used computational setup and how formation energies and lateral interactions are calculated can be found in Section S1, S2 and S3 in the Supporting Information, respectively. Note that the choice of 4 atoms for the Ni cluster is because experiments suggests the active particles to be small (few atoms) and 2D [19], and subsequent computational studies confirmed the high activity of Ni_4 clusters for the CO_2 and H_2 activation [20]. Morevoer, this particular size features a compact, high symmetry structure that maximizes the atomic coordination with *fcc* TiC and is thus highly likely to be energetically stable.

Kinetic Monte Carlo simulations. The simulations have been carried out using the graph-theoretical kMC approach [26] combined with cluster expansion Hamiltonians [27,28] for the surface energetics as implemented in the Zacros code (version 3.01) [26,27]. The kMC lattice model (Fig. 1b) is built so as to mimic the slab model used for the DFT calculations (Fig. 1a), and consists of a 4×4 periodic custom grid of 68 points— or a total of 1088 points— representing surface sites, where the different species can adsorb, desorb, react or diffuse. A total of 8 different site types have been used, as described next. For the TiC region, surface C and Ti atoms are represented by tTi and tC sites. For the interface region, C atoms are represented by tC_{in} sites and the two different types of Ti atoms are represented by $tTi_{in\text{-}1NN}$ and $tTi_{in\text{-}2NN}$, where 1NN and 2NN stand for 1st-nearest neighbors and 2nd-nearest neighbors, respectively. Mapping the DFT calculations, all C and Ti sites can be occupied by monodentate species, such as CO adsorbed on tC, or multidentate species such as HCOO occupying two neighboring tTi sites. The supported Ni_4 cluster is represented by a single coarse-grained lattice site labeled as Ni. This special choice is made because most adsorbed species occupy the whole Ni_4 cluster. By using a single Ni site instead of four Ni sites, the use of many tridentate and tetradentate species is avoided, simplifying the input files. For the few cases in which two species are simultaneously adsorbed on the supported cluster, we make use of double labels; in this way, $OH+OH^{Ni}$ label represents two OH species coadsorbed on the Ni_4 cluster. Finally, to avoid the use of a "hard sphere" model for small adsorbates like H and H_2, we use special hydrogen reservoir sites [29]; h and h_{Ni} for those H or H_2 species far and near the Ni_4 cluster, respectively. We must point out that the convergence with respect to lattice size has been verified by computing the steady state TOFs at larger lattice sizes, finding no significant difference (Table S1).

The reaction network involves a total set of 82 reversible reactions, including adsorption, desorption, diffusion and surface reaction steps. The huge number of elementary reactions arises from the heterogeneity of the Ni/TiC model and from the possibility of having the different elementary steps occurring with both reactants/products at the same region, or in different regions with a concomitant change on the energetics. Obviously, the casuistic has been explicitly contemplated on the DFT calculations and transferred to the kMC simulations. The cluster expansion used in our model includes pairwise lateral interactions between all possible reactant/product pairs as well as all other relevant species and has been truncated to 1NN two-body terms, although some 2NN two-body terms have also been included. Overall, it contains 40 one-body terms and 105 two-body terms, which are summarized in Table S2 and S3 in the Supporting Information. Making use of the cluster expansion and of the Brønsted-Evans-Polanyi relations is it possible to capture the effect that local reaction environment has on the coverage-dependent energy barriers which is crucial to properly describe the temporal evolution on the catalyst surface [30–33]. The difference in time scales of all processes has been handled by manual scaling of the transition probabilities of the fastest processes by some scaling factor $\alpha < 1$ to speed up the kMC simulations while ensuring that this does not affect the final results. This pragmatic solution has been previously applied in several studies [29,34–37].

We have considered an initial mixture of CO_2 and H_2 continuously impinging on an initially empty surface, in which different

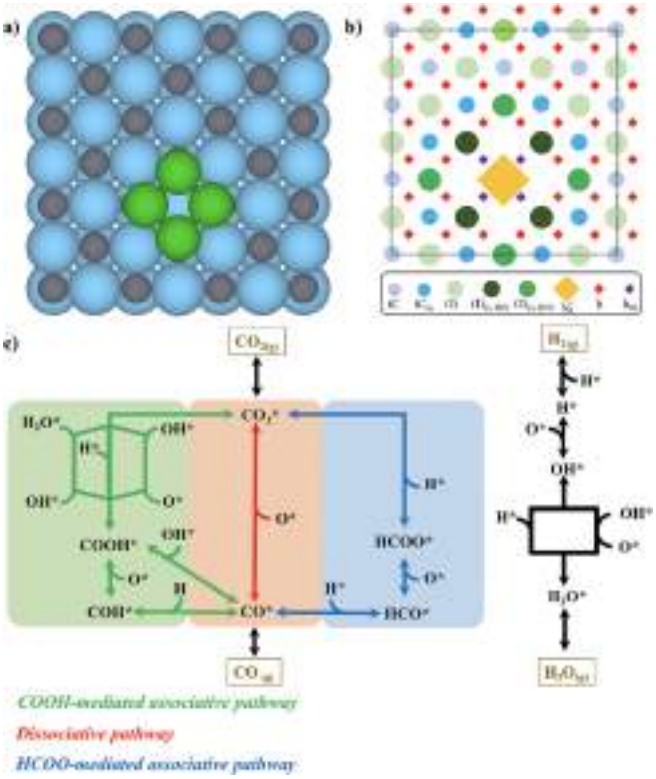

Fig. 1. a) Unit cell for the Ni/TiC surface model used on the DFT calculations. Grey, light blue and green represent C, Ti and Ni atoms, respectively. b) Lattice model used for the kMC simulations of the Ni/TiC model. Black dashed lines show the unit cell. c) Possible reaction pathways of the RWGS reaction. (For interpretation of the references to colour in this figure legend, the reader is referred to the web version of this article.)

surface processes can take place, and afterward, the formed products can desorb and leave the surface without allowing for subsequent re-adsorption. The working conditions are chosen as in the experiments by Rodriguez *et al.* [19], which are: $P(H_2)$ = 4.5 bar and $P(CO_2)$ = 0.5 bar and temperatures ranging from 500 K to 600 K. All the simulations have been run until at least 1000 molecules of CO have been produced under steady state conditions. For each operating condition, we have run 5 different simulations that differ from each other only in the sequence of random numbers used. Therefore, the overall macroscopic properties here reported correspond to an average of the production stage of five independent kMC simulation replicas. The kMC setup used for the clean TiC model is summarized in Section S4. From the results of the kMC simulations, we obtain *(i)* the event frequencies of the different processes, defined as the number of times an event is executed per unit time and area (the TOF is therefore the event frequency for CO or H_2O desorption); and *(ii)* the site occupancy for each adsorbate species in each site type, defined as the average number of labels of a particular adsorbate (or dentates in the case of multidentate species) on a particular site type divided by the total number of sites of that type. The site occupancy is therefore a measure of the surface coverage.

3. Results

3.1. The static atomistic picture.

In principle, the reasons why the RWGS activity on Ni/TiC is two orders of magnitude higher than on TiC can be obtained from inspecting the PES. More in detail, by locating the relevant stationary points corresponding to reactants, intermediates, products and the transition states between them. The RWGS reaction mechanism can proceed either through the dissociative (CO_2* dissociation) or associative (COOH* or HCOO* formation) pathways as shown in Fig. 1c. Let us start by considering the associative mechanisms. From the energy barriers listed in Table S4, it appears that one can consider just the COOH* intermediate because the HCOO* intermediate is generally harder to form simply because COOH* formation is favored on the TiC and interface regions while HCOO* formation is only preferred over the Ni region. Results in Table S4 also suggest that the COOH formation always occurs through CO_2* reacting with H* and not with OH*. For each region in the Ni/TiC catalyst, we focus now on the dissociative (CO_2*→ CO*+O*) and the COOH-mediated associative (CO_2*+H*→ COOH*→ CO*+OH*) pathways. In the TiC region, the free energy diagram in Fig. 2a, at

the specified realistic conditions, suggests that the dissociation pathway, with a barrier of 1.03 eV, probably dominates. The COOH* formation step, despite having a quite low barrier of 0.80 eV, is very uphill, resulting in a reverse energy barrier from COOH* back to CO_2* of 0.31 eV only. Moreover, bimolecular steps such as COOH* formation are limited by the availability of reactants and therefore less likely to occur than unimolecular ones. In the interface region, the free energy diagram indicates that the dissociative pathway clearly dominates, with an energy barrier of 0.72 eV compared to the 1.02 eV barrier for COOH* formation as shown in Fig. 2b. This is also the case for the supported Ni cluster (Fig. 2c), where the energy barriers for CO_2* dissociation and COOH* formation are 0.54 and 1.42 eV, respectively. From this information one would conclude that the RWGS reaction activity of the different regions increases in the order TiC < interface < Ni; this is following the trend of the energy barriers for CO_2 dissociation— 1.03, 0.72 and 0.54 eV for TiC, interface, and Ni, respectively— as shown in Fig. 2d. Therefore, the analysis of the DFT derived free energy diagram suggests that the dissociative pathway is the dominant reaction mechanism; and that the higher activity of Ni/TiC for the RWGS reaction, compared to TiC, is mainly due to the superior ability of the Ni cluster (and the interface, to a lower extend) to break CO_2* compared to the TiC region. In the next section, we will show why this is a largely oversimplified picture.

3.2. Accounting for kinetics and going to macroscopic scale leads to surprises

One may naively think that the outcome of a kinetic study is just to complement the picture arising from the analysis of the PES, bringing details concerning conversion at given conditions of pressure and temperature. This implies accepting that the conclusions from the static picture hold when going to a macroscopic scale, when temperature and pressure are properly defined. While this may be the case for simple model systems with few elementary steps and no different regions, it is not at all the case here where the system under study closely resembles a real catalyst. In fact, the present kMC simulations, carried out with rates derived from the same DFT calculations, show that almost all CO is produced over the TiC region— 98 % at 500 K and 89 % at 600 K— mainly following the COOH-mediated associative pathway, and the remaining CO is produced at the interface (see TOF values in Fig. 3a). This is in clear contradiction with the activity order and dominant reaction mechanism extracted from the analysis of the DFT PES. A careful inspection of the kMC simulation results shows that the coverage effects along with site availability are responsible for this mismatch between DFT predictions and kMC results, as explained in detail below. In other words, when the catalyst starts to be populated the picture obtained from a single reaction breaks down.

To further support the claims above it is enough to see that, at the initial stage of the simulations (see Fig. 3b), CO_2 adsorbs and dissociates over the Ni cluster, producing O* on the interface and CO* on the cluster which further diffuses to the interface and desorb. Next, H_2 adsorbs and dissociates over the Ni cluster to produce H* that hydrogenates the O* species to produce OH* at the cluster. Then, attractive adsorbate–adsorbate interactions between OH* and neighboring H*, CO_2* and O* species make the OH*+OH* → H_2O*+O* reaction over the Ni cluster very endothermic (Figure S1), with the concomitant cluster poisoning with OH* species, while hindering the adsorption of other species on the cluster. Meanwhile, CO_2 adsorbs at the interface and dissociates producing CO* and more O* at the interface sites. The produced CO* desorbs while most of the O* adatoms remain on the interface, creating a partial poisoning of that region. CO_2 can still be adsorbed at the interface

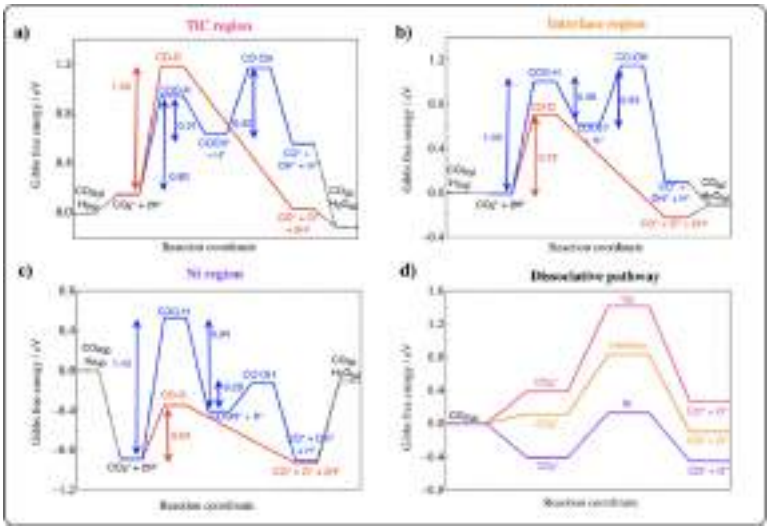

Fig. 2. Gibbs free energy diagrams at T = 550 K and P(CO_2) = 0.5 bar, P(H_2) = 4.5 bar, P(CO) = 0.001 bar and P(H_2O) = 0.001 bar for the dissociative (red) and the COOH-mediated associative (blue) pathways in a) the TiC region; b) the interface region; and c) the Ni cluster. d) Gibbs free energy profiles for CO_2 adsorption and dissociation over the Ni cluster, the interface region and TiC region (purple, orange, and pink lines, respectively). (For interpretation of the references to colour in this figure legend, the reader is referred to the web version of this article.)

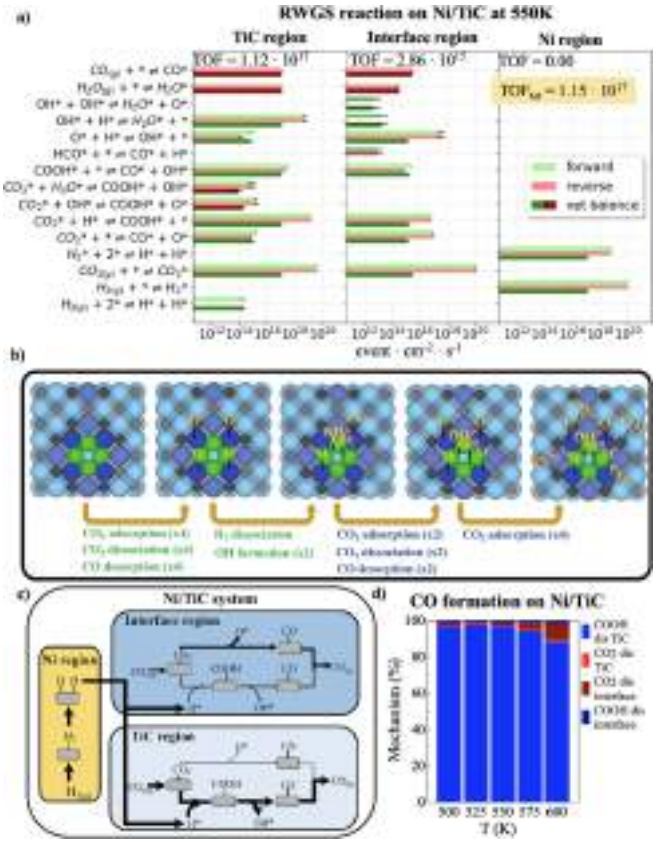

Fig. 3. a) Event frequency of the RWGS reaction on Ni/TiC at T = 550 K and P(H_2) = 4.5 bar and P(CO_2) = 0.5 bar at the different regions. b) Cluster and interface poisoning at the initial stages of the kMC simulations. c) Scheme of the observed mechanism for Ni/TiC model with the role of each region of the catalyst. d) Percentage of the dissociative and COOH-mediated pathways on the final CO production at five different temperatures.

region, but it cannot dissociate due to the site blocking produced by the O* atoms at the interface. Table 1 shows that, at the steady state, all Ni sites are poisoned by OH*, while the interface is partially poisoned by O*. Therefore, the RWGS reaction at steady state conditions occurs almost entirely at the TiC region contrary to what one can infer from the DFT potential energy surface. This

Table 1
Percentage of site occupancy for the different species that are adsorbed on the surface of the Ni/TiC model catalyst at 550 K under steady state conditions. Values of 0.0 represent an occupation lower than 0.05 % while dashes (-) means that this species cannot adsorb at that site.

T = 550 K	Site occupancy (%)							
Species	**tC**	**tTi**	**tC_{in}**	**$tTi_{in\text{-}1NN}$**	**$tTi_{in\text{-}2NN}$**	**Ni**	**h**	**h_{Ni}**
H_2O^*	–	0.1	–	–	0.0	0.0	–	–
COOH*	0.0	0.0	0.0	–	0.0	0.0	–	–
CO*	1.7	–	0.0	–	0.0	0.0	–	–
O*	12.8	–	5.0	89.0	0.1	0.0	–	–
CO_2^*	11.9	59.6	49.3	–	98.5	0.0	–	–
OH*	–	0.8	–	–	0.0	0.0	–	–
OH*+OH*	–	–	–	–	–	100.0	–	–
H*	–	–	–	–	–	–	34.8	50.2
H_2^*	–	–	–	–	–	–	–	2.4
Total	26.4	60.5	54.3	89.0	98.6	100.0	34.8	52.6

unexpected and interesting phenomenon can only be captured by kMC simulations, which naturally accounts for the effect of surface coverage.

At this point, one could argue that it is also possible to include coverage effects in the PES by performing the pertinent energy barrier calculations at a chosen coverage, thus improving the accuracy of the prediction from the PES. This possibility, however, becomes unpractical when the structure of the adlayer under operating conditions is unknown and the number of possible combinations of adsorbates in the neighboring sites is very high, as it is the case for the RWGS on Ni/TiC. Note that the equilibrium coverage does not only depend on the formation energies of all species, but also on the lateral interactions between them and kinetic effects due to the interconnection of the possible elementary steps and correlations in the occupation of neighboring sites due to reactions. Kinetic models are thus required to appropriately account for the effect of the coverage. Finally, one can use the predicted coverage from the kMC simulations to re-calculate the PES at the new conditions, which would enable a better agreement between the kMC simulations and the predictions from the PES. Additional details on the coverage of surface species and number of product molecules produced during the initial stage of the reaction can be found in Figures S2 and S3, respectively.

A deeper analysis at the steady state event frequencies provides additional interesting insights into the reaction mechanism of the RWGS on Ni/TiC and about the main contributions of each region of the catalyst. Fig. 3b displays the event frequency plot at T = 550 K whereas information for the event frequency and coverages at all the temperatures studied are reported in Figure S4 and Table S5. Most H* species are formed over the Ni cluster in which only H_2 can adsorbs and dissociate, followed by a spillover of H* to the TiC region where it reacts with CO_2* to produce the COOH* intermediate. The role of the Ni cluster is, therefore, to facilitate hydrogenation reactions by dissociating H_2 and the subsequent spillover. The interface region produces some CO*, either via CO_2* dissociation or the COOH-mediated associative pathways, although to a much lesser extent than the TiC region. This is due to the high O* coverage that blocks available sites, as explained above. The contribution of the interface region increases with the reaction temperature, since the O* coverage is reduced. Last but not least, the TiC region is the main responsible for CO production, mainly via the COOH-mediated associative route because of the significant H* coverage (Table 1) that facilitates the COOH* formation. Note that CO_2* needs a free neighboring tC site to dissociate, an unlikely situation due to the high coverage, favoring the COOH-mediated associative pathway. This observation shows the importance of site availability and that it is necessary to consider free sites as actual reactants involved in the reaction. Note also that most of the water formation comes from the hydrogenation of OH* formed during the COOH* dissociation at the TiC region. A scheme of the overall reaction mechanism is illustrated in Fig. 3c, showing the synergy between the Ni cluster and the TiC surface, the former acting as a H* source and the latter using this H* to form COOH* and subsequently dissociating it to produce CO*. Moreover, the supported Ni cluster also changes the energetics of the neighboring Ti and C surface atoms (i.e., interface region), which can be very reactive at much higher temperatures (Fig. 3d), when the partial O* poisoning effect of the tTi sites is diluted.

3.3. Why is Ni/TiC much more active than TiC?

The analysis in the previous subsection shows that the TiC region dominates the RWGS reaction catalytic activity in Ni/TiC, which raises the question of why then TiC is two orders of magnitude less active than Ni/TiC. This controversy requires comparing kMC simulations for the two systems. Fig. 4a shows that the calculated turn over frequencies of both systems and the experimental ones [19] are in remarkable agreement, meaning that the chemistry of both systems is well captured by the kMC simulations employing the DFT derived rates. Nevertheless, some differences exist between the experimental systems and the theoretical model that are worth to note when aiming at a quantitative comparison. First, the Ni/TiC model corresponds to a Ni coverage of 0.14 ML, instead of the 0.10 ML coverage used in the experiments, and the experimental system corresponds to an ensemble of Ni clusters of different sizes and morphologies, while our model assumes that all clusters are flat and composed of 4 Ni atoms. Furthermore, additional deviations may arise from the limitations of the kMC method itself, errors in the computed DFT energetics or also in the truncation to two-body terms in the cluster expansion, which could be important at high surface coverages, among other limitations. These considerations explain why the agreement between kMC results and experiments is excellent for the RWGS on TiC(001) and just almost quantitatively correct for the Ni/TiC. In the TiC (001), the model closely approaches the real system, whereas in Ni/TiC, the complexity of the real system is not completely reproduced. In spite of these differences, the kMC simulations properly predict a much higher activity of the Ni/TiC system. In the following, we unveil the origin of this difference.

Fig. 4b shows that the dissociative pathway is responsible for most of the CO molecules produced on TiC, becoming even more dominant as the temperature rises. This is in contrast with the TiC region of Ni/TiC, in which the contribution of the dissociative route is practically negligible, with most of CO molecules produced from the COOH-mediated associative pathway. Since, for the relevant elementary steps, the energy barriers in either clean TiC or TiC region of Ni/TiC are the same, the natural question is where the calculated and experimentally observed difference in activity comes from. Again, the answer lies in the catalyst surface coverage, which plays a fundamental role. Table 2 shows that, on the clean TiC surface, only O* and CO_2* species have a significant coverage. Compared to the coverage of the TiC region in Ni/TiC (Table 1), we observe similar values for CO_2* but important differences for the O* and H*. At 550 K, the O* site occupancy of tC sites increases from 13 % for Ni/TiC to 46 % for TiC, while the H* site occupancy of h sites decreases from 35 % for Ni/TiC to 1 % for TiC. These differences are directly related to the change in the mechanism that drives the reaction, as the probability of some elementary reactions to be executed change with these magnitudes. The low H* coverage on clean TiC makes the COOH* formation more unlikely, decreasing not only the weight that the associative pathway has in comparison to the TiC region of Ni/TiC, but also drastically lowering the total TOF of the reaction. In spite of this, the event frequency plot shows that the COOH* formation step still occurs more times than the CO_2* dissociation, but in the vast majority of cases it goes backwards to CO_2* due to the low energy barrier of the reverse direction of only 0.26 eV (R15). Moreover, the high O* coverage on clean TiC also contributes to more COOH* going backwards to CO_2* due to its reaction with O* (i.e., COOH* + O* → CO_2* + OH*), further decreasing the overall TOF of the reaction. The direct CO_2* dissociation occurs less frequently, but this is a much more irreversible process: the energy barrier in the reverse direction is 1.08 eV (-R11), relatively high. Therefore, the net balance is higher for the dissociative pathway, making it the dominant reaction mechanism on clean TiC as schematically shown in Fig. 4c and as can be anticipated from the analysis of the PES. The event frequency and coverages at all the temperatures studies are reported in Figure S5 and Table S6.

The dominant reaction mechanism can change with temperature due to changes in the coverage, which can also be captured in kMC simulations. For instance, the amount of CO molecules produced from the dissociative pathway in the clean TiC surface

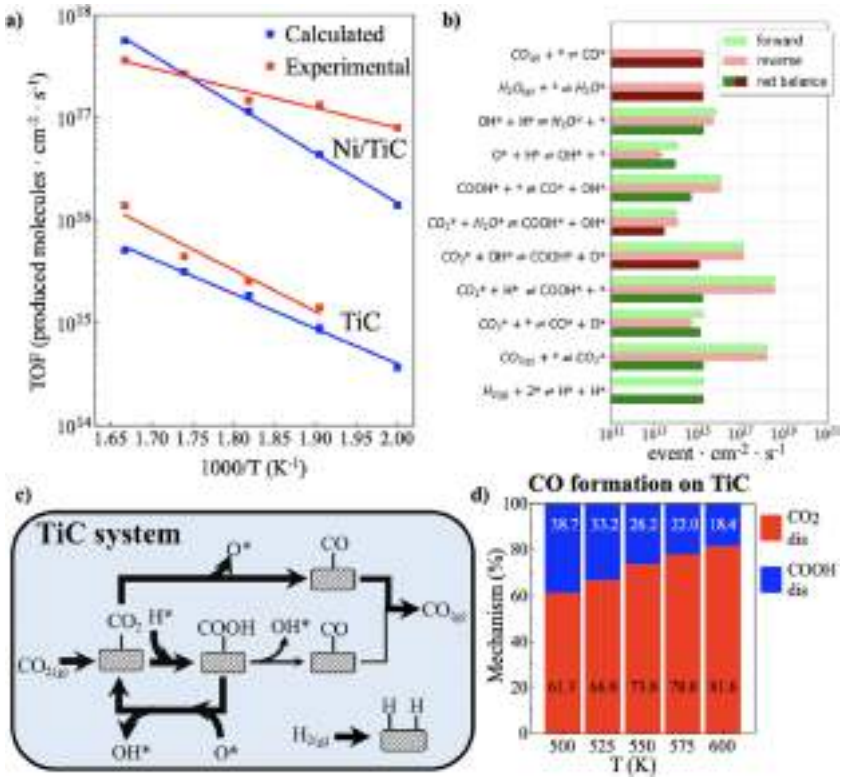

Fig. 4. a) Calculated and experimental (from ref. 19) turn over frequencies for the CO production at different temperatures for the TiC and Ni/TiC systems. b) Event frequency of the RWGS reaction on the TiC model at T = 550 K and P(H_2) = 4.5 bar and P(CO_2) = 0.5 bar. c) Scheme of the observed mechanism for the TiC model. d) Percentage of the dissociative and COOH-mediated pathways on the final CO production at five different temperatures.

Table 2
Percentage of site occupancy for the different species that are adsorbed on the TiC surface at 550 K under steady state conditions. Values of 0.0 represent an occupation lower than 0.05 % while dashes (-) means that this species cannot adsorb at that site.

T = 550 K	Site occupancy (%)		
Species	**tC**	**tTi**	**h**
CO*	0.0	–	–
O*	46.1	–	–
OH*	–	0.1	–
H_2O*	–	0.1	–
CO_2*	10.0	19.9	–
COOH*	0.2	0.4	–
H*	–	–	0.9
Total	**56.3**	**20.5**	**0.9**

increases from 61 % at 500 K to 82 % at 600 K (Fig. 4d). This change is directly related to the lower CO_2* and H* surface coverage at higher temperatures, hindering even more the COOH-mediated associative pathway. Note that the total coverage, in general, decreases with temperature, favoring unimolecular reactions over bimolecular ones. Finally, it is important to recall that the energetic interactions of reactants with neighboring spectator species can influence the energy barriers of elementary steps, as shown in Table S7. For instance, the energy barrier at the zero-coverage limit (i.e., obtained from DFT calculations with no spectator species) for COOH* dissociation to CO* + OH* in the TiC region is 0.50 eV (R29), but the average energy barrier computed by the cluster expansion in the kMC simulations is only 0.31 eV (550 K, Ni/TiC system). Since this is one of the most important elementary steps, this decrease has a significant impact in the overall TOF.

4. Conclusions

DFT calculations combined with kMC simulations have been performed to unravel the boost of activity experimentally observed for the RWGS reaction on Ni/TiC compared to TiC. The agreement between experimental and calculated data is remarkable and provides strong support to the conclusions that are derived from the present study. We show that, to a large extent, the conclusions that can be extracted from the analysis of the DFT potential energy surface coincide with those of the kMC simulations for the reaction taking place at the bare TiC surface. However, a completely different situation is found for the reaction at the more complex Ni/TiC

system. The analysis of the PES suggest that the dissociative pathway is the dominant reaction mechanism in all three regions of Ni/TiC, with the catalytic activity increasing in the order: TiC < interface < Ni, but spatially resolved kMC simulations point to the opposite direction, unveiling that CO is mainly produced in the TiC region via the COOH-mediated associative pathway. Moreover, kMC simulations show that the increased activity of Ni/TiC compared to TiC is not because of the lower energy barriers of many elementary steps on the Ni cluster, but due to a synergic effect between the supported Ni clusters and TiC. The former break H_2* to H*+H* much faster, and the H* spillover from the Ni clusters to the TiC region drastically boosts its catalytic activity towards the RWGS reaction. A surface poisoning of the Ni and interface regions at the initial stages of the reaction is responsible for the TiC region to be the active one as site blocking forbid reactivity on the Ni and interface regions, which is not possible to predict from the calculated PES.

While (free) energy profiles, mainly derived from DFT, have been instrumental in advancing our understanding of catalytic processes, they may be insufficient to come out with sound predictions or even to explain observations. Among other limitations, they do not easily account for the effect of surface coverage, which will require updating the potential energy surface for each situation, which becomes unpractical. Indeed, the present work shows that coverage effects and site blocking play a key role in determining the catalytic activity of the Ni/TiC system and it is likely that this conclusion will hold for complex catalysts that cannot be represented by an extended, almost perfect surface. This study highlights the importance of combining the electronic structure derived picture of the reactivity with kinetic modeling techniques, in particular kMC simulations, as a fundamental tool to delve deeper into the inner workings of complex catalytic systems, unravelling the role of complexity and developing a fundamental understanding towards the rational design of novel catalysts.

Data availability

The data used in this work have been made available on a public GitHub repository: https://github.com/plozanore/Surface_coverage_DFT_vs_kMC.

Declaration of Competing Interest

The authors declare that they have no known competing financial interests or personal relationships that could have appeared to influence the work reported in this paper.

Acknowledgments

The research at the Universitat de Barcelona has been supported by the Spanish Ministry of Science, Innovation and Universities (MICIUN) Spanish MCIN/AEI/10.13039/501100011033 PID2021-126076NB-I00 project, funded partially by FEDER Una manera de hacer Europa, and María de Maeztu CEX2021-001202-M grants, including funding from European Union and, in part, by and COST Action CA18234 by the Generalitat de Catalunya grant 2021SGR00079. PLR acknowledges MICIUN for a predoctoral FPU18/02313 grant. HPG acknowledges the funding received from the European Union's Horizon 2020 research and innovation programme under the Marie Skłodowska-Curie Grant Agreement No. 891756. Computational resources provided by Consorci de Serveis Universitaris de Catalunya (CSUC, former CESCA) with financial support from Universitat de Barcelona and Red Española de Supercomputación (grants QS-2020-1-0003 and QS-2020-2-0009) are gratefully acknowledged.

Appendix A. Supplementary material

Supplementary data to this article can be found online at https://doi.org/10.1016/j.jcat.2023.05.026.

References

[1] J.M. Thomas, W.J. Thomas, Principles and Practice of Heterogeneous Catalysis, VCH, Weinheim, 1997.
[2] M.A. Bañares, Operando methodology: combination of in situ spectroscopy and simultaneous activity measurements under catalytic reaction conditions, Catal. Today 100 (2005) 71–77.
[3] B.M. Weckhuysen, Determining the active site in catalytic process: operando spectroscopy is more than a buzzword, Phys. Chem. Chem. Phys. 5 (2003) 4351–4360.
[4] H. Topsøe, Developments in operando studies and in situ characterization of heterogeneous catalysts, J. Catal. 216 (2003) 155–164.
[5] A.D. Handoko, F. Wei, Jenndy, B.S. Yeo, Z.W. She, Understanding heterogeneous electrocatalytic carbon dioxide reduction through operando techniques, Nat. Catal. 1 (2018) 922–934.
[6] K. Feng, Y. Wang, M. Guo, J. Zhang, Z. Li, T. Deng, Z. Zhang, B. Yan, In-situ/Operando techniques to identify active sites for thermochemical conversion of CO_2 over heterogeneous catalysis, J. Energy Chem. 62 (2021) 153–171.
[7] Y. Li, S. Zhao, R. Tappero, U. Jung, A. Elsen, P.h. Baumman, R.G. Nuzzo, E.A. Stach, A.I. Frenkel, Complex structural dynamics of nanocatalysts revealed in operando conditions by correlated imaging and spectroscopy probes, Nat. Commun. 6 (2015) 7583.
[8] J. Goetze, I. Yarulina, J. Gascon, F. Kapteijn, B.M. Weckhuysen, Revealing lattice expansion of small-pore zeolite catalysts during the methanol-to-olefins process using combined operando X-ray diffraction and UV-vis spectroscopy, ACS. Catal. 8 (2018) 2060–2070.
[9] E.A. Walker, D. Mitchell, G.A. Terejanu, A. Heyden, Identifying active sites of the water-gas shift reaction over titania supported platinum catalysts under uncertainty, ACS. Catal. 8 (2018) 3990–3998.
[10] B. Kreitx, K. Sargsyan, K. Blöndal, E.J. Mazeau, R.H. West, G.H. Wehinger, T. Turek, C.F. Goldsmith, Quantifying the impact of parametric uncertainity on automatic mechanism generation for CO_2 hydrogenation on Ni(111), JACS Au 1 (2021) 1656–1673.
[11] A. Bruix, J.T. Margraf, M. Andersen, K. Reuter, First-principles-based multiscale modeling of heterogeneous catalysis, Nat. Catal. 2 (2019) 659–670.
[12] M. Pineda, M. Stamatakis, Kinetic Monte Carlo simulations for heterogeneous catalysis: fundamentals, current status, and challenges, J. Chem. Phys. 156 (2022).
[13] L. Grajciar, C.J. Heard, A.A. Bondarenko, M.V. Polynski, J. Meeprasert, A.E. Pidko, P. Nachtigall, Towards operando computational modeling in heterogeneous catalysis, Chem. Soc. Rev. 47 (2018) 8307–8348.
[14] A.H. Motagamwala, J.A. Dumesic, Microkineti33c modeling: a tool for rational catalyst design, Chem. Rev. 121 (2021) 1049–1076.
[15] J.A. Rodriguez, J.P. Ramírez, A.R. Gutierrez, Highly active Pt/MoC and Pt/TiC catalysts for the low-temperature water-gas shift reaction: effects of the carbide metal/carbon ration on the catalyst performance, Catal. Today 289 (2017) 47–52.
[16] H. Prats, M. Stamatakis, Atomistic and electronic structure of metal clusters supported on transition metal carbides: implications for catalysis, J. Mater. Chem. A 10 (2022) 1522–1534.
[17] P. Lozano-Reis, R. Sayós, J.A. Rodriguez, F. Illas, Structural, electronic, and magnetic properties of Ni nanoparticles supported on the TiC(001) surface, Phys. Chem. Chem. Phys. 22 (2020) 26145–26154.
[18] H. Prats, A.R. Gutiérrez, J.J. Piñero, F. Viñes, T.S. Bromley, J.P. Ramírez, J.A. Rodriguez, F. Illas, Room temperature methane capture and activation by Ni clusters supported in TiC(001): effects of metal-carbide interactions on the cleavage of the C-H bond, J. Am. Chem. Soc. 141 (2019) 5303–5313.
[19] J.A. Rodriguez, J. Evans, L. Feria, A.B. Vidal, P. Liu, K. Nakamura, F. Illas, CO_2 hydrogenation on Au/TiC, Cu/TiC and Ni/TiC catalysts: production of CO, methanol, and methane, J. Catal. 307 (2013) 162–169.
[20] P. Lozano-Reis, H. Prats, R. Sayós, J.A. Rodriguez, F. Illas, Assessing the activity of Ni cluster supported on TiC(001) toward CO_2 and H_2 dissociation, J. Phys. Chem. C 125 (2021) 12019–12027.
[21] J. Wellendorff, K.T. Lundgaard, A. Møgelhøj, V. Petzold, D.D. Landis, J.K. Nørskov, T. Bligaard, K.W. Jacobsen, Density functionals for surface science: Exchange-correlation model development with Bayesian error estimation, Phys. Rev. B. 85 (2012).
[22] G. Kresse, J. Hafner, Ab initio molecular dynamics for liquid metals, Phys. Rev. B. 47 (1993) 558–561.
[23] G. Kresse, J. Furthmüller, Efficient iterative schemes for ab initio total-energy calculations using a plane-wave basis set, Phys. Rev. B. 54 (1996) 11169–11186.
[24] G. Kresse, J. Furthmüller, Efficiency of ab-initio total energy calculations for metals and semiconductors using a plane-wave basis set, Comp. Mater. Sci. 6 (1996) 15–50.
[25] J.K. Nørskov, F. Studt, F. Abild-Pedersen, T. Bligaard, Fundamental Concepts in Heterogeneous Catalysis, Wiley, Hoboken, NJ, 2014.

[26] M. Stamatakis, D.G. Vlachos, A graph-theoretical kinetic Monte Carlo framework for on-lattice chemical kinetics, J. Chem. Phys. 134 (2011).
[27] M. Stamatakis, D.G. Vlachos, Unraveling the complexity of catalytic reactions via kinetic Monte Carlo simulation: current status and frontiers, ACS Catal. 2 (2012) 2648–2663.
[28] J. Nielsen, M. d'Avezac, J. Hetherington, M. Stamatakis, Parallel kinetic Monte Carlo simulation framework incorporating accurate models of adsorbate lateral interactions, J. Chem. Phys. 139 (224706) (2013) 1–13.
[29] H. Prats, S. Posada-Pérez, J.A. Rodriguez, R. Sayós, F. Illas, Kinetic Monte Carlo simulations unveil synergic effects at work on bifunctional catalysts, ACS Catal. 9 (2019) 9117–9126.
[30] A. Goswami, H. Ma, W.F. Schneider, Consequences of adsorbate-adsorbate interactions for apparent kinetic of surface catalytic reactions, J. Catal. 405 (2022) 410–418.
[31] X. Li, L.C. Grabow, Evaluating the benefits of kinetic Monte Carlo and microkinetic modeling for catalyst design studies in the presence of lateral interactions, Catal. Today 387 (2022) 150–158.
[32] S. Piccinin, M. Stamatakis, Steady-state CO oxidation on Pd(111): First-Principles kinetic Monte Carlo simulations and microkinetic analysis, Top. Catal. 60 (2017) 141–151.
[33] M. Jørgensen, H. Grönbeck, Scaling relations and kinetic Monte Carlo simulations to bridge the materials gap in heterogeneous catalysis, ACS. Catal. 7 (2017) 5054–5061.
[34] P. Lozano-Reis, H. Prats, P. Gamallo, F. Illas, R. Sayós, Multiscale study of the mechanism of catalytic CO_2 hydrogenation: role of the Ni(111) facets, ACS Catal. 10 (2020) 8077–8089.
[35] H. Prats, L. Álvarez, F. Illas, R. Sayós, Kinetic Monte Carlo simulations of the water gas shift reaction on Cu(1 1 1) from density functional theory based calculations, J. Catal. 333 (2016) 217–226.
[36] S. Piccinin, M. Stamatakis, CO oxidation on Pd(111): a first-principles-based kinetic Monte Carlo study, ACS Catal. 4 (2014) 2143–2152.
[37] L. Yang, A. Karim, J.T. Muckerman, Density functional kinetic Monte Carlo simulation of water gas shift reaction on Cu/ZnO, J. Phys. Chem. C. 117 (2013) 3414–3425.

4.6. References

1. J. M. Thomas and W. J. Thomas, Principles and Practice of Heterogeneous Catalysis, VCH, Weinheim, **1997**.

2. Aziz, M. A. A.; Jalil, A. A.; Triwahyono, S.; Mukti, R. R.; Taufiq-Yap, Y. H.; Sazegar, M. R. Highly Active Ni-promoted Mesostructured Silica Nanoparticles for CO_2 Methanation. *Appl. Catal., B*, **2014**, 147, 359–368.

3. Ocampo, F.; Louis, B.; Kiwi-Minsker, L.; Roger, A.-C. Effect of Ce/Zr Composition and Noble Metal Promotion on Nickel Based $Ce_xZr_{1-x}O_2$ Catalysts for Carbon Dioxide Methanation. *Appl. Catal., A*, **2011**, 392, 36–44.

4. Zhou, G.; Liu, H.; Cui, K.; Xie, H.; Jiao, Z.; Zhang, G.; Xiong, K.; Zheng, X. Methanation of Carbon Dioxide over Ni/CeO_2 Catalysts: Effects of Support CeO_2 Structure. *Int. J. Hydrog. Energy*, **2017**, 42, 16108–16117.

5. Hwang, S.; Hong, U. G.; Lee, J.; Baik, J. H.; Koh, D. J.; Lim, H.; Song, I. K. Methanation of Carbon Dioxide over Mesoporous Nickel-M-Alumina (M= Fe, Zr, Ni, Y, and Mg) Xerogel Catalysts: Effect of Second Metal. *Catal. Lett.*, **2012**, 142, 860–868.

6. Yang, L.; Pastor-Pérez, L.; Gu, S.; Sepúlveda-Escribano, A.; Reina, T. R. Highly Efficient Ni/CeO_2-Al_2O_3 Catalysts for CO_2 Upgrading via Reverse Water-Gas Shift: Effect of Selected Transition Metal Promoters. *Appl. Catal., B*, **2018**, 232, 464–471.

7. Sun, F.; Yan, C.; Wang, Z.; Guo, C.; Huang, S. Ni/Ce-Zr-O Catalysts for High CO_2 Conversion during Reverse Water Gas Shift Reaction (RWGS). *Int. J. Hydrog. Energy*, **2015**, 40, 15985–15993.

8. Tauster, S. J.; Fung, S. C.; Garten, R. L. Strong Metal-Support Interactions. Group 8 Noble Metals Supported on Titanium Dioxide. *J. Am. Chem. Soc.*, **1978**, 100, 170-175.

9. Tauster, S. J.; Fung, S. C.; Baker, R. T. K.; Horsely, J. A. Strong Interactions in Supported-Metal Catalysts. *Science*, **1981**, 211, 1121-1125.

10. Tauster S. J. Strong Metal-Support Interactions. *J. Acc. Chem. Res.*, **1987**, 20, 389–394.

11. Bruix, A.; Rodriguez, J. A.; Ramírez, P. J.; Senanayake, S. D.; Evans, J.; Park, J. B.; Stacchiola, D.; Liu, P.; Hrbek, J.; Illas, F. A New Type of Strong Metal-Support Interaction and the Production of H_2 through the Transformation of Water on Pt/CeO_2(111) and Pt/CeO_x/TiO_2(110) Catalysts. *J. Am. Chem. Soc.*, **2012**, 134, 8968-8974.

12. Klyushin, A. Y.; Jones, T. E.; Lunkenbein, T.; Kube, P.; Li, X.; Hävecker, M.; Knop-Gericke, A.; Schlögl, R. Strong Metal Support Interaction as a Key Factor of Au Activation in CO Oxidation. *ChemCatChem.*, **2018**, 10, 3985-3989.

13. Prats, H.; Posada-Pérez, S.; Rodriguez, J. A.; Sayós, R.; Illas, F. Kinetic Monte Carlo Simulations Unveil Synergic Effect at Work on Bifunctional Catalysts. *ACS Catal*., **2019**, 9, 9117-9126.

14. Lin, S.; Li, Z.; Li, M. Tailoring Metal-Support Interactions via Tuning CeO_2 Particle Size for Enhancing CO_2 Methanation Activity over Ni/CeO_2 Catalysts. *Fuel*, **2023**, 333, 126369-126383.

15. Rui, N.; Zhang, X.; Zhang, F.; Liu, Z.; Cao, X.; Xie, Z.; Zou, R.; Senanayake, S. D.; Yang, Y.; Rodriguez, J. A.; Liu, C. Highly active Ni/CeO_2 Catalyst for CO_2 Methanation: Preparation and Characterization. *App. Catal. B*, **2021**, 282, 119581-199593.

16. Pu, T.; Chen, J.; Tu, W.; Xu, J.; Han, Y.; Wachs, I. E.; Zhu, M. Dependency of CO_2 Methanation on the Strong Metal-Support Interaction for Supported Ni/CeO_2 Catalysts. *J. Catal.*, **2022**, 413, 821-828.

17. Van Deelen, T. W.; Mejia, C. H.; P. de Jong, K.; Control of Metal-Support Interactions in Heterogeneous Catalysts to Enhance Activity and Selectivity. *Nat Catal*., **2019**, 2, 955–970.

18. Hwu, H. H.; Chen, J. G. Surface Chemistry of Transition Metal Carbides. *Chem. Rev*., **2005**, 105, 185–212

19. L. E. Toth, *Transition Metal Carbides and Nitrides,* Academic, New York, **1971**.

20. Levy, R. B.; Boudart, M. Platinum-like Behavior of Tungsten Carbide in Surface Catalysis. *Science*, **1973**, 181, 547–549.

21. Kojima, I.; Miyazaki, E.; Inoue, Y.; Yasumore, I. Catalytic Activities of TiC, WC, and TaC for Hydrogenation of Ethylene. *J. Catal*., **1979**, 59, 472–474.

22. Jimenez-Orozco, C.; Flórez, E.; Viñes, F.; Rodriguez, J. A.; Illas, F. Critical Hydrogen Coverage Effect on the Hydrogenation of Ethylene Catalyzed by δ.MoC(001): An Ab Initio Thermodynamic and Kinetic Study. *ACS Catal*., **2020**, 10, 6213–6222.

23. Prats, H.; Gutiérrez, R. A.; Piñero, J. J.; Bromley, S. T.; Ramírez, P. J.; Rodriguez, J. A.; Illas, F. Room Temperature Methane Capture and Activation by Ni clusters Supported on TiC(001): Effects of Metal-Carbide Interactions on the Cleavage of the C-H Bond. *J. Am. Chem. Soc*., **2019**, 141, 5303–5313.

24. Liu, P.; Rodriguez, J. A. Interaction of Sulfur Dioxide with Titanium-carbide Nanoparticles and Surfaces: A Density Functional Study. *J. Chem. Phys.*, **2003**, 119, 10895–10903.

25. Rodriguez, J. A.; Liu, P.; Takahashi, Y.; Viñes, F.; Feria, L.; Florez, E.; Nakamura, K.; Illas, F. Novel Au-TiC Catalysts for CO Oxidation and Desulfurization Processes. *Catal. Today*, **2011**, 166, 2–9.

26. Feria, L.; Rodriguez, J. A.; Jirsak, T.; Illas, F. Interaction of SO2 with Cu/TiC(001) and Au/TiC(001): Toward a New Family of $DeSO_x$ Catalysts. *J. Catal*., **2011**, 279, 352–360.

27. Rodriguez, J. A.; Liu, P.; Takahashi, Y.; Nakamura, K.; Viñes, F.; Illas, F. Desulfurization of Thiophene on Au/TiC(001): Au-C Interactions and Charge Polarization. *J. Am. Chem. Soc*., **2009**, 131, 8595–8602.

28. Rodriguez, J. A.; Liu, P.; Viñes, F.; Illas, F.; Takahashi, Y.; Nakamura, K. Dissociation of SO_2 on Au/TiC(001): Effects of Au-C interactions and Charge Polarization. *Angew. Chem*., **2008**, 120, 6787–6791.

29. Rodriguez, J. A.; Liu, P.; Stacchiola, D. J.; Senanayake, S. D.; White, M. G.; Chen, J. G. Hydrogenation of CO_2 to Methanol: Importance of Metal-Oxide and Metal-Carbide Interfaces in the Activation of CO_2. *ACS Catal.*, **2015**, 5, 6696–6706.

30. Vidal, A. B.; Feria, L.; Evans, J.; Takahashi, Y.; Liu, P.; Nakamura, K.; Illas, F.; Rodriguez, J. A. CO_2 Activation and Methanol Synthesis on Novel Au/TiC and Cu/TiC catalysts. *J. Phys. Chem. Lett.*, **2012**, 3, 2275–2280.

31. Rodriguez, J. A.; Liu, P.; Dvorak, J.; Jirsak, T.; Gomes, J.; Takahashi, Y.; Nakamura, K. The Interaction of Oxygen with TiC(001): Photoemission and First-Principles Studies. *J. Chem. Phys.*, **2004**, 121, 465-474.

32. Viñes, F.; Sousa, C.; Illas, F.; Liu, P.; Rodriguez, J. A. A Systematic Density Functional Study of Molecular Oxygen Adsorption and Dissociation on the (001) Surface of Group IV-VI Transition Metal Carbides. *J. Phys. Chem. C.*, **2007**, 111, 16982–16989.

33. Rodriguez, J. A.; Feria, L.; Jirsak, T.; Takahashi, Y.; Nakamura, K.; Illas, F. Role of Au-C interactions on the Catalytic Activity of Au Nanoparticles Supported on TiC(001) Toward Molecular Oxygen Dissociation. *J. Am. Chem. Soc.*, **2010**, 132, 3177–3186.

34. Rodriguez, J. A.; Evans, J.; Feria, L.; Vidal, A. B.; Liu, P.; Nakamura, K.; Illas, F. CO_2 Hydrogenation on Au/TiC, Cu/TiC and Ni/TiC Catalysts: Production of CO, Methanol, and Methane. *J. Catal.*, **2013**, 307, 162–169.

35. Bañares, M. A. Operando Methodology: Combination of in situ Spectroscopy and Simultaneous Activity Measurements under Catalytic Reaction Conditions. *Catal. Today*, **2005**, 100, 71-77.

36. Weckhuysen, B. M. Determining the Active Site in Catalytic Process: Operando Spectroscopy is More than a Buzzword. *Phys. Chem. Chem. Phys.* **2003**, 5, 4351-4360.

37. Topsøe, H. Developments in Operando Studies and in situ Characterization of Heterogeneous Catalysts. *J. Catal.*, **2003,** 216, 155-164.

38. Handoko, A. D.; Wei, F.; Jenndy; Yeo, B. S.; She, Z. W. Understanding Heterogeneous Electrocatalytic Carbon Dioxide Reduction through Operando Techniques. *Nat. Catal.,* **2018**, 1, 922–934.

39. Feng, K.; Wang, Y.; Guo, M.; Zhang, J.; Li, Z.; Deng, T.; Zhang, Z.; Yan, B. In-situ/Operando Techniques to Identify Active Sites for Thermochemical Conversion of CO_2 over Heterogeneous Catalysis. *J. Energy Chem.*, **2021**, 62, 153-171.

40. Li, Y.; Zhao, S.; Tappero, R.; Jung, U.; Else, A.; Baumman, Ph.; Nuzzo, R. G.; Stach, E. A.; Frenkel, A. I. Complex Structural Dynamics of Nanocatalysts Revealed in Operando Conditions by Correlated Imaging and Spectroscopy Probes. *Nat. Commun.*, **2015**, 6, 7583-7589.

41. Goetze, J.; Yarulina, I.; Gascon, J.; Kapteijn, F.; Weckhuyen, B. M. Revealing Lattice Expansion of Small-pore Zeolite Catalysts during the Methanol-to-olefins Process using Combined Operando X-ray Diffraction and UV-vis Spectroscopy. *ACS. Catal.* **2018**, 8, 2060-2070.

42. Bruix, A.; Margraf, J. T.; Andersen, M.; Reuter, K. First-principles-based Multiscale Modeling of Heterogeneous Catalysis. *Nat. Catal*., **2019**, 2, 659-670.

43. Pineda, M.; Stamatakis, M. Kinetic Monte Carlo Simulations for Heterogeneous Catalysis: Fundamentals, Current Status, and Challenges. *J. Chem. Phys.* **2022**, 156, 120902-120931.

44. Grajciar, L.; Heard, C. J.; Bondarenki, A. A.; Polynski, M. V.; Meeprasert, J.; Pidko, A. E.; Nachtigall, P. Towards Operando Computational Modeling in Heterogeneous Catalysis. *Chem. Soc. Rev.* **2018**, 47, 8307-8348.

45. Motagmawala, A. H.; Dumesic, J. A. Microkinetic Modeling: a Tool for Rational Catalyst Design. *Chem. Rev*., **2021**, 121, 1049-1076.

46. Lozano-Reis, P.; Sayós, R.; Rodriguez, J. A.; Illas, F. Structural, Electronic, and Magnetic Properties of Ni Nanoparticles Supported on the TiC(001) Surface. *Phys. Chem. Chem. Phys.* **2020**, 22, 26145-26154.

47. Lozano-Reis, P.; Prats, H.; Sayós, R.; Rodriguez, J. A.; Illas, F. Assessing the Activity of Ni Cluster Supported on TiC(001) Toward CO_2 and H_2 Dissociation. *J. Phys. Chem. C*, **2021**, 125, 12019-12027.

48. Lozano-Reis, P.; Prats, H.; Sayós, R.; Illas, F. Limitations of Free Energy Diagrams to Predict the Catalytic Activity: The Reverse Water Gas Shift Reaction Catalyzed by Ni/TiC. *J.Catal.*, **2023**, 425, 203-211.

49. Cadi-Essadek, A.; Roldan, A.; De Leeuw, N. H. Stability and Mobility of Supported Ni_n (n=1-10) clusters on ZrO_2(111) and YSZ(111) Surfaces: A Density Functional Theory Study. *Faraday Discuss.*, **2018**, 208, 87–104.

50. Cadi-Essadek, A.; Roldan, A.; De Leeuw, N. H. Density Functional Theory Study of Ni Clusters Supported on the ZrO_2(111) Surface. *Fuel Cells*, **2017**, 17, 125–131.

51. Yang, J.; Ren, J.; Guo, H.; Qin, X.; Han, B.; Lin, J.; Li, Z. The Growth of Ni_n Clusters and Their Interaction with Cubic, Monoclinic, and Tetragonal ZrO_2 Surfaces-A Theoretical and Experimental Study. *RSC Adv.*, **2015**, 5, 59935–59945.

52. Giordano, L.; Pacchioni, G.; Ferrari, A. M.; Illas, F.; Rösch, N. Electronic Structure and Magnetic Moments of Co_4 and Ni_4 Clusters Supported on the MgO(001) Surface. *Surf. Sci.*, **2001**, 473, 213–226.

53. Di Valentin, C.; Giordano, L.; Pacchioni, G.; Rösch, N. Nucleation and Growth of Ni Clusters on Regular Sites and F Centers on the MgO(001) Surface. *Surf. Sci.*, **2003**, 522, 175–184.

54. Carrasco, J.; Barrio, L.; Liu, P.; Rodriguez, J. A.; Ganduglia-Pirovano, M. V. Theoretical Studies of the Adsorption of CO and C on Ni(111) and Ni/CeO_2(111): Evidence of a Strong Metal-Support Interaction. *J. Phys. Chem. C.*, **2013**, 117, 8241–8250.

55. Mao, Z.; Lustemberg, P. G.; Rumptz, J. R.; Ganduglia-Pirovano, M. V.; Campbell, C. T. Ni Nanoparticles on CeO_2(111): Energetics, Electron Transfer, and Structure by Ni Adsorption Calorimetry, Spectroscopies, and Density Functional Theory. *ACS Catal.*, **2020**, 10, 5101–5114

56. Wang, Y.; Su, Y.; Zhu, M.; Kang, L. Ni Cluster Nucleation and Growth on the Anatase TiO_2(101) Surface: a Density Functional Theory Study. *RSC Adv.*, **2015**, 5, 16582–16591.

57. Kittle, C. *Introduction to Solid State Physics*, 8th edition, Hoboken, NJ: John Wiley & Sons, Inc, **2005**.

58. Bader, R.F.W. A Quantum Theory of Molecular Structure and its Applications. *Chem. Rev.*, **1991**, 91, 893–928.

59. Kunkel, C.; Viñes, F.; Illas, F. Transition Metal Carbides as Novel Materials for CO_2 Capture, Storage, and Activation. *Energy Environ. Sci.* **2016**, 9, 141−144.

60. López, M.; Broderick, L.; Carey, J. J.; Viñes, F.; Nolan, M.; Illas, F. Tuning Transition Metal Carbide Activity by Surface Metal Alloying: A Case Study on CO_2 Capture and Activation. *Phys. Chem. Chem. Phys.* **2018**, 20, 22179−22186.

61. López, M.; Viñes, F.; Nolan, M.; Illas, F. Predicting the Effect of Dopants on CO_2 Adsorption in Transition Metal Carbides: Case Study on TiC (001). *J. Phys. Chem. C* **2020**, 124, 15969−15976.

62. Florez, E.; Gomez, T.; Liu, P.; Rodriguez, J. A.; Illas, F. Hydrogenation Reactions on Au/TiC(001): Effects of Au↔C Interactions on the Dissociation of H_2. *ChemCatChem* **2010**, 2, 1219–1222.

63. Gomez, T.; Florez, E.; Rodriguez, J. A.; Illas, F. Reactivity of Transition Metals (Pd, Pt, Cu, Ag, Au) toward Molecular Hydrogen Dissociation: Extended Surfaces versus Particles Supported on TiC(001) or Small Is Not Always Better and Large Is Not Always Bad. *J. Phys. Chem. C* **2011**, 115, 11666–11672.

64. Mohsenzadeh, A.; Richards, T.; Bolton, K. DFT Study of the Water Gas Shift Reaction on Ni(111), Ni(100) and Ni(110) Surfaces. *Surf. Sci.* **2016**, 644, 53−63.

65. Vogt, C.; Monai, M.; Sterk, E. B.; Palle, J.; Melcherts, A. E. M.; Zijlstra, B.; Groeneveld, E.; Berben, P. H.; Boereboom, J. M.; Hensen, E. J. M.; Meirer, F.; Filot, I.

A. W.; Weckhuysen, B. M. Understanding Carbon Dioxide Activation and Carbon−Carbon Coupling over Nickel. *Nat. Commun*. **2019**, 10, 5330-5340.

66. Prats, H.; Piñero, J. J.; Viñes, F.; Bromley, S. T.; Sayós, R.; Illas, F. Assessing the Usefulness of Transition Metal Carbides for Hydrogenation Reactions. *Chem. Commun.* **2019**, 55, 12797–12800.

Chapter 5

CO_2 hydrogenation over Ni_4/CeO_2

5.1. Introduction

The power to gas[1,2] (PtG) technology has increased attraction as a promising option for CO_2 valorization taking benefit of surplus renewable energies. Particularly, the power to methane (PtM) technology[3,4] offers an interesting chemical route for methane formation, which is further used as a fuel, thus, creating a C_1 cycle. Regarding this reaction, Ni-based catalysts are widely used as they present a really good compromise between catalytic activity and economic cost in comparison to other catalysts using noble metals.[5,6] In this regard, several studies have shown that Ni/CeO_2 catalysts present superior catalytic activity than other Ni nanoparticles supported over different types of metal oxides.[7-11] For that reason, in the past years considerable effort has been made to understand the intricacies that make Ni/CeO_2 catalysts such a good option for the CO_2 methanation reaction.[12-20] However, there is still not a full consensus about this issue and different hypothesis have been proposed.

Among the different proposed hypothesis, some researchers have focused on the particle size and morphology effect and the particular metal-support interactions in this reducible oxide just to name a few. For the former hypothesis, even several studies have dealt with it, different conclusions have been reached and some studies claim that large nanoparticles are more active[21-23] while other studies argue the opposite.[24,25] Interestingly, in the studies that found the higher activity for the smaller nanoparticles they attributed the increase of activity due to the metal-support interactions that these nanoparticles featured. Therefore, some results from the literature point to correlation between the catalytic activity and the metal-support interactions rather than because of the nanoparticle size. Precisely, Pu et al.,[26] studied the so-called strong metal-support interaction (SMSI) effect for nanoparticles of the same size but different level of encapsulation and found that the larger the encapsulation, the larger the strong metal-support interaction and the higher the catalytic activity. In this regard, several studies combining theoretical modelling and experiments have claimed that small Ni clusters or

nanoparticles supported on CeO_2 display metal-support interactions, not necessarily of the type of detrimental SMSI, together to high catalytic activity for several reactions such as methane steam reforming,[27] water-gas shift reaction,[28] direct conversion of methane to methanol,[29] dry reforming of methane,[30-33] water dissociation[34] and CO_2 methanation reaction.[35] Regarding theoretical studies of the CO_2 hydrogenation reaction over Ni/CeO_2 there is, to the best of our knowledge, the work of Zhang et al.,[35] in which they proposed that CH_4 was formed by a combination of the carboxyl pathway of the RWGS reaction followed by the CO-hydrogenation pathway for methane formation. Nevertheless, just from a DFT study of the reaction mechanisms at 0K, it is not possible to firmly conclude which is the main mechanism that governs to overall reaction, the activity and the CH_4 selectivity under real working conditions, which calls for a multiscale study to accurately describe the system evolution under real working conditions.

The present chapter aims to study the CO_2 hydrogenation reaction over a Ni/CeO_2 model system with well-defined support and Ni cluster by means of a multiscale approach coupling DFT calculations with kMC simulations. The present results provide compelling evidence about the mechanism that governs the reaction, the activity and CH_4 selectivity and highlights the role of including Eley-Rideal reactions on the final results. A full description of the work done can be found in Ref 36.

5.2. Lattice model and reaction network

In the present study we have modeled the Ni/CeO_2 system by a small flat Ni_4 cluster supported on the stoichiometric CeO_2 (111) surface as shown in Figure 5.1a. The particular choice of this system is to have a representative model of a flat Ni cluster supported on CeO_2 (111) presenting metal support interactions.[29,35-39] Note that, in general, bifunctional catalysts such as Ni/CeO_2 contain three distinct regions, namely, the support region, the metal region and the interface region that lies in between these two others, each one with different energetics. Nevertheless, in this study we will focus on the reactivity of the supported Ni cluster for different reasons. First, we aim at understanding the effect of the metal-support interactions which, in this case, is thought to be beneficial for catalytic purposes. Moreover, it has been shown that the CeO_2(111) surface is inactive for the CO_2 hydrogenation reaction, so one can discard this region.[23] Finally, it has been

shown that CO_2 adsorbs with a higher adsorption energy on the Ni cluster than over the interface region[35] and, as a noticeable adsorption is required for the catalytic process to take place, we have discarded the interface region as well. Therefore, as we have restricted our calculations to the supported Ni cluster, we have only considered this region for the lattice model of the kMC simulations as shown in Figure 5.1b.

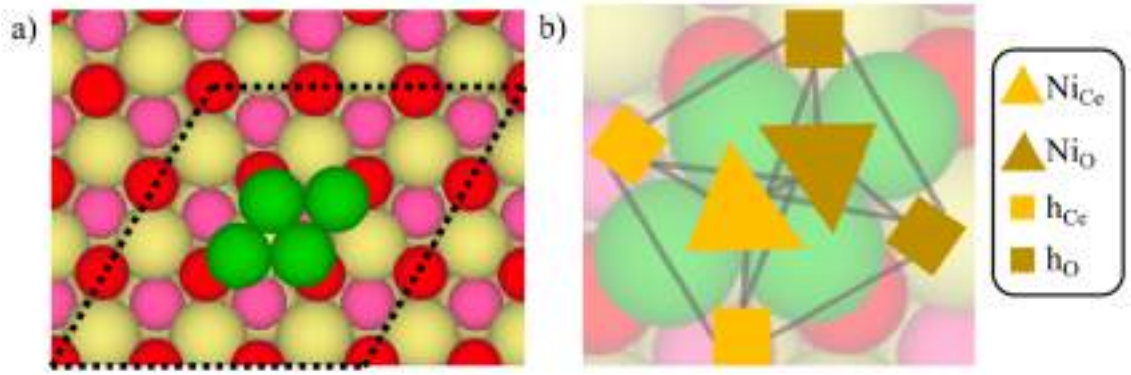

Figure 5.1. a) Surface model of the Ni_4/CeO_2 system used for the DFT calculations. Green, pale yellow, red and pink stand for Ni, Ce uppermost O and subsurface O atoms, respectively. b) lattice model used for the kMC simulations representing the Ni cluster. Triangles and squares represent Ni hollow and hydrogen reservoir sites, respectively. Note that on the hydrogen reservoir sites only H and H_2 species can be adsorbed. Green lines depict the connectivity between sites. Orange and brown colors refer to the Ce and O types of sites. Picture directly taken from ref 36.

To provide an accurate enough study of the CO_2 hydrogenation reaction, we have considered a quite large reaction network as shown in Figure 5.2. We have considered several elementary reactions and the possible formation of different products during the complete CO_2 hydrogenation reaction (i.e. CO, CH_2O, CH_3OH, CH_4 and H_2O). We have also included some Eley-Rideal reactions for the hydrogenation of O and OH species. Note that to correctly define the energetics we have considered all the different reactions shown in Figure 5.2 twice as the energetics on the two different three-fold Ni hollow sites are not exactly the same. Moreover, for some hydrogenation reactions we have considered two possible situations in which the reaction can happen. These are: the situation in which the H atom and the other species are at the same type of sites (i.e. h_{Ce}/Ni_{Ce} or h_O/Ni_O) or when they are on the opposite sites (i.e., h_{Ce}/Ni_O or h_O/Ni_{Ce}). This is done to correctly capture the reactivity and consider blocking effects, so that if one species is present at the opposite site, the H atom can only attack that species if the other site is not occupied. For instance, let us imagine a situation in which we have C, O and H adsorbed at Ni_{Ce}, Ni_O

and h_O, respectively. In this particular case, H cannot attack the C as O is blocking the attack so that H can react with the O atom or diffuse to the h_{Ce} site and then react with C.

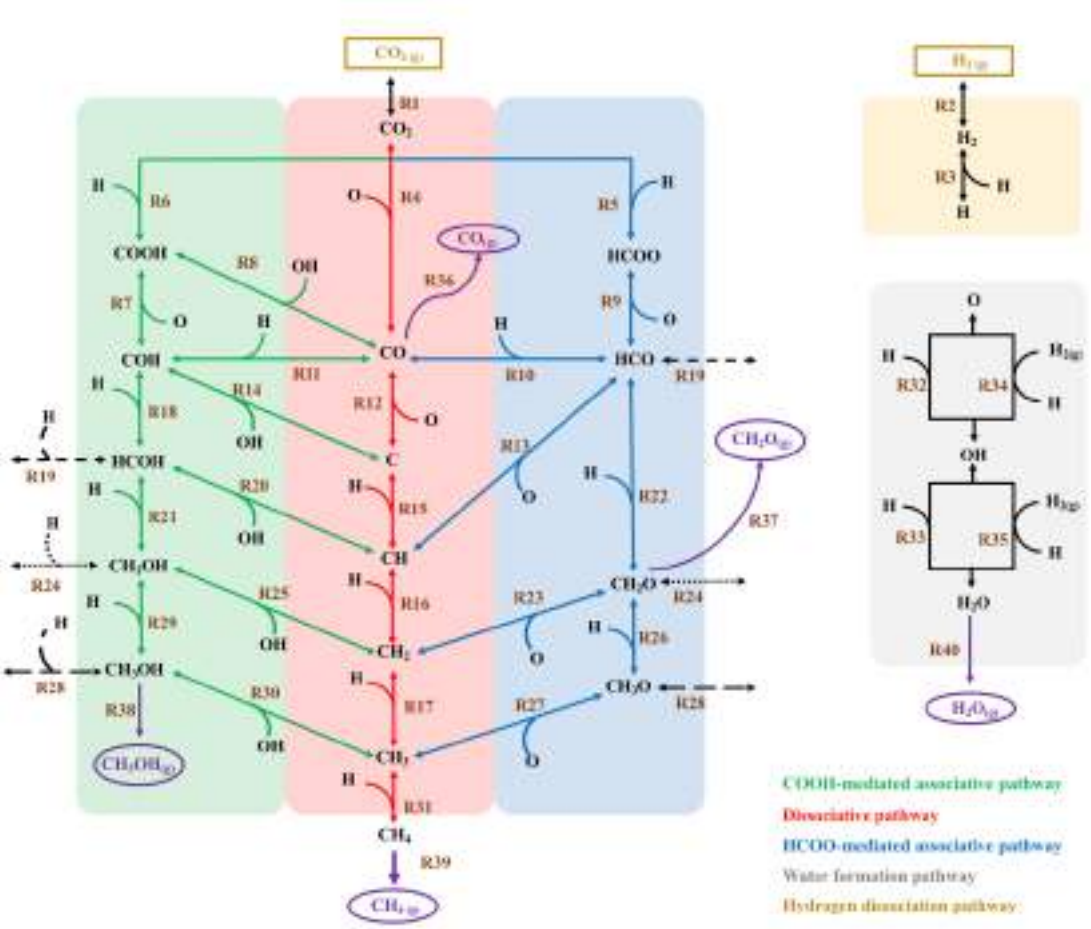

Figure 5.2. Reaction network proposed for the CO_2 hydrogenation reaction. The dissociative, COOH-mediated, HCOO-mediated, hydrogen dissociation and water formation pathways are shown in red, green, blue, pale yellow and grey, respectively. Black doted/dashed lines are for elementary steps that interconnect different pathways. Purple and dark yellow stand for reactants and products, respectively. Reversible steps are represented by double arrows. Picture directly taken from ref 36.

5.3. Results

The main DFT and kMC results for the study of the CO_2 hydrogenation reaction over the well-defined Ni_4/CeO_2 surface model are presented below. The reader interested in more details is referred to ref 36.

5.3.1. DFT results

Figure 5.1a shows that the Ni_4 cluster adsorbs above the oxygen atoms of the uppermost layer of the $CeO_2(111)$ surface adopting the (111) facet shape of this surface. Interestingly, the cluster adsorption generates a charge transfer between the metal cluster and the support so that two Ce^{4+} atoms of the surface are reduced to Ce^{3+} atoms, while the Ni atoms of the cluster are partially oxidized to $Ni^{0.5+}$ atoms as a results of the metal-support interaction, in agreement with previous results.[27,37,38,40] This change in the electronic structure of the Ni atoms of the Ni cluster due to the metal-support interactions, is thought to be beneficial for catalytic purposes. To evaluate this effect, we have studied the adsorption of the reactants and products of the CO_2 hydrogenation reaction as well as the energetics for the different possible elementary steps of our reaction network. Table 5.1 summarizes the adsorption energy over the different adsorption sites along with results from our previous study of the CO_2 hydrogenation on Ni (111) which are included just for comparison.[41]

Table 5.1. Adsorption energy for the different reactants and products of the CO_2 hydrogenation reaction on the supported Ni cluster at the most stable adsorption sites along with already published data for the Ni(111) surface for comparison. Note that all values include the ZPE term. Table directly taken from ref 36.

	$E_{ads,0}$ /eV	
Species	**This work**	**Ni (111) Ref. 41**
CO_2	-1.46 (Ni_{Ce}), -1.51 (Ni_O)	-0.16
CO	-2.47 (Ni_{Ce}), -2.33 (Ni_O)	-1.61
CH_2O	-2.10 (Ni_{Ce}), -2.06 (Ni_O)	-0.58
CH_3OH	-0.89 (Ni_{Ce}), -0.91 (Ni_O)	-0.36
CH_4	-0.26 (Ni_{Ce}), -0.26 (Ni_O)	-0.13
H_2O	-0.73 (Ni_{Ce}), -0.75 (Ni_O)	-0.26
H_2	-0.63 (h_{Ce}-h_O)	0.00

As shown in Table 5.1 the most stable sites are the two three-fold hollow sites with very similar adsorption energies for the two sites. Let us start by comparing our reported values for the Ni cluster with values on the literature for the same system, first, pointing out that our values include the ZPE term while this does not seem the case in the other studies. Regarding the CO_2 adsorption energy, Alvarez-Galvan et al.[37] and Zhang et al.[35] reported a CO_2 adsorption energy of -1.26 and -1.64 eV, respectively, which are comparable to our adsorption energies of -1.51 and -1.46 eV. We attribute the difference between our values and the one reported by Alvarez-Galvan et al.[37] to the different

structure of CO_2 upon adsorption. In our case, we have found a CO_2 structure that is bent to the Ni cluster, thus, featuring a higher interaction with the surface that can explain our higher value. Regarding the study of Zhang et al.[35] we attribute the differences due to the different computational code and different computational methodology used in the calculations. In this particular case, we found a very similar CO_2 adsorption energy for calculations with and without the ZPE term, thus, we suggest that the differences are likely to be as indicated in the comments above. Alvarez-Galvan et al.[37] also reported an H_2 adsorption energy of -0.95 eV which is comparable to our value. Again, we find a different Ni atom in which H_2 is adsorbed that can explain the differences observed. Moreover, our H_2 adsorption energy with and without the ZPE term is -0.63 and -0.75 eV, respectively, the latter value being closer to the previously reported one. Therefore, we suggest that the differences are due to the ZPE term and the different adsorption site. Finally, Lustemberg et al.[38] reported the H_2O and CH_4 adsorption energies with values of -0.93 and -0.24 eV, respectively, in agreement with our values. Again, the differences are attributed to the ZPE term that plays a more important role for H_2O than for CH_4, our values being -0.75 and -0.82 eV for H_2O and -0.26 and -0.28 eV for CH_4 when including or not the ZPE term, respectively. We suggest that further deviations can be as a consequence of the different computational methodology used but, in general, our values are close enough to the literature values which points to a proper definition of our model system.

Let us now compare our values for the Ni cluster and the ones reported for the Ni (111) surface[41] to evaluate the effect of the metal-support interactions on the adsorption energy of possible reactants and products of the CO_2 hydrogenation reaction. Note that further differences on the adsorption energies can also come from to the different coordination of the Ni atoms. Nevertheless, the above-mentioned charge transfer from the Ni cluster to the CeO_2(111) support is likely to dominate the differences. From Table 5.1. one can clearly see that, as a result of the metal-support interaction along with the mentioned different Ni atomic coordination, the adsorption energies on the Ni cluster are larger than the ones reported for the Ni(111) surface. For instance, CO_2 and H_2 molecules are chemisorbed on the Ni clusters while this is not the case for the Ni(111) surface where they just physisorb. Interestingly, the higher adsorption energies could translate into a higher catalytic activity for the Ni cluster as these two molecules are the reactants of the CO_2 hydrogenation reaction. However, one should be aware that high adsorption energies

do not directly correlate to a better catalytic activity as smaller energy barriers are required for the reaction to proceed (*vide infra*). Regarding the possible side products of the CO_2 hydrogenation reaction to methane, namely, CO, CH_2O and CH_3OH, we see again an increase of the adsorption energy which in principle would benefit CH_4 formation. In fact, one of the hurdles for methane formation on the Ni(111) surface is the low CO adsorption energy compared to other competing reactions. Finally, it can be seen that the adsorption energy of the desired product (CH_4) is quite small, although higher than for the Ni(111) surface, which would favor methane desorption. All these results point to the Ni cluster as a good candidate for selective methane formation

Now we examine how metal-support interactions can affect the energy barrier of the different elementary steps for the CO_2 hydrogenation reaction, which are essential to gain insights about the catalytic activity and selectivity of a catalyst. In Table 5.2 we have summarized the reaction energy and energy barriers for some of the elementary steps of the CO_2 hydrogenation reaction along with values for the Ni (111) surface[41] for comparison. For simplicity we have only included the most relevant reactions for our discussion. We have also restricted the elementary reactions to those that happen on the Ni_{Ce} site for simplicity but similar conclusions can be extracted for the reactions that happen at Ni_O. The overall reactions are summarized in Table S3 in Appendix A.

We start by comparing our reported values with the ones in the literature for the same system. Comparing our values (see Table 5.2 and Table S3 in Appendix A) with the ones reported by Zhang et al.[35] huge differences can be observed. They reported very high energy barriers for several elementary reaction with values ranging from 2 to 4 eV in disagreement with our reported values, which are generally smaller with values ranging from almost null energy barriers for some steps to the largest energy of 2.18 eV. A careful comparison with their reported data suggests that the differences should be due to the different initial and final states used in their calculations with respect the ones we have used. This interpretation is supported by the very good agreement between our values and the ones reported by Alvarez-Galvan et al.[37] for the CO_2 dissociation and H_2 dissociation reactions. They reported a value of 0.75 eV for the former reaction which nicely agree with our value of 0.77 eV and they also found a barrierless H_2 dissociation reaction as we have found. Moreover, we also found very good agreement with the reported values of Lustemberg et al.[38] for the CH_4 and H_2O dissociation and CH_3OH formation reactions. They reported energy barriers of 0.14, 0.41 and 1.40 eV, respectively, that neatly agree

with our reported values of 0.14, 0.35 and 1.33 eV for the same reactions. Overall, the very good agreement between our calculated values and the ones reported by these two works clearly point to a good definition of our model system while question the results of Zhang et al.[35] or at least point to a not clear enough explanation.

Table 5.2. Reaction energies ($\Delta E_{0,r}$) and forward and reverse energy barriers ($\Delta E^{\neq}_{0,f}$, $\Delta E^{\neq}_{0,r}$) for the selected elementary reactions including the ZPE for the Ni_4/CeO_2 system and the Ni(111) surface[41] for comparison. For reactions in which two possible hydrogen attacks are considered the *f* and *n* subscript stands for the H atom being at the site that is far or near the species that is attacking, respectively. TW stands for This Work. Table directly taken from ref 36.

ID	Reaction	$\Delta E_{0,r}$ / eV		$\Delta E^{\neq}_{0,f}$ / eV		$\Delta E^{\neq}_{0,r}$ / eV	
		TW	Ref 41	TW	Ref 41	TW	Ref 41
R1$_{NiCe}$	$CO_{2,(g)} + *_{NiCe} \rightleftharpoons CO^*_{2,NiCe}$	-1.46	-0.16	0.00	0.00	1.46	0.16
R2	$H_{2,(g)} + *_{hCe} + *_{hO} \rightleftharpoons H^{**}_{2,hCehO}$	-0.63	0.00	0.00	0.00	0.63	0.00
R3	$H^{**}_{2,hCehO} \rightleftharpoons H^*_{hCe} + H^*_{hO}$	-0.70	-0.33	0.00	0.26	0.70	0.59
R4$_{NiCe}$	$CO^*_{2,NiCe} + *_{NiO} \rightleftharpoons CO^*_{NiCe} + O^*_{NiO}$	-0.70	-0.57	0.77	0.86	1.47	1.43
R5$_{NiCe}$	$CO^*_{2,NiCe} + H^*_{hO} \rightleftharpoons HCOO^*_{NiCe} + *_{hO}$	-0.07	0.04	0.39	1.05	0.45	1.01
R6$_{NiCe}$	$CO^*_{2,NiCe} + H^*_{hO} \rightleftharpoons COOH^*_{NiCe} + *_{hO}$	0.22	0.49	1.20	1.33	0.98	0.84
R9$_{NiCe}$	$HCOO^*_{NiCe} + *_{NiO} \rightleftharpoons HCO^*_{NiCe} + O^*_{NiO}$	0.23	0.85	0.65	1.39	0.42	0.54
R10$_{NiCe}$	$CO^*_{NiCe} + H^*_{hO} \rightleftharpoons HCO^*_{NiCe} + *_{hO}$	0.60	1.21	0.90	1.42	0.30	0.21
R12$_{NiCe}$	$CO^*_{NiCe} + *_{NiO} \rightleftharpoons C^*_{NiCe} + O^*_{NiO}$	1.03	1.84	1.52	2.98	0.49	1.15
R13$_{NiCe}$	$HCO^*_{NiCe} + *_{NiO} \rightleftharpoons CH^*_{NiO} + O^*_{NiCe}$	0.31	-0.07	0.64	1.10	0.33	1.17
R16$_{NiCe,n}$	$CH^*_{NiCe} + H^*_{hCe} \rightleftharpoons CH^*_{2,NiCe} + *_{hCe}$	-0.38	0.30	0.03	0.63	0.41	0.34
R17$_{NiCe,n}$	$CH^*_{2,NiCe} + H^*_{hCe} \rightleftharpoons CH^*_{3,NiCe} + *_{hCe}$	-0.53	-0.11	0.09	0.57	0.62	0.68
R22$_{NiCe}$	$HCO^*_{NiCe} + H^*_{hO} \rightleftharpoons CH_2O^*_{NiCe} + *_{hO}$	0.29	0.26	0.46	0.71	0.17	0.45
R23$_{NiCe}$	$CH_2O^*_{NiCe} + *_{NiO} \rightleftharpoons CH^*_{2,NiO} + O^*_{NiCe}$	-0.39	-0.40	0.68	0.96	1.07	1.37
R31$_{NiCe,n}$	$CH^*_{3,NiCe} + H^*_{hO} \rightleftharpoons CH^*_{4,NiCe} + *_{hO}$	0.77	-0.30	0.91	0.79	0.14	0.96
R36$_{NiCe}$	$CO^*_{NiCe} \rightleftharpoons CO_{(g)} + *_{NiCe}$	2.47	1.61	2.47	1.61	0.00	0.00
R37$_{NiCe}$	$CH_2O^*_{NiCe} \rightleftharpoons CH_2O_{(g)} + *_{NiCe}$	2.10	0.58	2.10	0.58	0.00	0.00
R39$_{NiCe}$	$CH^*_{4,NiCe} \rightleftharpoons CH_{4,(g)} + *_{NiCe}$	0.26	0.13	0.26	0.13	0.00	0.00

Now we compare the values for the Ni cluster with the ones reported for the Ni (111) surface[41] as shown in Table 5.2 and Table S3 in Appendix A. It can be seen that, mostly as a result of the metal-support interaction, the energy barriers of the different elementary steps are, in general, lower for the Ni cluster which suggests Ni clusters as potentially more active than the Ni(111) surface. Focusing on some reactions of interest, one can clearly see that the H_2 dissociation would be easier on the supported Ni cluster as it is a barrierless reaction while it has an energy barrier of 0.26 eV on the Ni (111) surface. Regarding the different routes for CO_2 conversion (i.e., CO_2 dissociation, COOH formation and HCOO formation), the energy barriers are slightly smaller for the Ni cluster with the exception of the HCOO formation that it is clearly favored on the Ni cluster. These values point to the HCOO-mediated pathway as the most probable pathway followed by the direct CO_2 dissociation pathway, which contrast with the kMC results for the Ni (111) surface in which CO was produced mainly via the CO_2 dissociation pathway and also the COOH-mediated pathway to a lower extent. Let us now focus on the evolution from CO to methane which starts with the COH formation, CO dissociation or HCO formation reactions. The former reaction has the largest energy barrier among the three different reactions, thus, being the less probable one. Regarding the CO dissociation energy barrier, one can clearly see a huge difference for the supported Ni cluster and the Ni (111) surface, with values of 1.52 and 2.98 eV, respectively. The lower value for the Ni cluster opens the CO dissociation route as a possible pathway for methane formation on the Ni cluster while this reaction is kinetically impeded on the extended surface, thus, very unlikely to occur. Finally, for the HCO formation reaction one can spot a decrease on the energy barrier and a decrease on the endothermicity of the reaction for the supported Ni cluster with respect to the extended surface. Interestingly, the high endothermicity of the HCO formation reaction on the Ni (111) surface has been reported to be one of the hurdles for methane production as after HCO formation it rapidly dissociates to form CO that further desorbs.[41] Therefore, the lowest endothermicity of the HCO formation reaction and the higher CO adsorption energy observed for the supported Ni cluster could be of great importance for methane production. After HCO is formed, it can dissociate to CH or being hydrogenated to CH_2O that further dissociates to CH_2 with energy barriers of 0.64, 0.46 and 0.68 eV for the Ni cluster and energy barriers of 1.10, 0.71 and 0.96 eV for the extended surface, respectively. Again metal-support interactions produce a lowering of the energy barriers for the cluster which open two possible routes for CH_x formation and further hydrogenation to methane.

To sum up, we have shown that metal-support interactions induce an effect on the Ni cluster that produces a general lowering of the energy barriers and an increase on the adsorption energy of some side products (*i.e.,* CO and CH_2O) with respect to the Ni (111) surface which suggests that small supported Ni clusters could be potential good candidates for methane formation. From the previous analysis it appears that the most probable pathway for methane formation would be a combination of the HCOO-mediated pathway and in a lower extent the CO_2 dissociation pathway for the RWGS reaction followed by the CO hydrogenation to HCO which can either being hydrogenated to CH_2O that further dissociates to CH_2 or directly dissociate to CH and finally the CH_x species are hydrogenated to CH_4. Our proposed mechanism agrees well with the one proposed by Zhang et al.[35] with the exception of the CO formation that they claim it is formed via the COOH-mediated pathway of the RWGS reaction. Nevertheless, as has been recently shown for the RWGS on a Ni/TiC catalyst model,[42] it is not possible to extract firm conclusions about the mechanism, activity and selectivity from the DFT picture only and it is necessary to couple the DFT calculations with some kinetic modelling technique. To this end, we combine the DFT results with kMC simulations to reach a more accurate and realistic description of the system evolution under real working conditions and provide insights about the mechanism that drives the reaction, the activity and the selectivity.

5.3.2. kMC results

To thoroughly study the CO_2 hydrogenation over Ni_4/CeO_2 under real working conditions we have performed several kMC simulations at varying temperatures and pressure conditions. From the results of the kMC simulations we provide compelling evidence of the role of the different sites and the important role of, often neglected, Eley-Rideal reactions on the reaction mechanism, catalytic activity and CH_4 selectivity. Note that methane selectivity is conditioned by the competition between the partial CO_2 hydrogenation to CO or the complete CO_2 hydrogenation to CH_4 via the well-known RWGS and Sabatier reactions, respectively. Note that for comparison we have chosen the working conditions as the ones used in the experimental work of Zheng et al.[23] This particular choice is because they studied a system with low Ni loading in which small Ni clusters and nanoparticles are likely to be present. Nevertheless, it is important to point out that we do not aim to a quantitative agreement but rather a qualitative one. This is

because of the differences present in our model system and the real experimental system. For instance, our model system consists of a flat Ni_4 cluster while the experimental system is likely to contain an ensemble of different Ni clusters or nanoparticles of different sizes and morphologies. Moreover, we focus on the reactivity of the supported cluster while in the experiments there could be other active sites. Furthermore, they might be additional deviations from the experiment due to errors in the computed DFT energies or the kMC method itself. Last but not least, the structure of the CeO_2 support in the present work and in the experiments above commented is also different, with the latter in the form of nanotubes whereas the former corresponds to a well-defined fluorite single crystal with the $CeO_2(111)$ surface termination. Nevertheless, in spite of these structural differences, the conclusions extracted from the kMC simulations provides useful insights about the catalytic activity and methane selectivity of small Ni clusters supported on $CeO_2(111)$ that are likely to be present in low Ni loaded Ni/CeO_2 catalyst. Finally, and just as a reminder for the reader, we want to point out that the ER reactions that we have included involve the hydrogenation of O and OH species (see Figure 5.2).

Table 5.3 summarizes the CH_4, CO and total total turn-over frequencies (TOFs) as well as the selectivity for the different studied temperatures and for the scenarios in which ER reactions are included or not.

Table 5.3. Total, CO and CH_4 TOFs and methane selectivity for the simulations including the Eley-Rideal steps (W/ER) and without them (Wo/ER) at five different temperature conditions and with $P(H_2) = 0.528$ bar and $P(CO_2) = 0.132$ bar for all he simulations. The TOF units are in molec · site^{-1} · s^{-1} while the CH_4 selectivity is given in percentage. Note that the methane selectivity is calculated as CH_4 selectivity = (CH_4 TOF / total TOF)·100. Table directly taken from ref 36.

	Total TOF		**CO TOF**		**CH_4TOF**		**CH_4 Selectivity**	
T	**W/ER**	**Wo/ER**	**W/ER**	**Wo/ER**	**W/ER**	**Wo/ER**	**W/ER**	**Wo/ER**
483	0.136	0.063	0.034	0.029	0.102	0.034	75.1	53.9
503	0.373	0.206	0.195	0.158	0.178	0.049	47.7	23.5
523	1.175	0.752	0.896	0.687	0.279	0.065	23.8	8.7
543	2.733	1.927	2.447	1.870	0.286	0.057	10.5	3.0
563	4.534	3.441	4.332	3.407	0.202	0.034	4.5	1.0

From Table 5.3 it can be seen that for both the simulations with and without the ER reactions, the highest the temperature the highest the total TOF and the lower the CH_4 selectivity. Not surprisingly, the higher the temperature the higher the total TOF as at higher temperatures the system has more energy to overcome the different energy barriers, thus, increasing the final catalytic activity. The change in methane selectivity

can be explained as a thermodynamic effect as the RWGS reaction is an endothermic reaction while the Sabatier reaction is exothermic. Therefore, the higher the temperature the more favored the RWGS reaction with respect to the Sabatier reaction, thus, an increase in temperature produce a higher increase on CO production rather than on CH_4 formation. Interestingly, the highest methane formation is around 523-543 K for both scenarios. This shows that, above these temperatures, thermodynamic effects start to be more important than kinetic effects and directly points to work at these temperatures for higher CH_4 production. However, for high selective methane formation one should work at the lowest temperature condition. From Table 5.3 one can spot similar trends for the simulations with or without including the ER reactions although the absolute magnitudes are larger when the ER reactions are included. Comparing our results at 563 K with the experimental values reported by Zheng et al.,[23] we have found a larger total TOF (4.534 vs. 0.187 $mol_{CO_2} \cdot site^{-1}\ s^{-1}$) but a lower methane selectivity (4.5 vs. 21.1 %). As the TOF for CO is normally larger than for methane, it is not surprising that our total TOF is larger as we have also found a lower CH_4 selectivity with a concomitant higher weight of the CO TOF on the total production. We suggest that the higher CO production we have observed is due to the very repulsive adsorbate-adsorbate interactions present in our small supported cluster model. This is because, in this small cluster, species tend to be in less stable sites due to steric effects, thus increasing the adsorbate-adsorbate interactions. This finally translates into a lower CO adsorption energy than the one reported in Table 5.1, and a higher CO desorption. However, one must also note that the experimental system is likely to contain large clusters or even nanoparticles where species can better adapt, reducing the repulsive interactions with the concomitant lowering of the experimental activity and higher methane selectivity. As a final remark, we have found a similar activity but 3 times larger methane selectivity for the simulations at 483 K compared to the experimental values at 563 K. Therefore, from the present results we suggest that flat small Ni clusters supported on $CeO_2(111)$ surface are potential good catalysts for selective methane formation at mild working conditions.

We now examine in detail the role of the ER steps on the mechanism, activity and selectivity at 523 K. Figure 5.3a and 5.3b show a schematic representation of the net executed processes at the different sites for the simulations with and without the ER reactions, respectively. Note that similar results have been obtained at different temperatures. Interestingly, there is a clear synergy between the two different sites (i.e.

Ni_{Ce} and Ni_O sites) so that some reactions are dominant in one site while others reactions are preferred in the other, as shown in Figure 5.3a and 5.3b.

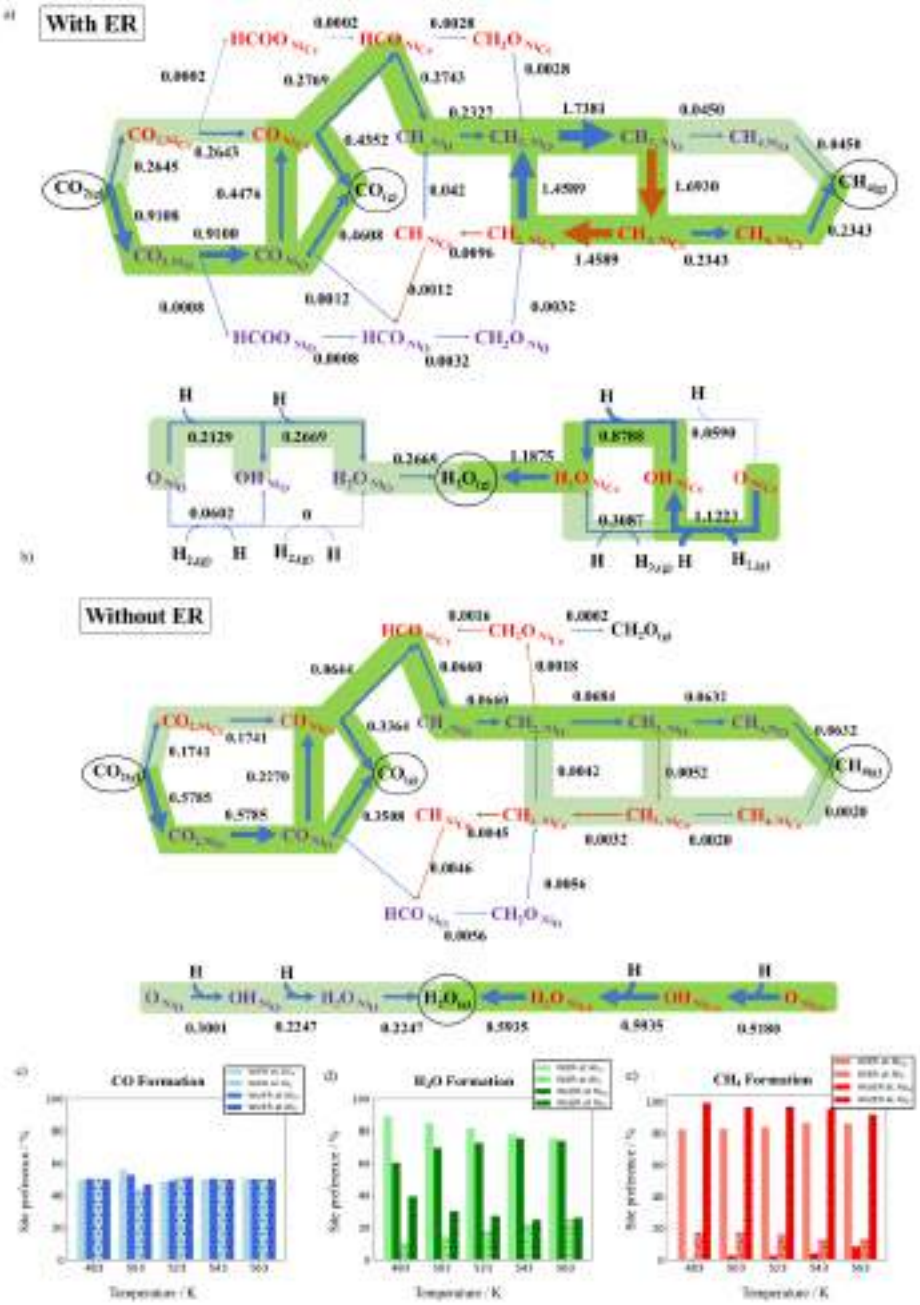

Figure 5.3. Schematic representation of the different executed events at a temperature of 523 K and P(H_2) = 0.528 bar and P(CO_2) = 0.132 bar for simulations with and without ER reactions in a) and b), respectively. Purple and red letters stand for species adsorbed on the Ni_O and Ni_{Ce} sites, respectively. Black numbers represent net number of executed processes as the average of 5 different kMC simulations in units of events · $site^{-1}$ · s^{-1}. Blue arrows stand for events executed from right to left and from bottom to up while brown arrows stand for events executed in the opposite directions. The size of the arrows represents the weight of the elementary step. Green and light green colors highlight the most important and secondary pathways, respectively. c-e) Formation of CO, H_2O and CH_4 on the Ni_{Ce} and Ni_O sites for the simulations with and without the ER reactions, in blue, green and red colors, respectively. Light colors stand for the simulations with ER reactions while dark colors stand for the simulations without ER reactions. Segments with no texture represent desorption on the Ni_{Ce} site while segments with "." texture stand for desorption on the Ni_O site. Picture directly taken from ref 36.

For both scenarios, CO_2 is mostly adsorbed on the Ni_O site (due to the higher adsorption energy at this site) while a non-negligible amount of CO_2 is also adsorbed at Ni_{Ce}. After CO_2 adsorption, it can dissociate to CO or being hydrogenated to HCOO which further dissociates to HCO. From Figure 5.3a and 5.3b one can spot that the CO_2 dissociation is the dominant reaction and only very few HCOO is formed. Interestingly the latter only occurs for the simulations with the ER reactions. As shown in Table S3 in Appendix A, the HCOO formation reaction has a lower energy barrier than the direct CO_2 dissociation, which would suggest that the former reaction would be more probable. However, the HCOO formation is less exothermic than the CO_2 dissociation reaction and the following HCOO dissociation to HCO is an endothermic reaction that tends to go backward to form HCOO again. This explains why the $CO_2 + H \rightarrow HCOO \rightarrow HCO + O$ total process is less probable than the direct CO_2 dissociation as after HCO is formed the overall process goes in the backward direction. Interestingly, for the simulations in which ER reactions are included, after HCOO dissociation to HCO and O, the O species can be hydrogenated more easily so that the $HCO + O \rightarrow HCOO$ reaction is less probable. This explains why this route is observed for the simulations with ER reactions but not for those simulations not including ER reactions (see Figure 5.3a and 5.3b). Regarding CO_2 dissociation, it mostly occurs on the Ni_O site to produce CO and O on Ni_O and Ni_{Ce} sites, respectively. After CO_2 dissociation the reaction can only proceed if CO desorbs or if O is hydrogenated to water that further desorbs thus freeing a site. As shown in Figure 5.3c CO desorbs in a similar amount in both sites for both scenarios, which points to water to be formed and desorb before CO desorption. This is because after H_2O desorbs from the Ni_{Ce} site it leaves this site available, where CO can diffuse and desorb, among other possible reactions. This is also confirmed by the highest water formation at the Ni_{Ce} site (see Figure 5.3d). On the contrary, if CO desorbs first, one should expect a CO desorption ratio at the different sites in the order of the CO_2 dissociation at the different sites while this is not the case (see Figure 5.3c). Moreover, the first water formation can also explain why for the simulations without the ER reactions the CO production is smaller as water formation is less probable; thus, CO needs more time to diffuse to the Ni_{Ce} site with the concomitant decrease on the catalytic activity.

Let us now take a look on how methane is formed starting from CO. The most probable reaction after CO formation is the CO hydrogenation to HCO. This reaction has a lower energy barrier at Ni_{Ce}, which is also the case for the HCO dissociation, thus being

both reactions more probable at Ni_{Ce} (see Table S3 in Appendix A). As shown in Figure 5.3a and 5.3b, this promote CO diffusion from Ni_O to Ni_{Ce} where some CO desorb while the rest is hydrogenated to HCO, which further dissociates to produce CH and O at Ni_O and Ni_{Ce}, respectively. Note that also a very small amount of HCO is hydrogenated to CH_2O that further dissociates to CH_2. This opens an alternative route for methane formation, although to a very low extent only. Interestingly, this alternative route goes in the backward direction for the simulations without including ER reactions (i.e., $CH_2 + O \rightarrow CH_2O \rightarrow HCO + H$) generating a cycle that hinders CH_4 formation. This is because in this type of simulations the O hydrogenation is less probable, which favors the $CH_2 + O \rightarrow CH_2O$ reaction. Coming back to the HCO dissociation at Ni_{Ce} to produce CH and O at Ni_O and Ni_{Ce}, respectively, there are two possibilities for the reaction to continue: O hydrogenation to water or CH hydrogenation to methane. Interestingly, again water formation plays an important role guiding the final activity and selectivity. We have found that for the simulations without ER reactions methane is formed first while for the simulations with the ER reactions water is formed before methane. This is supported by the difference in the diffusion steps of the CH_x species between the two sites as if water is formed first, then the Ni_{Ce} site is available and the CH_x species can diffuse which is the case for the simulations with ER reactions but not for the simulations without the ER reactions as clearly shown in Figure 5.3a and 5.3b. This is also sustained by locking Figure 5.3d in which one can spot a higher amount of water molecules being produced on the Ni_O sites for the simulations without ER reactions. This is a consequence of the previous methane formation at Ni_O for this type of simulations (see Figure 5.3e), leaving the Ni_O site available where O can diffuse and further hydrogenate to water. Figure 5.3a shows that after water formation CH is hydrogenated to CH_3 on the Ni_O site, which then a small part hydrogenates to CH_4 that further desorbs while most of the CH_3 diffuse to Ni_{Ce}. Next some CH_3 forms methane while another part dissociates to CH_2 that diffuses to the Ni_O site creating a cycle that, in the end, is beneficial for methane formation as methane is easily formed on the Ni_{Ce}, probably due to the adsorbate-adsorbate interactions, which explains the highest CH_4 selectivity observed for these simulations.

Up to this point we have shown the mechanism for CO and methane formation. We have shown that CO is formed via the dissociative pathway of the RWGS reaction while methane is formed as a combination of the RWGS reaction and a mix of the HCOO-mediated and dissociative pathways for the Sabatier reaction (*i.e.*, $CO_{2(g)} \rightarrow CO_2 \rightarrow CO$

$\rightarrow$ HCO $\rightarrow$ CH $\rightarrow$ CH_2 $\rightarrow$ CH_3 $\rightarrow$ CH_4 $\rightarrow$ $CH_{4(g)}$). We have also shown that the Eley-Rideal reactions play an unexpected important role on the mechanism, activity and selectivity. Moreover, we have revealed that there is a synergy between the two different three-fold hollow sites. In spite of the differences noted above, our DFT results partially agree with the ones reported by Zhang et al.[35] which proposed the dominant reaction mechanism for methane formation to be a combination of the carboxyl pathway for the RWGS reaction followed by the CO-hydrogenation pathway for the Sabatier reaction (*i.e.,* $CO_2 \rightarrow COOH \rightarrow CO \rightarrow HCO \rightarrow CH_2O \rightarrow CH_2 \rightarrow CH_3 \rightarrow CH_4$). However, our kMC results show that the direct CO_2 dissociation is the dominant pathway for the RWGS reaction rather than the carboxyl pathway. Moreover, we have clearly shown that the HCO dissociation reaction is key for methane formation rather than the CH_2O dissociation reaction. In fact, it has been shown that CH_2O formation hinders the final methane formation for the simulations without ER reactions. Finally, comparing our results with previous kMC results for the Ni(111) surface,[41] we have clearly shown that some of the hurdles for methane formation observed on the Ni(111) surface are not present in the supported Ni cluster. These are: the higher CO adsorption energy, the lower endothermicity of the HCO formation reaction and the smaller HCO dissociation energy barrier present on the supported Ni cluster. These differences open the HCO dissociation to CH as a possible route to obtained CH_x species that are further hydrogenated to CH_4. Our results clearly point to small Ni clusters supported over CeO_2(111) as promising candidates for active and selective methane formation at mild conditions.

Finally, we present the results for the apparent activation energy and partial orders of reaction with respect of both reactants (*i.e.,* CO_2 and H_2) for the RWGS and Sabatier reactions as shown in Figure 5.4. First, we compare our values for the simulations with the ER reactions and the experimental values[23] keeping in mind that our model system even being similar is not identical to the experimental system. Lastly, we compare our values for the simulations with and without the ER reactions. From Figure 5.4a and 5.4b we extract an apparent activation energy of 139.2 and 52.9 kJ/mol for the RWGS and Sabatier reactions, respectively, which contrast with the experimental values of 92.7 and 131.6 kJ/mol, respectively. We suggest that these differences are related to the higher CO adsorption energy and higher methane reactivity present on the supported Ni_4 cluster, which, again, puts small supported Ni clusters as potential candidates for efficient CO_2 hydrogenation to methane at mild conditions.

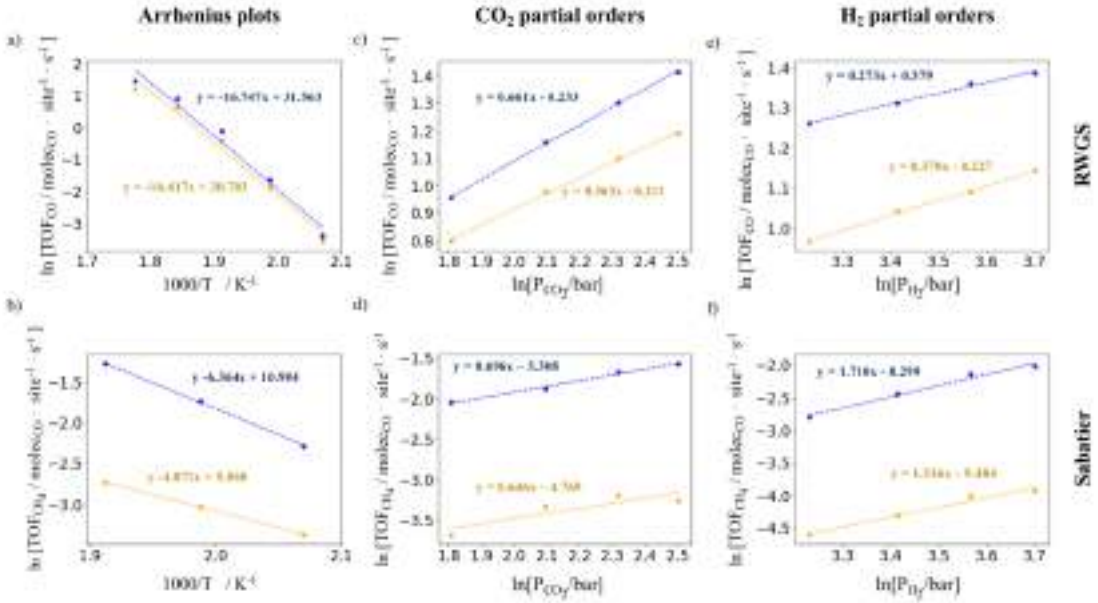

Figure 5.4. Arrhenius plot for the RWGS (a) and Sabatier (b) reactions, respectively at $P(H_2)$ = 0.528 bar and $P(CO_2)$ = 0.132 bar. CO_2 partial orders for the RWGS (c) and Sabatier (d) reactions, respectively at fixed $P(H_2)$ = 0.54 bar. H_2 partial orders for the RWGS (e) and Sabatier (f) reactions, respectively at fixed $P(CO_2)$ = 0.135 bar. Blue and orange colors stand for the simulations with and without including the ER reactions, respectively. Picture directly taken from Ref 36.

Comparing our CO_2 and H_2 partial orders of reaction with the experimental values,[23] we have found smaller CO_2 partial orders of reaction (i.e., 0.66 vs. 1.42 and 0.70 vs. 1.08 for the RWGS and Sabatier reactions, respectively) but larger H_2 partial orders of reaction (i.e. 0.27 vs. -0.04 and 1.71 vs. 1.07 for the RWGS and Sabatier reactions, respectively) as shown in Figures 5.4c to 5.4f. We attribute the differences for both the CO_2 and H_2 partial orders of reaction to the large nanoparticles likely to be present in the experiments. Regarding the CO_2 partial order of reaction, we attribute our smaller values to the limited number of sites of our model. This implies that an increase of the CO_2 partial pressure does not change the actual number CO_2 molecules adsorbed on the surface (as only one can be adsorbed at a time) but it produces an increase on the probability of CO_2 to adsorbed which results in an increase of the catalytic activity. However, for the experimental system with larger nanoparticles, an increase of CO_2 pressure actually changes the number of CO_2 molecules adsorbed on the nanoparticle which explains their higher values. Regarding the H_2 partial order of reaction, in our model we have seen that both CO and CH_4 formation are somehow linked to the previous water formation so that the higher the H_2 partial pressure the more probable is for water to be formed with the

concomitant increase of the catalytic activity. Moreover, CH_4 formation requires more hydrogenation steps which also explains the high H_2 partial order of reaction for the Sabatier reaction. However, large nanoparticles are likely to have more free sites so that CO and CH_4 are not conditioned by previous water formation which explains the lower experimental values.

Finally, we compare our values for the simulations with and without the ER reactions. From Figure 5.4a and Figure 5.b one can extract the apparent activation energies for the RWGS and Sabatier reactions for the two different scenarios. These are 139.2 and 136.5 kJ/mol for the RWGS reaction 52.9 and 33.8 kJ/mol for the Sabatier reaction, for the simulations with and without ER reactions, respectively. From these values one can spot almost no change for the RWGS reaction which point that CO desorption occurs similarly for both situations. However, a large difference can be seen for the Sabatier reaction which suggest that temperature has a higher effect on the ER reactions rather than on surface reactions and for that reason methane formation including the ER reactions is more affected by changes on temperature. From Figure 5.4c and 5.4d one can spot slightly higher CO_2 partial orders of reaction for the simulations in which the ER reactions are included. As explained above the higher CO_2 partial pressure the higher the probability of CO_2 to be adsorbed and react. Therefore, as the simulations with ER reactions predict higher activities, a higher probability of CO_2 to be adsorbed on the surface translates into a higher activity. Regarding the H_2 partial order of reaction, from Figure 5.4e and 5.4f it can be seen that the simulations with ER reactions predict a lower value for the RWGS reaction but a higher value for the Sabatier reaction, which suggests that ER reactions are more important for methane formation than for CO production. We suggest that this is because a high methane formation requires of available Ni_{Ce} sites in which CH_3 is hydrogenated a situation more probable for the simulations with ER reactions. As a final remark, these results suggest that high methane selectivity requires working at high H_2 partial pressures.

5.4. Summary and conclusions

To sum up, we have thoroughly studied the CO_2 hydrogenation reaction on a well-defined model of a Ni/CeO_2 catalyst, consisting of a Ni_4 cluster supported on the stoichiometric

CeO_2(111) surface, by means of a multiscale approach coupling DFT calculations with kMC simulations. The DFT calculations evidences that, in general, the adsorption energies and energy barriers of the different elementary steps are significantly different from those for the extended Ni(111) surface, as expected. In general, DFT results show higher adsorption energies and lower energy barriers for the Ni_4/CeO_2 model system which suggest that similar systems will be good candidates for the CO_2 hydrogenation reaction. We attribute the differences between Ni(111) and Ni_4/CeO_2 due to the metal-support interaction that change the Ni electronic structure along with differences in the Ni atomic coordination of the Ni_4 cluster, the former likely to be the dominant one.

To further understand the mechanism of the CO_2 hydrogenation reaction on the Ni_4 cluster we have performed several kMC simulations at different working conditions. From our kMC simulations we have unraveled the role of including some Eley-Rideal reactions on the reaction network and studied how they change the mechanism, activity and CH_4 selectivity. Interestingly, the kMC simulations show a synergic effect between the two different three-fold hollow sites present on the supported Ni_4 cluster, in which some reactions are dominant in one site while other reactions are preferred on the other site, being this effect even more evident comparing the simulations with and without the Eley-Rideal reactions. The kMC simulations unravel the mechanism that drives the overall reaction for CO and methane formation, being CO the most important product at the highest temperatures as shown on the experiments, while being methane the most significant product at the lowest temperatures. The former is produced via the dissociative pathway of the RWGS reaction. The latter is formed as a combination of the dissociative pathway to produce CO followed by a mixture of the HCOO-mediated and dissociative pathways for the final methane formation (*i.e.*, $CO_{2(g)} \rightarrow CO_2 \rightarrow CO \rightarrow HCO \rightarrow CH \rightarrow CH_2 \rightarrow CH_3 \rightarrow CH_4 \rightarrow CH_{4(g)}$). From our analysis we have shown that CO_2 dissociation is dominant on the Ni_O site to produce CO and O at Ni_O and Ni_{Ce}, respectively. Then, after water formation some CO desorb while some CO diffuses to the Ni_{Ce} site, where it desorbs or hydrogenates to HCO that further dissociates to CH and O at Ni_O and Ni_{Ce}, respectively. Interestingly, for the simulations with the ER reactions, water is formed before methane, leaving the Ni_{Ce} site available where methane can be formed easily. Nevertheless, for the simulations without the ER reactions methane is formed first in the less reactive Ni_O site with the concomitant decrease on the catalytic activity and methane selectivity. Last but not least, the analysis of the partial orders of reactions suggest

working at high H_2 pressure for higher methane selectivity. Finally, the present simulations show the important role of the Eley-Rideal reactions and reveal that small Ni clusters supported over $CeO_2(111)$ could be good candidates for selective methane formation at mild conditions.

5.5. Publications

A comprehensive density functional and kinetic Monte Carlo study of CO_2 hydrogenation on a well-defined Ni/CeO_2 catalyst: role of Eley-Rideal reactions

Pablo Lozano-Reis, Pablo Gamallo, Ramón Sayós, Francesc Illas

Departament de Ciència de Materials i Química Física & Institut de Química Teòrica i Computacional (IQTCUB), Universitat de Barcelona, C. Martí i Franquès 1, 08028 Barcelona, Spain

ABSTRACT

A detailed multiscale study of the mechanism of CO_2 hydrogenation on a well-defined Ni/CeO_2 catalyst model system is reported that couples periodic density functional theory (DFT) calculations with kinetic Monte Carlo (kMC) simulations. The study includes an analysis of the role of Eley-Rideal elementary steps, that are usually neglected on the overall picture of the mechanism, catalytic activity and selectivity. The DFT calculations for the chosen model consisting of a Ni_4 cluster supported on CeO_2 (111) show large enough adsorption energies along with low energy barriers that suggest this catalyst to be an excellent option for high selective CO_2 methanation. The kMC simulations results show a synergic effect between the two three-fold hollow sites of the supported Ni_4 cluster with some elementary reactions dominant in one site while other reactions prefer the other, nearly equivalent site. This effect is even more evident for the simulations explicitly including Eley-Rideal steps. The kMC simulations reveal that CO is formed via the dissociative pathway of the RWGS reaction while methane is formed via a $CO_{2(g)} \rightarrow CO_2 \rightarrow CO \rightarrow HCO \rightarrow CH \rightarrow CH_2 \rightarrow CH_3 \rightarrow CH_4 \rightarrow CH_{4(g)}$ mechanism. Overall our results show the importance of including the Eley-Rideal reactions and point to small Ni clusters supported on CeO_2 (111) surface as potential good catalysts for high selective CO_2 methanation at mild conditions while potential good catalysts for highly active and selective CO formation at high temperatures conditions.

KEYWORDS : Ni/CeO_2, Eley-Rideal reactions, metal-support interactions, methane selectivity, CO_2 hydrogenation, kinetic Monte Carlo,

INTRODUCTION

The continuous use of carbon-rich fossil fuels has dramatically increased the atmospheric amounts of carbon dioxide producing devastating effects on our ecosystem. In order to reverse this situation, CO_2 valorization has emerged as a low-cost strategy to simultaneously reduce the environmental impact related to carbon dioxide and, at the same time, generate value-added chemicals. In this regard, the power to gas[1,2] (PtG) technology has gained attraction as a promising option to absorb and exploit surplus renewable energies using CO_2 as a feedstock. The PtG concept is based on using excesses of energy produced from renewable sources for carrying out water splitting to further use the produced H_2 for CO_2 hydrogenation toward different chemicals. Among the different possible processes, the power to methane (PtM) technology[3] provides an interesting chemical route to produce methane that is further used as a fuel, now in a circular way. Regarding this reaction, Ni-based catalysts are commonly used due to their relatively high activity and its economic viability in comparison to catalysts using other noble metals.[4,5] In particular, Ni/CeO_2 catalysts have been shown to exhibit superior catalytic activity than other Ni-based catalysts.[6-9]

In the past years, considerable effort has been devoted to understand the intricacies that make Ni/CeO_2 catalysts so active for the CO_2 methanation reaction. Unfortunately, there is still not a clear consensus around this issue and different hypotheses have been proposed. Among them, researchers have focused on the effect of support, of particle size and morphology, and of the strong metal-support interaction (SMSI) just to name a few. Regarding the support, Martin et al.[7] studied the CO_2 hydrogenation reaction over different Ni-based catalysts and reported that the highest activity and methane selectivity corresponds to the Ni/CeO_2 catalyst. They attributed the increase of activity and selectivity to the quite small Ni nanoparticles that were present on these systems. Similarly, Lee et al.[9] studied the CO and CO_2 hydrogenation reaction over several catalysts consisting on Ni nanoparticles supported over different metal oxides. They reported the highest catalytic activity for Ni/CeO_2 systems, and again attributed this boost of activity to the small size of Ni nanoparticles that were present in that system. These conclusions point to the nanoparticle size as a key defining the final catalytic activity and selectivity, which probably stimulated other research groups to focus their attention on the particle size effect for the Ni/CeO_2 catalyst. Even though several studies have focused on the Ni nanoparticle size, different conclusions have been reached and there is still not a clear consensus on how the nanoparticle size affects the catalytic activity. Thus, some studies claim that large nanoparticles are more active while other studies argue the opposite. For instance, Lin et al.[10] studied three systems with Ni nanoparticles supported on CeO_2 featuring different sizes (i.e., 2, 4 and 8 nm) and found that the larger Ni nanoparticles were more active. They attributed the higher activity of the larger particles to their ability to dissociate H_2 thus producing a higher amount of H adatoms that further hydrogenate interfacial species to methane. Similar results were obtained by Winter et al.[11] and Zheng et al.[12] who also reported higher catalytic activity and selectivity for the systems containing larger nanoparticles. Interestingly, in both works they observed a rapid increase in the methane selectivity when increasing the nanoparticle size. On other hand, Lin

et al.[13], in a very recent paper, studied different Ni/CeO_2 systems with Ni nanoparticle sizes ranging from 9 to 11 nm and reported that the system with the smallest nanoparticles, although rather large particles with size ~9 nm, had the highest catalytic activity and selectivity towards methane. They attributed the boost of activity to a large number of interfacial oxygen vacancies as a response of the strong metal-support interaction that smallest nanoparticles feature. Similarly, Rui et al.[14] prepared two different Ni/CeO_2 systems following two different preparation methods and observed that, the smaller the nanoparticle, the larger the metal-support interaction which was translated into more oxygen vacancies and a higher catalytic activity.

Thus, some results from the literature points to a correlation between the strong metal-support interaction and the catalytic activity rather than a correlation between the Ni nanoparticle size and the catalytic activity. Precisely, in a very recent work, Pu et al.[15] studied the effect of strong metal-support interactions for three different Ni/CeO_2 systems with nanoparticles of ~5 nm but with different metal-support interactions due to the level of the nanoparticles encapsulation. They suggested that the SMSI effect is closely related to the encapsulation and the larger the encapsulation, the larger the metal-support interaction, which was translated into a large amount of oxygen vacancies where CO_2 can be activated with the concomitant increase of the catalytic activity. Combining theoretical modelling and experiments, several studies claim that small Ni clusters or nanoparticles supported on CeO_2 exhibit large metal-support interactions together to high catalytic activity for a variety of reactions such as the dry reforming of methane,[16-19] direct conversion of methane to methanol,[20] water dissociation,[21] methane steam reforming reaction,[22] water-gas shift (WGS) reaction,[23] and CO_2 methanation.[24] Regarding theoretical studies dealing with CO_2 hydrogenation reaction to methane over Ni/CeO_2 there is, to the best of our knowledge, only the work of Zhang et al.[24] In their DFT study they propose different mechanisms for the CO_2 hydrogenation reaction and suggest that methane is formed via the reverse water gas shift reaction followed by the CO-hydrogenation pathway.

However, for such CO_2 hydrogenation reaction involving a complex network of elementary steps and several active sites, one cannot always rely on the static picture offered by the typical DFT based energy or free-energy profiles to accurately describe the system evolution under real working conditions. In these cases, it is necessary to couple DFT calculations to some kinetic modeling techniques as we have very recently shown for the RWGS reaction on Ni/TiC systems.[25] Precisely, the goal of the present work is to reach a thoroughly description of the CO_2 hydrogenation reaction over a Ni/CeO_2 model system, where both support composition and crystal structure and supported Ni atomic structure are well-defined. To this end we couple a very detailed study of all elementary steps to kinetic Monte Carlo simulations. This multiscale approach provides compelling evidence of the role of each part of the model catalyst and unravel the main mechanism that govern the overall reaction, highlighting the unexpected role of the Eley-Rideal (ER) elementary steps on the final activity and selectivity.

METHODS

The Ni/CeO_2 structural model. The Ni/CeO_2 system is modelled by a flat Ni_4 cluster supported on a slab model of the stoichiometric CeO_2(111) surface. The slab model consists of an appropriate 3×3 CeO_2(111) supercell built from the calculated fluorite structure of ceria bulk with an equilibrium lattice parameter of a_o = 5.445 Å. The slab contains a total of nine atomic layers, or three O-Ce-O trilayers. A Ni_4 cluster is deposited on top of the surface with its equilibrium structure as shown in Figure 1a. A 13 Å vacuum width between periodically repeated slabs has been included in order to avoid spurious interactions between the periodic replicas in the perpendicular direction to the surface.

DFT Calculations. To characterize the energetics of the CO_2 hydrogenation reaction for the Ni_4 cluster supported on the CeO_2 (111) surface model, periodic spin-polarized DFT calculations have been carried out by means of the Vienna Ab-initio Simulation Package (VASP) code[26-28] using the frozen-core augmented (PAW)[29] method to describe the interaction between the atomic cores and the valence electron density. All calculations have been done using the DFT+U formalism involving the PBE functional[30] and a value of 4.5 eV for the Hubbard U-like term, which is included to correctly represent the Ce 4f states.[31,32] In addition, we have included the Grimme D3[33] term to capture the effect of dispersion in the calculated energies. The particular choice of the Ni_4 cluster is to have a representative model of a small flat cluster exhibiting electronic metal-support interaction.[20,24,34-36] In all calculations, the three lowermost layers (one O-Ce-O trilayer) have been kept fixed at their bulk position to provide an adequate bulk environment to the top surface layers. The atomic structure of the six uppermost layers, of the Ni_4 cluster and of the different adsorbed species have been allowed to fully relax during the calculations. The Brillouin zone has been sampled with a (3×3×1) ***k***-point mesh using the Monkhorst-Pack scheme[37] and a cutoff energy of 415 eV has been used for the plane wave basis expansion. The electronic energy criterion has been selected to 10^{-5} eV while a value of 0.01 eV · $Å^{-1}$ has been used for the ionic relaxation criterion.

Transition states (TS) structures have been located using the climbing-image nudged elastic band (CI-NEB) method.[38,39] To generate the initial images guesses the Image Dependent Pair Potential procedure[40] has been used as implemented in the Atomic Simulation Environment (ASE) package.[41] The located TS structures have been properly characterized by vibrational frequency analysis to ensure that all TS have only the desired imaginary frequency corresponding to the coordinate reaction. Frequency calculations have also been performed for all the adsorbed and co-adsorbed structures ensuring that they correspond to real minima on the potential energy surface (PES). The calculated frequencies have been used to calculate the zero-point energy (ZPE) contribution of the different structures as well as to calculate the vibrational partition functions, which are required for the calculation of preexponential factors that are necessary to compute the transition probabilities used in the kinetic Monte Carlo simulations. Note that low-frequency modes below a cutoff value

of 6.9 meV have been set to this cutoff value in order to approximate the entropy from a pseudorotational/pseudotranslational degree of freedom as previously done.[42] The energy of the gas-phase species has been calculated by placing a single molecule in an asymmetric box of dimension $9 \times 10 \times 11$ Å^3 and considering the Γ point only. Finally, the reaction energies ($\Delta E_{0,r}$) and energy barriers ($\Delta E_0^{\neq}$) including the ZPE contribution have been calculated as:

$$\Delta E_{0,r} = E_{FS,0} - E_{IS,0} \quad (1)$$

$$\Delta E_0^{\neq} = E_{TS,0} - E_{IS,0} \quad (2)$$

where $E_{FS,0}$, $E_{IS,0}$ and $E_{TS,0}$ are the total energy of the final, initial and transition states, respectively, also including the ZPE contribution.

Kinetic Monte Carlo simulations. In order to gain insights of the system evolution under real working conditions, kMC simulations have been carried out using the graph-theoretical kMC approach[43] combined with cluster expansion Hamiltonians[44,45] as implemented in the Zacros software.[43,44] The kMC lattice (Figure 1b) is built so as to mimic the Ni_4 cluster used for the DFT calculations (Figure 1a) and consists of a non-periodic custom grid of 6 points representing surface sites, where the different species can adsorb, desorb, react or diffuse. A total of 4 different sites have been considered, as described next. Two different coarse-grained (*i.e.*, Ni_{Ce} and Ni_O) sites have been used to represent the three-fold hollow sites of the Ni_4 cluster. We have used two different types of sites because the two hollow sites of the Ni_4 cluster are not exactly the same as one has a Ce atom underneath (*i.e.*, Ni_{Ce}) while the other has an O atom (*i.e.*, Ni_O). These differences translate into different adsorption energies depending on the site the species adsorbs. Finally, to avoid the use of a "hard sphere" model for small adsorbates like H and H_2, we have used a special hydrogen reservoir site[25,46] in which these two species can adsorb. As for the Ni sites we have considered two different types of hydrogen reservoirs (*i.e.*, h_{Ce} and h_O). The presence of two non-identical sites involves considering the energetics of the different adsorbed species and the energetics of the possible elementary reactions twice, each one for each site. Moreover, to correctly define the reactivity, we have considered that if the two Ni sites are occupied, hydrogenation reactions can only occur if both species are on the same type of site (*i.e.*, both species in Ce sites or both species in O sites). For instance, let us imagine a situation in which CH, O and H species are adsorbed onto Ni_O, Ni_{Ce} and h_O, respectively. In this case, the H adatom cannot attack the oxygen as it is blocked by the CH and it can only react with CH or diffuse to the h_{Ce} site. This is done to correctly capture blocking effects.

The reaction network involves a total of 98 reversible reactions, including adsorption, desorption, surface reaction and diffusion steps. Besides, we have also considered some Eley-Rideal steps for the hydrogenation of O (i.e., R34) and OH species (i.e., R35) as shown in Figure 2. Note that, as explained above,

reactions are considered twice as the adsorbed species can be either at the Ni_{Ce} site or at the Ni_O site. Moreover, for some hydrogenation reactions we have considered two different possibilities: (*i*) the H adatom and the other species are at the same type of site (i.e., both at Ce or O type of sites) and (*ii*) the H adatom and the other species are at different type of sites (i.e., one at Ce and the other at O type of sites or *vice versa*). The cluster expansion used in our model includes pairwise lateral interactions between all possible reactant/product pairs as well as between all other relevant species. The cluster expansion has been truncated to first-nearest neighbors two-body terms as well as second-nearest neighbors two-body terms. Overall, it contains 41 one-body terms and 93 two-body terms as summarized in Table S1 and S2 in the Supporting Information. For very fast and quasi-equilibrated processes the transition probabilities have been scaled by a factor $\alpha < 1$ to speed up the kMC simulations while ensuring that these processes are still very fast and quasi-equilibrated. This pragmatic solution has been extensively applied in several studies.[25,42,46-49]

To study the CO_2 hydrogenation reaction over the Ni cluster, we have considered an initial mixture of CO_2 and H_2 continuously impinging on a pristine surface in which different processes can take place and where the products formed are considered to desorb without allowing re-adsorption. Note that for convenience, we have considered that CO_2 can only adsorb if both Ni sites are unoccupied contemporarily so that for each CO_2 species a CH_4, CH_2O, CO or CH_3OH species has to be formed as well as the appropriate number of water molecules before another CO_2 species can be adsorbed. This is done as a pragmatic solution to avoid exceedingly large simulations in which the system spends time doing CO_2 adsorption/desorption steps without the reaction evolving due to the limit of two sites of our model. The working conditions are chosen as in the experiments of Zheng et al.[12], which are $P(H_2)$ = 0.528 bar and $P(CO_2)$ = 0.132 bar and temperatures ranging from 483 K to 563 K. Additional simulations for a temperature of 563 K and different partial pressures are also performed in order to study the partial order of reaction. Moreover, for all the different working conditions we have run the simulations including some Eley-Rideal steps and without including them to gain insights about the role of this kind of reactions. Finally, in order to better sample the configurational space, we have run 5 different simulations which only differ from each other in the sequence of random numbers and the macroscopic magnitudes are given as the average of the five different replicas.

RESULTS AND DISCUSSION

DFT Results. The Ni_4 cluster adsorbs above the oxygen atoms of the $CeO_2(111)$ uppermost layer, adopting a structure that is reminiscent of that of the Ni(111) facet (see Figure 1a). Interestingly, the cluster adsorption triggers a charge transfer between the metal cluster and the surface so that two formally Ce^{4+} atoms are reduced to Ce^{3+} atoms while the Ni atoms are partially oxidized to $Ni^{0.5+}$, a clear indication of metal-support interactions, which is in agreement with previous results for similar Ni/CeO_2 systems.[22,34,35,50] Precisely, the metal-support interactions affect the electronic structure of the Ni atoms of the Ni adcluster, making them

different from those of the Ni (111) surface. In general, this is beneficial for the adsorption and activation of the different species with a concomitant increase of the catalytic activity as shown below. Therefore, we have studied the adsorption of the possible reactants and products of the CO_2 hydrogenation reaction (see Figure 2) over the Ni cluster sites with results summarized in Table 1, where some data from our previous study of the CO_2 hydrogenation reaction on Ni(111) have been included for comparison.[42] Note that, in general, bifunctional catalysts such as Ni/CeO_2 contain three different regions with different energetics, namely, the metal region, the support region and the interface region that lies in between the two former regions. In this study, we have restricted our calculations to the Ni cluster for several reasons. First, we want to understand the effect of the metal-support interactions which is thought to increase the metal activity. Moreover, the clean $CeO_2(111)$ surface is inactive for CO_2 hydrogenation,[12] so that one can discard this region. Finally, adsorption energies for CO_2 on the Ni cluster are larger than those at the interface region [24] and a noticeable CO_2 adsorption energy is a necessary step for its catalytic hydrogenation.

As shown in Table 1, the most favorable sites for the different stable gas-phase species are, in general, the two different three-fold hollow sites. The adsorption energies are similar for the two different sites. Let us start by comparing our values in Table 1 for the Ni cluster with reported values for similar systems. For instance, the present CO_2 adsorption energies of -1.51 eV and -1.46 eV at both three-fold hollow sites are similar to the values reported by Alvarez-Galvan et al.[34] and Zhang et al.[24] of -1.26 and -1.64 eV, respectively, lying in between them. A careful comparison between present and previous values, shows the origin of the differences in adsorption energy. For instance, we have found a CO_2 structure that is bent to the surface, hence, featuring a higher interaction with the surface that can explain the higher adsorption energy we have found with respect to the study of Alvarez-Galvan et al.[34] Regarding the latter study by Zhang et al.[24], the differences are smaller—less than 0.2 eV— and can be attributed to the different computational code used and the different methodology used in the calculations. Moreover, our values include the ZPE term while it does not seem to be included in the commented previous works. Alvarez-Galvan et al.[34] also reported an H_2 adsorption energy of -0.95 eV, which again is slightly larger than the present values of -0.63 eV. The difference is clearly due to the different Ni atom in which H_2 adsorbs as well as to the lack of the ZPE term. For instance, our H_2 adsorption energy with and without the ZPE term is -0.63 and -0.75 eV, respectively, the latter being closer to the value reported by Alvarez-Galvan et al.[34] Finally, Lustemberg et al.[35] reported adsorption energies of -0.93 eV and -0.24 eV for H_2O and CH_4, respectively, which are in agreement with our reported values. Again, we attribute the differences between our values and the reported ones due to the inclusion or not of the ZPE term, our values being -0.75 and -0.82 eV for H_2O and -0.26 and -0.28 eV for CH_4 when including or not the ZPE term. In general, the present values are close enough to those reported in the literature and we suggest that further differences are due to the different methodology used in the calculations. Next, we compare the values obtained for the Ni clusters and the ones reported for the Ni(111) surface.[42] From Table 1 one can clearly see how the metal-support interactions together to differences in the Ni atomic coordination lead to

larger adsorption energies with the former, implying a considerable charge transfer, being likely to dominate. For instance, CO_2 and H_2 molecules physisorb on the Ni(111) surface while they are clearly adsorbed on the supported Ni cluster. As these two molecules are the reactants of the CO_2 hydrogenation reaction, higher adsorption energies would, in principle, favor the catalytic activity of the Ni cluster suggesting Ni clusters to be more active than the Ni(111) surface. Nevertheless, it is important to point out that only from the adsorption energy values it is not possible to conclude which system will be more catalytically active as small energy barriers are required for the reaction to proceed (*vide infra*). Regarding the desired product (CH_4), the adsorption energy on the Ni cluster is also larger than on Ni (111). Nevertheless, in both cases, CH_4 has a small adsorption energy which would favor methane desorption. Focusing on the other possible products, namely CO, CH_2O and CH_3OH, we see again that the support effect leads to an increase of the adsorption energies of these species. Interestingly, a larger adsorption energy of the different products would, in principle, benefit CH_4 formation. In fact, as reported for the Ni (111) facet,[42] one of the problems that makes it inactive for methane formation is the low CO adsorption energy compared to other competitive reactions, favoring CO desorption rather than subsequent reactions. Therefore, a large CO adsorption energy would, in principle, favor methane selectivity, pointing to the Ni cluster to be more selective than the Ni (111) surface.

We have shown that metal-support interactions strongly increase the adsorption capacity of the Ni cluster compared to the Ni (111) facet. Nevertheless, as explained above, to gain insights about the catalytic behavior of a given catalyst one must evaluate the energy barriers of the different competing elementary reactions. In Table 2 we summarize the reaction energy and energy barrier for some elementary steps of the CO_2 hydrogenation reaction (see Figure 2). For simplicity we have only selected the ones that are the most relevant for our discussion while information regarding all the studied elementary reactions can be found in Table S3. For simplicity, we restrict the discussion to the elementary steps at the Ni_{Ce} site but similar conclusions can be extracted focusing on the Ni_O site. First, we start by comparing our calculated values with those already published for the same system. Comparing our values (see Table S3) and the values reported by Zhang et al.,[24] one can rapidly see a huge difference in the energy barriers reported by these authors and the present ones. In general, they reported significantly larger energy barriers with several elementary reactions with barriers ranging from 2 to 4 eV. This contrast with the present calculated values that are generally smaller with nearly vanishing barriers for some steps and the largest one being 2.18 eV. We suggest that these differences are due to the different initial and final states used and to the different computational methodology used for the calculations. On the contrary, Alvarez-Galvan et al.,[34] reported a CO_2 dissociation energy barrier of 0.75 eV which nicely agree with our calculated value of 0.77 eV. Moreover, they also found a barrierless H_2 dissociation reaction in line with our results. Similarly, Lustemberg et al.,[35] reported values that are in good agreement with our values. Note that for some reactions, these authors considered the presence of some spectator species while for others the presence of the spectators is not considered, which clearly change the energetics of the studied elementary reaction as shown for the CH_4 dissociation reaction. For a better

comparison with the present values we focus on the situation without spectator species. These authors studied CH_4 and H_2O dissociation and CH_3OH formation reactions, reporting energy barriers of 0.14, 0.41 and 1.40 eV, respectively which closely resemble our reported values of 0.14, 0.35 and 1.33 eV, respectively. The very good agreement between our calculated values and these two works point to a proper definition of our model system, while questions results of Zhang et al.[24]

Let us now evaluate the effect of the metal-support interaction on the energy barriers of the different elementary reactions and the possible mechanism that drive the overall reaction by comparing the values obtained for the Ni cluster and the values previously reported for the Ni(111) facet. Comparing the calculated values and the values reported in Ref. 42 (see Table 2 and Table S3) it can be seen that, as a result of the metal-support interaction, the energy barriers of the different elementary steps are reduced, which, in the end, could be beneficial for catalytic purposes. Focusing on some of the reactions, one can clearly spot from Table 2 that H_2 dissociation would be more favorable on the supported Ni cluster than on the extended surface, as for the first system it is a barrierless reaction while it has an energy barrier of 0.26 eV on Ni(111). Moreover, H_2 adsorption is more favorable on the supported Ni cluster, which also points to a higher activity. Comparing the different routes to CO_2 conversion, namely, direct CO_2 dissociation, COOH formation and HCOO formation reactions, similar barriers are obtained for the two former reactions (although smaller for the supported Ni cluster), while a large difference is observed for HCOO formation with values of 0.39 and 1.05 eV for the Ni cluster and the Ni(111) surface, respectively. The values for the Ni cluster suggest that the most probable reaction will be the HCOO formation followed by the CO_2 dissociation, which clearly opens the HCOO-mediated pathway as a possible route for CO or methane formation. This contrast with the kMC results obtained for the Ni (111) surface in which the CO_2 dissociation pathway and, to a lower extent, the COOH-mediated pathway were the active pathways, while the formate path was inactive.[42] Let us assume now that CO has been produced and evaluate the possible pathways for methane formation that start with COH formation, CO dissociation and HCO formation reactions. The former has similar energy barriers for both systems being the largest one among the three different reactions, hence, the less probable. Regarding CO dissociation, one can spot a huge change on the energy barriers with values of 1.52 and 2.98 eV for the supported cluster and the extended surface, respectively. This suggests that direct CO dissociation could compete with other routes on the supported cluster while this reaction is very unlikely on Ni (111). However, for the supported cluster, even with a reasonable energy barrier, the reaction is highly endothermic and thus, thermodynamically impeded. For HCO formation, one can also see a decrease on the energy barrier and, at the same time, a decrease on the endothermicity of the reaction. Precisely, one of the drawbacks for methane formation on the Ni (111) facet has been reported to be the high endothermicity of the HCO formation reaction, so that whenever HCO is formed it rapidly dissociates to CO, which further desorbs.[42] At the supported cluster, the lower endothermicity added to the highest CO adsorption energy could be paramount for the methane formation. After HCO is formed, it can also dissociate to CH or hydrogenated to CH_2O, with energy barriers

of 0.64 and 0.46 eV for the supported cluster and values of 1.10 and 0.71 eV for the Ni (111) surface, respectively. Again, both reactions have lower energy barriers for the supported cluster; thus, being more probable to be executed and more competitive with respect to the HCO dissociation to CO. Regarding, CH_2O dissociation to CH_2, the energy barrier on the supported cluster is lower than on the Ni (111) surface, which opens another route for methane formation. Finally, the CH_x species can be easily hydrogenated on both surfaces, albeit with lower values for the cluster, to finally form methane.

To sum up, we have shown that metal-support interaction induces an effect on the supported Ni cluster resulting in a decrease of the energy barriers of some of the relevant elementary steps and, at the same time, increases the adsorption energy of some side products, suggesting the possible formation of methane. From the DFT analysis, it appears that the most probable pathway for methane formation will be a combination of the CO formation—either via the HCOO-mediated pathway and, to a lower extent, the CO_2 dissociation pathway— followed by the CO hydrogenation to HCO, which can either dissociate to CH or being hydrogenated to CH_2O, that further dissociates to CH_2 that finally, can be further hydrogenated to CH_4. Also, the quite large CO and CH_2O adsorption energies suggest high methane selectivity. Our proposed mechanism agrees with the one proposed by Zhang et al.,[24] with the solely exception of the CO formation, that they suggested it is formed via the COOH-mediated pathway. Nevertheless, from the DFT picture only it is not possible to obtain any firm conclusion about the catalytic activity and selectivity and on the actual mechanism that governs the reaction. Moreover, as shown by Lustemberg et al.,[35] for CH_4 dissociation, neighboring spectator species can change the reactivity due to the adsorbate-adsorbate interactions. Therefore, to reach a more accurate and realistic description, the evolution of the system under real working conditions must be considered. To this end, in the next section we couple the DFT calculations with kMC simulations that naturally accounts for the effect of neighboring species and provide insights about the activity, selectivity and mechanistic aspects at the pressure and temperature conditions of interest.

kMC Results. To clearly understand the system evolution under real working conditions kMC simulations have been carried out. This allows us to gain insights about the role of the different sites and of the different elementary steps, such as Eley-Rideal reactions, on the global reaction mechanism, the catalytic activity and the selectivity towards CH_4, the latter being conditioned by the competition between the partial CO_2 hydrogenation to CO via the RWGS reaction and the complete CO_2 hydrogenation to CH_4 via the Sabatier reaction. Also, we compare our values with the experimental results reported in the literature for a system in which small Ni nanoparticles or clusters are likely to be present although, unfortunately, the structure of the CeO_2 support is different.[12] Hence, we must emphasize that we do not aim for quantitative agreement but rather a qualitative one. More in detail, the present model involved a supported flat Ni_4 cluster, while in the experiments by Zheng et al.[12] an ensemble of Ni clusters or nanoparticles of different sizes and morphologies are likely to be present. Also, our study focuses only on the reactivity of the supported Ni cluster, while in

experiments other active sites may be present, especially at the interface because the support structure is also different. Furthermore, additional deviations from the experimental values may arise from errors in the computed DFT energies, the kMC method itself or the truncation to two-body terms in the cluster expansion. In spite of these limitations, our multiscale study gives useful insights about the catalytic activity and selectivity of small supported Ni clusters that are likely to be present in Ni/CeO_2 systems with low Ni loading. Finally, and just as a reminder for the reader, we want to point out that the ER reactions that we have included involve the hydrogenation of O and OH species.

Table 3 summarizes the CO, CH_4 and total turnover frequencies (TOFs) as well as the selectivity towards methane for the scenarios in which ER reactions are include or not. From Table 3 one can spot that for both scenarios, the higher the temperature the higher the total TOF and the lower the CH_4 selectivity. The former is not surprising as the higher the temperature the higher the system energy and the easier to overcome the different energy barriers with the concomitant increase in the catalytic activity. The latter is due to thermodynamic effects, the higher the temperature the more favored the RWGS reaction with respect to the Sabatier reaction as the first one is endothermic while the latter is exothermic. Moreover, as CO is an intermediate product of the complete CO_2 hydrogenation reaction, the easier to form CO the lower the CH_4 selectivity. Therefore, a temperature increase translates into higher CO production, while this is not always the case for CH_4. Interestingly, the highest CH_4 formation is observed at 543 and 523 K including or not the ER reactions, respectively, although in both cases the values are very similar. This shows that above 523-543 K the thermodynamic effects become more important than kinetic effects and directly points to this temperature range as a limit for a higher CH_4 production. Note however, that the highest CH_4 selectivity is observed for the lowest temperature, which points to work at this condition for high selective methane formation although the overall production is smaller than at other temperatures. From Table 3 one can also see similar trends for the different reported magnitudes for the simulations with(out) the ER steps while higher absolute values are found when ER steps are included. We now compare our results at 563 K with the experimental values reported by Zheng et al.[12] We have found a qualitative good agreement with the experimental values that point to CO to be the major product. In comparison, we have found a lower CH_4 selectivity (4.5 vs. 21.1 %) and a larger total TOF (4.534 vs. 0.187 molec·site^{-1} s^{-1}). Note that for a better comparison we have adapted their reported values to our units. This is done just by using the Ni atomic mass, the Avogadro's number and considering that each site contains two Ni atoms. Note that the CO TOF is normally larger than the CH_4 TOF, hence, it is not surprising that our total TOF is higher than the experimental value as we have found a lower CH_4 selectivity that translates into a higher influence of CO on the total TOF.. In fact, for a temperature of 523 K in which the methane selectivity (for the simulations with ER steps) is similar to the experimental value at 563 K, our total TOF (see Table 3) better agrees with the experimental value. Nevertheless, we suggest that the higher CO production we observe is due to the very repulsive adsorbate-adsorbate interactions (see Table S2) present in such a small supported cluster in which steric effects

induce species to be in less stable sites, increasing the repulsive interactions between species. This translates into a CO adsorption energy lower than the one reported in Table 1, which turns into an easier CO desorption. Regarding the experimental system it is likely that it also contains large clusters or nanoparticles in which species can better adapt to the system with the concomitant decrease of the adsorbate-adsorbate interactions that can explain the lower experimental activity and higher CH_4 selectivity. Finally, the present results suggest that flat small Ni clusters supported over the CeO_2 (111) surface are potential good candidates for highly active and selective CO formation at high temperatures while are promising good candidates for selective methane formation at mild conditions as our reported value for 483 K points to a similar activity that the one found by Zheng et al.[12] at 563 K, while the CH_4 selectivity is 3 times larger.

We now examine in detail the role of the ER steps on the overall reaction mechanism, the activity and methane selectivity. We chose to carry out the analysis at 523 K as the highest CH_4 TOF is observed at this temperature. Note that, regarding the dominant mechanism, no important changes are observed for the other working conditions. Figure 3a and 3b show a schematic representation of the net executed processes for the simulations with and without the ER reactions, respectively. The event frequency plots at the different temperatures and different sites are included in Figure S1. As shown in Figure 3a and 3b there is a clear synergy between the two different sites, in which some reactions are dominant in one site while other reactions happen on the other site. For both scenarios, CO_2 has a large adsorption energy at the Ni_O site (see Table 1) although a non-negligible amount of CO_2 also adsorbs at Ni_{Ce}. Once CO_2 is adsorbed, it can dissociate or be hydrogenated to HCOO, which further dissociates to produce HCO. From Figure 3a and 3b one can spot that the CO_2 dissociation is the dominant reaction and only very few HCOO moieties are formed for the simulations in which the ER reactions are included. As shown in Table S3, HCOO formation has a lower energy barrier than CO_2 dissociation, which points to the former reaction to be more probable. However, the former reaction is less exothermic than the CO_2 dissociation. Moreover, once HCOO is formed, it has to dissociate to HCO, which is an endothermic reaction, that tends to go backward to form HCOO again. In fact, the $CO_2 + H \rightarrow HCOO \rightarrow HCO + O$ total process is executed more times than the direct CO_2 dissociation (see Figure S1) but due to the endothermic nature of the last reaction, the overall process goes backward and the net balance is for CO_2 dissociation. Interestingly, the HCOO path is observed when including the ER reactions because in this situation it is easier for the O species to be hydrogenated hence the $HCO + O \rightarrow HCOO$ reaction is less probable. Regarding CO_2 dissociation, it can be seen in Figure 3a and 3b that it is predominant on the Ni_O sites, producing CO and O on Ni_O and Ni_{Ce} sites, respectively. At this point, there are only two possibilities for the reaction to continue: CO desorption or O hydrogenation to water that further desorbs. Interestingly, Figure 3c shows that CO desorbs in a similar amount from both sites, which points to water to be formed, in general, first, hence, leaving a free Ni_{Ce} site in which CO can diffuse and further desorbs (among other possible reactions). On the contrary, if CO desorbs first, one should expect a CO desorption ratio similar to the one for the CO_2 dissociation reaction at the different sites, which is not the case as can be

shown in Figure 3c. In this regard, Figure 3d also points to water to be formed first as it is formed mostly on the Ni_{Ce} site. Moreover, this can also explain why the activity is lower when the ER reactions are not included as water is more difficult to be formed in this situation and the system spend more time to produce water, which is a necessary step for the latter CO diffusion and desorption with the concomitant decrease on the catalytic activity.

Now we focus on the CH_4 formation starting from CO. Once CO is formed, the most probable reaction is CO hydrogenation to HCO. This reaction is more probable at the Ni_{Ce} site than at the Ni_O one due to the slightly lower energy barrier on the former. This is similar for HCO dissociation that is also favored at the Ni_{Ce} site (see Table S3). This fact promotes CO diffusion from Ni_O to Ni_{Ce}, where some CO desorbs and some CO hydrogenates to HCO that further dissociates to CH and O at Ni_O and Ni_{Ce}, respectively (see Figure 3a and 3b). Note that there is also a very small amount of HCO that is hydrogenated to CH_2O that further dissociates to CH_2. However, for the simulations without the ER reactions this alternative route goes backward (i.e., $CH_2 + O \rightarrow CH_2O \rightarrow HCO + H$) generating a cycle that is detrimental for methane formation. This is because in this type of simulations, the O adatom is less likely to be hydrogenated, hence, favoring the $CH_2 + O \rightarrow CH_2O$ reaction. Coming back to HCO dissociation to produce CH and O on Ni_O and Ni_{Ce}, respectively, there are two possibilities for the reaction to proceed: CH hydrogenation to methane or O hydrogenation to water. Interestingly, water formation plays again an important role for the final activity and selectivity. We found that in the simulations including ER reactions, water is formed before methane while the opposite behavior is observed in the simulations without ER reactions. This is supported by the difference in the diffusion steps of the CH_x species between the two different sites because if water is formed first, then the Ni_{Ce} site become free so that CH_x species can diffuse to this site as clearly seen in Figure 3a but not in Figure 3b. This is also supported by the fact that, in the simulations without ER reactions, there is a larger number of events for water formation at the Ni_O site (see Figure 3d). This is because methane is formed earlier at the Ni_O site (see Figure 3e), leaving the Ni_O site available so that O can diffuse to the Ni_O site, where it is further hydrogenated to water. For the scenario with ER reactions, Figure 3a shows that, after water formation, CH hydrogenates to CH_2 that further hydrogenates to CH_3 at Ni_O. Then a minor part of CH_3 hydrogenates to CH_4, which further desorbs, while most of CH_3 diffuse to Ni_{Ce}. Next, a fraction of CH_3 hydrogenates to CH_4 that further desorbs, while another fraction dissociates to CH_2 that diffuses to the Ni_O site generating a cycle. At the end, this cycle is beneficial for the final methane production as methane is easily formed at the Ni_{Ce} site, probably because of the larger adsorbate-adsorbate interactions at that site, which explains the highest CH_4 site preference for this site in this type of simulations (see Figure 3e).

So far, we have unveiled the mechanism for CO and methane formation. First, we have shown that CO is formed via the dissociative pathway of the RWGS reaction. Then we have revealed that methane is formed as a combination of the dissociative pathway to produce CO followed by a mixture of the HCOO-mediated

and dissociative pathways for the Sabatier reaction (*i.e.*, $CO_2 \rightarrow CO \rightarrow HCO \rightarrow CH \rightarrow CH_2 \rightarrow CH_3 \rightarrow CH_4$). We have also shown that there is a clear synergy between the two different sites and that the Eley-Rideal reactions play an important role on the final mechanism, activity and selectivity. In spite of the differences noted above, our results partially agree with those reported by Zhang et al.,[24] which proposed the dominant reaction mechanism to be a mix of the carboxyl pathway for the CO formation followed by the CO-hydrogenation pathway for the Sabatier reaction (*i.e.*, $CO_{2(g)} \rightarrow CO_2 \rightarrow CO \rightarrow HCO \rightarrow CH \rightarrow CH_2 \rightarrow CH_3 \rightarrow CH_4 \rightarrow CH_{4(g)}$). The present kMC simulations, also show that CO is mainly formed via the direct dissociation of CO_2 rather than the carboxyl pathway. Moreover, the HCO dissociation reaction is key for methane formation rather than the CH_2O dissociation. Finally, comparing our results with previous kMC simulations for the Ni (111) surface,[42] we have shown that some of the drawbacks that make Ni (111) surface not selective towards methane formation are not present in the Ni supported model catalyst. Compared to Ni(111), these are the higher CO adsorption energy, the lower endothermicity of the HCO formation reaction (R10) and the smaller HCO dissociation energy barrier (R13) present for the supported Ni_4 cluster that opens the HCO dissociation route as a possible source of CH_x species that are further hydrogenated. This fact directly points to small Ni cluster supported on ceria as potential active and selective catalysts, in agreement with the main experimental findings.

The coverage of the different species at the different sites with(out) the ER reactions for a temperature of 523 K deserves further comments. Results in Table 4 show that, as expected, H coverage is slightly higher for the simulations with the ER reactions. This is because once the Eley-Rideal reaction is executed, a H atom is released to the surface. Regarding O coverage, for the simulations without the ER reactions, it is higher as in these simulations O is less likely to be hydrogenated. Interestingly, this difference is more pronounced for the Ni_{Ce} sites as O is generally formed at this site. Moreover, the high O coverage at Ni_{Ce} agrees with a higher site preference of water formation on the Ni_O site found in the simulations without the ER reactions, as the oxygen atoms at the Ni_{Ce} site require more time to be hydrogenated (see Figure 3d). For the simulations without the ER reactions, Table 3 also shows a larger CO coverage at Ni_O but a lower one on Ni_{Ce}. This is directly related to water formation at Ni_{Ce}, since water is produced before CO desorption, the less probable the H_2O formation the longer the CO stays at the Ni_O site with the concomitant increase of the CO coverage at that site. Similarly, as CO is blocked by the O atom, it cannot diffuse to the Ni_{Ce} site with the concomitant decrease of CO coverage at this site. Finally, for the simulations with the ER reactions, comparing the coverage at different temperatures (see Table S4) one can see that, as expected, the higher the temperature the lower the coverage. However, for the situation in which ER reactions are not considered, an increase of the temperature only decreases the coverage of H_2 and H. Interestingly, the higher the temperature the higher the coverage of CO and O on Ni_O and Ni_{Ce}, respectively, which is associated to a more difficult water formation at higher temperatures.

Finally, we have obtained the apparent activation energy and partial orders of the overall reaction with respect of both reactants (*i.e.*, CO_2 and H_2) for the RWGS and Sabatier reactions which are shown in Figure 4. First, for the sake of simplicity we focus on the values for the simulations including the ER steps and compare them with the experimental values,[12] keeping in mind that the experimental system and the model system are similar but not identical. Next, we compare our values for the simulations with(out) the ER reactions. From Figures 4a and 4b we extract apparent activation energies of 139.2 and 52.9 kJ/mol, for the RWGS and Sabatier reactions, respectively. Note that for the Sabatier reaction we have only found an Arrhenius like behavior for a temperature range between 483 and 523 K. Comparing our results with the experimental values reported by Zheng et al.[12] of 92.7 and 131.6 kJ/mol for the RWGS and Sabatier reactions, respectively, we found higher values for the CO production but smaller values for methane formation. We assign the difference for the RWGS to the stronger CO adsorption on the small Ni cluster and the smaller apparent activation energy for methane production to the increased activity towards CH_4 on the supported Ni_4 cluster. Thus, the present results point to small supported clusters as prominent candidates for CO_2 hydrogenation to methane at mild conditions. Comparing the CO_2 and H_2 partial orders of reaction (*cf.* Figures 4c to 4f) with the experimental values,[12] we found smaller CO_2 partial orders of reaction (*i.e.*, 0.66 and 0.70 for the RWGS and Sabatier reactions, respectively, vs. 1.42 and 1.08), while larger H_2 partial orders of reaction (*i.e.*, 0.27 and 1.71 for the RWGS and Sabatier reactions, respectively, vs. -0.04 and 1.07). In both cases we attribute the differences to the larger nanoparticles likely to be present in the experimental system as well as to differences in the support structure. For the CO_2 partial orders, our smaller values are directly associated to the limited number of available sites of our model, where an increase of the CO_2 partial pressure only makes more probable CO_2 to be adsorbed but does not change the number of CO_2 adsorbed molecules (only one can be adsorbed at a time), which is not the case in the larger nanoparticles used in the experiments, thus, producing a higher effect on the final reactivity. Regarding the H_2 partial order of reaction, in our model CO and CH_4 formation are somehow linked to previous water formation. Therefore, the higher the H_2 partial pressure the more probable the water formation is, which increases the CO and CH_4 formation. Nevertheless, in larger nanoparticles with more available free sites, CO and CH_4 are not conditioned by water formation which explains the lower experimental values. Finally, we compare our values for the simulations with and without explicit consideration of the ER elementary steps. From Figure 4a and 4b we extract apparent activation energies of 139.2 and 136.5 kJ for the RWGS reaction and 52.9 and 33.8 kJ/mol for the Sabatier reaction, for the simulations with and without including the ER reactions, respectively. Regarding the values for the RWGS reaction there are almost no differences and we suggest that this is due to a similar CO desorption in both situations. For the Sabatier reaction one can see a large difference, which suggests that the temperature has a higher effect on the ER reactions rather than on the surface reactions, hence, simulations with ER reactions are more affected by the temperature. For the CO_2 partial orders, we have found slightly higher partial orders for the simulations with the ER reactions as shown in Figures 4c and 4d. As explained above, a higher CO_2 pressure does not directly translate into a large number of CO_2 molecules adsorbed on the surface.

Nevertheless, the higher the CO_2 partial pressure, the higher the probability of CO_2 adsorption and reaction is. As the simulations with the ER reactions predict a higher activity, a higher probability of CO_2 to be at the surface translates into a higher activity, which explains why CO_2 partial orders are slightly higher when considering the ER reactions. Finally, regarding the H_2 partial orders of reaction, in the simulations with the ER reactions there is a lower value for the RWGS reaction but a higher value for the Sabatier reaction. This shows that ER reactions are more important for methane formation than for CO formation. We suggest that this is because a high methane formation requires available Ni_{Ce} sites and this situation is more likely to be achieved when ER reactions are included. As a final remark, the overall results suggest that high methane selectivity requires working at higher H_2 partial pressures.

CONCLUSIONS

The mechanism of CO_2 hydrogenation on a well-defined model of a Ni/CeO_2 catalyst, consisting of a Ni_4 cluster supported on the stoichiometric CeO_2 (111) surface, has been thoroughly investigated by coupling DFT calculations to kMC simulations. The DFT calculations, carried out for an extensive reaction network, evidence that the adsorption energies and energy barriers of some important intermediates and elementary steps are significantly different to those corresponding to the extended Ni (111) surface. To a large extent, the origin of the different reactivity is due to metal-support interactions that change the Ni electronic structure along with differences in Ni atomic coordination that could be beneficial for catalytic purposes.

To further understand the mechanism of CO_2 hydrogenation on the supported Ni cluster, we have performed several kMC simulations at different temperature and pressure conditions. From the kMC results we are able to unravel the mechanism that governs the overall reactions as well as to gain insights about conditions defining the catalytic activity and the selectivity to methane, Moreover, we have thoroughly studied the role of including some Eley-Rideal reactions on the final mechanisms, and their effect on the catalytic activity and selectivity. The kMC simulations unravel the existence of a synergic effect between the two different three-fold Ni hollow sites present on the Ni_4 cluster, in such a way that some reactions are dominant in one site while other reactions are mostly done on the other site. Remarkably, this effect is even more evident comparing the simulations with or without including the Eley-Rideal reactions.

The kMC simulations unveil the mechanism for CO and methane formation being CO the most significant product at the highest temperatures, which agrees with the experimental observations, while being methane the most important product at the lowest temperature, hence, pointing to work at mild conditions for high methane selectivity. CO is produced via the dissociative pathway of the RWGS reaction while methane is formed as a combination of the dissociative pathway for the CO formation followed by a mixture of the HCOO-mediated and dissociative pathways for the final methane formation(*i.e.*, $CO_{2(g)} \rightarrow CO_2 \rightarrow CO \rightarrow HCO \rightarrow CH \rightarrow CH_2 \rightarrow CH_3 \rightarrow CH_4 \rightarrow CH_{4(g)}$). We have shown that CO is mainly formed on the Ni_O site

following CO_2 dissociation; then, once water is formed, some CO desorbs while some CO diffuses to the Ni_{Ce} site in which it can either desorb or being hydrogenated to HCO, which further dissociates to CH on the Ni_O site. Interestingly, for the simulations with ER reactions water formation occurs before methane formation and it helps methane formation to occur at the more reactive Ni_{Ce} site. However, for the simulations without the ER reactions methane is formed on the less reactive Ni_O site before water formation, with a concomitant decrease on the activity and methane selectivity. Finally, the analysis of the partial order of reaction suggests that working at high H_2 pressure leads to improved CH_4 selectivity. The present simulations clearly reveal that small Ni clusters supported on ceria are potential good candidates for high selective methane formation at mild conditions while are highly active and selective for CO at high temperatures. Finally, the present results show that an accurate simulation of the CO_2 hydrogenation on Ni/CeO_2 catalyst requires including Eley-Rideal steps, and it is likely that this will be the case for other supported catalysts as well.

ASSOCIATED CONTENT

Supporting Information

The supporting information is available free of charge at DOI:

Information about details on the calculation of formation energies, the cluster expansion Hamiltonians and how to calculate lateral interactions, the reaction energies and energy barriers for the different considered process on the Ni_4/CeO_2 system, the coverages at different temperatures and the event frequencies at the Ni_{Ce} and Ni_O sites at the different studied temperatures. Optimized structures (i.e., VASP CONTCAR files) of all relevant structures and kMC inputs have been also made available on a public GitHub repository:

AUTHOR INFORMATION

Corresponding Authors

Authors

Pablo Lozano-Reis - *Departament de Ciència de Materials i Química Física & Institut de Química Teòrica i Computacional (IQTCUB), Universitat de Barcelona, C. Martí i Franquès 1, 08028 Barcelona, Spain.*

Pablo Gamallo - *Departament de Ciència de Materials i Química Física & Institut de Química Teòrica i Computacional (IQTCUB), Universitat de Barcelona, C. Martí i Franquès 1, 08028 Barcelona, Spain.*

Francesc Illas - *Departament de Ciència de Materials i Química Física & Institut de Química Teòrica i Computacional (IQTCUB), Universitat de Barcelona, C. Martí i Franquès 1, 08028 Barcelona, Spain.*

Ramón Sayós - *Departament de Ciència de Materials i Química Física & Institut de Química Teòrica i Computacional (IQTCUB), Universitat de Barcelona, C. Martí i Franquès 1, 08028 Barcelona, Spain.*

COMPETING INTERESTS

There are no conflicts of interest to declare.

ACKNOWLEDGMENTS

The research at the *Universitat de Barcelona* has been supported by the Spanish Ministry of Science, Innovation and Universities (MICIUN) Spanish MCIN/AEI/10.13039/501100011033 PID2021-126076NB-I00 and PID2022-138180OB-I00 projects, funded partially by FEDER *Una manera de hacer Europa*, and *María de Maeztu* CEX2021-001202-M grants, including funding from European Union and, in part, by and COST Action CA18234 by the *Generalitat de Catalunya* grant 2021SGR00079. P. L-R. acknowledges MICIUN for a predoctoral FPU18/02313 grant. Computational resources provided by *Consorci de Serveis Universitaris de Catalunya* (CSUC, former CESCA) with financial support from *Universitat de Barcelona* and by *Red Española de Supercomputación* are gratefully acknowledged.

Table 1. Adsorption energy for the different reactants and products of the CO_2 hydrogenation reaction on the supported Ni cluster at the most stable adsorption sites along with already published data for the Ni(111) surface. Note that all values include the ZPE term.

	$E_{ads,0}$ /eV	
Species	**This work**	**Ni (111) Ref. 42**
CO_2	-1.46 (Ni_{Ce}), -1.51 (Ni_O)	-0.16
CO	-2.47 (Ni_{Ce}), -2.33 (Ni_O)	-1.61
CH_2O	-2.10 (Ni_{Ce}), -2.06 (Ni_O)	-0.58
CH_3OH	-0.89 (Ni_{Ce}), -0.91 (Ni_O)	-0.36
CH_4	-0.26 (Ni_{Ce}), -0.26 (Ni_O)	-0.13
H_2O	-0.73 (Ni_{Ce}), -0.75 (Ni_O)	-0.26
H_2	-0.63 (h_{Ce}-h_O)	0.00

Table 2. Reaction energies ($\Delta E_{0,r}$) and forward and reverse energy barriers ($\Delta E^{\neq}_{0,f}$, $\Delta E^{\neq}_{0,r}$) for the selected elementary reactions including the ZPE for the Ni_4/CeO_2 system and the Ni(111) surface[42] for comparison. For reactions in which two possible hydrogen attacks are considered the *f* and *n* subscript stands for the H atom being at the site that is far or near the attacking species, respectively. For instance, *f* stands for situations in which H and the other species are at h_O/Ni_{Ce} or h_{Ce}/Ni_O, respectively, and *n* stands for situations in which H and the other species are at h_{Ce}/Ni_{Ce} or h_O/Ni_O, respectively.

ID	Reaction	$\Delta E_{0,r}$ / eV		$\Delta E^{\neq}_{0,f}$ / eV		$\Delta E^{\neq}_{0,r}$ / eV	
		This Work	Ref 42	This Work	Ref 42	This Work	Ref 42
$R1_{NiCe}$	$CO_{2,(g)} + *_{NiCe} \rightleftharpoons CO^*_{2,NiCe}$	-1.46	-0.16	0.00	0.00	1.46	0.16
R2	$H_{2,(g)} + *_{hCe} + *_{hO} \rightleftharpoons H^{**}_{2,hCehO}$	-0.63	0.00	0.00	0.00	0.63	0.00
R3	$H^{**}_{2,hCehO} \rightleftharpoons H^*_{hCe} + H^*_{hO}$	-0.70	-0.33	0.00	0.26	0.70	0.59
$R4_{NiCe}$	$CO^*_{2,NiCe} + *_{NiO} \rightleftharpoons CO^*_{NiCe} + O^*_{NiO}$	-0.70	-0.57	0.77	0.86	1.47	1.43
$R5_{NiCe}$	$CO^*_{2,NiCe} + H^*_{hO} \rightleftharpoons HCOO^*_{NiCe} + *_{hO}$	-0.07	0.04	0.39	1.05	0.45	1.01
$R6_{NiCe}$	$CO^*_{2,NiCe} + H^*_{hO} \rightleftharpoons COOH^*_{NiCe} + *_{hO}$	0.22	0.49	1.20	1.33	0.98	0.84
$R9_{NiCe}$	$HCOO^*_{NiCe} + *_{NiO} \rightleftharpoons HCO^*_{NiCe} + O^*_{NiO}$	0.23	0.85	0.65	1.39	0.42	0.54
$R10_{NiCe}$	$CO^*_{NiCe} + H^*_{hO} \rightleftharpoons HCO^*_{NiCe} + *_{hO}$	0.60	1.21	0.90	1.42	0.30	0.21
$R12_{NiCe}$	$CO^*_{NiCe} + *_{NiO} \rightleftharpoons C^*_{NiCe} + O^*_{NiO}$	1.03	1.84	1.52	2.98	0.49	1.15
$R13_{NiCe}$	$HCO^*_{NiCe} + *_{NiO} \rightleftharpoons CH^*_{NiO} + O^*_{NiCe}$	0.31	-0.07	0.64	1.10	0.33	1.17
$R16_{NiCe,n}$	$CH^*_{NiCe} + H^*_{hCe} \rightleftharpoons CH^*_{2,NiCe} + *_{hCe}$	-0.38	0.30	0.03	0.63	0.41	0.34
$R17_{NiCe,n}$	$CH^*_{2,NiCe} + H^*_{hCe} \rightleftharpoons CH^*_{3,NiCe} + *_{hCe}$	-0.53	-0.11	0.09	0.57	0.62	0.68
$R22_{NiCe}$	$HCO^*_{NiCe} + H^*_{hO} \rightleftharpoons CH_2O^*_{NiCe} + *_{hO}$	0.29	0.26	0.46	0.71	0.17	0.45
$R23_{NiCe}$	$CH_2O^*_{NiCe} + *_{NiO} \rightleftharpoons CH^*_{2,NiO} + O^*_{NiCe}$	-0.39	-0.40	0.68	0.96	1.07	1.37
$R31_{NiCe,n}$	$CH^*_{3,NiCe} + H^*_{hO} \rightleftharpoons CH^*_{4,NiCe} + *_{hO}$	0.77	-0.30	0.91	0.79	0.14	0.96
$R36_{NiCe}$	$CO^*_{NiCe} \rightleftharpoons CO_{(g)} + *_{NiCe}$	2.47	1.61	2.47	1.61	0.00	0.00
$R37_{NiCe}$	$CH_2O^*_{NiCe} \rightleftharpoons CH_2O_{(g)} + *_{NiCe}$	2.10	0.58	2.10	0.58	0.00	0.00
$R39_{NiCe}$	$CH^*_{4,NiCe} \rightleftharpoons CH_{4,(g)} + *_{NiCe}$	0.26	0.13	0.26	0.13	0.00	0.00

Table 3. Total, CO and CH_4 TOFs and methane selectivity for the simulations including the Eley-Rideal steps (W/ER) and without them (Wo/ER) at five different temperature conditions and with $P(H_2)$ = 0.528 bar and $P(CO_2)$ = 0.132 bar for all he simulations. The TOF units are in molec · $site^{-1}$ · s^{-1} while the CH_4 selectivity is given in percentage. Note that the methane selectivity is calculated as CH_4 selectivity = (CH_4 TOF / total TOF)·100.

	Total TOF		**CO TOF**		**CH_4 TOF**		**CH_4 Selectivity**	
T	**W/ER**	**Wo/ER**	**W/ER**	**Wo/ER**	**W/ER**	**Wo/ER**	**W/ER**	**Wo/ER**
483	0.136	0.063	0.034	0.029	0.102	0.034	75.1	53.9
503	0.373	0.206	0.195	0.158	0.178	0.049	47.7	23.5
523	1.175	0.752	0.896	0.687	0.279	0.065	23.8	8.7
543	2.733	1.927	2.447	1.870	0.286	0.057	10.5	3.0
563	4.534	3.441	4.332	3.407	0.202	0.034	4.5	1.0

Table 4. Coverage of the different species considered at the different sites for the simulations including the Eley-Rideal reactions (W/ER) and without them (Wo/ER) at T = 523 K, $P(H_2)$ = 0.528 bar and $P(CO_2)$ = 0.132 bar.

T=523K	**Ni_{Ce}**		**Ni_O**		**h_{Ce}**		**h_O**	
Species	**W/ER**	**Wo/ER**	**W/ER**	**Wo/ER**	**W/ER**	**Wo/ER**	**W/ER**	**Wo/ER**
CO	71.5	66.7	27.2	30.7	-	-	-	-
O	0.7	7.1	0	0.7	-	-	-	-
OH	0.8	0.7	0	0	-	-	-	-
H_2	-	-	-	-	28.8	29.0	28.8	29.0
H	-	-	-	-	19.1	17.8	17.2	16.2
Total	73.0	74.5	27.2	31.4	47.9	46.8	46.9	45.2

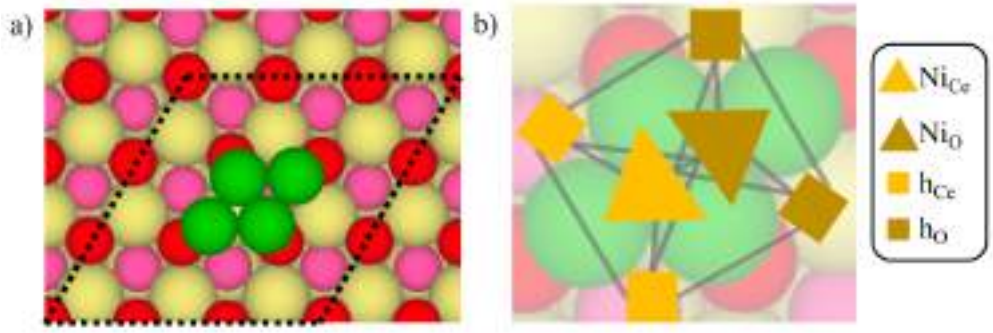

Figure 1. a) Surface model of the Ni_4/CeO_2 system used for the DFT calculations. Green, pale yellow, red and pink stand for Ni, Ce, uppermost O and subsurface O atoms, respectively. b) Lattice model representing the supported Ni_4 cluster used for the kMC simulations. Triangles represent the Ni hollow sites while squares represent the hydrogen reservoir sites in which H and H_2 can adsorb. Grey lines depict the connectivity between sites.

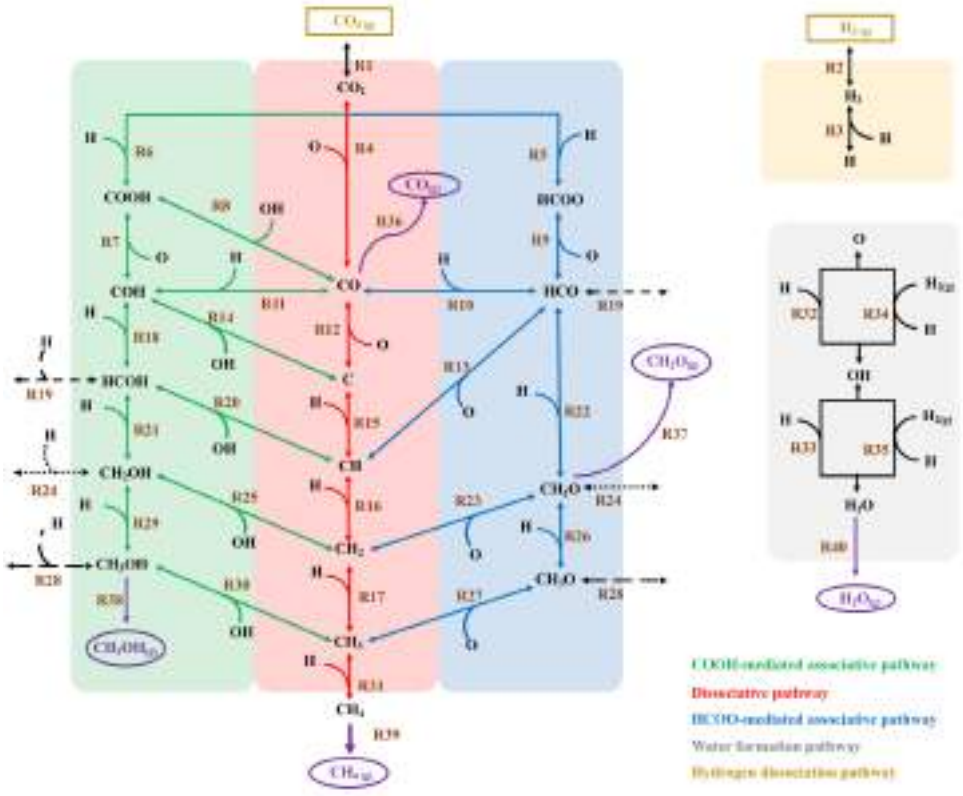

Figure 2. Reaction network proposed for the CO_2 hydrogenation reaction. The dissociative pathway, COOH-mediate pathway, HCOO-mediated pathway, hydrogen dissociation pathway and water formation pathway are shown in red, green, blue, pale yellow and grey, respectively. Black doted/dashed lines are for elementary steps that interconnect different pathways. Dark yellow and purple stand for reactants and products, respectively. Reversible steps are represented by double arrows.

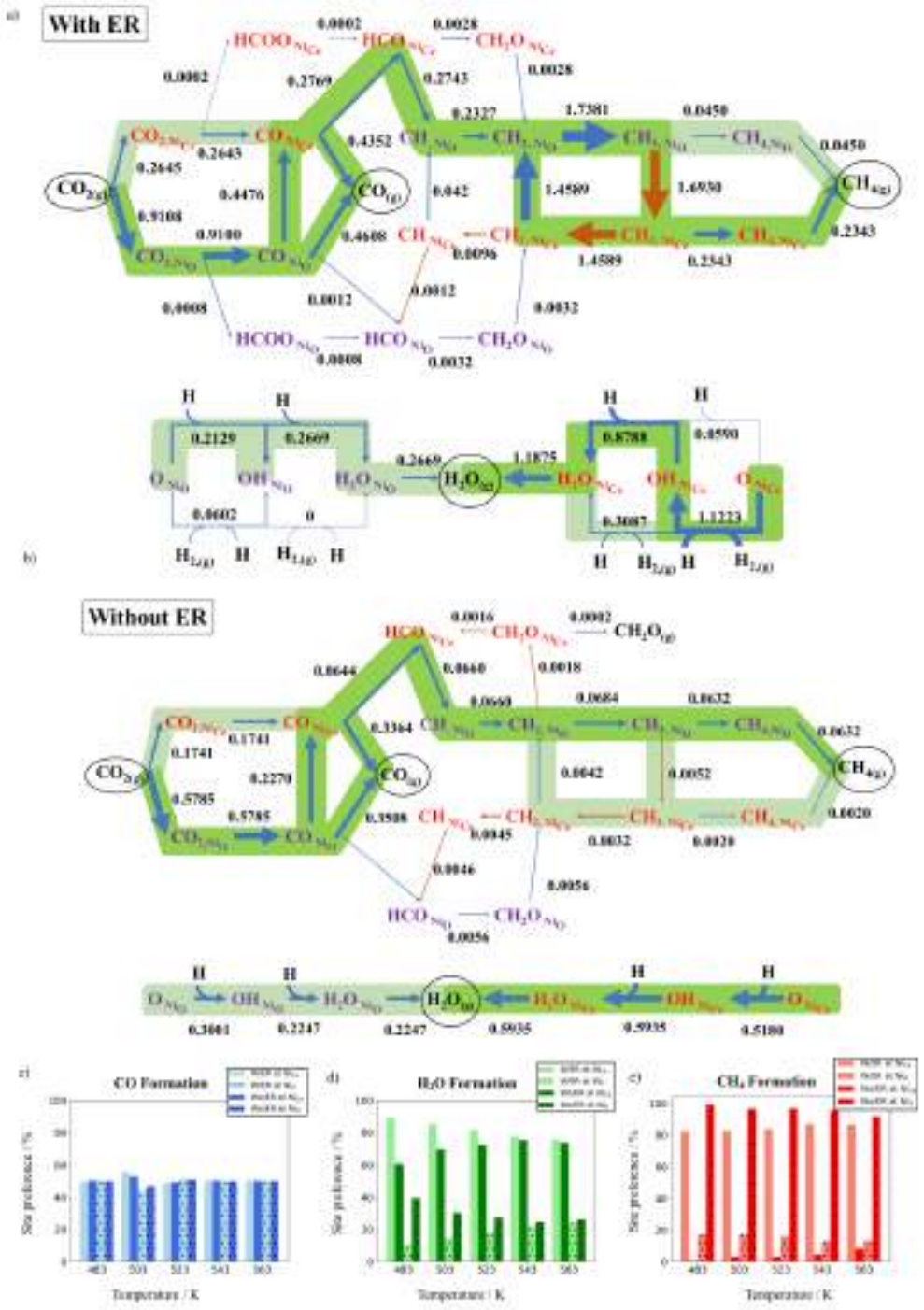
a)
With ER
b)
Without ER
c)
CO Formation
d)
H_2O Formation
e)
CH_4 Formation
Site preference / %
Temperature / K

Figure 3. Schematic representation of the different executed events at a temperature of 523 K and $P(H_2)$ = 0.528 bar and $P(CO_2)$ = 0.132 bar for simulations with and without ER reactions in a) and b), respectively. Purple and red letters stand for species adsorbed on the Ni_O and Ni_{Ce} sites, respectively. Black numbers represent net number of executed processes as the average of 5 different kMC simulations in units of events · $site^{-1}$ · s^{-1}. Blue arrows stand for events executed from right to left and from bottom to up while brown arrows stand for events executed in the opposite directions. The size of the arrows represents the weight of the elementary step. Green and light green colors highlight the most important and secondary pathways, respectively. c-e) Site preference formation of CO, H_2O and CH_4 on the Ni_{Ce} and Ni_O sites for the simulations with and without the ER reactions, in blue, green and red colors, respectively. Light colors stand for the simulations with ER reactions while dark colors stand for the simulations without ER reactions. Segments with no texture represent desorption on the Ni_{Ce} site while segments with "." texture stand for desorption on the Ni_O site.

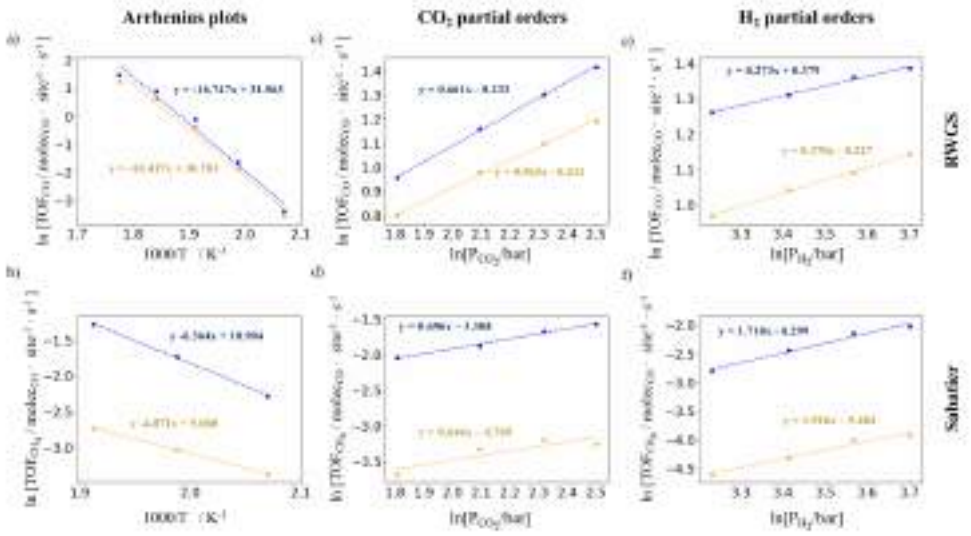

Figure 4. Arrhenius plot for the RWGS (a) and Sabatier (b) reactions, respectively at $P(H_2)$ = 0.528 bar and $P(CO_2)$ = 0.132 bar. CO_2 partial orders for the RWGS (c) and Sabatier (d) reactions, respectively at fixed $P(H_2)$ = 0.54 bar. H_2 partial orders for the RWGS (e) and Sabatier (f) reactions, respectively at fixed $P(CO_2)$ = 0.135 bar. Blue and orange colors stand for the simulations with and without including the ER reactions, respectively.

REFERENCES

[1] Götz, M.; Lefebvre, J.; Mörs, F.; Koch, A. M.; Graf, F.; Bajohr, S.; Reimert, R.; Kolb, T. Renewable Power-to-Gas: A Technological and Economic Review. *Renew. Energy,* **2016**, 85, 1371-1390.

[2] Mazza, A.; Bompard, E.; Chicco, G. Application of Power to Gas Technologies in Emerging Electrical Systems. *Renew. Sust. Energ. Rev.*, **2018**, 92, 794-806.

[3] Ghaib, K.; Ben-Fares, F-Z. Power-to-Methane: A State-of-the-art review. *Renew. Sust. Ener. Rev.*, **2018**, 81, 433-446.

[4] Aziz, M.A.A.; Jalil, A.A.; Triwahyono, S.; Ahmad, A. CO_2 Methanation over Heterogeneous Catalysts: Recent Progress and Future Prospects. *Green Chem*., **2015**, 17, 2647–2663.

[5] Wei, W.; Jinlong, G. Methanation of Carbon Dioxide: an Overview. *Front. Chem. Sci. Eng*., **2011**, 5, 2–10.

[6] Tada, S.; Shimizu, T.; Kameyama, H.; Haneda, T.; Kikuchi, R. Ni/CeO_2 Catalysts with High CO_2 Methanation Activity and High CH_4 Selectivity at Low Temperatures. *Int. J. Hydrog. Energy*, **2012**, 37, 5527–553.

[7] Martin. N. M.; Velin, P.; Skoglundh, M.; Bauer, M.; Carlsson, P.A. Catalytic Hydrogenation of CO_2 to Methane over Supported Pd, Rh and Ni Catalysts. *Catal. Sci. Technol.*, **2017**, 7, 1086-1094.

[8] Cárdenas-Arenas, A.; Quindimil, A.; Davó-Quiñonero, A.; Bailón-García, E.; Lozano-Castelló, D.; De-La-Torre, U.; Pereda-Ayo, B.; González-Marcos, J. A.; González-Velasco, J. R.; Bueno-López, A. Isotopic and In Situ DRIFTS Study of the CO_2 Metahanation Mechanism using Ni/CeO_2 and Ni/Al_2O_3 Catalysts. *App. Catal. B,* **2020**, 265, 118538-118547.

[9] Le, T. A.; Kim, M. S.; Lee, S. H.; Kim, T. W.; Park, E. D. CO and CO_2 Methanation over Supported Ni Catalysts. *Catal. Today*, **2017**, 293–294, 89–96.

[10] Lin, L.; Gerlak, C. A.; Liu, C.; Llorca, J.; Yao, S.; Rui, N.; Zhang, F.; Liu, Z.; Zhang, S.; Deng, K.; Murray, C. B.; Rodriguez, J. A.; Senanayake, S. D. Effect of Ni Particle Size on the Production of Renewable Methane from CO_2 over Ni/CeO_2. *J. Energy Chem.*, **2021**, 61, 602–611.

[11] Winter, L. R.; Gomez, E.; Yan, B.; Yao, S.; Chen, J. G. Tuning Ni-Catalyzed CO_2 Hydrogenation Selectivity via Ni-ceria Support Interactions and Ni-Fe Bimetallic Formation. *App. Catal. B*, **2018**, 224, 442–450.

[12] Zheng, H.; Liao, W.; Ding, J.; Xu, F.; Jia, A.; Huang, W.; Zhang, Z. Unveiling the Key Factors in Determining the Activity and Selectivity of CO_2 Hydrogenation over Ni/CeO_2 Catalysts. *ACS Catal.*, **2022**, 12, 15451−15462.

[13] Lin, S.; Li, Z.; Li, M. Tailoring Metal-Support Interactions via Tuning CeO_2 Particle Size for Enhancing CO_2 Methanation Activity over Ni/CeO_2 Catalysts. *Fuel*, **2023**, 333 126369-126383.

[14] Riu, N.; Zhang, X.; Zhang, F.; Liu, Z.; Cao, X.; Xie, Z.; Zou, R.; Senanayake, S. D.; Yang, Y.; Rodriguez, J. A.; Liu, C-J. Highly Active Ni/CeO_2 Catalyst for CO_2 Methanation: Preparation and Characterization. *App. Catal. B*, **2021**, 282, 119581-119593.

[15] Pu, T.; Chen, J.; Tu, W.; Xu, W.; Han, Y-F.; Wachs, I. E.; Zhu, M. Dependency of CO_2 Methanation on the Strong Metal-Support Interaction for Supported Ni/CeO_2 Catalysts. *J. Catal.*, **2022**, 413, 821–828.

[16] Liu, Z.; Grinter, D. C.; Lustemberg, P. G.; Nguyen-Phan, T-D.; Zhou, Y.; Luo, Si, Waluyo, I.; Crumlin, E. J.; Stacchiola, D. J.; Zhou, J.; Carrasco, J.; Busnengo, H. F.; Ganguglia-Pirovano, M. V.; Senanayake, S. D.; Rodriguez, J. A. Dry Reforming of Methane on a Highly-Active Ni-CeO_2Catalyst: Effects of Metal-Support Interactions on C−H Bond Breaking. *Angew. Chem. Int. Ed.*, **2016**, 55, 7455-7459.

[17] Liu, Z.; Lustemberg, P.; Gutiérrez, R. A.; Carey, J. J.; Palomino, R. M.; Vorokhta, M.; Grinter, D. C.; Ramírez, P. J.; Matolín, V.; Nolan, M.; Ganduglia-Pirovano, M. V.; Senanayake, S. D.; Rodriguez, J. A. In Situ Investigation of Methane Dry Reforming on Metal/Ceria(111) Surfaces: Metal–Support Interactions and C−H Bond Activation at Low Temperature. *Angew, Chem. Int. Ed.*, **2017**, 56, 13041-13046.

[18] Lustemberg, P. G.; Ramírez, P. J.; Liu, Z.; Gutiérrez, R. A.; Grinter, D. G.; Carrasco, J.; Senanayake, S. D.; Rodriguez, J. A.; Ganduglia-Pirovano, M. V. Room-Temperature Activation of Methane and Dry Reforming with CO_2 on Ni-CeO_2(111) Surfaces: Effect of Ce^{3+} Sites and Metal-Support Interactions on C-H Bond Cleavage. *ACS Catal.*, **2016**, 6, 12, 8184–8191.

[19] Lustemberg, P. G.; Mao, Z.; Salcedo, A.; Irigoyen, B.; Ganduglia-Pirovano, M. V.; Campbell, C. T.; Nature of the Active Sites on Ni/CeO_2 Catalysts for Methane Conversions. *ACS Catal.*, **2021**, 11, 10604−10613.

[20] Lustemberg, P. G.; Palomino, R. M.; Gutiérrez, R. A.; Grinter, D. C.; Vorokhta, M.; Liu, Z.; Ramírez, P. J.; Matolín, V.; Ganduglia-Pirovano, M. V.; Senanayake, S. D.; Rodriguez, J. A. Direct Conversion of Methane to Methanol on Ni-Ceria Surfaces: Metal-Support Interactions and Water-Enabled Catalytic Conversion by Site Blocking. *J. Am. Chem. Soc.*, **2018**, 140, 7681−7687.

[21] Carrasco, J.; Lopez-Duran, D.; Liu, Z.; Duchon, T.; Evans, J.; Senanayake, S. D.; Crumlin, E. J.; Matolín, V.; Rodriguez, J. A.; Ganduglia-Pirovano, M. V. In Situ and Theoretical Studies for the Dissociation of Water on an Active Ni/CeO_2 Catalyst: Importance of Strong Metal–Support Interactions for the Cleavage of O–H Bonds. *Angew. Chem. Int. Ed,*. **2015**, 54, 3917-3921.

[22] Salcedo, A.; Lustemberg, P. G.; Rui, N.; Palomino, R. M.; Liu, Z.; Nemsak, S.; Senanayake, S. D.; Rodriguez, J. A.; Ganduglia-Pirovano, M. V.; Irigoyen, B. Reaction Pathway for Coke-Free Methane Steam Reforming on a Ni/CeO_2 Catalyst: Active Sites and the Role of Metal-Support Interactions. *ACS Catal.*, **2021**, 11, 8327−8337.

[23] Lustemberg, P. G.; Feria, L.; Ganduglia-Pirovano, M. V. Single Ni Sites Supported on CeO_2(111) Reveal Cooperative Effects in the Water-Gas Shift Reaction. *J. Phys. Chem. C*, **2019**, 123, 7749–7757.

[24] Zhang, J.; Yang, Y.; Liu, J.; Xiong, B. Mechanistic Understanding of CO_2 Hydrogenation to Methane over Ni/CeO_2. *App. Surf. Sci.*, **2021**, 558, 149866-149875.

[25] Lozano-Reis, P.; Prats, H.; Sayós, R.; Illas, F. Limitations of Free Energy Diagrams to Predict the Catalytic Activity: The Reverse Water Gas Shift Reaction Catalyzed by Ni/TiC. *J. Catal.*, **2023**, 425, 203-211.

[26] Kresse, G.; Hafner, J. Ab Initio Molecular Dynamics for Liquid Metals. *Phys. Rev. B.* **1993**, 47, 558–561.

[27] Kresse, G.; Furthmüller, J. Efficient Iterative Schemes for Ab Initio Total-energy Calculations Using a Plane-wave Basis Set. *Phys. Rev. B.*, **1996**, 54, 11169–11186.

[28] Kresse, G.; Furthmüller, J. Efficiency of Ab-initio Total Energy Calculations for Metals and Semiconductors Using a Plane-wave Basis Set. *Comp. Mater. Sci*. **1996**, 6, 15–50.

[29] Kresse, G.; Joubert, D. From Ultrasoft Pseudopotentials to the Projector Augmented-wave Method. *Phys. Rev. B*. **1999**, 59, 1758–1775.

[30] Perdew, J. P.; Burke, K.; Ernzerhof, M. Generalized Gradient Approximation Made Simple. *Phys. Rev. Lett.*, **1996**, 77, 3865−3868.

[31] Fabris, S.; Vicario, G.; Balducci, G.; de Gironcoli, S.; Baroni, S. Electronic an Atomistic of Clean and Reduced Ceria Surfaces. *J. Phys. Chem. B*, **2005**, 109, 22860−22867.

[32] Cococcioni, M.; de Gironcoli, S. Linear Response Approach to the Calculation of the Effective Interaction Parameters in the LDA + U Method. *Phys. Rev. B*, **2005**, 71, 35105−35120.

[33] Grimme, S.; Antony, J.; Ehrlich, S., Krieg, H. A Consistent and Accurate Ab Initio Parametrization of Density Functional Dispersion Correction (DFT-D) for the 94 Elements H-Pu, *J. Chem. Phys.*, **2010**, 132, 154104

[34] Alvarez-Galvan, C.; Lustemberg, P. G.; Oropeza, F. E.; Bachiller-Baeza, B.; Ospina, M. D.; Herranz, M.; Cebollada, J.; Collado, L.; Campos-Martin, J. M.; de la Peña-O'Shea, V. A.; Alonso, J. A.; Ganduglia-Pirovano, M. V. *ACS Appl. Mater. Interfaces*, **2022**, 14, 50739−50750.

[35] Lustember, P. G.; Senanayake, S.D.; Rodriguez, J. A.; Ganduglia-Pirovano, M. V. Tuning Selectivity in the Direct Conversion of Methane to Methanol: Bimetallic Synergistic Effects on the Cleavage of C-H and O-H Bonds over $NiCu/CeO_2$ Catalysts. *J. Phys. Chem. Lett.*, **2022**, 13, 5589−5596.

[36] Lustemberg, P. G.; Zhang, F.; Gutiérrez, R. A.; Ramírez, P. J.; Senanayake, S. D.; Rodriguez, J. A.; Ganduglia-Pirovano, M. V. Breaking Simple Scaling Relations through Metal-Oxide interactions: Understanding Room-Temperature Activation of Methane on M/CeO_2 (M = Pt, Ni or Co) Interfaces. *J. Phys. Chem. Lett.* **2020**, 11, 9131–9137.

[37] Monkhorst, H.J.; Pack, J.D. Special Points for Brillouin-zone Integrations. *Phys. Rev. B.* **1976**, 13, 5188–5192.

[38] Jónsson, H.; Mills, G.; Jacobsen, K.W. Nudged Elastic Band Method for Finding Minimum Energy Paths of Transitions, in: Classical and Quantum Dynamics in Condensed Phase Simulations, World scientific, Lerici, Villa Marigola, **1998**, 385–404.

[39] Henkelman, G.; Uberuaga, B.P.; Jónsson, H. A Climbing Image Nudged Elastic Band Method for Finding Saddle Points and Minimum Energy Paths, *J. Chem. Phys.*, **2000**, 113, 9901–9904.

[40] Smidstrup, S.; Pedersen, A.; Stokbro, K.; Jónsson, H. Improved Initial guess for Minimum Energy Path Calculations. *J. Chem. Phys.*, **2014**, 140, 214106:1-6.

[41] Hjorth Larsen, A.; Jørgen Mortensen, J.; Blomqvist, J.; Castelli, I.E.; Christensen, R.; Dułak, M.; Friis, J.; Groves, M.N.; Hammer, B.; Hargus, C.; Hermes, E.D.; Jennings, P.C.; Bjerre Jensen, P.; Kermode, J.; Kitchin, J.R.; Leonhard Kolsbjerg, E.; Kubal, J.; Kaasbjerg, K.; Lysgaard, S.; Bergmann Maronsson, J.; Maxson, T.; Olsen, R.; Pastewka, L.; Peterson, A.; Rostgaard, C.; Schiøtz, J.; Schütt, O.; Strange, M.;

Thygesen, K.S.; Vegge, T.; Vilhelmsen, L.; Walter, M.; Zeng, Z.; Jacobsen, K.W. The Atomic Simulation Environment—a Python Library for Working with Atoms. *J. Phys.: Condens. Matter*., **2017**, 29, 273002.

[42] Lozano-Reis, P.; Prats, H.; Gamallo, P.; Illas, F.; Sayós R. Multiscale Study of the Mechanism of Catalytic CO_2 Hydrogenation: Role of the Ni(111) Facets. *ACS Catal*. **2020**, 10, 8077–8089.

[43] Stamatakis, M.; Vlachos, D.G.; A Graph-theoretical Kinetic Monte Carlo Framework for on-lattice Chemical Kinetics. *J. Chem. Phys*. **2011**, 134, 214115:1-13.

[44] Stamatakis, M.; Vlachos, D.G.; Unraveling the Complexity of Catalytic Reactions Via kinetic Monte Carlo Simulation: Current Status and Frontiers. *ACS Catal*., **2012**, 2, 2648–2663.

[45] Nielsen, J.; d'Avezac, M.; Hetherington, J.; Stamatakis, M.; Parallel kinetic Monte Carlo Simulation Framework Incorporating Accurate Models of Adsorbate Lateral Interactions. *J. Chem. Phys*., **2013**, 139, 224706:1-13.

[46] Prats, H.; Posada-Pérez, S.; Rodriguez, J.A.; Sayós, R.; Illas, F. Kinetic Monte Carlo Simulations Unveil Synergic Effects at Work on Bifunctional Catalysts. *ACS Catal*., **2019**, 9, 9117–9126.

[47] Prats, H.; Álvarez, L.; Illas, F.; Sayós, R. Kinetic Monte Carlo Simulations of the Water Gas Shift reaction on Cu(1 1 1) From Density Functional Theory Based Calculations. *J. Catal.*, **2016**, 333, 217–226.

[48] Piccinin, S.; Stamatakis, M. CO Oxidation on Pd(111): a First-principles-based Kinetic Monte Carlo Study. *ACS Catal.* **2014**, 4, 2143–2152.

[49] Yang, L.; Karim, A.; Muckerman, J.T. Density Functional Kinetic Monte Carlo Simulation of Water–gas Shift Reaction on Cu/ZnO. *J. Phys. Chem. C*. **2013**, *117*, 3414–3425.

[50] Mao, Z.; Lustemberg, P. G.; Rumptz, J. R.; Gundiglia-Pirovano, M. V.; Campbell, C. T. Ni Nanoparticles on CeO2(111): Energetics, Electron Transfer, and Structure by Ni Adsorption Calorimetry, Spectroscopies, and Density Functional Theory. *ACS. Catal*., **2020**, 10, 5101-5114.

5.6. References

1. Götz, M.; Lefebvre, J.; Mörs, F.; Koch, A. M.; Graf, F.; Bajohr, S.; Reimert, R.; Kolb, T. Renewable Power-to-Gas: A Technological and Economic Review. *Renew. Energy*, **2016**, 85, 1371-1390.

2. Mazza, A.; Bompard, E.; Chicco, G. Application of Power to Gas Technologies in Emerging Electrical Systems. *Renew. Sust. Energ. Rev.,* **2018**, 92, 794-806.

3. Ghaib, K.; Ben-Fares, F-Z. Power-to-Methane: A State-of-the-art review. *Renew. Sust. Ener. Rev.*, **2018**, 81, 433-446.

4. Ren, J.; Lou, H.; Xu, N.; Zeng, F.; Pei, G.; Wang, Z. Methanation of CO/CO2 for Power to Methane Process: Fundamentals, Status and Perspectives. *J. Energ. Chem.*, **2023**, 80, 182-206.

5. Aziz, M.A.A.; Jalil, A.A.; Triwahyono, S.; Ahmad, A. CO_2 Methanation over Heterogeneous Catalysts: Recent Progress and Future Prospects. *Green Chem.*, **2015**, 17, 2647–2663.

6. Wei, W.; Jinlong, G. Methanation of Carbon Dioxide: an Overview. *Front. Chem. Sci. Eng.*, **2011**, 5, 2–10.

7. Tada, S.; Shimizu, T.; Kameyama, H.; Haneda, T.; Kikuchi, R. Ni/CeO_2 Catalysts with High CO_2 Methanation Activity and High CH_4 Selectivity at Low Temperatures. *Int. J. Hydrog. Energy*, **2012**, 37, 5527–5531.

8. Martin. N. M.; Velin, P.; Skoglundh, M.; Bauer, M.; Carlsson, P.A. Catalytic Hydrogenation of CO_2 to Methane over Supported Pd, Rh and Ni Catalysts. *Catal. Sci. Technol.*, **2017**, 7, 1086-1094.

9. Cárdenas-Arenas, A.; Quindimil, A.; Davó-Quiñonero, A.; Bailón-García, E.; Lozano-Castelló, D.; De-La-Torre, U.; Pereda-Ayo, B.; González-Marcos, J. A.; González-Velasco, J. R.; Bueno-López, A. Isotopic and In Situ DRIFTS Study of the CO_2 Metahanation Mechanism using Ni/CeO_2 and Ni/Al_2O_3 Catalysts. *App. Catal. B*, **2020**, 265, 118538-118547.

10. Le, T. A.; Kim, M. S.; Lee, S. H.; Kim, T. W.; Park, E. D. CO and CO_2 Methanation over Supported Ni Catalysts. *Catal. Today*, **2017**, 293–294, 89–96

11. Fukuhara, C.; Hayakawa, K.; Suzuki, Y.; Kawasaki, W.; Watanabe, R. A Novel Nickel-based Structured Catalyst for CO_2 Methanation: A Honeycomb-type Ni/CeO_2 Catalyst to Transform Greenhouse Gas into Useful Resources. *App. Catal. A*, **2017**, 532, 12-18.

12. Xie, Y.; Chen, J.; Wu, X.; Wen, J.; Zhao, R.; Li, Z.; Tian, G.; Zhang, Q.; Ning, P.; Hao, J. Frustrated Lewis Pairs Boosting Low-Temperature CO_2 Methanation Performance over Ni/CeO_2 Nanocatalysts. *ACS Catal.*, **2022**, 12, 10587-10602.

13. Jomjaree, T.; Sintuya, P.; Srifa, A.; Koo-amornpattana, W.; Kiatphuengporn, S.; Assabumurungrat, S.; Sudoh, M.; Watanabe, R.; Fukuhara, C.; Ratchahat, S. Catalytic Performance of Ni Catalysts Supported on CeO_2 with Different Morphologies for Low-Temperature CO_2 Methanation. *Catal. Today*, **2021**, 375, 234-244.

14. Tada, S.; Nagase, H.; Fujiwara, N.; Kikuchi, R. What Are the Best Active Sites for CO_2 Methanation over Ni/CeO_2? *Energ. Fuel.*, **2021**, 35, 5241-5251.

15. Ye, R-P.; Li, Q.; Gong, W.; Wang, T.; Razink, J. J.; Lin, L.; Qin, Y-Y.; Zhou, Z.; Adidharma, H.; Tang, J.; Rusell, A. G.; Fan, M.; Yao, Y-G. High-performance of Nanostructured Ni/CeO_2 Catalyst on CO_2 Methanation. *App. Catal. B*, **2020**, 268, 11874-11885.

16. Bian, Z.; Chan, Y. M.; Yu, Y.; Kawi, S. Morphology Dependence of Catalytic Properties of Ni/CeO_2 for Methanation: A Kinetic and Mechanism Study. *Catal. Today*, **2020**, 347, 31-38.

17. Konishcheva, M. V.; Potemkin, D. I.; Badmaev, S. D.; Snytnikokv, P. V.; Paukshtis, E. A.; Sobyanin, V. A.; Parmon, V. N. On the Mechanism of CO and CO_2 Methanation over Ni/CeO_2 Catalysts. *Top. Catal*, **2016**, 59, 1424-1430.

18. Ashok, J.; Ang, M. L.; Kawi, S. Enhanced Activity of CO_2 Methanation over Ni/CeO_2-ZrO_2 Catalysts: Influence of Preparation Methods. *Catal. Today*, **2017**, 281, 304-311.

19. Tang, R.; Ullah, N.; Hui, Y.; Li, X.; Li, Z. Enhanced CO_2 Methanation Activity over Ni/CeO_2 Catalyst by One-Pot Method. *Molec. Catal.*, **2021**, 508, 111602-111614

20. Yu, Y.; Bian, Z.; Wang, J.; Wang, Z.; Tan, W.; Zhong, Q.; Kawi, S. CO_2 Hydrogenation to CH_4 over Hydrothermal Prepared Ceria-Nickel Catalysts: Performance and Mechanism Study. *Catal. Today*, **2023**, 424, 113345 – 113354.

21. Lin, L.; Gerlak, C. A.; Liu, C.; Llorca, J.; Yao, S.; Rui, N.; Zhang, F.; Liu, Z.; Zhang, S.; Deng, K.; Murray, C. B.; Rodriguez, J. A.; Senanayake, S. D. Effect of Ni Particle Size on the Production of Renewable Methane from CO_2 over Ni/CeO_2. *J. Energy Chem.*, **2021**, 61, 602–611

22. Winter, L. R.; Gomez, E.; Yan, B.; Yao, S.; Chen, J. G. Tuning Ni-Catalyzed CO_2 Hydrogenation Selectivity via Ni-ceria Support Interactions and Ni-Fe Bimetallic Formation. *App. Catal. B*, **2018**, 224, 442–450.

23. Zheng, H.; Liao, W.; Ding, J.; Xu, F.; Jia, A.; Huang, W.; Zhang, Z. Unveiling the Key Factors in Determining the Activity and Selectivity of CO_2 Hydrogenation over Ni/CeO_2 Catalysts. *ACS Catal.*, **2022**, 12, 15451−15462

24. Lin, S.; Li, Z.; Li, M. Tailoring Metal-Support Interactions via Tuning CeO_2 Particle Size for Enhancing CO_2 Methanation Activity over Ni/CeO_2 Catalysts. *Fuel*, **2023**, 333 126369-126383.

25. Riu, N.; Zhang, X.; Zhang, F.; Liu, Z.; Cao, X.; Xie, Z.; Zou, R.; Senanayake, S. D.; Yang, Y.; Rodriguez, J. A.; Liu, C-J. Highly Active Ni/CeO_2 Catalyst for CO_2 Methanation: Preparation and Characterization. *App. Catal. B*, **2021**, 282, 119581-119593.

26. Pu, T.; Chen, J.; Tu, W.; Xu, W.; Han, Y-F.; Wachs, I. E.; Zhu, M. Dependency of CO_2 Methanation on the Strong Metal-Support Interaction for Supported Ni/CeO_2 Catalysts. *J. Catal.*, **2022**, 413, 821–828.

27. Salcedo, A.; Lustemberg, P. G.; Rui, N.; Palomino, R. M.; Liu, Z.; Nemsak, S.; Senanayake, S. D.; Rodriguez, J. A.; Ganduglia-Pirovano, M. V.; Irigoyen, B. Reaction Pathway for Coke-Free Methane Steam Reforming on a Ni/CeO_2 Catalyst: Active Sites and the Role of Metal-Support Interactions. *ACS Catal.*, **2021**, 11, 8327−8337.

28. Lustemberg, P. G.; Feria, L.; Ganduglia-Pirovano, M. V. Single Ni Sites Supported on CeO_2(111) Reveal Cooperative Effects in the Water-Gas Shift Reaction. *J. Phys. Chem. C*, **2019**, 123, 7749–7757.

29. Lustemberg, P. G.; Palomino, R. M.; Gutiérrez, R. A.; Grinter, D. C.; Vorokhta, M.; Liu, Z.; Ramírez, P. J.; Matolín, V.; Ganduglia-Pirovano, M. V.; Senanayake, S. D.; Rodriguez, J. A. Direct Conversion of Methane to Methanol on Ni-Ceria Surfaces: Metal-Support Interactions and Water-Enabled Catalytic Conversion by Site Blocking. *J. Am. Chem. Soc.*, **2018**, 140, 7681−7687

30. Liu, Z.; Grinter, D. C.; Lustemberg, P. G.; Nguyen-Phan, T-D.; Zhou, Y.; Luo, Si, Waluyo, I.; Crumlin, E. J.; Stacchiola, D. J.; Zhou, J.; Carrasco, J.; Busnengo, H. F.; Ganguglia-Pirovano, M. V.; Senanayake, S. D.; Rodriguez, J. A. Dry Reforming of Methane on a Highly-Active Ni-CeO_2Catalyst: Effects of Metal-Support Interactions on C−H Bond Breaking. *Angew. Chem. Int. Ed.*, **2016**, 55, 7455-7459.

31. Liu, Z.; Lustemberg, P.; Gutiérrez, R. A.; Carey, J. J.; Palomino, R. M.; Vorokhta, M.; Grinter, D. C.; Ramírez, P. J.; Matolín, V.; Nolan, M.; Ganduglia-Pirovano, M. V.; Senanayake, S. D.; Rodriguez, J. A. In Situ Investigation of Methane Dry Reforming on Metal/Ceria(111) Surfaces: Metal–Support Interactions and C−H Bond Activation at Low Temperature. *Angew, Chem. Int. Ed.*, **2017**, 56, 13041-13046.

32. Lustemberg, P. G.; Ramírez, P. J.; Liu, Z.; Gutiérrez, R. A.; Grinter, D. G.; Carrasco, J.; Senanayake, S. D.; Rodriguez, J. A.; Ganduglia-Pirovano, M. V. Room-Temperature Activation of Methane and Dry Re-forming with CO_2 on Ni-CeO_2(111) Surfaces: Effect of Ce^{3+} Sites and Metal-Support Interactions on C-H Bond Cleavage. *ACS Catal.*, **2016**, 6, 8184–8191

33. Lustemberg, P. G.; Mao, Z.; Salcedo, A.; Irigoyen, B.; Ganduglia-Pirovano, M. V.; Campbell, C. T.; Nature of the Active Sites on Ni/CeO_2 Catalysts for Methane Conversions. *ACS Catal.*, **2021**, 11, 10604−10613.

34. Carrasco, J.; Lopez-Duran, D.; Liu, Z.; Duchon, T.; Evans, J.; Senanayake, S. D.; Crumlin, E. J.; Matolín, V.; Rodriguez, J. A.; Ganduglia-Pirovano, M. V. In Situ and Theoretical Studies for the Dissociation of Water on an Active Ni/CeO_2 Catalyst:

Importance of Strong Metal–Support Interactions for the Cleavage of O–H Bonds. *Angew. Chem. Int. Ed.* **2015**, 54, 3917-3921.

35. Zhang, J.; Yang, Y.; Liu, J.; Xiong, B. Mechanistic Understanding of CO_2 Hydrogenation to Methane over Ni/CeO_2. *App. Surf. Sci.,* **2021**, 558, 149866-149875.

36. Lozano-Reis. P.; Gamallo, P.; Sayos, R.; Illas, F. A Comprehensive Density Functional and Kinetic Monte Carlo Study of CO_2 Hydrogenation on a Well-Defined Ni/CeO_2 Catalyst: Role of Eley-Rideal Reactions. (To be submitted, A full descrption of the work can be found in Section 5.5 and Appendix A)

37. Alvarez-Galvan, C.; Lustemberg, P. G.; Oropeza, F. E.; Bachiller-Baeza, B.; Ospina, M. D.; Herranz, M.; Cebollada, J.; Collado, L.; Campos-Martin, J. M.; de la Peña-O'Shea, V. A.; Alonso, J. A.; Ganduglia-Pirovano, M. V. *ACS Appl. Mater. Interfaces,* **2022**, 14, 50739−50750.

38. Lustemberg, P. G.; Senanayake, S.D.; Rodriguez, J. A.; Ganduglia-Pirovano, M. V. Tuning Selectivity in the Direct Conversion of Methane to Methanol: Bimetallic Synergistic Effects on the Cleavage of C-H and O-H Bonds over NiCu/CeO_2 Catalysts. *J. Phys. Chem. Lett.*, **2022**, 13, 5589−5596

39. Lustemberg, P. G.; Zhang, F.; Gutiérrez, R. A.; Ramírez, P. J.; Senanayake, S. D.; Rodriguez, J. A.; Ganduglia-Pirovano, M. V. Breaking Simple Scaling Relations through Metal-Oxide interactions: Understanding Room-Temperature Activation of Methane on M/CeO_2 (M = Pt, Ni or Co) Interfaces. *J. Phys. Chem. Lett.* **2020**, 11, 9131–9137

40. Mao, Z.; Lustemberg, P. G.; Rumptz, J. R.; Gundiglia-Pirovano, M. V.; Campbell, C. T. Ni Nanoparticles on CeO2(111): Energetics, Electron Transfer, and Structure by Ni Adsorption Calorimetry, Spectroscopies, and Density Functional Theory. *ACS. Catal.*, **2020**, 10, 5101-5114.

41. Lozano-Reis, P.; Prats, H.; Gamallo, P.; Illas, F.; Sayós R. Multiscale Study of the Mechanism of Catalytic CO_2 Hydrogenation: Role of the Ni(111) Facets. *ACS Catal.*, **2020**, 10, 8077–8089

42. Lozano-Reis, P.; Prats, H.; Sayós, R.; Illas, F. Limitations of Free Energy Diagrams to Predict the Catalytic Activity: The Reverse Water Gas Shift Reaction Catalyzed by Ni/TiC. *J. Catal.*, **2023**, 425, 203-211.

Conclusions

In the present doctoral thesis, the CO_2 hydrogenation reaction over different Ni-based catalysts has been investigated by combining periodic density functional theory calculations and kinetic Monte Carlo simulations. The motivation for this study comes from the urgency in mitigating global warming and climate change, being a possible strategy the design of new and efficient catalysts for CO_2 valorization at mild working conditions. To this end, an in-depth understanding of the processes that occurs on the catalyst at working conditions is essential. This has been precisely the aim of the current doctoral thesis. Although the conclusions of the different studies have been already covered at the end of each section, the overall conclusions of the doctoral thesis are outlined here.

- The Ni(111) surface itself is active for the RWGS reaction but it is inactive for the CO_2 methanation reaction. The main limitations for CH_4 formation are, first, the very high energy barriers of the CO and COH dissociation reactions, that impedes the formation of C. Second, the very endothermic HCO formation reaction with a small reverse energy barrier compared to other competing processes, thus whenever HCO is formed it goes backward to CO again. Finally, the very similar energy barrier of HCO formation and CO desorption energy, the latter guiding the selectivity towards CO.
- Methane production observed experimentally is not due to the Ni(111) surface itself but rather to other active Ni facets, to a cooperative effect between the Ni(111) surface and other facets, to the effect of the support or due to the interfacial sites lying in between the metal and the support.
- Small Ni_n clusters supported on the TiC(001) surface with 2D structures present higher metal-support interaction than 3D ones, while the latter seem to be easier to form and slightly more stable.
- The 2D Ni_n clusters supported on the TiC(001) surface adsorb strongly and dissociate CO_2 easily than the 3D counterparts, the TiC(001) surface and the Ni(111) surface.
- The 2D Ni_n clusters supported on the TiC(001) surface adsorb H_2 stronger than the 3D ones but both types dissociate H_2 very easily. Both supported

clusters dissociate H_2 with a lower energy barrier than the Ni(111) surface and the TiC(001) surface.

- The larger 2D Ni_n clusters supported on the TiC(001) surface adsorb CO_2 slightly stronger than the smaller 2D Ni_n clusters and dissociate it easily, due to a better reorganization of the larger systems.
- The Ni_4 cluster supported on the TiC(001) surface is a good model to study the RWGS reaction over Ni/TiC as it is easy to form, stable and can activate both H_2 and CO_2 molecules.
- The COOH-mediated pathway is the mechanism that drives the RWGS reaction on the Ni_4/TiC system, while for the clean TiC surface the mechanism that drives the reaction is a combination of the CO_2 dissociative pathway and, to a lower extent, the COOH-mediated pathway.
- The boost of activity of the Ni_4/TiC relative to clean TiC surface is originated by a synergic effect between the Ni cluster in which H_2 adsorbs and dissociates to produce H that further spillover to the TiC region in which the overall reactivity occurs.
- For the Ni_4/TiC system, there is a poisoning of the Ni and interface regions at the initial stages of the simulation that blocks these sites and forbids the reactivity over the Ni and interface region, which is the reason why all the reactivity occurs at the TiC region.
- For the Ni_4/TiC results, there is a discrepancy between the predictions of the main mechanism and activity derived from the DFT and kMC calculations, the former suggesting the activity to increase in the order TiC < interface < Ni via the dissociative pathway and the latter pointing to the opposite direction, the activity increasing in the order Ni < interface < TiC via the COOH-mediated pathway.
- Accounting for coverage effects is essential to correctly describe the active region and the main mechanism that drives the overall reaction. These are difficult to include in the DFT calculations while can be correctly included in the kMC simulations.
- For the species involved in the RWGS and Sabatier reactions, the Ni_4 supported on CeO_2(111) presents adsorption energies and energy barriers very different from those for the extended Ni(111) surface, with higher

adsorption energies and lower energy barriers suggesting this system as a good candidate for the CO_2 hydrogenation reaction.

- For the Ni_4/CeO_2 system, there is a synergic effect between the two different three-fold hollow sites present on the Ni_4 cluster, in which some reactions are preferred in one site while other reactions are dominant on the other site.
- For the Ni_4/CeO_2 system, $CO_{(g)}$ is formed via the dissociative pathway of the RWGS reaction, while methane formation is a combination of the dissociative pathway to produce CO followed by a combination of the HCOO-mediated and dissociative pathways for the final methane formation (*i.e.,* $CO_{2(g)} \rightarrow CO_2 \rightarrow CO \rightarrow HCO \rightarrow CH \rightarrow CH_2 \rightarrow CH_3 \rightarrow CH_4 \rightarrow CH_{4(g)}$).
- Eley-Rideal reactions play an important role on the mechanism, activity and CH_4 selectivity. Both the catalytic activity and CH_4 selectivity are higher when including the Eley-Rideal reactions, the former because the system spend less time in forming water and the latter because Eley-Rideal reactions helps methane to be formed on the more reactive Ni_{Ce} site after water formation, which is not the case for simulations without the Eley-Rideal reactions.
- Small Ni clusters supported on $CeO_2(111)$ could be good candidates for active and selective CO formation at high temperatures, while for they seem to be suitable catalysts for selective methane formation at mild conditions.

List of Publications

Published articles in refereed journals included in this doctoral thesis:

- **Lozano-Reis, P.**; Prats, H.; Gamallo, P.; Illas, F.; Sayós, R. Multiscale Study of the Mechanism of Catalytic CO_2 Hydrogenation: Role of the Ni (111) facets. *ACS Catal.*, **2020**, 10, 8077-8089.
- **Lozano-Reis, P.**; Sayós, R.; Rodriguez, J. A.; Illas, F. Structural, Electronic, and Magnetic Properties of Ni Nanoparticles Supported on the TiC(001) Surface. *Phys. Chem. Chem. Phys.* **2020**, 22, 26145-26154.
- **Lozano-Reis, P.**; Prats, H.; Sayós, R.; Rodriguez, J. A.; Illas, F. Assessing the Activity of Ni Cluster Supported on TiC(001) Toward CO_2 and H_2 Dissociation. *J. Phys. Chem. C*, **2021**, 125, 12019-12027.
- **Lozano-Reis, P.**; Prats, H.; Sayós, R.; Illas, F. Limitations of Free Energy Diagrams to Predict the Catalytic Activity: The Reverse Water Gas Shift Reaction Catalyzed by Ni/TiC. *J.Catal.*, **2023**, 425, 203-211.
- **Lozano-Reis. P.**; Gamallo, P.; Sayos, R.; Illas, F. A Comprehensive Density Functional and Kinetic Monte Carlo Study of CO_2 Hydrogenation on a Well-Defined Ni/CeO_2 Catalyst: Role of Eley-Rideal Reactions. *(To be submitted)*

Appendices

A. Supporting information: “A Comprehensive Density Functional and Kinetic Monte Carlo Study of CO_2 Hydrogenation on Well-Defined Ni/CeO_2: Role of Eley-Rideal Reactions”

Supporting Information

A comprehensive density functional and kinetic Monte Carlo study of CO_2 hydrogenation on a well-defined Ni/CeO_2 catalyst: role of Eley-Rideal reactions

Pablo Lozano-Reis, Pablo Gamallo, Ramón Sayós, Francesc Illas

Departament de Ciència de Materials i Química Física & Institut de Química Teòrica i Computacional (IQTCUB), Universitat de Barcelona, C. Martí i Franquès 1, 08028 Barcelona, Spain

S1. Formation energies calculation.

The reference set for the formation energy values is {slab, $H_{2(g)}$, $H_2O_{(g)}$ and $CO_{(g)}$} where slab stands for the energy of the Ni_4/CeO_2 surface while $H_{2(g)}$, $H_2O_{(g)}$ and $CO_{(g)}$ are the DFT energies of the gas-phase molecules. Therefore, the formation energy on the *i* adsorbate is calculated as:

$$E_i^f = U_{i-slab} - U_{slab} - \sum_j (n_j R_j) \quad (1)$$

Where U_{slab} is the DFT energy of the pristine slab, U_{i-slab} is the DFT energy of the adsorbate *i* on the slab, n_j is the number of atoms *j* in species *i*, and R_j is the reference energy of the atom *j*, defined in our reference set as:

$$R_H = 0.5 \left(U_{H_{2(g)}}\right) \quad (2)$$

$$R_O = U_{H_2O_{(g)}} - 2R_H \quad (3)$$

$$R_C = U_{CO_{(g)}} - R_O \quad (4)$$

where $U_{i_{(g)}}$ is the DFT energy for the *i* gas-phase species. Following the above definition, the formation energy (FE) of the different species at the different sites for the Ni_4/CeO_2 system is calculated and summarized in Table S1.

Table S1. Formation energies, including the ZPE term for all the different species at the different considered sites on the Ni_4/CeO_2 system.

Species	FE /eV	Species	FE / eV	Species	FE / eV	Species	FE / eV
$H^{**}_{2,hCehO}$	-0.63	CO^{*}_{NiO}	-2.33	$CH_2OH^{*}_{NiCe}$	-2.43	$H_2O^{*}_{NiO}$	-0.75
$CO^{*}_{2,NiO}$	-2.35	CO^{*}_{NiCe}	-2.47	$CH^{*}_{3,NiO}$	-3.15	$H_2O^{*}_{NiCe}$	-0.73
$CO^{*}_{2,NiCe}$	-2.30	C^{*}_{NiO}	-1.36	$CH^{*}_{3,NiCe}$	-3.22	H^{*}_{hO}	-0.74
$COOH^{*}_{NiO}$	-2.36	C^{*}_{NiCe}	-1.43	$CH_3O^{*}_{NiO}$	-2.83	H^{*}_{hCe}	-0.81
$COOH^{*}_{NiCe}$	-2.44	CH^{*}_{NiO}	-1.91	$CH_3O^{*}_{NiCe}$	-2.92	$HCOH^{*}_{NiO}$	-1.96
$HCOO^{*}_{NiO}$	-2.70	CH^{*}_{NiCe}	-2.09	$CH^{*}_{4,NiO}$	-2.62	$HCOH^{*}_{NiCe}$	-1.94
$HCOO^{*}_{NiCe}$	-2.73	$CH^{*}_{2,NiO}$	-2.49	$CH^{*}_{4,NiCe}$	-2.62	$CH_3OH^{*}_{NiO}$	-2.13
HCO^{*}_{NiO}	-2.26	$CH^{*}_{2,NiCe}$	-2.62	O^{*}_{NiO}	-1.01	$CH_3OH^{*}_{NiCe}$	-2.11
HCO^{*}_{NiCe}	-2.22	$CH_2O^{*}_{NiO}$	-2.36	O^{*}_{NiCe}	-1.23		
COH^{*}_{NiO}	-1.90	$CH_2O^{*}_{NiCe}$	-2.39	OH^{*}_{NiO}	-1.40		
COH^{*}_{NiCe}	-1.99	$CH_2OH^{*}_{NiO}$	-2.43	OH^{*}_{NiCe}	-1.49		

S2. Cluster expansion Hamiltonians and how to approximate lateral interactions.

To correctly define the energetics of the system of interest, at each surface configuration, cluster expansion Hamiltonians are used which account for the interactions between the different adsorbed species. With this definition the energy of a specific configuration is calculated as a sum of the different clusters that can represent one-body to multi-body terms. Hence, a cluster could be a single absorbed species or a group of neighboring species interacting among them. For instance, the cluster representing a two-body term interaction (normally called lateral interactions) between two species A-A is calculated as:

$$CE(A-A) = E^f_{A-A} - 2E^f_A \quad (5)$$

where E^f_A and E^f_{A-A} stands for the formation energy of the A species alone and the formation energy of the two neighboring species, respectively.

Finally, the energetics of a specific *i* lattice configuration is expressed as the sum of cluster energies:

$$E(i) = \sum_{k=1}^{N_C} n_k(i) \cdot CE_k \quad (6)$$

where $E(i)$ is the total energy of the system (*i.e.*, the energy of the i lattice configuration), N_C is the total number of clusters included in the model, CE_k is the cluster energy of cluster k and $n_k(i)$ is the number of times that a pattern for *k*-cluster appears. Note that the formation energy of a single adsorbed species is equivalent to the cluster energy of the adsorbed species. Table S2 summarize the different two-body terms (or lateral interactions) used in the cluster expansion.

Table S2. Pairwise lateral interactions (LI), including the ZPE term, between the most relevant species involved in the CO_2 hydrogenation reaction on the Ni_4/CeO_2 system. These values correspond to the two-body terms used in the cluster expansion. The "-" symbol is used to distinguish the two different species in the kMC simulation

Species	LI / eV	Species	LI / eV	Species	LI / eV
H^*_{hCe}- H^*_{hO}	0.21	$CH_2O^*_{NiCe}$ - H^*_{hCe}	0.91	$HCOO^*_{NiO}$- H^*_{hCe}	0.38
CO^*_{NiCe} - O^*_{NiO}	0.48	$CH_2O^*_{NiO}$ - H^*_{hO}	0.84	$HCOO^*_{NiCe}$- H^*_{hCe}	0.70
CO^*_{NiO} - O^*_{NiCe}	0.38	$CH_2O^*_{NiCe}$- H^*_{hO}	0.35	$HCOO^*_{NiCe}$- H^*_{hO}	0.22
$CO^*_{2,NiO}$ - H^*_{hCe}	0.53	$CH_2O^*_{NiO}$- H^*_{hCe}	0.30	$CO^*_{2,NiCe}$- H^*_{hCe}	0.96
$CO^*_{2,NiCe}$ - H^*_{hO}	0.38	$CH^*_{2,NiCe}$ - O^*_{NiO}	1.07	$CO^*_{2,NiO}$- H^*_{hO}	0.73
CO^*_{NiCe} - OH^*_{NiO}	0.24	$CH^*_{2,NiO}$ - O^*_{NiCe}	0.94	CO^*_{NiO}- H^*_{hO}	0.74
CO^*_{NiO} - OH^*_{NiCe}	0.10	CH^*_{NiO}- OH^*_{NiCe}	0.55	CO^*_{NiCe}- H^*_{hCe}	0.55
HCO^*_{NiO} - O^*_{NiCe}	0.99	CH^*_{NiCe} - OH^*_{NiO}	0.64	C^*_{NiO}- H^*_{hO}	0.78
HCO^*_{NiCe} - O^*_{NiO}	0.73	C^*_{NiCe}- OH^*_{NiO}	0.57	C^*_{NiCe}- H^*_{hCe}	0.77
C^*_{NiO} - O^*_{NiCe}	1.07	C^*_{NiO} - OH^*_{NiCe}	0.58	CH^*_{NiCe}- H^*_{hCe}	0.66
C^*_{NiCe} - O^*_{NiO}	0.99	$CH^*_{2,NiCe}$ - OH^*_{NiO}	0.66	CH^*_{NiO}- H^*_{hO}	0.57
C^*_{NiO} - H^*_{hCe}	0.23	$CH^*_{2,NiO}$ - OH^*_{NiCe}	0.64	$CH^*_{2,NiO}$- H^*_{hO}	0.72
C^*_{NiCe} - H^*_{hO}	0.26	$CH_3O^*_{NiCe}$- H^*_{hO}	0.44	$CH^*_{2,NiCe}$- H^*_{hCe}	0.74
CH^*_{NiO} - H^*_{hCe}	0.21	$CH_3O^*_{NiO}$- H^*_{hCe}	0.42	COH^*_{NiCe}- H^*_{hCe}	0.71
CH^*_{NiCe}- H^*_{hO}	0.25	$CH^*_{3,NiCe}$ - OH^*_{NiO}	0.80	COH^*_{NiO}- H^*_{hO}	0.68
$CH^*_{2,NiO}$ - H^*_{hCe}	0.21	$CH^*_{3,NiO}$ - OH^*_{NiCe}	0.76	$COOH^*_{NiO}$- H^*_{hO}	0.77
$CH^*_{2,NiCe}$ - H^*_{hO}	0.24	$CH^*_{3,NiCe}$ - O^*_{NiO}	0.91	$COOH^*_{NiCe}$- H^*_{hCe}	0.83
$CH^*_{3,NiCe}$ - H^*_{hCe}	0.88	$CH^*_{3,NiO}$ - O^*_{NiCe}	0.97	$COOH^*_{NiO}$- H^*_{hCe}	0.41
$CH^*_{3,NiO}$ - H^*_{hO}	0.84	COH^*_{NiCe}- H^*_{hO}	0.18	$COOH^*_{NiCe}$- H^*_{hO}	0.48
O^*_{NiO} - H^*_{hCe}	0.35	COH^*_{NiO}- H^*_{hCe}	0.17	$HCOH^*_{NiCe}$- H^*_{hCe}	0.74
O^*_{NiCe} - H^*_{hO}	0.43	COH^*_{NiCe}- O^*_{NiO}	0.86	$HCOH^*_{NiO}$- H^*_{hO}	0.72
OH^*_{NiO}- H^*_{hCe}	0.44	COH^*_{NiO}- O^*_{NiCe}	0.96	$CH^*_{3,NiCe}$ - H^*_{hO}	0.56
OH^*_{NiCe}- H^*_{hO}	0.48	$CH_2OH^*_{NiCe}$- H^*_{hO}	0.57	$CH^*_{3,NiO}$ - H^*_{hCe}	0.49

CO^*_{NiO}- H^*_{hCe}	0.08	$CH_2OH^*_{NiO}$- H^*_{hCe}	0.54	$CH_3O^*_{NiCe}$- H^*_{hCe}	0.92
CO^*_{NiCe}- H^*_{hO}	0.39	$HCOH^*_{NiCe}$- H^*_{hO}	0.46	$CH_3O^*_{NiO}$- H^*_{hO}	0.89
CH^*_{NiCe}- O^*_{NiO}	1.18	$HCOH^*_{NiO}$- H^*_{hCe}	0.55	$CH_2OH^*_{NiCe}$- H^*_{hCe}	0.88
CH^*_{NiO} - O^*_{NiCe}	1.22	O^*_{NiO}- H^*_{hO}	0.76	$CH_2OH^*_{NiO}$- H^*_{hO}	0.74
HCO^*_{NiO}- H^*_{hCe}	0.29	O^*_{NiCe}- H^*_{hCe}	0.84	HCO^*_{NiO} - OH^*_{NiCe}	1.03
HCO^*_{NiCe} - H^*_{hO}	0.28	OH^*_{NiO}- H^*_{hO}	0.89	HCO^*_{NiCe} - OH^*_{NiO}	0.89
HCO^*_{NiO} - H^*_{hO}	0.77	OH^*_{NiCe}- H^*_{hCe}	0.93	H^*_{hCe}- H^*_{hCe}	0.88
HCO^*_{NiCe}- H^*_{hCe}	0.75	$HCOO^*_{NiO}$- H^*_{hO}	0.67	H^*_{hO}- H^*_{hO}	0.91

Table S3. Reaction energies ($\Delta E_{0,r}$) and forward and reverse energy barriers ($\Delta E^{\neq}_{0,f}$, $\Delta E^{\neq}_{0,r}$), including the ZPE term, for the different elementary reactions considered for the CO_2 hydrogenation reaction for the Ni_4/CeO_2 system with corresponding values for the reaction at the Ni(111) surface[1] included for comparison. For reactions in which two possible hydrogen attacks are considered the *f* and *n* subscript stands for the H atom being at the site that is far or near the attacking species, respectively. For instance, *f* stands for situations in which H and the other species are at h_O/Ni_{Ce} or h_{Ce}/Ni_O, respectively, and *n* stands for situations in which H and the other species are at h_{Ce}/Ni_{Ce} or h_O/Ni_O, respectively

ID	Reaction	$\Delta E_{0,r}$ / eV		$\Delta E^{\neq}_{0,f}$ / eV		$\Delta E^{\neq}_{0,r}$ / eV	
		This Work	Ref 1	This Work	Ref 1	This Work	Ref 1
$R1_{NiO}$	$CO_{2,(g)} + *_{NiO} \rightleftharpoons CO^*_{2,NiO}$	-1.51	-0.16	0.00	0.00	1.46	0.16
$R1_{NiCe}$	$CO_{2,(g)} + *_{NiCe} \rightleftharpoons CO^*_{2,NiCe}$	-1.46	-0.16	0.00	0.00	1.46	0.16
R2	$H_{2,(g)} + *_{hCe} + *_{hO} \rightleftharpoons H^{**}_{2,hCehO}$	-0.63	0.00	0.00	0.00	0.63	0.00
R3	$H^{**}_{2,hCehO} \rightleftharpoons H^*_{hCe} + H^*_{hO}$	-0.70	-0.33	0.00	0.26	0.70	0.59
$R4_{NiO}$	$CO^*_{2,NiO} + *_{NiCe} \rightleftharpoons CO^*_{NiO} + O^*_{NiCe}$	-0.82	-0.57	0.78	0.86	1.60	1.43
$R4_{NiCe}$	$CO^*_{2,NiCe} + *_{NiO} \rightleftharpoons CO^*_{NiCe} + O^*_{NiO}$	-0.70	-0.57	0.77	0.86	1.47	1.43
$R5_{NiO}$	$CO^*_{2,NiO} + H^*_{hCe} \rightleftharpoons HCOO^*_{NiO} + *_{hCe}$	-0.07	0.04	0.60	1.05	0.45	1.01
$R5_{NiCe}$	$CO^*_{2,NiCe} + H^*_{hO} \rightleftharpoons HCOO^*_{NiCe} + *_{hO}$	-0.07	0.04	0.39	1.05	0.45	1.01
$R6_{NiO}$	$CO^*_{2,NiO} + H^*_{hCe} \rightleftharpoons COOH^*_{NiO} + *_{hCe}$	0.26	0.49	1.16	1.33	0.90	0.84
$R6_{NiCe}$	$CO^*_{2,NiCe} + H^*_{hO} \rightleftharpoons COOH^*_{NiCe} + *_{hO}$	0.22	0.49	1.20	1.33	0.8	0.84
$R7_{NiO}$	$COOH^*_{NiO} + *_{NiCe} \rightleftharpoons COH^*_{NiCe} + O^*_{NiO}$	0.23	0.07	1.33	1.28	1.10	1.21
$R7_{NiCe}$	$COOH^*_{NiCe} + *_{NiO} \rightleftharpoons COH^*_{NiO} + O^*_{NiCe}$	0.28	0.07	1.35	1.28	1.07	1.21
$R8_{NiO}$	$COOH^*_{NiO} + *_{NiCe} \rightleftharpoons CO^*_{NiO} + OH^*_{NiCe}$	-1.36	-1.02	0.49	0.49	1.85	1.51
$R8_{NiCe}$	$COOH^*_{NiCe} + *_{NiO} \rightleftharpoons CO^*_{NiCe} + OH^*_{NiO}$	-1.20	-1.02	0.64	0.49	1.84	1.51
$R9_{NiO}$	$HCOO^*_{NiO} + *_{NiCe} \rightleftharpoons HCO^*_{NiO} + O^*_{NiCe}$	0.20	0.85	0.59	1.39	0.39	0.54
$R9_{NiCe}$	$HCOO^*_{NiCe} + *_{NiO} \rightleftharpoons HCO^*_{NiCe} + O^*_{NiO}$	0.23	0.85	0.65	1.39	0.42	0.54
$R10_{NiO}$	$CO^*_{NiO} + H^*_{hCe} \rightleftharpoons HCO^*_{NiO} + *_{hCe}$	0.80	1.21	1.12	1.42	0.32	0.21
$R10_{NiCe}$	$CO^*_{NiCe} + H^*_{hO} \rightleftharpoons HCO^*_{NiCe} + *_{hO}$	0.60	1.21	0.90	1.42	0.30	0.21
$R11_{NiO}$	$CO^*_{NiO} + H^*_{hCe} \rightleftharpoons COH^*_{NiO} + *_{hCe}$	1.16	1.07	2.18	2.28	1.02	1.21
$R11_{NiCe}$	$CO^*_{NiCe} + H^*_{hO} \rightleftharpoons COH^*_{NiCe} + *_{hO}$	0.83	1.07	1.98	2.28	1.15	1.21
$R12_{NiO}$	$CO^*_{NiO} + *_{NiCe} \rightleftharpoons C^*_{NiO} + O^*_{NiCe}$	0.82	1.84	1.24	2.98	0.42	1.15
$R12_{NiCe}$	$CO^*_{NiCe} + *_{NiO} \rightleftharpoons C^*_{NiCe} + O^*_{NiO}$	1.03	1.84	1.52	2.98	0.49	1.15
$R13_{NiO}$	$HCO^*_{NiO} + *_{NiCe} \rightleftharpoons CH^*_{NiCe} + O^*_{NiO}$	0.34	-0.07	0.75	1.10	0.41	1.17
$R13_{NiCe}$	$HCO^*_{NiCe} + *_{NiO} \rightleftharpoons CH^*_{NiO} + O^*_{NiCe}$	0.31	-0.07	0.64	1.10	0.33	1.17
$R14_{NiO}$	$COH^*_{NiO} + *_{NiCe} \rightleftharpoons C^*_{NiO} + OH^*_{NiCe}$	-0.37	0.67	1.09	1.81	1.46	1.14
$R14_{NiCe}$	$COH^*_{NiCe} + *_{NiO} \rightleftharpoons C^*_{NiCe} + OH^*_{NiO}$	-0.28	0.67	1.07	1.81	1.35	1.14
$R15_{NiO,f}$	$C^*_{NiO} + H^*_{hCe} \rightleftharpoons CH^*_{NiO} + *_{hCe}$	0.02	-0.63	0.58	0.64	0.56	1.27

$R15_{NiCe,f}$	$C^*_{NiCe} + H^*_{hO} \rightleftharpoons CH^*_{NiCe} + *_{hO}$	-0.18	-0.63	0.48	0.64	0.66	1.27
$R15_{NiO,n}$	$C^*_{NiO} + H^*_{hO} \rightleftharpoons CH^*_{NiO} + *_{hO}$	-0.59	-0.63	0.03	0.64	0.62	1.27
$R15_{NiCe,n}$	$C^*_{NiCe} + H^*_{hCe} \rightleftharpoons CH^*_{NiCe} + *_{hCe}$	-0.62	-0.63	0.12	0.64	0.75	1.27
$R16_{NiO,f}$	$CH^*_{NiO} + H^*_{hCe} \rightleftharpoons CH^*_{2,NiO} + *_{hCe}$	0.01	0.30	0.37	0.64	0.36	0.34
$R16_{NiCe,f}$	$CH^*_{NiCe} + H^*_{hO} \rightleftharpoons CH^*_{2,NiCe} + *_{hO}$	-0.04	0.30	0.33	0.64	0.37	0.34
$R16_{NiO,n}$	$CH^*_{NiO} + H^*_{hO} \rightleftharpoons CH^*_{2,NiO} + *_{hO}$	-0.41	0.30	0.20	0.64	0.43	0.34
$R16_{NiCe,n}$	$CH^*_{NiCe} + H^*_{hCe} \rightleftharpoons CH^*_{2,NiCe} + *_{hCe}$	-0.38	0.30	0.03	0.63	0.41	0.34
$R17_{NiO,f}$	$CH^*_{2,NiO} + H^*_{hCe} \rightleftharpoons CH^*_{3,NiO} + *_{hCe}$	-0.07	-0.11	0.44	0.57	0.51	0.68
$R17_{NiCe,f}$	$CH^*_{2,NiCe} + H^*_{hO} \rightleftharpoons CH^*_{3,NiCe} + *_{hO}$	-0.10	-0.11	0.44	0.57	0.54	0.68
$R17_{NiO,n}$	$CH^*_{2,NiO} + H^*_{hO} \rightleftharpoons CH^*_{3,NiO} + *_{hO}$	-0.64	-0.11	0.03	0.57	0.67	0.68
$R17_{NiCe,n}$	$CH^*_{2,NiCe} + H^*_{hCe} \rightleftharpoons CH^*_{3,NiCe} + *_{hCe}$	-0.53	-0.11	0.09	0.57	0.62	0.68
$R18_{NiO}$	$COH^*_{NiO} + H^*_{hCe} \rightleftharpoons HCOH^*_{NiO} + *_{hCe}$	0.56	0.67	1.21	0.82	0.65	0.14
$R18_{NiCe}$	$COH^*_{NiCe} + H^*_{hO} \rightleftharpoons HCOH^*_{NiCe} + *_{hO}$	0.60	0.67	1.26	0.82	0.66	0.14
$R19_{NiO}$	$HCO^*_{NiO} + H^*_{hO} \rightleftharpoons HCOH^*_{NiO} + *_{hO}$	0.26	0.40	0.88	0.93	0.62	0.53
$R19_{NiCe}$	$HCO^*_{NiCe} + H^*_{hCe} \rightleftharpoons HCOH^*_{NiCe} + *_{hCe}$	0.33	0.40	0.89	0.93	0.55	0.53
$R20_{NiO}$	$HCOH^*_{NiO} + *_{NiCe} \rightleftharpoons CH^*_{NiCe} + OH^*_{NiO}$	-0.23	-0.48	0.24	0.72	0.47	1.19
$R20_{NiCe}$	$HCOH^*_{NiCe} + *_{NiO} \rightleftharpoons CH^*_{NiO} + OH^*_{NiCe}$	-0.28	-0.48	0.36	0.72	0.63	1.19
$R21_{NiO}$	$HCOH^*_{NiO} + H^*_{hCe} \rightleftharpoons CH_2OH^*_{NiO} + *_{hCe}$	-0.20	0.22	0.73	0.63	0.93	0.41
$R21_{NiCe}$	$HCOH^*_{NiCe} + H^*_{hO} \rightleftharpoons CH_2OH^*_{NiCe} + *_{hO}$	-0.20	0.22	0.68	0.63	0.93	0.41
$R22_{NiO}$	$HCO^*_{NiO} + H^*_{hCe} \rightleftharpoons CH_2O^*_{NiO} + *_{hCe}$	0.42	0.26	0.51	0.71	0.09	0.45
$R22_{NiCe}$	$HCO^*_{NiCe} + H^*_{hO} \rightleftharpoons CH_2O^*_{NiCe} + *_{hO}$	0.29	0.26	0.46	0.71	0.17	0.45
$R23_{NiO}$	$CH_2O^*_{NiO} + *_{NiCe} \rightleftharpoons CH^*_{2,NiCe} + O^*_{NiO}$	-0.19	-0.40	0.64	0.96	0.83	1.37
$R23_{NiCe}$	$CH_2O^*_{NiCe} + *_{NiO} \rightleftharpoons CH^*_{2,NiO} + O^*_{NiCe}$	-0.39	-0.40	0.68	0.96	1.07	1.37
$R24_{NiO}$	$CH_2O^*_{NiO} + H^*_{hO} \rightleftharpoons CH_2OH^*_{NiO} + *_{hO}$	-0.17	0.31	0.68	0.86	0.75	0.55
$R24_{NiCe}$	$CH_2O^*_{NiCe} + H^*_{hCe} \rightleftharpoons CH_2OH^*_{NiCe} + *_{hCe}$	-0.14	0.33	0.63	0.86	0.77	0.55
$R25_{NiO}$	$CH_2OH^*_{NiO} + *_{NiCe} \rightleftharpoons CH^*_{2,NiCe} + OH^*_{NiO}$	-0.93	-0.30	0.25	0.71	1.18	1.01
$R25_{NiCe}$	$CH_2OH^*_{NiCe} + *_{NiO} \rightleftharpoons CH^*_{2,NiO} + OH^*_{NiCe}$	-0.92	-0.30	0.34	0.71	1.26	1.01
$R26_{NiO}$	$CH_2O^*_{NiO} + H^*_{hCe} \rightleftharpoons CH_3O^*_{NiO} + *_{hCe}$	0.03	-0.50	0.65	0.34	0.62	0.85
$R26_{NiCe}$	$CH_2O^*_{NiCe} + H^*_{hO} \rightleftharpoons CH_3O^*_{NiCe} + *_{hO}$	-0.14	-0.50	0.40	0.34	0.53	0.85
$R27_{NiO}$	$CH_3O^*_{NiO} + *_{NiCe} \rightleftharpoons CH^*_{3,NiO} + O^*_{NiCe}$	-0.57	-0.16	0.98	1.36	1.55	1.52
$R27_{NiCe}$	$CH_3O^*_{NiCe} + *_{NiO} \rightleftharpoons CH^*_{3,NiCe} + O^*_{NiO}$	-0.39	-0.16	1.27	1.26	1.67	1.52
$R28_{NiO}$	$CH_3O^*_{NiO} + H^*_{hCe} \rightleftharpoons CH_3OH^*_{NiO} + *_{hCe}$	1.09	0.44	1.31	1.38	0.22	0.95
$R28_{NiCe}$	$CH_3O^*_{NiCe} + H^*_{hO} \rightleftharpoons CH_3OH^*_{NiCe} + *_{hO}$	1.11	0.44	1.33	1.38	0.22	0.95
$R29_{NiO}$	$CH_2OH^*_{NiO} + H^*_{hCe} \rightleftharpoons CH_3OH^*_{NiO} + *_{hCe}$	0.56	-0.42	1.20	0.61	0.64	1.03
$R29_{NiCe}$	$CH_2OH^*_{NiCe} + H^*_{hO} \rightleftharpoons CH_3OH^*_{NiCe} + *_{hO}$	0.48	-0.42	1.04	0.61	0.56	1.03
$R30_{NiO}$	$CH_3OH^*_{NiO} + *_{NiCe} \rightleftharpoons CH^*_{3,NiO} + OH^*_{NiCe}$	-1.76	-0.29	1.13	1.80	2.88	2.09

R30$_{NiCe}$	$CH_3OH^*_{NiCe} + *_{NiO} \rightleftharpoons CH^*_{3,NiCe} + OH^*_{NiO}$	-1.71	-0.29	1.09	1.80	2.80	2.09
R31$_{NiO,f}$	$CH^*_{3,NiO} + H^*_{hCe} \rightleftharpoons CH^*_{4,NiO} + *_{hCe}$	0.85	-0.30	1.00	0.79	0.15	0.96
R31$_{NiO,n}$	$CH^*_{3,NiO} + H^*_{hO} \rightleftharpoons CH^*_{4,NiO} + *_{hO}$	0.43	-0.30	0.71	0.79	0.28	0.96
R31$_{NiCe,f}$	$CH^*_{3,NiCe} + H^*_{hO} \rightleftharpoons CH^*_{4,NiCe} + *_{hO}$	0.77	-0.30	0.91	0.79	0.14	0.96
R31$_{NiCe,n}$	$CH^*_{3,NiCe} + H^*_{hCe} \rightleftharpoons CH^*_{4,NiCe} + *_{hCe}$	0.52	-0.30	0.77	0.79	0.25	0.96
R32$_{NiO,f}$	$O^*_{NiO} + H^*_{hCe} \rightleftharpoons OH^*_{NiO} + *_{hCe}$	0.06	0.04	1.00	1.16	0.94	1.12
R32$_{NiCe,f}$	$O^*_{NiCe} + H^*_{hO} \rightleftharpoons OH^*_{NiCe} + *_{hO}$	0.04	0.04	0.99	1.16	0.95	1.12
R32$_{NiO,n}$	$O^*_{NiO} + H^*_{hO} \rightleftharpoons OH^*_{NiO} + *_{hO}$	-0.42	0.04	0.61	1.16	1.03	1.12
R32$_{NiCe,n}$	$O^*_{NiCe} + H^*_{hCe} \rightleftharpoons OH^*_{NiCe} + *_{hCe}$	-0.30	0.04	0.66	1.16	0.96	1.12
R33$_{NiO,f}$	$OH^*_{NiO} + H^*_{hCe} \rightleftharpoons H_2O^*_{NiO} + *_{hCe}$	1.03	0.25	1.27	1.16	0.24	0.91
R33$_{NiCe,f}$	$OH^*_{NiCe} + H^*_{hO} \rightleftharpoons H_2O^*_{NiCe} + *_{hO}$	1.02	0.25	1.26	1.16	0.24	0.91
R33$_{NiO,n}$	$OH^*_{NiO} + H^*_{hO} \rightleftharpoons H_2O^*_{NiO} + *_{hO}$	0.50	0.25	0.76	1.16	0.26	0.91
R33$_{NiCe,n}$	$OH^*_{NiCe} + H^*_{hCe} \rightleftharpoons H_2O^*_{NiCe} + *_{hCe}$	0.64	0.25	0.99	1.16	0.35	0.91
R34$_{NiO}$	$H_{2,(g)} + O^*_{NiO} + *_{hO} \rightleftharpoons OH^*_{NiO} + H^*_{hO}$	-0.24		0.53		0.77	
R34$_{NiCe}$	$H_{2,(g)} + O^*_{NiCe} + *_{hCe} \rightleftharpoons OH^*_{NiCe} + H^*_{hCe}$	-0.15		0.48		0.63	
R35$_{NiO}$	$H_{2,(g)} + OH^*_{NiO} + *_{hO} \rightleftharpoons H_2O^*_{NiO} + H^*_{hO}$	0.69		1.32		0.63	
R35$_{NiCe}$	$H_{2,(g)} + OH^*_{NiCe} + *_{hCe} \rightleftharpoons H_2O^*_{NiCe} + H^*_{hCe}$	0.63		0.63		0.0	
R36$_{NiO}$	$CO^*_{NiO} \rightleftharpoons CO_{(g)} + *_{NiO}$	2.33	1.61	2.33	1.61	0.0	0.0
R36$_{NiCe}$	$CO^*_{NiCe} \rightleftharpoons CO_{(g)} + *_{NiCe}$	2.47	1.61	2.47	1.61	0.0	0.0
R37$_{NiO}$	$CH_2O^*_{NiO} \rightleftharpoons CH_2O_{(g)} + *_{NiO}$	2.06	0.58	2.06	0.58	0.0	0.0
R37$_{NiCe}$	$CH_2O^*_{NiCe} \rightleftharpoons CH_2O_{(g)} + *_{NiCe}$	2.10	0.58	2.10	0.58	0.0	0.0
R38$_{NiO}$	$CH_3OH^*_{NiO} \rightleftharpoons CH_3OH_{(g)} + *_{NiO}$	0.91	0.36	0.91	0.36	0.0	0.0
R38$_{NiCe}$	$CH_3OH^*_{NiCe} \rightleftharpoons CH_3OH_{(g)} + *_{NiCe}$	0.89	0.36	0.89	0.36	0.0	0.0
R39$_{NiO}$	$CH^*_{4,NiO} \rightleftharpoons CH_{4,(g)} + *_{NiO}$	0.26	0.13	0.26	0.13	0.0	0.0
R39$_{NiCe}$	$CH^*_{4,NiCe} \rightleftharpoons CH_{4,(g)} + *_{NiCe}$	0.26	0.13	0.26	0.13	0.0	0.0
R40$_{NiO}$	$H_2O^*_{NiO} \rightleftharpoons H_2O_{(g)} + *_{NiO}$	0.75	0.26	0.75	0.26	0.0	0.0
R40$_{NiCe}$	$H_2O^*_{NiCe} \rightleftharpoons H_2O_{(g)} + *_{NiCe}$	0.73	0.26	0.73	0.26	0.0	0.0
D1	$H^*_{NiCe} + *_{NiO} \rightleftharpoons H^*_{NiO} + *_{NiCe}$	0.03	0.02	0.16	0.12	0.13	0.10
D2	$CO^*_{NiCe} + *_{NiO} \rightleftharpoons CO^*_{NiO} + *_{NiCe}$	0.14	-0.01	0.19	0.11	0.05	0.12
D3	$O^*_{NiCe} + *_{NiO} \rightleftharpoons O^*_{NiO} + *_{NiCe}$	0.22	0.10	0.60	0.42	0.38	0.32
D4	$OH^*_{NiCe} + *_{NiO} \rightleftharpoons OH^*_{NiO} + *_{NiCe}$	0.09	0.09	0.44	0.19	0.35	0.10
D5	$C^*_{NiCe} + *_{NiO} \rightleftharpoons C^*_{NiO} + *_{NiCe}$	0.08	-0.04	1.70	0.31	1.62	0.35
D6	$CH^*_{NiCe} + *_{NiO} \rightleftharpoons CH^*_{NiO} + *_{NiCe}$	0.19	0.02	0.62	0.32	0.44	0.30
D7	$CH^*_{2,NiCe} + *_{NiO} \rightleftharpoons CH^*_{2,NiO} + *_{NiCe}$	0.13	0.04	0.48	0.19	0.35	0.15
D8	$CH^*_{3,NiCe} + *_{NiO} \rightleftharpoons CH^*_{3,NiO} + *_{NiCe}$	0.06	0.02	0.33	0.15	0.27	0.13

Table S4. Species coverage at the different considered sites for the simulations with the Eley-Rideal reactions (W/ER) and without them (Wo/ER) at the five different temperatures considered and at $P(H_2)$ = 0.528 bar and $P(CO_2)$ = 0.132 bar.

T=483K	**Ni_{Ce}**		**Ni_O**		**h_{Ce}**		**h_O**	
Species	**W/ER**	**Wo/ER**	**W/ER**	**Wo/ER**	**W/ER**	**Wo/ER**	**W/ER**	**Wo/ER**
CO	70.0	65.7	28.80	29.7	-	-	-	-
O	0.6	5.4	0	1.6	-	-	-	-
OH	1.0	0.9	0	0	-	-	-	-
H_2	-	-	-	-	35.1	35.4	35.1	35.4
H	-	-	-	-	17.7	16.5	16.2	15.5
Total	71.6	72.0	28.8	31.3	52.8	51.9	51.3	50.9
T=503K	**Ni_{Ce}**		**Ni_O**		**h_{Ce}**		**h_O**	
Species	**W/ER**	**Wo/ER**	**W/ER**	**Wo/ER**	**W/ER**	**Wo/ER**	**W/ER**	**Wo/ER**
CO	72.1	67.5	26.9	28.7	-	-	-	-
O	0.5	5.1	0	1.1	-	-	-	-
OH	0.6	1.1	0	0	-	-	-	-
H_2	-	-	-	-	32.5	32.6	32.5	32.6
H	-	-	-	-	18.1	17.3	16.4	15.6
Total	73.2	74.7	26.9	29.8	50.6	49.9	48.9	48.2
T=523K	**Ni_{Ce}**		**Ni_O**		**h_{Ce}**		**h_O**	
Species	**W/ER**	**Wo/ER**	**W/ER**	**Wo/ER**	**W/ER**	**Wo/ER**	**W/ER**	**Wo/ER**
CO	71.5	66.7	27.2	30.7	-	-	-	-
O	0.7	7.1	0	0.7	-	-	-	-
OH	0.8	0.7	0	0	-	-	-	-
H_2	-	-	-	-	28.8	29.0	28.8	29.0
H	-	-	-	-	19.1	17.8	17.2	16.2
Total	73.0	74.5	27.2	31.4	47.9	46.8	46.9	45.2
T=543K	**Ni_{Ce}**		**Ni_O**		**h_{Ce}**		**h_O**	
Species	**W/ER**	**Wo/ER**	**W/ER**	**Wo/ER**	**W/ER**	**Wo/ER**	**W/ER**	**Wo/ER**
CO	70.8	63.9	26.9	33.2	-	-	-	-
O	1.0	10.3	0	0.2	-	-	-	-
OH	0.8	0.8	0	0	-	-	-	-
H_2	-	-	-	-	25.1	25.4	25.1	25.4
H	-	-	-	-	19.2	17.3	17.3	15.7
Total	72.6	75.0	26.9	33.4	44.3	42.7	42.4	41.1
T=563K	**Ni_{Ce}**		**Ni_O**		**h_{Ce}**		**h_O**	

Species	W/ER	Wo/ER	W/ER	Wo/ER	W/ER	Wo/ER	W/ER	Wo/ER
CO_2	0.9	0.8	0.9	0.7	-	-	-	-
CO	69.8	61.3	25.8	34.2	-	-	-	-
O	1.0	13.3	0	0.1	-	-	-	-
OH	0.4	0.5	0	0	-	-	-	-
H_2	-	-	-	-	21.5	21.9	21.5	21.9
H	-	-	-	-	19.2	16.9	17.4	15.5
Total	72.1	75.9	26.7	35.0	40.7	38.8	38.9	37.4

Plots summarizing the event frequencies for the different sites at the different temperature conditions for the simulations with the ER reactions (W/ER) and without the ER reactions (Wo/ER)

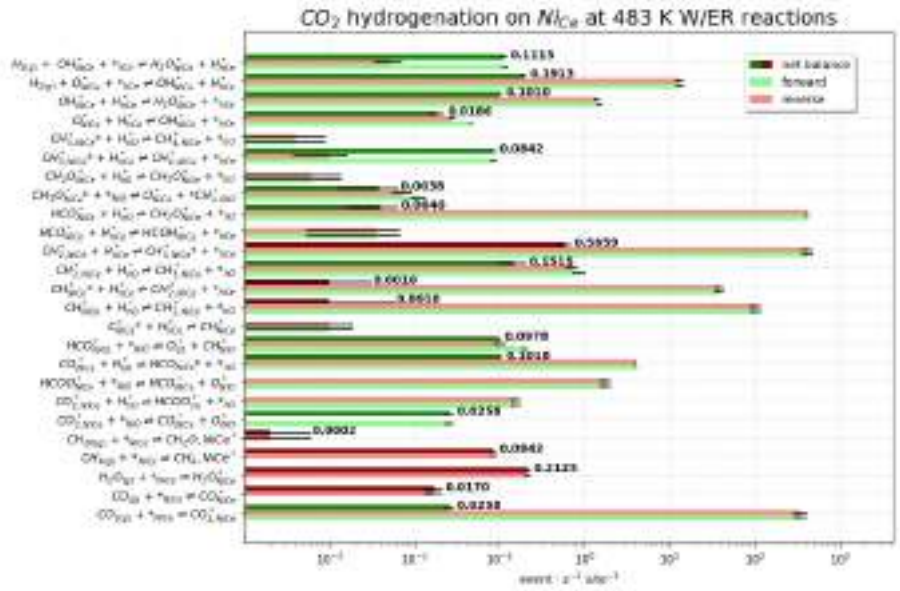

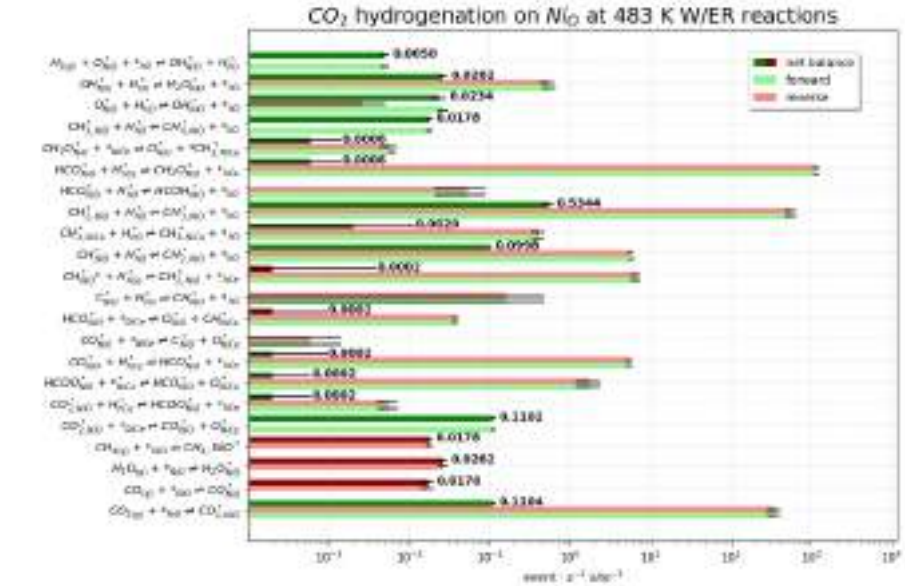
CO_2 hydrogenation on Ni_O at 483 K W/ER reactions
net balance
forward
reverse

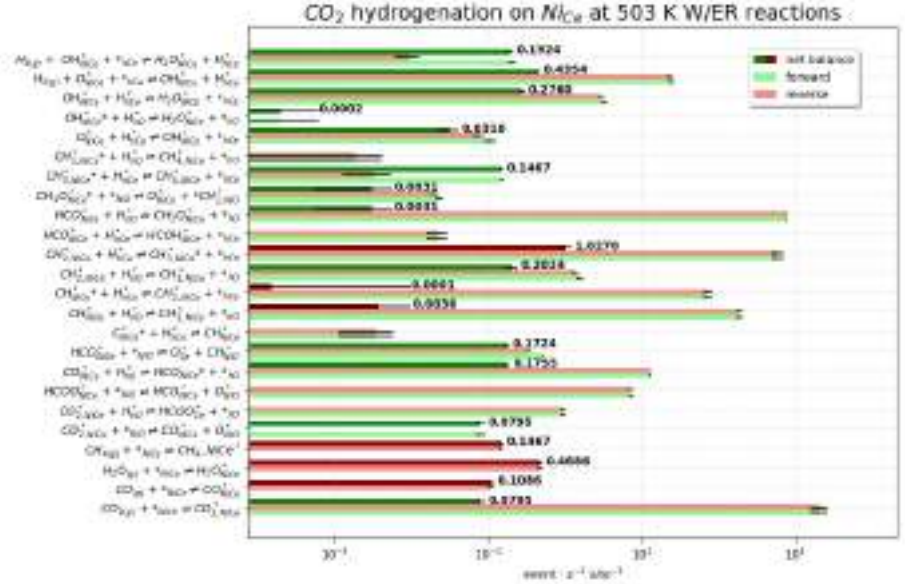
CO_2 hydrogenation on Ni_{Ce} at 503 K W/ER reactions
net balance
forward
reverse

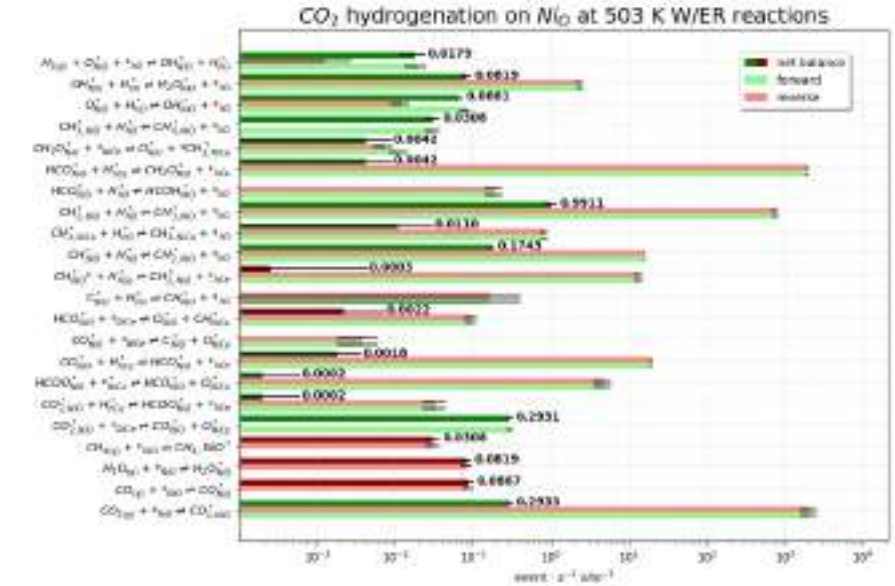
CO_2 hydrogenation on $Ni_{(0)}$ at 503 K W/ER reactions
net balance
forward
reverse
0.0179
0.0619
0.0681
0.0306
0.0642
0.0642
0.9911
0.0116
0.1745
0.0005
0.0022
0.0010
0.0002
0.0002
0.2931
0.0306
0.0819
0.0867
0.2933

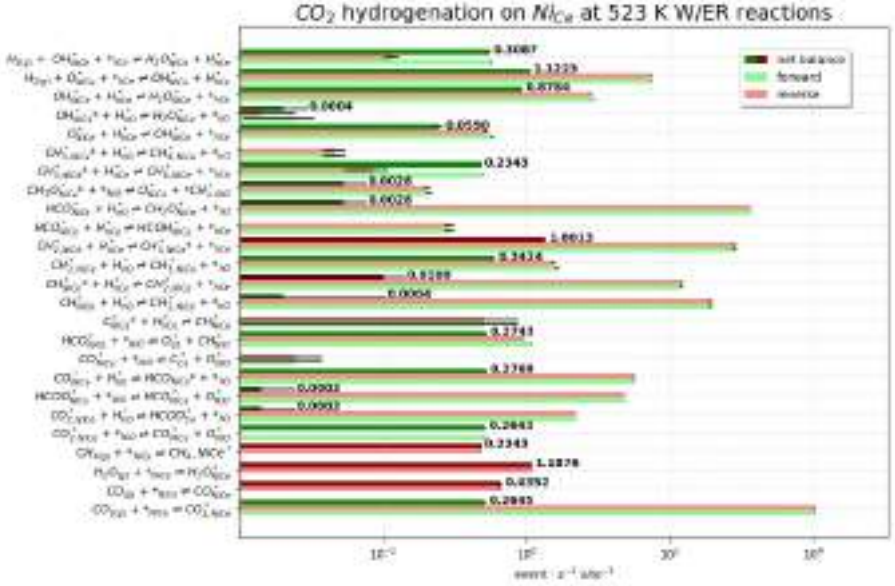
CO_2 hydrogenation on Ni_{Ce} at 523 K W/ER reactions
net balance
forward
reverse
0.3087
1.3229
0.8756
0.0404
0.0550
0.2343
0.0026
0.0026
1.0013
0.3424
0.1109
0.0004
0.2743
0.2768
0.0002
0.0002
0.2843
0.2343
1.1878
0.0392
0.2893

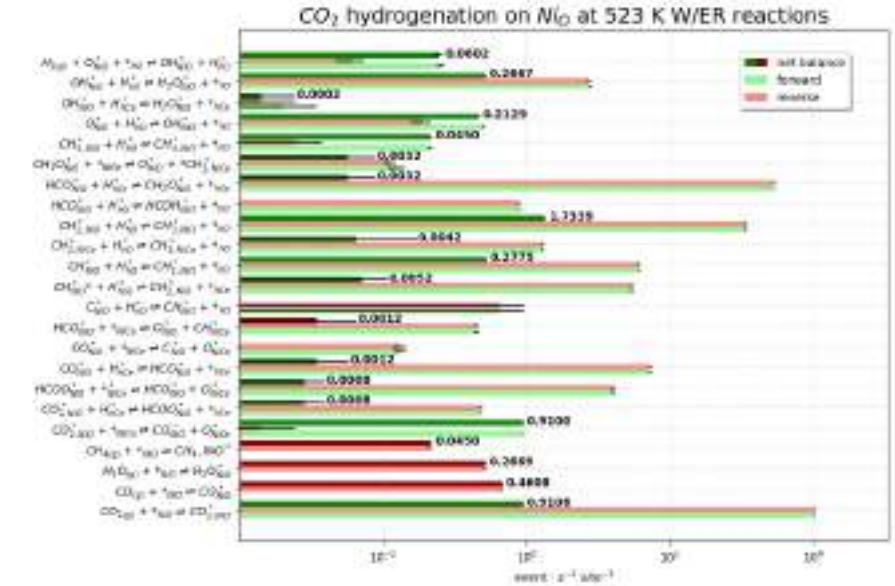
CO2 hydrogenation on Ni(O) at 523 K W/ER reactions
net balance
forward
reverse

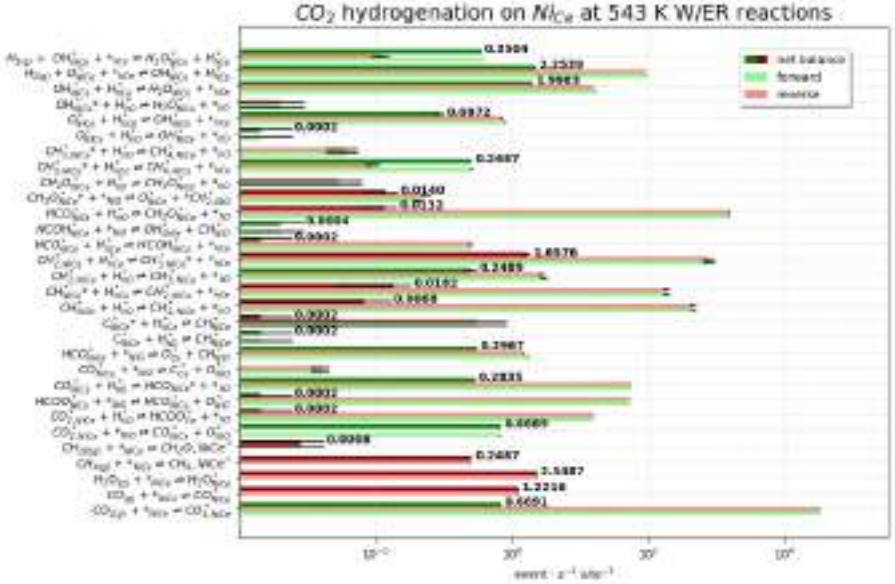
CO2 hydrogenation on Ni(Ce) at 543 K W/ER reactions
net balance
forward
reverse

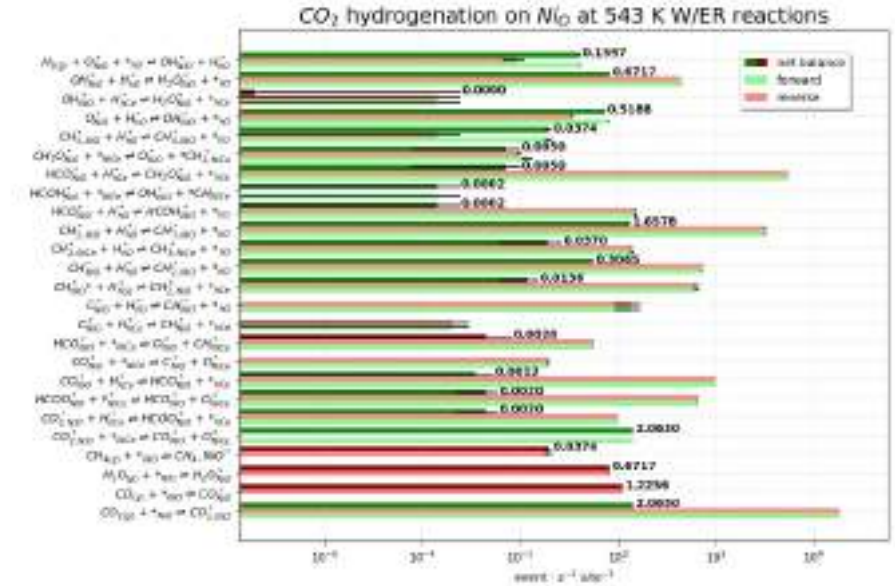
CO_2 hydrogenation on $Ni_{(0)}$ at 543 K W/ER reactions
net balance
forward
reverse

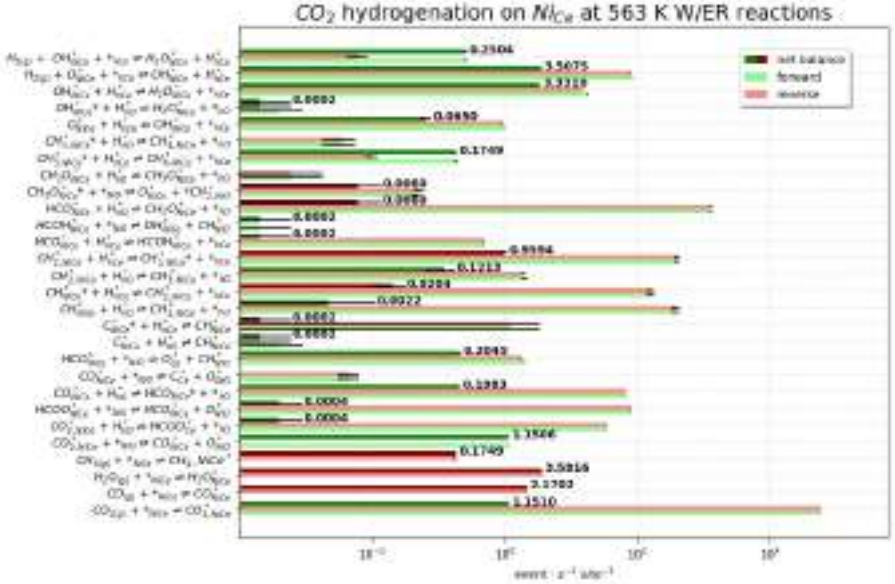
CO_2 hydrogenation on Ni_{Ce} at 563 K W/ER reactions
net balance
forward
reverse

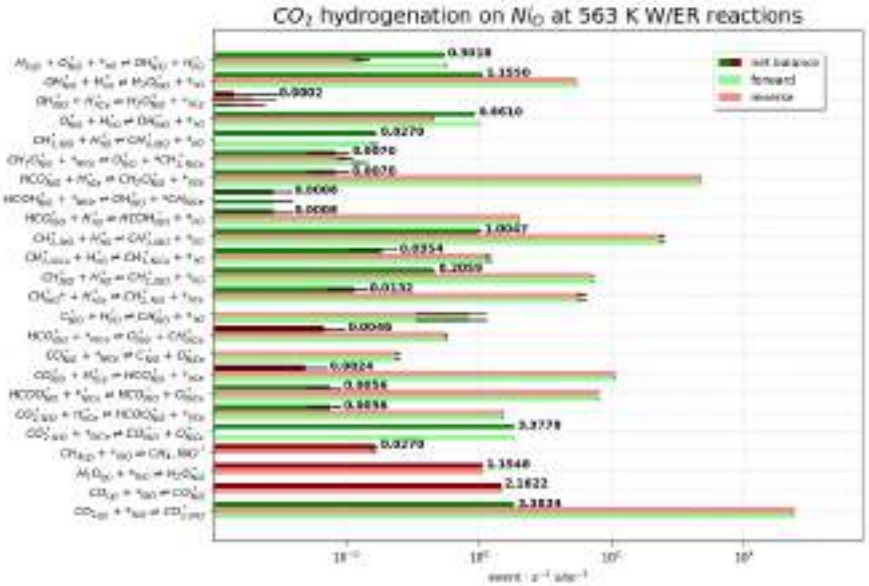
CO_2 hydrogenation on Ni_O at 563 K W/ER reactions
net balance
forward
reverse
0.9018
1.1550
0.0002
0.6610
0.0270
0.0030
0.0026
0.0008
0.0008
1.0047
0.0254
0.2059
0.0132
0.0008
0.0024
0.0056
0.0056
3.3778
0.0270
1.1548
2.1622
2.3834

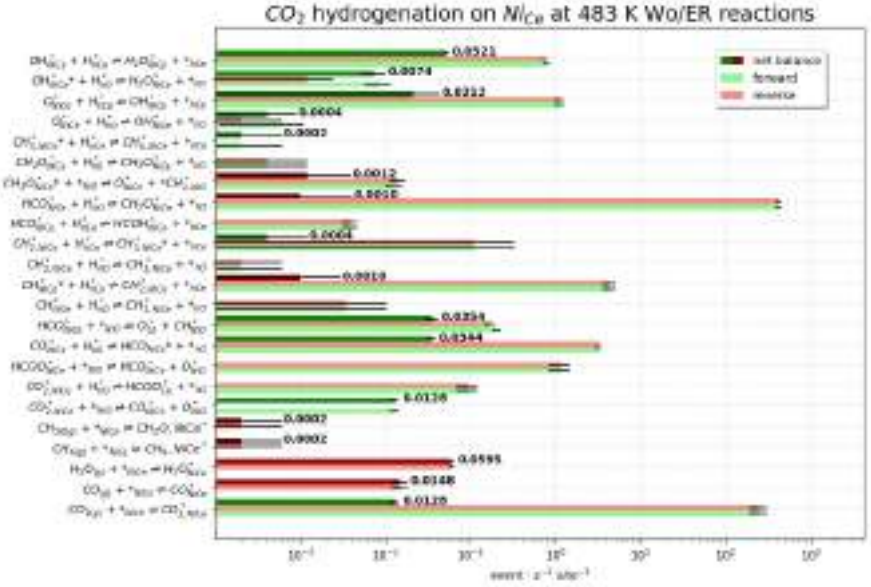
CO_2 hydrogenation on Ni_{Ce} at 483 K Wo/ER reactions
net balance
forward
reverse
0.0521
0.0074
0.0212
0.0004
0.0002
0.0012
0.0026
0.0004
0.0010
0.0294
0.0244
0.0116
0.0007
0.0002
0.0595
0.0148
0.0120

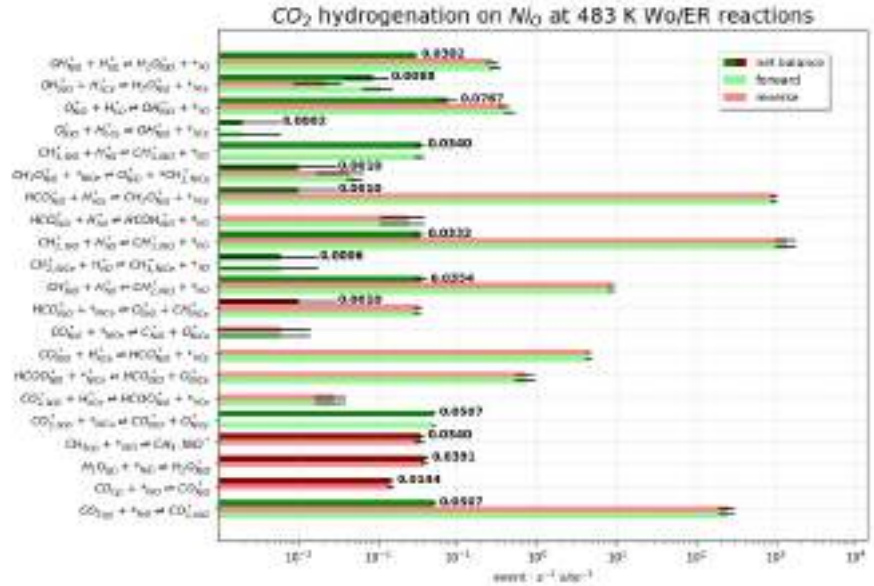
CO_2 hydrogenation on Ni_O at 483 K Wo/ER reactions
net balance
forward
reverse

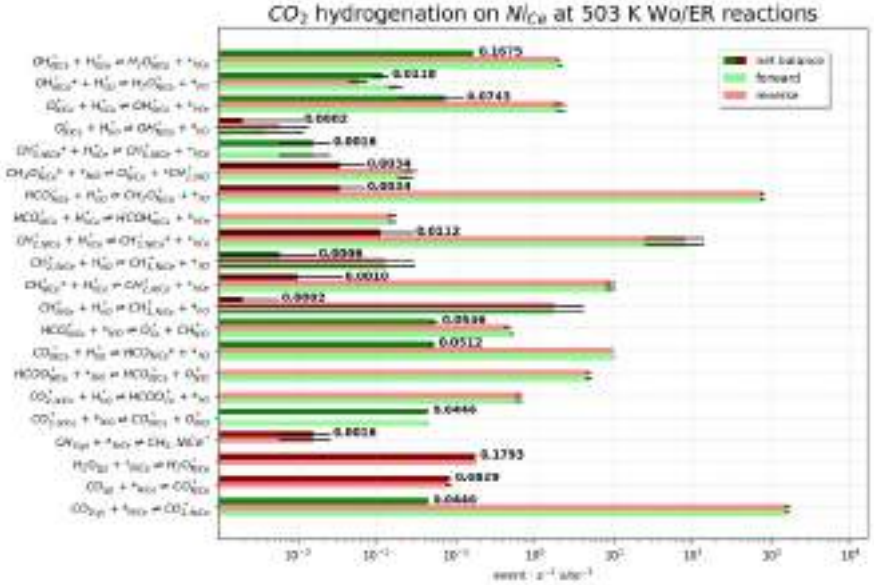
CO_2 hydrogenation on Ni_{Ce} at 503 K Wo/ER reactions
net balance
forward
reverse

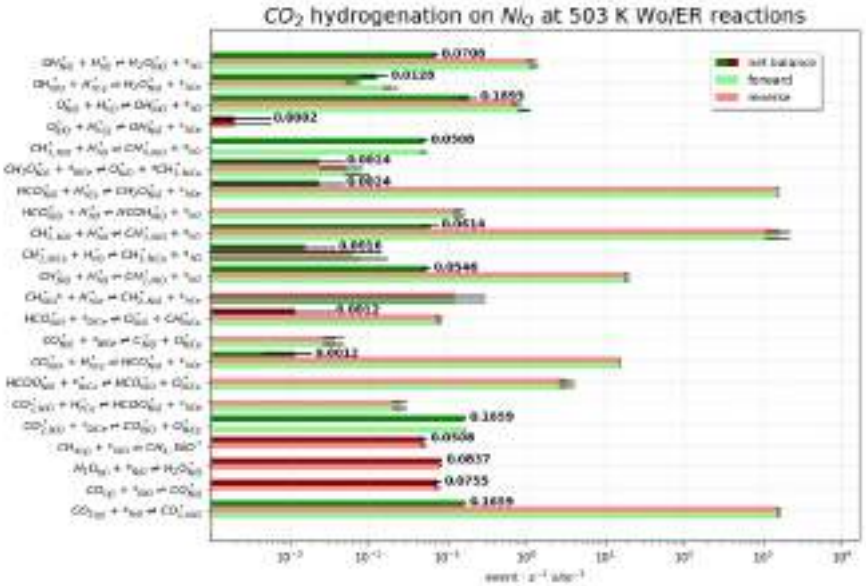
CO_2 hydrogenation on Ni_O at 503 K Wo/ER reactions
net balance
forward
reverse
0.0709
0.0129
0.1892
0.0992
0.0508
0.0034
0.0024
0.0614
0.0016
0.0548
0.0012
0.0012
0.1659
0.0508
0.0837
0.0755
0.1659

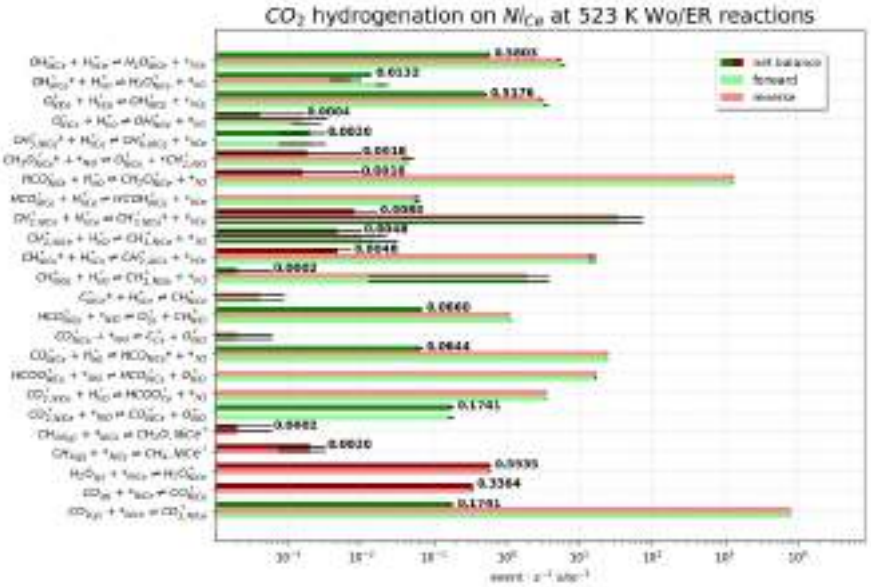
CO_2 hydrogenation on Ni_{Ce} at 523 K Wo/ER reactions
net balance
forward
reverse
0.5003
0.0132
0.3178
0.0004
0.0020
0.0018
0.0018
0.0065
0.0048
0.0002
0.0060
0.0044
0.1741
0.0002
0.0020
0.0935
0.3364
0.1741

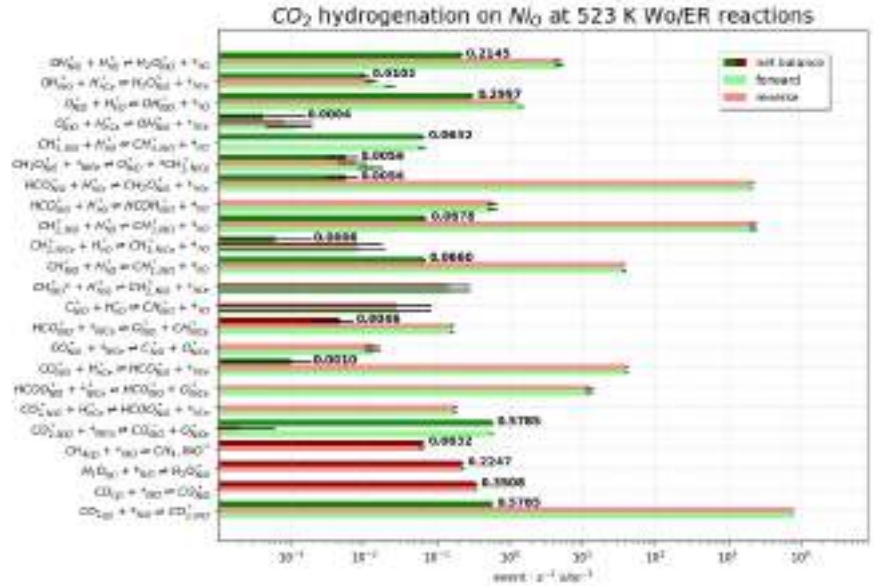
CO_2 hydrogenation on Ni_O at 523 K Wo/ER reactions
net balance
forward
reverse

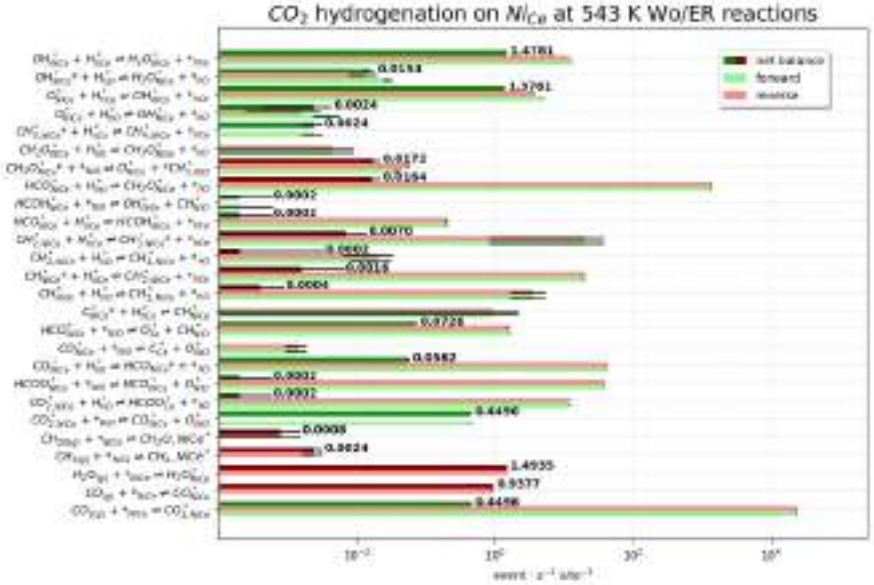
CO_2 hydrogenation on Ni_{Ce} at 543 K Wo/ER reactions
net balance
forward
reverse

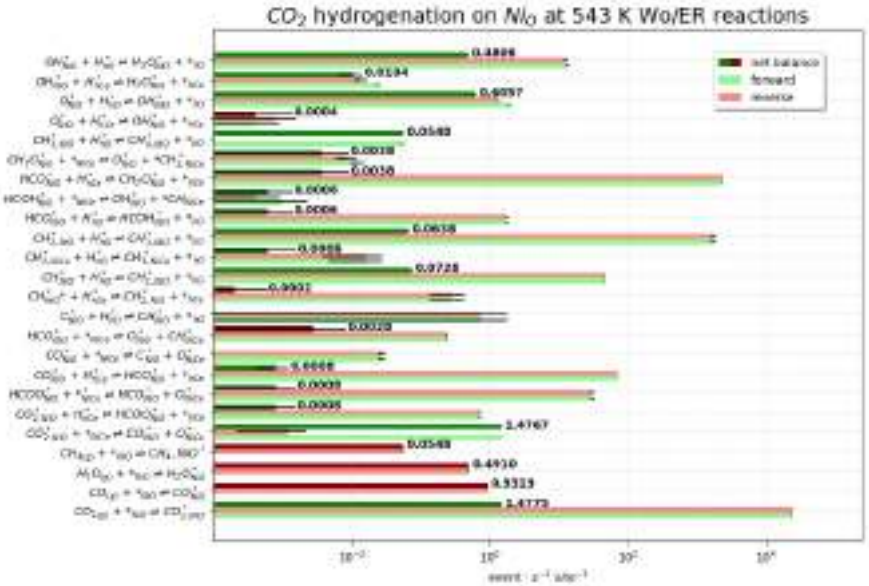
CO_2 hydrogenation on Ni_O at 543 K Wo/ER reactions
net balance
forward
reverse

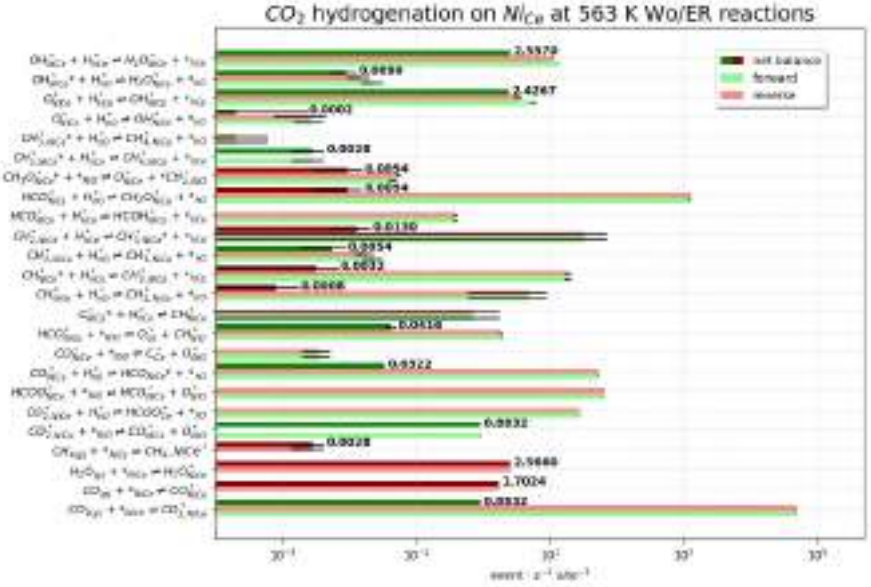
CO_2 hydrogenation on Ni_{Ce} at 563 K Wo/ER reactions
net balance
forward
reverse

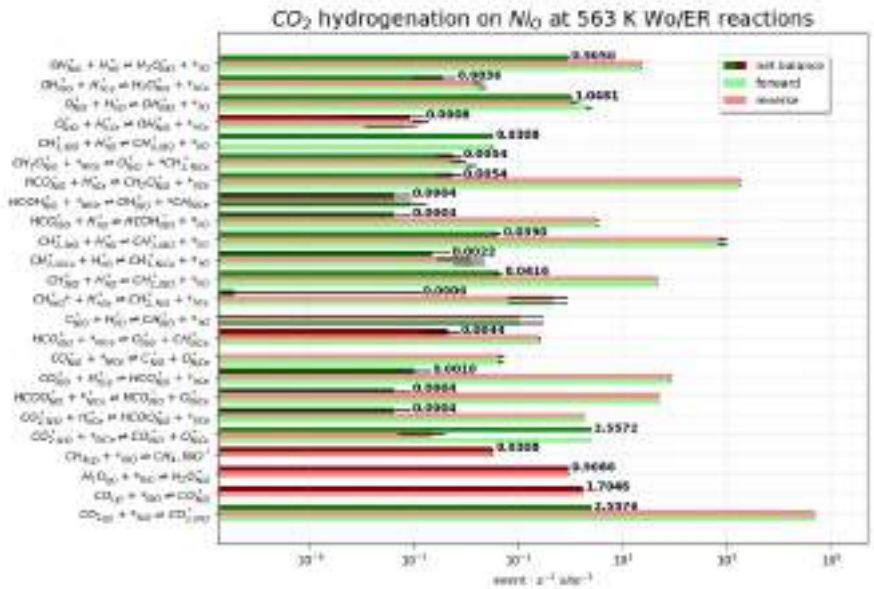

Figure S1. Plots summarizing the event frequencies for the different sites at the different temperature conditions and with $P(H_2)$ = 0.528 bar and $P(CO_2)$ = 0.132 bar, for the simulations with the ER reactions (W/ER) and without the ER reactions (Wo/ER), respectively. Light green and light red stand for the event frequency for the forward and reverse reactions, respectively. The net balance of the reaction is shown by the dark color, depicted by the dark green color for a net forward balance and dark red color for a net reverse balance. Bold numbers represent the number of events · s^{-1} · $site^{-1}$ taken as the average of 5 different kMC runs at the same conditions. Black lines show the standard deviation between the different kMC runs.

REFERENCES

1. Lozano-Reis, P.; Prats, H.; Gamallo, P.; Illas, F.; Sayós R. Multiscale Study of the Mechanism of Catalytic CO_2 Hydrogenation: Role of the Ni(111) Facets. *ACS Catal.*, **2020**, 10, 8077–8089.